



**HAL**  
open science

# Représentation de structures poreuses d'alumine gamma par modélisation numérique

Gabriel Alejandro Ledezma Lopez

► **To cite this version:**

Gabriel Alejandro Ledezma Lopez. Représentation de structures poreuses d'alumine gamma par modélisation numérique. Chemical and Process Engineering. Université de Lyon, 2021. English. NNT : 2021LYSE1333 . tel-03789640

**HAL Id: tel-03789640**

**<https://theses.hal.science/tel-03789640>**

Submitted on 27 Sep 2022

**HAL** is a multi-disciplinary open access archive for the deposit and dissemination of scientific research documents, whether they are published or not. The documents may come from teaching and research institutions in France or abroad, or from public or private research centers.

L'archive ouverte pluridisciplinaire **HAL**, est destinée au dépôt et à la diffusion de documents scientifiques de niveau recherche, publiés ou non, émanant des établissements d'enseignement et de recherche français ou étrangers, des laboratoires publics ou privés.



N°d'ordre NNT : 2021LYSE1333

## **THESE de DOCTORAT DE L'UNIVERSITE DE LYON**

opérée au sein de  
**l'Université Claude Bernard Lyon 1**

**Ecole Doctorale N° 206**  
**Chimie, Procédés, Environnement**

**Discipline :**  
Procédés

Soutenue publiquement le 17/12/2021, par :  
**Gabriel Alejandro Ledezma Lopez**

---

# **Suitable Representations of Gamma Alumina Porous Structures by Computational Modeling**

---

Devant le jury composé de :

Mme. TAYAKOUT-FAYOLLE Mélaz	Professeur des universités, UCBL	Présidente du jury
M. JALLUT Christian	Professeur des universités, UCBL	Directeur de thèse
M. DENOYEL Renaud	Professeur des universités, Aix-Marseille Université	Rapporteur
M. FAVRE Eric	Professeur des universités, Université de Lorraine	Rapporteur
M. RIGBY Sean	Professeur, Université de Nottingham	Examineur
Mme. SPECCHIA Stefania	Professeur, Ecole Polytechnique de Turin	Examinatrice
M. VERSTRAETE Jan	IFPEN	Promoteur
M. SORBIER LOIC	IFPEN	Co-Promoteur
Mme JOLIMAITRE Elsa	IFPEN	Invitée
M. LEINEKUGEL-LE-COCQ Damien	Praticien hospitalier, UCBL	Invité



N°d'ordre NNT : 2021LYSE1333

**THESE de DOCTORAT DE L'UNIVERSITE DE LYON**

Opérée au sein de  
**L'Université Claude Bernard Lyon 1**

**École Doctorale 206**  
**(Chimie, Procédés, Environnement)**

**Spécialité de doctorat : Procédés**  
**Gabriel Alejandro Ledezma Lopez**

**Suitable Representations of Gamma Alumina Porous Structures  
by Computational Modeling**

Devant le jury composé de :

M. FAVRE Eric	LRPG	Rapporteur
M. DENOYEL Renaud	MADIREL	Rapporteur
Mme. SPECCHIA Stefania	PolITO	Examinatrice
Mme. TAYAKOUT-FAYOLLE Mélaz	UCBL	Examinatrice
M. RIGBY Sean	UoN	Examineur
M. JALLUT Christian	UCBL	Directeur de Thèse
M. VERSTRAETE Jan	IFPEN	Promoteur
M. SORBIER LOIC	IFPEN	Co-Promoteur
Mme JOLIMAITRE Elsa	IFPEN	Invitée
M. LEINEKUGEL-LE-COCQ Damien	IFPEN	Invité

December 2021

# **Université Claude Bernard – LYON 1**

Président de l'Université	M. Frédéric FLEURY
Président du Conseil Académique	M. Hamda BEN HADID
Vice-Président du Conseil d'Administration	M. Didier REVEL
Vice-Président du Conseil des Etudes et de la Vie Universitaire	M. Philippe CHEVALLIER
Vice-Président de la Commission de Recherche	M. Petru MIRONESCU
Directeur Général des Services	M. Pierre ROLLAND

## **COMPOSANTES SANTE**

Département de Formation et Centre de Recherche en Biologie Humaine	Directrice : Mme Anne-Marie SCHOTT
Faculté d'Odontologie	Doyenne : Mme Dominique SEUX
Faculté de Médecine et Maïeutique Lyon Sud - Charles Mérieux	Doyenne : Mme Carole BURILLON
Faculté de Médecine Lyon-Est	Doyen : M. Gilles RODE
Institut des Sciences et Techniques de la Réadaptation (ISTR)	Directeur : M. Xavier PERROT
Institut des Sciences Pharmaceutiques et Biologiques (ISBP)	Directrice : Mme Christine VINCIGUERRA

## **COMPOSANTES & DEPARTEMENTS DE SCIENCES & TECHNOLOGIE**

Département Génie Electrique et des Procédés (GEP)	Directrice : Mme Rosaria FERRIGNO
Département Informatique	Directeur : M. Behzad SHARIAT
Département Mécanique	Directeur M. Marc BUFFAT
Ecole Supérieure de Chimie, Physique, Electronique (CPE Lyon)	Directeur : Gérard PIGNAULT
Institut de Science Financière et d'Assurances (ISFA)	Directeur : M. Nicolas LEBOISNE
Institut National du Professorat et de l'Education	Administrateur Provisoire : M. Pierre CHAREYRON
Institut Universitaire de Technologie de Lyon 1	Directeur : M. Christophe VITON
Observatoire de Lyon	Directrice : Mme Isabelle DANIEL
Polytechnique Lyon	Directeur : Emmanuel PERRIN
UFR Biosciences	Administratrice provisoire : Mme Kathrin GIESELER
UFR des Sciences et Techniques des Activités Physiques et Sportives (STAPS)	Directeur : M. Yannick VANPOULLE
UFR Faculté des Sciences	Directeur : M. Bruno ANDRIOLETTI

## Acknowledgments

I want to thank God for always inspiring me to pursue the mysteries of his creation through science.

I want to thank IFPEN for providing the material resources for this research work. Thanks to Dr. Cécile Barrère-Tricca (head of the IFPEN-Lyon site), Dr. Pierre Porot (head of the Process Design and Modeling Division), Dr. Christophe Boyer (head of the department of the Reactions and Chemical Reactors Modeling), and Dr. Andreas Ehinger (head of the Doctoral Studies).

I would like to express my gratitude to LAGEPP (Laboratoire d'Automatique, de Génie des Procédés et de Génie Pharmaceutique) for counting me among its members too.

I would like to thank my thesis director Prof. Christian Jallut (LAGEPP) for all his time and support. I enjoyed a lot our scientific discussions. I would like to thank also my supervisors Dr. Jan Verstraete (IFPEN), Dr. Loïc Sorbier (IFPEN), Dr. Damien Leinekugel Le-Cocq (IFPEN), and Dr. Elsa Jolimaitre (IFPEN) for their support and scientific spirit.

Thanks, Jan, for all the experiences we have shared. You are a teacher, a role model, and a friend. If I could choose you again as my supervisor, I would choose you the same number of pores that are in 1 gram of gamma alumina.

Thanks to Isabel Sebbane (Secretary R12) and Martine Glo (Secretary R12) for their support.

I would like to thank all my teachers and professors. It would be difficult to name them all here, but I would like them to know that they have my deepest respect and gratitude. There are 2 special teachers I would like to thank for introducing me to science at the tender age of 8 years, Mrs. Dilia Ramos and Mrs. Carmen Machin. I want to express my gratitude to Prof. Juan Matos Lale for his guidance, the time, and experiences we shared, and for becoming my friend.

Thanks to my dear friends and colleagues: Giulia, Aleksandra, Polina, Maxime, Florencia, Kris, Edoardo, Lucas, Laura M, Laura DC, Viktor, Mehdi, Adam, Giovannino, Iana, Deisy, Ricardo, Alberto, Maria, Raquel, Andrea, Angela, Gonzague, Jose Luis, Jose Angel, Moira, Erika, Conor, Jorge, Jhon, David, Adriana, Stefano, Miguel, Mei, Jhonathan, Luz, Manuel M., Jesus V.

I would like to thank my beloved parents, aunt, and sister for always being there. Thanks to all my family for their love and support.

Thanks, Estefany, for joining me during the first part of this adventure.

**Sometimes I think that life can be described with a population balance equation.** What are we for our universe but dust? A grain of dust that travels in space and time. A grain which *exchanges* mass with other grains (friends, families, acquaintances, role models) through interactions. Part of ourselves will be *lost* in this travel. We will *gain* some mass when particles of other grains will aggregate to us, and parts of us will aggregate to other grains as a result of our exchanges. Finally, we will *generate* some mass through our inventions, ideas, beliefs, and motivations. A quantity of mass so small that at a cosmic scale someone will consider that it cannot be measured, or it can be considered null (which is a nice particle accelerator joke).

Thanks to all of you. You are and will be a part of me and my work.

To Maria Dolores Lopez Arrieta and Eliut Oswaldo Velazquez Blanco.

## **Abstract**

Porous materials are widely used in chemical engineering. At the mesoporous scale, confinement effects influence the thermodynamic of the system and the transport conditions. Indeed, the architecture of the pore network is the origin of mass transfer limitations within disordered porous materials. Therefore, it is important to understand not just the textural properties of the solid but also its pore network characteristics.

Gamma-alumina is a disordered porous material with an elevated tortuosity very often used in the oil refining and petrochemistry, whose topology is not yet fully understood (1, 43, 44). Recent research articles propose that this material has different pore domains, each one characterized by its own pore size distribution and void fraction (45). The interplay among these different levels clearly plays a role in effective diffusion.

This work intends to better understand the textural and topological descriptors of gamma alumina by creating a digital representation of it. The catalyst is represented using a pore network model. The pore network representation is then characterized using originally developed computational equivalents of textural and mass transfer characterization techniques. The experimental validation was done through the generation of digital twins for real gamma alumina samples.

Using diffusion simulations on the pore network model fitted to the nitrogen sorption curves, a tortuosity factor was predicted that differs by less than 20% from the tortuosity factor measured by PFG-NMR. This illustrates how a digital twin allows to provide a reasonable estimate for the tortuosity factor from readily available nitrogen porosity experiments.

The research work in this thesis is the start of the path to ultimate goal of improving the catalytic performance of disordered porous catalyst by the digital optimal design of the material architecture. At the same time, the accuracy of the models used to design and evaluate heterogeneous reactor performance will be improved.

### **Keywords**

Gamma Alumina Supports, Pore Network Models, Computational Characterization, Diffusion in Porous Media, Digital Twin.

# Résumé

Les matériaux poreux sont largement utilisés en génie chimique. À l'échelle mésoporeuse, les effets de confinement influencent la thermodynamique et les conditions de transport. En effet, l'architecture du matériau poreux peut augmenter les limitations de transfert de masse à l'intérieur du catalyseur. Par conséquent, comprendre non seulement les propriétés texturales mais aussi la topologie du solide est important pour améliorer les performances du catalyseur et la précision des différents modèles permettant de concevoir et d'évaluer les performances des réacteurs hétérogènes. L'alumine gamma est un matériau poreux désordonné à tortuosité élevée très souvent utilisé dans le raffinage du pétrole et la pétrochimie, dont la topologie n'est pas encore totalement comprise (1, 43, 44). Des articles de recherche récents suggèrent que ce matériau a différents domaines de pores, chacun caractérisé par sa propre distribution de taille de pores et sa propre fraction de vide (45). L'interaction entre ces différents niveaux joue clairement un rôle dans une diffusion efficace. En créant des jumeaux numériques d'échantillons réels d'alumine, il est possible de mieux comprendre comment les propriétés texturales et la topologie du réseau influencent la diffusion à travers le réseau à un niveau fondamental. Dans ce travail, un modèle de génération de réseau de pores rapide et flexible est créé. Ensuite, différents algorithmes pour caractériser le réseau de pores numériques sont développés. Ces algorithmes simulent la porosimétrie à l'azote, la porosimétrie au mercure, la cryoporométrie et la résonance magnétique nucléaire à gradient de champ pulsé (PFG-RMN). Un jumeau numérique d'alumine gamma est finalement créé en optimisant les paramètres d'entrée du modèle de réseau de pores pour s'adapter à une isotherme de sorption mesurée expérimentalement. En utilisant des simulations de diffusion sur le modèle de réseau de pores ajusté aux courbes de sorption d'azote, un facteur de tortuosité a été prédit qui diffère de moins de 20 % du facteur de tortuosité mesuré par PFG-RMN. Cela illustre comment un jumeau numérique permet de fournir une estimation raisonnable du facteur de tortuosité à partir d'expériences de porosité à l'azote facilement disponibles.

## Mots clés

Supports d'alumine gamma ; Modèles de réseau de pores ; Caractérisation numérique ; Diffusion en milieux poreux ; Jumeau numérique.

# Scientific Production

## 1. ARTICLES

- Ledezma Lopez, Gabriel Alejandro; Verstraete, Jan J.; Sorbier, Loïc; Leinekugel-Le-Cocq, Damien; Jolimaitre, Elsa; Jallut, Christian: **Computational Characterization Techniques Applied to Pore Network Models by Using a Fast Percolation Algorithm**, Chemical Engineering Science, 2022 (accepted).
- Ledezma Lopez, Gabriel Alejandro; Verstraete, Jan J.; Sorbier, Loïc; Glowska, Aleksandra; Leinekugel-Le-Cocq, Damien; Jolimaitre, Elsa; Jallut, Christian: **Generation of  $\gamma$ -Alumina Digital Twins Using a Nitrogen Porosimetry Simulation**. Industrial & Engineering Chemistry Research, 2021, vol. 60 (46), p. 16728–16738. <https://doi.org/10.1021/acs.iecr.1c02849>.
- Ledezma, G.; Verstraete, J. J.; Sorbier, L.; Leinekugel-Le Cocq, D.; Jolimaitre, E.; Jallut, C.: **Computational Characterization of a Pore Network Model by Using a Fast Nitrogen Porosimetry Simulation**, Computer Aided Chemical Engineering, 2021, vol. 50, p. 1111-1116, <https://doi.org/10.1016/B978-0-323-88506-5.50171-6>.

## 2. CONFERENCES

- **Using Pore Network Models to Characterize the Topology of Gamma Alumina Samples** (Oral presentation), 11<sup>th</sup> International Colloids Conference 2022, Lisbon (Portugal), June 12-15, 2022.
- **Computational Characterization of Pore Network Models for Gamma-Alumina Catalysts** (Oral presentation), 2022 AIChE Spring Meeting and 18<sup>th</sup> Global Congress on Process Safety, San Antonio, TX (USA), April 10-14, 2022.
- **Pore Network Models: Computer Representation of Experimental Characterization Techniques** (Oral presentation), 26<sup>th</sup> International Symposium on Chemical Reaction Engineering (ISCRE26), New Delhi (India), December 5-8, 2021.
- **Modelling intragranular transport: Digitalization of a  $\gamma$ -alumina support by implementing computational versions of three different characterization techniques** (Oral presentation), XXIV International Conference on Chemical Reactors (CHEMREACTOR-24), Milan (Italy), September 12-17, 2021.
- **Modelling intragranular transport in a catalytic reactor: Descriptors and representation of the porous structure** (Oral presentation), 11<sup>th</sup> International Symposium on Catalysis in Multiphase Reactors (CAMURE-11) and 10<sup>th</sup> International Symposium on Multifunctional Reactor (ISMR-10), Milan (Italy), March 21-24, 2021.
- **Computational Characterization of a Pore Network Model by Using a Fast Nitrogen Porosimetry Simulation** (Poster), 31<sup>st</sup> European Symposium on Computer Aided Process Engineering (ESCAPE-31), Istanbul (Turkey), June 6-9, 2021.
- **Porous network modeling - synthesis and discussion** (Oral presentation), Workshop on Scale-up Methodologies for Innovative Materials (Scale4MAT), Lyon (France), November 24-25, 2020.

- **Modelling intragranular transport: Implementing virtual versions of three characterization techniques to generate digital representations of  $\gamma$ -alumina supports** (Oral presentation), Journée Scientifique 2020 du CODEGEPRA (Comité de Développement du Génie des Procédés en Rhône-Alpes Auvergne), Clermont-Ferrand (France), November 19, 2020.
- **Modelling intragranular transport in a catalytic reactor: Descriptors and representation of the porous structure** (Oral presentation + Poster), Journée Scientifique 2019 du CODEGEPRA (Comité de Développement du Génie des Procédés en Rhône-Alpes Auvergne), Lyon (France), November 21, 2019.

# Table of Contents

GENERAL INTRODUCTION .....	1
OUTLINE OF THE THESIS .....	3
Chapter 1: Context .....	4
1.1. Introduction .....	4
1.2. Objective and general strategy.....	5
Chapter 2: Gamma Alumina porous structure modeling and characterization – State of the Art.....	9
2.1. Alumina crystalline structure .....	9
2.2. Alumina synthesis and shaping .....	12
2.2.1. Solution Chemistry .....	12
2.2.2. Industrial Synthesis .....	13
2.2.3. Shaping for Catalyst Industry .....	14
2.3. Alumina porous structure.....	15
2.4. Classification of pore structure models.....	17
2.4.1. Heterogeneous models .....	20
2.4.2. Grain-Based Models .....	21
2.4.3. Pore Network models.....	22
2.5. Porous structure experimental characterization techniques.....	22
2.6. Pore Network Models: state of the art .....	30
Chapter 3: Pore Network Model Generation.....	43
3.1. Introduction .....	43
3.2. Pore Network Model (PNM).....	43
3.3. Input variables of the pore network model .....	44
3.3.1. Network size and dimensions .....	44
3.3.2. Grid distortion .....	45
3.3.3. Network lattice and connectivity pattern .....	46
3.3.4. Periodicity.....	47
3.3.5. Pore populations .....	47
3.3.6. Skeletal density .....	50

3.4.	Pore network construction.....	50
3.4.1.	Generation of the grid of nodes.....	50
3.4.2.	Generation of pores on the edges .....	51
3.4.3.	Generation of pores on the nodes .....	53
3.4.4.	Calculation of geometrical textural properties.....	53
3.4.5.	Output files with the network structural information .....	55
3.4.6.	Some examples of generated pore networks .....	56
3.4.7.	Conclusions.....	59
3.5.	Pore network minimum size and minimum number of generations.....	59
3.5.1.	Minimum size of the pore network.....	60
3.5.2.	Minimum number of network generations .....	62
3.6.	Sensitivity study on the average textural properties .....	64
3.7.	Percolation algorithm .....	66
3.7.1.	Pore Blocking Phenomenon .....	66
3.7.2.	Existing Invasion Percolation Algorithms.....	68
3.7.3.	The triggering diameter algorithm.....	69
3.7.4.	Binary Heap Algorithms.....	74
3.8.	Topological analysis of the pore network model .....	78
3.8.1.	Effect of the maximum connectivity .....	80
3.8.2.	Effect of the pore existence probability.....	82
3.8.3.	Effect of the Pore Size Distribution .....	84
3.8.4.	Effect of multiple populations.....	85
3.9.	Tortuosity of the pore network .....	92
3.9.1.	Diffusion simulation methodology and tortuosity factor estimation.....	92
3.9.2.	Influence of the pore network generation parameters on tortuosity.....	94
3.10.	Conclusion.....	100
Chapter 4: Simulating textural characterization techniques .....		102
4.1.	Introduction .....	102
4.2.	Methodology .....	103
4.3.	Nitrogen sorption simulation .....	103

4.3.1.	Thermodynamic Model .....	103
4.3.2.	Triggering diameter assignment for decreasing pressure step .....	104
4.3.3.	Nitrogen volume calculation .....	105
4.3.4.	Characteristic curve generation .....	106
4.3.5.	Scanning curves .....	106
4.3.6.	Brunauer, Emmett Teller (BET) surface area .....	108
4.3.7.	BJH Pore Size Distribution .....	109
4.4.	Mercury Intrusion Porosimetry .....	110
4.4.1.	Mechanical model .....	110
4.4.2.	Triggering diameter assignment adaptation .....	111
4.4.3.	Mercury volume calculation .....	111
4.4.4.	Characteristic curve generation .....	112
4.5.	Cryoporometry .....	112
4.5.1.	Thermodynamic Model .....	112
4.5.2.	Triggering diameter assignment adaptation .....	113
4.5.3.	Frozen volume calculation .....	113
4.5.4.	Characteristic curve generation .....	113
4.6.	Case Study .....	114
4.6.1.	Network Parameters .....	115
4.6.2.	Execution Time .....	115
4.6.3.	Connectivity Effect .....	116
4.6.4.	Execution time to generate a network with low variability .....	117
4.6.5.	Characteristic Curves .....	118
4.7.	Conclusions .....	121
Chapter 5: Parametric sensitivity analysis for the digital characterization techniques .....		122
5.1.	Nitrogen sorption .....	122
5.1.1.	Effect of the connectivity .....	125
5.1.2.	Effect of the pore existence probability (PEP) .....	126
5.1.3.	Effect of the average diameter of the pore size distribution .....	127
5.1.4.	Effect of the width of the pore size distribution .....	128

5.1.5. Summary .....	129
5.2. Mercury porosimetry.....	130
5.2.1. Effect of the connectivity .....	133
5.2.2. Effect of the pore existence probability (PEP) .....	133
5.2.3. Effect of the average diameter of the pore size distribution.....	134
5.2.4. Effect of the width of the pore size distribution .....	135
5.3. NMR Cryoporometry .....	136
5.3.1. Effect of the connectivity .....	138
5.3.2. Effect of the pore existence probability (PEP) .....	139
5.3.3. Effect of the average diameter of the pore size distribution.....	139
5.3.4. Effect of the width of the pore size distribution .....	140
Chapter 6: Porous model validation from porosimetry experiments.....	142
6.1. Alumina characterization.....	142
6.2. Pore network model parameter estimation.....	144
6.3. Conclusions.....	149
Chapter 7: Simulation of PFG-NMR experiments .....	151
7.1. Introduction .....	151
7.2. NMR Fundamentals .....	151
7.2.1. The nuclear spin .....	151
7.2.2. Spin Dynamics .....	152
7.2.3. Pulsed Field Gradient (PFG)-NMR .....	159
7.3. PFG-NMR experiment simulation model.....	168
7.3.1. Hypothesis.....	169
7.3.2. Methodology .....	170
7.4. Case study.....	174
7.5. Conclusions.....	176
Chapter 8: Conclusions and Future Work .....	177
8.1. Conclusions.....	177
8.2. Perspectives.....	180
Publication bibliography.....	182

APPENDICES.....202

## List of Figures

Figure 1. SEM images for two different representative alumina samples .....	5
Figure 2. Comparison between the tortuosity values obtained through stack correlations and experimental tortuosity values obtained by inverse chromatography. ....	6
Figure 3. General strategy of the present Ph.D. thesis .....	7
Figure 4. Dehydration temperature of the aluminum (oxy)hydroxides .....	9
Figure 5. Phase evolution of boehmite to alpha alumina as a function of temperature. ....	11
Figure 6. TEM of different morphologies of alumina elementary platelets. ....	16
Figure 7. Schematic distribution of pore volume distribution. ....	16
Figure 8. Influence of the orientation of aggregates on the porous structure. ....	17
Figure 9: Atomistic perspective of ZSM-5; silicon atoms are in yellow, oxygen atoms in red. ....	19
Figure 10: Extraction of Hollington sandstone pore network using watershed segmentation algorithm. ....	21
Figure 11. Intrusion/Extrusion Mercury Porosimetry typical curve. ....	26
Figure 12. Simulation snapshots of argon particles in graphitic cylindrical pores at 87.3 K before condensation and after evaporation. ....	27
Figure 13. Isotherm and hysteresis loop classification. ....	27
Figure 14. Examples of statistical thickness models. ....	29
Figure 15. Representation of three pores in a row. ....	29
Figure 16. Examples of regular transversal pore sections. ....	32
Figure 17. Different lattice examples. ....	32
Figure 18. 2D Cylinders and spheres regular square lattice pore network representation. ....	33
Figure 19. Cross-linked capillary model representation .....	34
Figure 20. 2D representation of the hierarchical pore network used by Gladden in 1992 .....	35
Figure 21. 3D representation of the pore network used by Spearing and Matthews in 1991. ....	36
Figure 22. Pore-network modeling of biofilm evolution in porous media .....	37
Figure 23. Dual site-bond network representation. ....	38
Figure 24. Graphical representation of a corrugated pore structure model (CPSM). ....	40
Figure 25. Huang pore network representation .....	40
Figure 26. Different fluid configurations for biphasic flow in a pore from the network .....	40
Figure 27. Sadeghi's model .....	41
Figure 28. Four different kinds of pore networks with one-holed ring border conditions .....	42
Figure 29. Random relocations for a node when grid distortion is activated. ....	45
Figure 30. Pore length distribution for a 2D pore network with a spacing of the fixed grid equal to 30 nm and a Grid distortion equal to 30 nm. ....	46
Figure 31. Different lattice representations and their unitary vectors. ....	46
Figure 32. Example of a network with periodicity in the X-direction. ....	47

Figure 33. Pore networks with different grid spacings. ....	48
Figure 34. Wrong representation of a pore network with 2 different pore populations. ....	49
Figure 35. Network with two pore populations. ....	49
Figure 36. Network with two pore populations. ....	50
Figure 37. Labelling sequence for nodes. ....	51
Figure 38. Labelling sequence process for pores in a network with PEP=1. ....	52
Figure 39. Periodic networks. ....	52
Figure 40. 2D Schematic representation of an elementary system node-pore for a square lattice with PEP equal to 1. ....	53
Figure 41. Pore label algebraic sign. ....	56
Figure 42. Example of different possible 2D configurations generated by the program. ....	57
Figure 43. Transversal section of 6 different pore networks. ....	58
Figure 44. Textural properties for different network sizes. ....	61
Figure 45. Average textural properties as a function of the number of generations. ....	63
Figure 46. Porosity for different pore network input configurations. ....	64
Figure 47. Specific pore volume for different pore network input configurations. ....	65
Figure 48. Specific surface area for different pore network input configurations. ....	65
Figure 49. Pore blocking phenomenon in a 2D pore network during mercury intrusion. ....	66
Figure 50. Pore blocking phenomenon in a 2D pore network during nitrogen desorption. ....	67
Figure 51. Triggering Diameter Algorithm. ....	70
Figure 52. Triggering diameter algorithm flow diagram. ....	73
Figure 53. Two-dimensional array for the dynamic list. ....	75
Figure 54. Algorithm Flowchart. Max Heap: Elimination Operation. ....	76
Figure 55. Algorithm Flowchart. Max Heap: Addition Operation. ....	76
Figure 56. Algorithm Flowchart. Max Heap: Elimination Operation. ....	77
Figure 57. Algorithm Flowchart. Max Heap: Bottom-Up Approach. ....	78
Figure 58. Variables that influences the topology, percolation and volume distribution of the network. ....	79
Figure 59. Effect of the maximum connectivity on the topological map. ....	81
Figure 60. Average Diameter by class (ADC) as a function of $f_e$ . ....	82
Figure 61. CVPF by class (CVPF_C) as a function of $f_e$ . ....	82
Figure 62. Number connectivity distribution for a triangular network ( $Z_{max}=6$ ). ....	83
Figure 63. Effect of the connectivity on the topological map. ....	84
Figure 64. Influence of the pores size distribution on the percolation map. ....	85
Figure 65. Pore network with a PEP=0.2. ....	86
Figure 66. Pore network with two different populations. ....	86
Figure 67. Domain sensitivity to PEP. ....	87
Figure 68. Domain size. ....	88

Figure 69. Cumulated explored percentage by population as a function of $f_e$ and pore connectivity distribution by population .....	90
Figure 70. Cumulated explored percentage by population as a function of $f_e$ and pore connectivity distribution by population .....	91
Figure 71. Variation of the tortuosity as a function of the PEP. ....	94
Figure 72. Variation of the tortuosity as a function of the pore average diameter. ....	95
Figure 73. Variation of the tortuosity as a function of the PSD standard deviation.....	96
Figure 74. Variation of the tortuosity as a function of the pore length.....	97
Figure 75. Variation of the tortuosity as a function of the grid distortion. ....	98
Figure 76. Variation of the tortuosity as a function of the PEP of the population 1. ....	99
Figure 77. SEM microscopies for two gamma alumina's A and B.....	100
Figure 78. PFG NMR tortuosity measurements for 5 gamma alumina's A, B, C, D and E.....	100
Figure 79. Elements of the algorithm for the characterization techniques simulations. ....	103
Figure 80. Representation of an example network of three pores. ....	105
Figure 81. Scanning curves input change logic .....	107
Figure 82. Modification on the nitrogen simulation algorithm for the scanning curves.....	108
Figure 83. Algorithm's modification for scanning curves .....	108
Figure 84. 2D Schematic representation of an elementary system node-pore for a square lattice with PEP equal to 1 .....	114
Figure 85. Comparison between the input and output CDF. ....	115
Figure 86. Effect of the network size on the algorithm's execution time for nodes with zero volume.....	116
Figure 87. Effect of the network size on the algorithm's execution time for nodes with volume. ....	116
Figure 88. Effect of the connectivity on the algorithm's execution time for nodes with zero volume.....	117
Figure 89. Effect of the connectivity on the algorithm's execution time for nodes with volume .....	117
Figure 90. Nitrogen sorption simulation output .....	119
Figure 91. Mercury intrusion simulation output: .....	119
Figure 92. Cryoporometry simulation output .....	120
Figure 93. Nitrogen sorption simulation output: Numerical Scanning Curves .....	120
Figure 94. Major indicators on a nitrogen isotherm .....	123
Figure 95. Analysis of the Kelvin equation and the Harkin Jura statistical thickness .....	124
Figure 96. Core and adsorbed layer volume fraction as a function of the relative pressure calculated using the Kelvin-Cohan for a cylindrical pore. ....	125
Figure 97. Effect of the connectivity on the nitrogen isotherm. ....	126
Figure 98. Effect of the pore existence probability on the nitrogen isotherm. ....	127

Figure 99. Effect of the average pore diameter on the nitrogen isotherm. ....	128
Figure 100. Effect of the pore existence probability variance on the nitrogen isotherm .....	129
Figure 101. Major indicators on a mercury intrusion curve. ....	131
Figure 102. Washburn equation derivative .....	132
Figure 103. Effect of the connectivity on the mercury intrusion curve. ....	133
Figure 104. Effect of the pore existence probability on the mercury intrusion curve. ....	134
Figure 105. Effect of the average pore diameter on the mercury intrusion curve.....	135
Figure 106. Effect of the width of the pore size distribution on the mercury intrusion curve....	135
Figure 107. Major indicators on a cryoporometry curve .....	136
Figure 108. Gibbs-Thompson equation derivative.....	137
Figure 109. Core and plastic ice layer volume fraction as a function of the temperature calculated using the Gibbs-Thompson thermodynamic model. ....	138
Figure 110. Effect of the connectivity on the cryoporometry curve. ....	138
Figure 111. Effect of the pore existence probability on the cryoporometry curve. ....	139
Figure 112. Effect of the average pore diameter on the cryoporometry curve. ....	140
Figure 113. Effect of the width of the pore size distribution on the cryoporometry curve. ....	141
Figure 114. Cubic section of one of the full networks .....	145
Figure 115. Experimental Isotherm compared to the simulated Isotherm .....	146
Figure 116. Experimental scanning curves compared to the simulated scanning curves. ....	148
Figure 117. BJH pore size distribution obtained from the desorption branch. ....	149
Figure 118. Proton spin energy differences .....	153
Figure 119. Vectorial representation .....	153
Figure 120. Magnetic moments orientations.....	154
Figure 121 Spin-Echo sequence .....	157
Figure 122 Vectorial model of a Spin-Echo sequence.....	158
Figure 123 Spin resonance and spin coherence.....	160
Figure 124 Stejskal and Tanner pulse sequence .....	161
Figure 125 Spins with different Larmor Frequencies .....	161
Figure 126. Phase Shift ( $\varphi$ ) after diffusion process. ....	162
Figure 127. Progression of the magnitude of the total magnetization vector as a function of the distance .....	162
Figure 128 PFG-NMR Signal decay .....	163
Figure 129 Signal attenuation progression comparison for free diffusion and restricted diffusion in a spherical medium. ....	165
Figure 130 Restricted diffusion regimes according to Price's Criteria reference .....	166
Figure 131. Simulation approaches.....	168
Figure 132. PFG-NMR simulation block diagram .....	169
Figure 133. Post treatment discretization for the PFG NMR simulation .....	171

Figure 134. Tracer pores graphical representation.....	172
Figure 135. Active zone graphical description .....	173
Figure 136. Simulations scheme for each $\Delta$ .....	174
Figure 137. Attenuation curve for network of PEP=0.71 .....	175
Figure 138. Tortuosity for different PEP using the PFG-NMR simulation and the semi-infinite plate simulation.....	176

## List of Tables

Table 1. Alumina polymorphisms.....	10
Table 2. Conventional characterization techniques for porous solids.....	22
Table 3. Connectivity matrix.....	55
Table 4. Pore dimensions and connections.....	55
Table 5. Minimum pore network dimension as a function of the pore network model input parameters .....	62
Table 6. Pore volume percentage represented by different populations .....	88
Table 7. Boundary conditions.....	93
Table 8. Conditions used to analyze the influence of PEP on the tortuosity factor .....	94
Table 9. Conditions used to analyze the influence of average diameter of a gaussian PSD on the tortuosity factor .....	95
Table 10. Conditions used to analyze the influence of the standard deviation of gaussian PSD on the tortuosity factor .....	96
Table 11. Conditions used to analyze the influence of the length on the tortuosity factor.....	97
Table 12. Conditions used to analyze the influence of length distortion on the tortuosity factor .....	98
Table 13. Conditions used to analyze the influence of different PEP in a hierarchical network on the tortuosity factor .....	99
Table 14. Execution time for the minimum required size of the network for NS. ....	117
Table 15. Execution time for the minimum required size of the network for MP. ....	118
Table 16. Execution time for the minimum required size of the network for CP.....	118
Table 17. Execution time for the minimum required size of the network for NS by using the Fortran 90 sorting algorithm. ....	118
Table 18. Kelvin equation relevant ranges.....	125
Table 19. Effect of the different input variables on the sorption isotherm.....	130
Table 20. Washburn equation relevant ranges.....	132
Table 21. Gibbs-Thompson thermodynamic model relevant ranges .....	137
Table 22. Molecular size and dipole moment of organic liquids used for diffusion measurements .....	143
Table 23. Acquisition parameters for PFG-NMR experiments.....	143
Table 24. Estimated parameters for the pore network generation .....	145
Table 25. Parameters used for the PFG-NMR ideal case simulation .....	175

## List of symbols

$B$	Magnetic field (T)
$C$	Concentration ( $\text{m}^3/\text{Kg}$ )
$D$	Diameter (m)
$D_p$	Pore Diameter (m)
$Db$	Biggest diameter (m)
$D_{eff}$	Effective diffusion coefficient ( $\text{m}^2/\text{s}$ )
$D_{eq}$	Equivalent diameter (m)
$D_m$	Diffusion coefficient ( $\text{m}^2/\text{s}$ )
$Ds$	Smallest diameter (m)
$E$	PFG-NMR Signal (???)
$fa$	Adsorbed volume fraction (-)
$fc$	Liquefaction volume fraction (-)
$fe$	Explored fraction (-)
$g$	gradient intensity (T/m)
$h$	Planck's constant ( $\text{m}^2 \text{ kg} / \text{s}$ )
$J$	Molar flux ( $\text{mol} \cdot \text{m}^{-2} \cdot \text{s}^{-1}$ )
$\kappa$	Boltzmann constant ( $\text{m}^2 \text{ kg} \text{ s}^{-2} \text{ K}^{-1}$ )
$L$	Pore length (m)
$L_{AZ}$	Active zone dimension (m)
$L_{\text{distort}}$	Distortion length (m)
$L_N$	Network Length (m)
$L_p$	Pore Length (nm)
$M_T$	Total mass (Kg)
$N_T$	Total number of nodes (-)
$N_t$	Total number of tracers (-)
$N_{\text{pores}}$	Number of Pores (-)
$N_X$	Number of nodes along the X direction (-)
$N_Y$	Number of nodes along the Y direction (-)
$N_Z$	Number of nodes along the Z direction (-)
$N_T \text{Edges}$	maximum initial total number of edges (-)
$N_p$	Number of pores (-)
$n_{\text{exp}}$	number of explored pores (-)
$n_m$	capacity of the monolayer (???)
$np_{\text{class}}$	number of pores by class (-)
$P$	Propagator (???)
$p^0$	Reference pressure (bar)
$PEP$	Pore existence probability (-)
$\overline{prop}$	Average property
$P_v$	Vapor Pressure (bar)
$R$	Universal constant of gases (J/mol/K)

$r$	Radius (m)
$r_1$	Curvature radius 1 (m)
$r_2$	Curvature radius 2 (m)
$r_{eq}$	Equivalent radius (m)
$S$	Surface area (m <sup>2</sup> )
$S_{geom}$	Specific geometric surface area (m <sup>2</sup> /g)
$S_p$	Cross-sectional area of a pore (m <sup>3</sup> )
$T$	Temperature (K)
$T^o$	Bulk freezing temperature (K)
$T1$	spin-lattice relaxation time (s)
$T2$	spin-spin relaxation time (s)
$t$	Adsorbed layer thickness (Å)
$t_l$	Non-frozen layer thickness (Å)
$V$	Volume (m <sup>3</sup> )
$V_N$	Total volume of the network (m <sup>3</sup> )
$V_{N_2}$	Nitrogen volume (m <sup>3</sup> )
$V_{Hg}$	Mercury volume (m <sup>3</sup> )
$V_{H_2O}$	Water volume (m <sup>3</sup> )
$V_p$	Pore volume (m <sup>3</sup> )
$w$	Larmor frequency (rad/s)
$Vp_{geom}$	Specific geometric pore volume (m <sup>3</sup> /g)
$Vp_{tl}$	total pore volume in the list (m <sup>3</sup> )
$x$	Cartesian coordinate (m)
$y$	Cartesian coordinate (m)
$z$	Cartesian coordinate (m)
$Z$	Connectivity (-)
$Z_{avg}$	Average connectivity (-)
$Z_{max}$	Maximum connectivity (-)

## Greek letters

$\Delta$	Diffusion time (s)
$\delta$	Gradient pulse duration (s)
$\sigma$	average cross sectional occupied by each molecule of nitrogen (m <sup>2</sup> /molecule)
$\sigma_{LV}$	Liquid-Vapor Surface tension (N.cm <sup>-1</sup> )
$\sigma_{prop}$	Standard deviation for a generic property
$\tau$	Tortuosity (-)
$\tau_e$	Time between two radio-frequency pulses (s)
$\gamma$	Gyromagnetic ratio (rad·s <sup>-1</sup> ·T <sup>-1</sup> )
$\varepsilon$	Porosity (-)

$\Phi$   
 $\rho_{material}$

Phase shift (rad)  
Solid phase or skeletal density (m<sup>3</sup>/kg)

## GENERAL INTRODUCTION

Porous materials are widely used in chemical engineering. At the mesoporous scale, confinement effects influence thermodynamics and transport conditions. Indeed, the architecture of the porous material can cause mass transfer limitations inside of the catalyst (Wood et al. 2002). Therefore, understanding not just the textural properties but also the topology of the solid is important to improve the catalyst performance and the accuracy of different models allowing to design and evaluate heterogeneous reactor performance (Johannessen et al. 2007; Ye et al. 2019b; Ye et al. 2016).

Modeling the phenomena that occur at the interior of the pore network can improve the assessment of critical descriptors that are valuable for the synthesis of industrial catalysts, supports, and adsorbents. When applied to the chemical reactors or adsorbents it would then be possible (i) to estimate the tortuosity of a catalyst sample through computer simulations starting from cheap and common characterization techniques, and (ii) to optimize the structural parameters of the gamma alumina to maximize activity, selectivity and/or stability of the catalyst.

In order to assess the phenomena that occur in the interior of the porous structure, it is possible to use either mimetic methods or reconstruction methods (Schüth 2002a). Mimetic methods try to create the final material by simulating its synthesis, starting from the genesis all the way to the final structure of the solid. On the other hand, reconstruction methods directly model the material in its final state. Among the reconstruction methods, pore network models are common representations. They are widely used because they can be easily assembled, its flexibility, and its reasonable CPU intensity. Such structures represent a useful solution to simulate adsorption, dissolution and precipitation (Peter Matthews et al. 1996), biomass growth (Ezeuko et al. 2011), permeability (Huang et al. 2016), carbon capture (Li et al. 2006), fuel cells (El Hannach et al. 2014), adsorbents (Ye et al. 2015), and chemical reactors (Ye et al. 2019a; Hannaoui et al. 2015). Pore network models were mentioned for the first time by Fatt in 1956 (Fatt 1956b). At that time, the novelty resided in the consideration of pore network connectivity, a concept that was lacking in the classic “bundle of tubes” model (Wheeler 1951). Since then, multiple variants have been proposed to understand the role of the different characteristics of the network architecture on thermodynamics and transfer phenomena. The new models consider different textural and topological characteristics that can be relevant to describe the material. Amongst the more recent models with the most relevant improvements are: The dual site bond model (DSBM), proposed by Cruz in 1989 (Cruz et al. 1989; Mayagoitia et al. 1996; Mayagoitia et al. 1997) and later modified by Riccardo, to create energetically consistent structures (Riccardo et al.

1993); The corrugated pore structure model (CPSM), first proposed by Mann and Andropoutsopoulos in 1981 (Mann and Golshan 1981; Mann and Thomson 1987; Andropoutsopoulos and Salmas 2000b), which accounts for the rugosity on the pore walls; The Hierarchical pore network models, which described in the works of Spearing and Matthews, Rieckmann and Keil, Gladden, Sharratt and Hollewand, and Sadeghi (Spearing and Matthews 1991; Hollewand and Gladden 1991, 1992; Sadeghi et al. 2017; Rieckmann and Keil 1997; Sharratt and Mann 1987).

It is necessary to have experimental information in order to correctly model the heterogeneity of the solid. The characterization is normally done using one or a combination of the following techniques: Small Angle X-ray Scattering (SAXS), X-ray computed micro-tomography (micro-CT), Focused Ion Beam (FIB) coupled with Scanning Electron Microscope (SEM), Nuclear Magnetic Resonance (NMR)-Relaxometry, Nuclear Magnetic Resonance-Cryoporometry, mercury porosimetry, and nitrogen sorption porosimetry.

In many cases, only nitrogen and mercury porosimetry are available because these techniques are the fastest, cheapest, and most common. They provide qualitative information on the topology and the architecture of the network. Hence, many studies have been carried out at different scales to improve the understanding and quality of the models used for the interpretation of the experimental data from these techniques

Molecular simulations are done to study the effect of confinement on the gas adsorption/condensation and evaporation/desorption (Nguyen et al. 2011; Bruschi et al. 2015; Coasne et al. 2004; Palmer et al. 2009; Kolesnikov et al. 2020). Other studies try to explain the effect of the connectivity and the architecture on reaction and transport properties at the mesoscopic scale (Armatas and Pomonis 2004; López-Ramón et al. 1997; Meyers et al. 2001; Murray et al. 1999b; Seaton 1991; Perkins et al. 2008; Rojas et al. 2002; Kikkinides et al. 2020; Gommès 2012).

Gamma-alumina is a disordered porous material very frequently used in the oil refining and petrochemical industries. It has an elevated tortuosity, and its topology is not yet fully understood (Schüth 2002a; Wang 2017; Rigby et al. 2017). Recent research articles propose that this material has different pore domains, each one characterized by its own pore size distribution and void fraction (Rigby et al. 2002). The interplay among these different levels clearly plays a role in effective diffusion. By creating digital twins of real gamma-alumina samples, it is possible to better understand how the textural properties and the topology of the network influence diffusion through the network at a fundamental level. At the same time, in applied R&D, this allows to create more accurate and flexible models that better represent the reactor performance.

## OUTLINE OF THE THESIS

This work intends to better understand the textural and topological descriptors of gamma alumina by creating a digital representation of it. The catalyst is represented using a pore network model. The pore network representation is then studied using computational equivalents of textural and mass transfer characterization techniques. The experimental validation is done through the generation of digital twins for real gamma alumina samples.

The second chapter of this work describes **the state of the art** of the synthesis, characterization, and modelling of gamma alumina-based materials.

The third chapter focuses on the **Pore Network Model** implemented to model gamma alumina. First, the generation algorithm is described. The next section describes in detail the characteristics of the model. Subsequently, a statistical analysis is done to know the minimum network size that should be used in order to represent appropriately the input variables. The last section of this chapter consists of a **topological analysis** of the pore network model.

The fourth chapter contains the description of the **algorithms developed for the simulation of three different textural characterization techniques**: Nitrogen Sorption, Mercury Porosimetry and Cryoporometry. At the end of the chapter a case study is presented.

A **trend analysis** is reported in chapter 5. The objective of this chapter is to show the effect of the input parameters used for the generation of the pore network model on the characteristic curves obtained from the digital characterization techniques.

The sixth chapter shows the creation of **gamma alumina digital twin** using a particle swarm optimization (PSO) algorithm. The structure is optimized based on an experimental nitrogen isotherm.

Chapter 7 presents the development of a **PFG-NMR simulation tool**. The state of the art and the basics of the physical phenomena that are involved are presented first. Then the foundations of the model are explained. A case study is presented in the last section.

The last chapter is dedicated to the conclusion and perspectives of this work.

## Chapter 1: Context

### 1.1. Introduction

Better understanding a material provides the opportunity to improve it. The technical upgrading and evolution of processes rely importantly on it. In chemical reactor design, the engineering and the scientific communities can model and predict hydrodynamic properties of fluids flowing through industrial equipment by using very complex equations derived from the Boltzmann equation (such as Navier-Stokes) with complex corrections for turbulent flow at different scales. Still, when it comes to mass transfer and chemical reaction through porous materials, reaction-diffusion is often modeled in a very idealized way considering continuum transport coefficients that average the influence of an important number of phenomena along with the heterogeneities of the material. The diffusion phenomena are usually modeled using Fickian transport, the interactions of the fluid components with the walls are not taken into account, their adsorption in some pores and the effect it has on the performance are not considered, while the topology effects and local heterogeneities of the pore distribution are also not considered. When the solid synthesis is altered, it is very hard to accurately consider the new transport properties of the material without performing new experimental studies.

Porous materials are very common in the industry, covering important and profitable applications such as adsorption, catalysis, separation, oil recovery, and energy storage. In these applications, there are chemical and/or physical interactions with different types of fluids. Hence, transport properties are intimately correlated to the pore media organization, its morphology, and its topology. To identify, measure, model and predict these transport properties, it is necessary to understand the pore network architecture and therefore to characterize its textural properties. The characterization can be very straightforward if the pores have a regular shape and are well organized, as is the case of zeolites such as ZMS-5 for example. However, when the pore structure of the material is disordered and possesses several relevant length scales, the characterization becomes a very complex topic, and is therefore a very active research domain. A case of particular interest is gamma-alumina.

Gamma alumina is a very important material present in the oil industry for processes such as hydrotreating, hydrocracking, catalytic reforming, and isomerization. It is used both as a support and as a catalyst. The material possesses micro-, meso-, and macroscopic pores as well as a high void fraction (0.5-0.75).

In Figure 1 are presented SEM images for two different representative alumina samples. Sample A and Sample B were prepared using different mixing intensities. The result leads to two different alumina samples, one in which the higher porosity fraction is concentrated

into the grains (Sample A) and another in which the higher porosity fraction is concentrated in the matrix (Sample B).

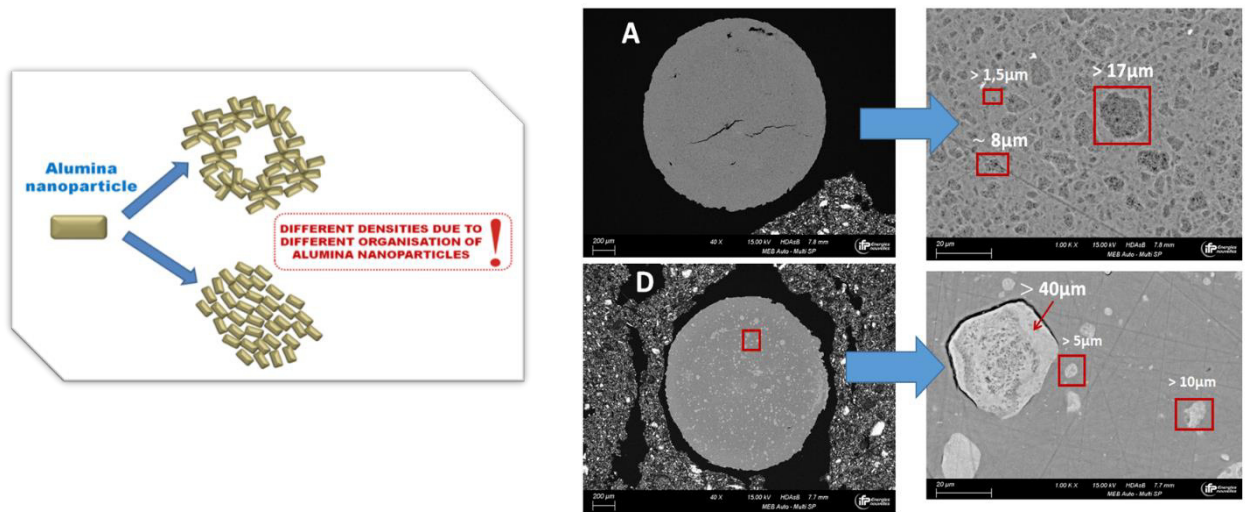


Figure 1. SEM images for two different representative alumina samples (Głowska 2021)

A better understanding of the material properties is an opportunity to improve it, hence, the characterization and modeling of alumina porous structures is a fertile field for technological breakthroughs.

## 1.2. Objective and general strategy

In 2017, Kolitcheff, during his Ph.D. thesis *“Multi-technique approach to diffusion phenomena in hydrotreating of distillates”*, characterized textural properties and mass transport properties of several samples of commercial gamma-alumina (Kolitcheff 2017). On this basis, he tried to find a plausible explanation for the very high tortuosity of gamma-alumina that appeared to be somehow inconsistent with its elevated porosity (Figure 2). He showed how different samples having the same porosity exhibited different tortuosities. These results can be explained by the topology of the structure. They demonstrated experimentally that solids with similar macroscopic textural properties can exhibit different tortuosity values based on the internal organization of the pore network, as already suggested by literature simulation works (Hollewand and Gladden 1995). In his conclusions, Kolitcheff suggests the existence of a hierarchical organization within the alumina represented by two different and intertwined porosity levels that influence the mass transport properties of the network.

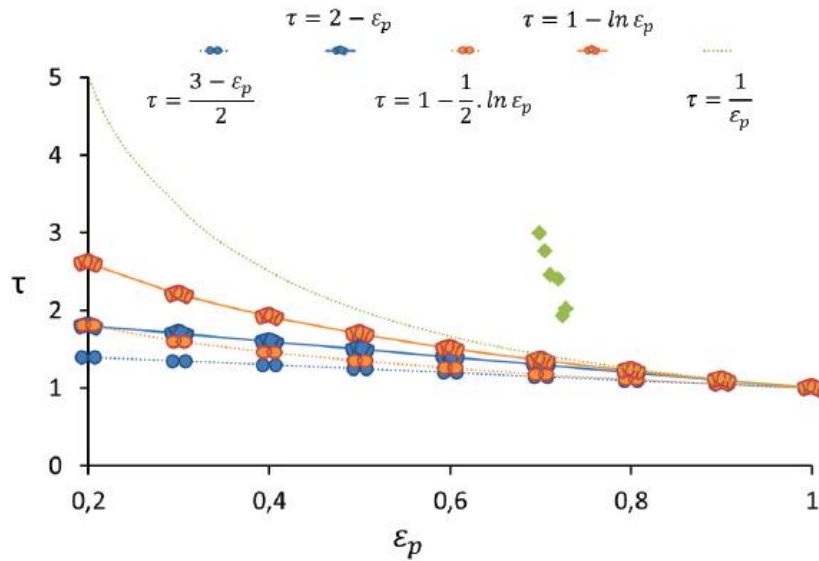


Figure 2. Comparison between the tortuosity values obtained through stack correlations and experimental tortuosity values obtained by inverse chromatography (Experimental values are in green) (Kolitcheff 2017).

Ferreira, in her Ph.D. thesis, proposed to model the porous solid using a pore network method based on a stochastic reconstruction algorithm, and represented the basic textural characteristics (pore volume, specific surface area, and pore size distribution) of the commercial samples employed by Kolitcheff using hierarchical structures (Ferreira 2018). However, several pore networks with different organizations were able to match the same macroscopic textural properties. This suggested that more parameters were required to obtain a more complete and unambiguous representation. To select the most appropriate representation, Ferreira compared the calculated pore network tortuosity to the experimentally measured tortuosities measured by Kolitcheff.

The general scope of the present thesis is generating a digital representation of the gamma-alumina pore network that can correctly represent the topology of the material (Figure 3). In order to validate the pore network model, modeling and simulation of commonly used characterization techniques are compared with experimental results. By using representative digital structures, it will be possible to investigate how textural and architectural descriptors influence tortuosity.

In a first step, a fast and flexible pore network model generation algorithm has been developed. The generation of a genuine representation of porous media is a fundamental part of the work. To create such a representation, new descriptors and relevant information to reproduce the architectural, morphological, and topological effects are employed considering the insights previously found (Morin 2014; Kolitcheff 2017; Wang 2017; Ferreira 2018). New tools that simulate characterization techniques (nitrogen sorption porosimetry, mercury porosimetry, and cryoporosimetry) that provide information about the topology of the system have been created. These models have been validated by checking their

ability to create digital twins that can reproduce the experimental curves obtained from these textural characterization techniques. To better understand the influence of the network architecture on tortuosity, the Pulse Field Gradient NMR mass transfer characterization technique has been simulated. The simulation of diffusion within the generated pore network has been compared to experimental values of effective diffusion coefficients. These experiments provide additional information on the organization and structure of the porous solid.

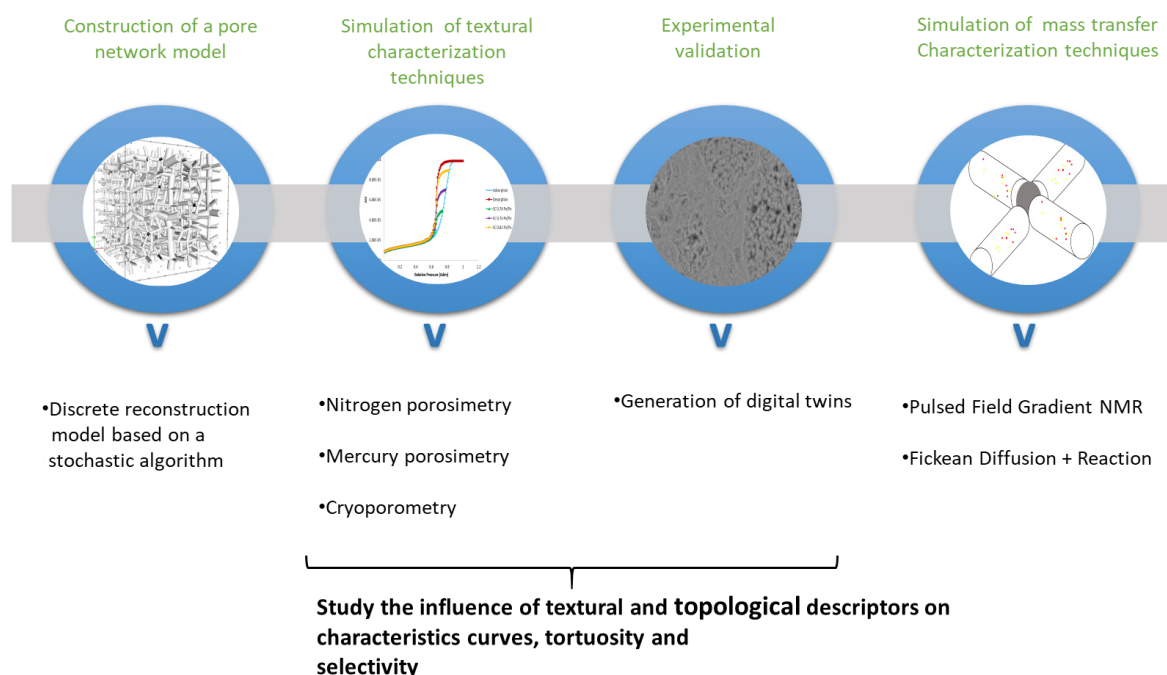


Figure 3. General strategy of the present Ph.D. thesis

In future work, understanding the impact of disorder and the degree of microstructural heterogeneity will aim at producing continuum models to design of chemical reactors and identifying the internal organization of catalysts given their performance. This knowledge could allow proposing optimized architectures for gamma-alumina catalysts. The complexity of the interaction of the fluid with the solid matrix can be considered for diffusion and diffusion/reaction steps. Surface adsorption, pore-blocking due to adsorption, non-ideality of the fluid, and different diffusion regimes can be considered.

This PhD thesis work has been performed in collaboration with the PhD thesis work of Aleksandra Glowska “Multi-technique analysis of porous networks in gamma-alumina supports” (IFPEN thesis 2018-R05-09, Ph.D. student: Aleksandra Glowska, IFPEN promotor: Elsa Jolimaitre, Ph.D. Director: Prof. Marc-Olivier Coppens, University College London) that has taken place in the IFPEN Physics and Analysis Division. This collaboration provided

experimental data from different characterization techniques for the validation of the computational models.

## Chapter 2: Gamma Alumina porous structure modeling and characterization – State of the Art

### 2.1. Alumina crystalline structure

Alumina is a polymorphous material that is composed of aluminum, oxygen, and hydrogen. Every crystalline form has its particular textural properties and can be transformed into another. Several reviews were published (Euzen P., Raybaud P. et al. 2002; Wefers and Misra 1987), which show the morphosis relation between most of the different polymorphisms (Figure 4). The alumina can be classified into aluminum hydroxides and aluminum oxides.

The aluminum hydroxides can be sub-classified in aluminum trihydroxides ( $\text{Al}(\text{OH})_3$ ) and aluminum (oxyhydr)oxides ( $\text{AlOOH}$ ). The gibbsite is the most common form obtained by mining and processing the most abundant mineral of aluminum, which is bauxite. In Table 1, the most common forms are presented according to the classification mentioned above.

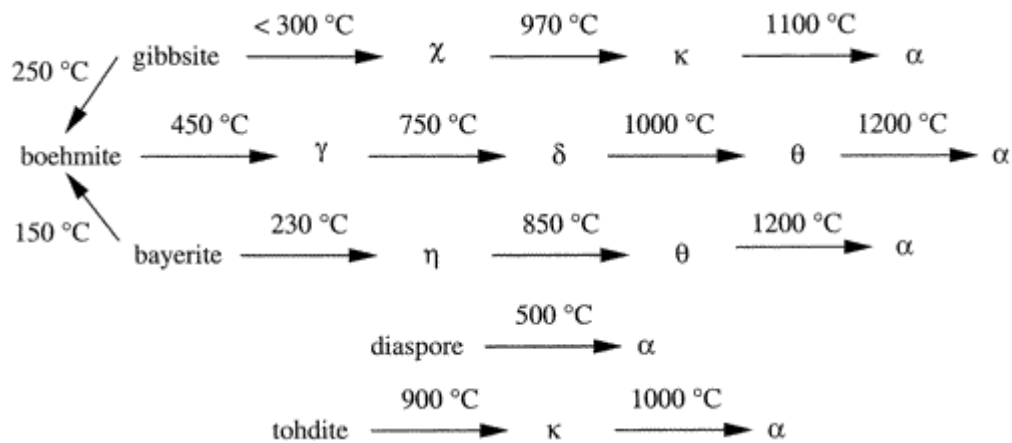


Figure 4. Dehydration temperature of the aluminum (oxy)hydroxides (Digne et al. 2002).

The thermodynamic stability of a form depends on the free energy of the solid, which in small particles mainly depends on the surface contribution. According to the energy of the bulk of the structure, corundum is the most stable form, while, in terms of the contribution of the surface, the amorphous oxide tends to be the most stable of the transitions aluminas (Schoen and Roberson 1970).

The characterization of the cell parameter and crystalline structure of aluminum hydroxides is widely described in literature. The most common reported experimental characterization techniques are XRD (X-ray diffraction), atomic force microscopy, neutron diffraction, Raman

spectroscopy, while theoretical ones are based on ab initio simulations (Saalfeld and Wedde 1974).

Table 1. Alumina polymorphisms.

<b>Type</b>	<b>Prefix</b>	<b>Common Name</b>
<b><u>Trihydroxides</u></b>	$\gamma$	Gibbsite/Hydrargyillite
	$\alpha$	Bayerite
		Nordstrandite
		Doyleite
<b><u>(Oxyhydr)oxides</u></b>	$\gamma$	Boehmite
		Diaspore
-	-	*Akdalaite
<b><u>Oxides</u></b>	$\alpha$	Alumina
	$\rho$	Alumina
	$\chi$	Alumina
	$\kappa$	Alumina
	$\eta$	Alumina
	$\gamma$	Alumina
	$\delta$	Alumina
	$\theta$	Alumina
	$\theta'$	Alumina
	$\theta''$	Alumina
	$\alpha$	Corundum

\*The Akdalaite is a form that contains a very low hydration degree.

In the latter review, boehmite has a central importance, as it is the most common precursor of gamma-alumina. The determination of the boehmite crystalline structure has been the object of many investigations, and several spatial groups (SGs) were proposed, differing in the hydrogen atoms setting only. The SG most frequently quoted in the literature is *Cmcm* (or *Amam*) (Schüth 2002a).

Boehmite (and also trihydroxides) are layered structures where crystal cohesion is guaranteed by interlayer hydrogen bridges. The coordination polyhedra in the alumina crystalline structure are mainly octahedral and tetrahedral. The chemical bonds that are present in the alumina are of the covalent type within the bulk (Al-O, O-H), ionic type in the surface, and hydrogen bridges everywhere (O.....H) (Demichelis et al. 2011).

Boehmite particles are monocrystals with a dimension of 2 to 50 nm. The commonly reported morphologies are fibrillary, oval, spherical, or orthorhombic plates. The morphology of the boehmite crystals can be controlled through the physicochemical, mechanical, and thermodynamic parameters of the synthesis: pH, viscosity, ionic strength, agitation, temperature, and pressure during the synthesis. The time of aging plays a fundamental role in the process.

The control of particle size, morphology, and functionalization will be fundamental in determining the textural properties (such as surface area, pore size distribution, and pore volume) in the porous network that will be produced with calcination of the solid (Morin 2014).

The solid (oxy)hydroxides and the hydroxides are amphoteric, but aluminum oxide exhibits an acid behavior that is associated with the morphology and the superficial area of the solid (Jolivet 2016). The character of the Al-O-H bond on the surface is predominately covalent, while within the bulk the character of the bond is ionic.

Aluminum oxides are produced by calcination of the aluminum hydroxides. The transition of boehmite to gamma-alumina is a topotactic transformation, which means that the gamma-alumina particle will maintain the same morphology as the (oxy)hydroxide particle. This does not mean that the two surfaces are atomically equivalent. According to the synthesis method, the morphology and the textural properties will vary (Lippens 1961). As the temperature of the calcination process is higher, the dehydration of the solid structure advances. The calcination will decrease the number of hydroxyl groups on the solid surface, which means that the number of Lewis acid sites is decreasing too. The loss of Lewis acid sites is also reinforced by the loss in surface area due to the sintering of the solid. The different alumina phases, from boehmite to alpha-alumina, are shown in **Error! Reference source not found.** As the oxide evolves to alpha alumina, the surface area decreases and the number of acid sites too, which leads to decreasing chemical reactivity.

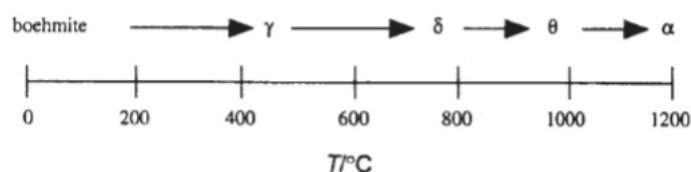


Figure 5. Phase evolution of boehmite to alpha alumina as a function of temperature (Ingram et al. 1996).

The force of the acid site is associated with the aluminum ion coordination: it can be tri coordinated (tetrahedral with a vacancy), tetrahedral coordinated, penta-coordinated (octahedral with a vacancy), and octahedral coordinated. It has been postulated that the strongest acid sites correspond to the tricoordinated  $\text{Al}^{3+}$  (Schüth 2002a; Lippens 1961). Several structural models have been proposed for gamma-alumina (the spinel model, the defective spinel model, and the non-spinel model), but the truth is that the position and the state of the hydroxyls are not yet fully determined for gamma-alumina.

The different aluminum oxide forms are suitable for different technological applications. Aluminum oxides are mainly used as isolating materials, adsorbents, catalysts, and catalyst supports. Among them, gamma-alumina is widely used in the field of catalysis due to its stability, its surface area, and the physical chemistry of its surface.

## **2.2. Alumina synthesis and shaping**

### **2.2.1. Solution Chemistry**

Jolivet gives a very exhaustive description of the solution chemistry of alumina synthesis. A summary of his theories will be exposed here (Jolivet 2016).

The precipitation of alumina from a solution (boehmite for example) can be done in three different ways: by neutralization with a base at room temperature, by thermohydrolysis, and by hydrothermal treatment. When the aluminum cation is in solution, it forms aquo complexes of the type  $[\text{Al}(\text{OH}_2)_N]^{3+}$  due to the Lewis acid behavior of the cation. The covalent O-H bond on the aquo complexes is weaker than that of the water solution, and the aquo complexes behave as a Bronsted acid, releasing protons by hydrolysis and hydroxylating the complex, forming an aquo hydro complex. The degree of hydroxylation (defined as the number of hydro groups in the coordination sphere of the cation) depends on the formal charge of the cation ( $z/r$ ) and the pH of the medium.

This aquo hydro complex can condense in oligomers by olation and hydroxylation. The number of elements of the oligomer is limited to the weakening of the polarization capacity of the cation.

The olation is the faster of the two mechanisms and it occurs by unimolecular substitution. The hydroxyl group (entering group) substitutes an aquo group (exiting group) forming a hydro bridge. The oxolation occurs through a slower two-step mechanism of bimolecular association by the nucleophilic attack of a hydroxo group to the cation, forming oxo bridges.

The polycationic structures are continuously and rapidly changing and are very sensitive to the pH of the medium. The formation of the crystal structure requires the right hydroxylation index and time to neutralize all the species in solution.

The germination of the crystal occurs due to the birth of neutral species and not from the addition of polycations. Once the particle nucleates, it grows during an aging process. Aging involves two mechanisms, **dissolution/crystallization** and/or **structural reorganization**. The first one is prominently present when the pH of the solution is far from the limit of solubility. This mechanism facilitates the dissolution of the species and favors the mass transfer through the medium. According to the pH value, the resultant crystalline structure obtained can correspond to gibbsite (pH=5) or bayerite (pH=10). Structural reorganization is always present, but it is predominant close pH=6, almost at the limit of solubility. This reorganization is governed by the Ostwald law (Euzen P., Raybaud P. et al. 2002). The mechanism leads to boehmite crystals due to a final dehydration process during the structural reorganization. This method usually leads to the formation of very small crystals (Jolivet 2016).

There are different methods to generate the neutral species and cause nucleation. These nucleation conditions will define which form will nucleate and which morphology will be favored.

### 2.2.2. Industrial Synthesis

According to the technological application, the synthesis path can differ since, for example, undesired impurities can remain present in the solid as traces depending on the synthesis. For example, this is the case for catalysts that are not favored by the presence of sodium on their surface.

Synthesis methods will fundamentally include the following routes:

- **Neutralization with a base** at room temperature.
- **Thermohydrolysis:** This implies heating the solution (below 100 °C, and at atmospheric pressure) in an acid medium to force the deprotonation of the aquo complexes and cause the hydroxylation beyond the thermodynamic limit that existed at room temperature. This allows obtaining a neutral precursor  $[\text{Al}(\text{OH})_3(\text{OH}_2)_3]^0$ . This process leads to the formation of boehmite crystals. The thermal effect favors condensation kinetics and dehydration and, as a consequence, the formation of the oxyhydroxide (Jolivet 2016).

- **Hydrothermal treatment** consists of increasing the temperature above 100 °C and increasing the pressure to maintain the solution in the liquid state. In those conditions, the physicochemical properties of the water vary. This modification in the synthesis conditions allows influencing the acidity and the orientation of the oligomers, allowing them to obtain crystals structurally and morphologically different from those obtained by thermolysis (Schüth 2002a).

A practical example is the *aluminum alkoxide hydrolysis*, into which the alkoxide is hydrolyzed to obtain boehmite plus long-chain alcohol; neutralization is obtained by decomposition of a base in solution with an acidic aluminum salt.

### 2.2.3. Shaping for Catalyst Industry

The industrial catalyst and adsorbents must satisfy several constraints. In the industry, the process is generally carried out under important stress conditions for the elements that are assembled conform to the chemical plant. Such stress comes from process conditions that imply high hydraulic loads, high temperature, pressure, friction, and abrasion produced by the fluid that goes through the system or by the movement of the system itself. The shaping of the solid obeys the primary necessity of having a solid structure with high mechanical resistance and thermal stability to face severe process conditions.

Additionally, the final shape should generate a low-pressure drop, while its external surface area should be high. At the same time, the internal surface area mandatorily needs to be high, and the structure of the porous network should reduce diffusion limitations of the molecules of interest.

Boehmite powder is composed of agglomerates with an approximate size between 5-40  $\mu\text{m}$ , which are composed of aggregates that are held by electrostatic forces. The mean size of these aggregates is between 0.3-5  $\mu\text{m}$ . The aggregates are formed by boehmite crystallite clusters, whose typical size is 2-50 nm. The typical size of the crystallite clusters matches the mesopore size range.

During the shaping, rheological modifiers and pore-forming agents (used to increase the meso- and macroporosity) are employed. The traditional methods to shape the solid element of alumina are:

- **Extrusion**  
Extrusion consists of producing a peptized dough of boehmite to be extruded in some particular geometry. The preparation of the paste consists of mixing the boehmite powder with water, a peptizing agent (an acid), and a rheological modifier (a plasticizer). The mix is mulled during a determined time and finally extruded. The

peptization grade of the boehmite influences the final pore volume and the pore size distribution obtained. The peptization extent will depend on the nature, concentration, and quantity of the acid, the mulling time, and the intrinsic dispersibility of the powder.

- ***Oil-drop coagulation***

This consists of making drops of a boehmite slurry suspension that fall into a non-miscible water fluid whose interaction with the drop will produce a surface tension that forces the drop to take a spherical shape. The slurry is composed of water, a peptizing agent, a rheological modifier, and a pore-forming agent. Several variants of the process exist, which use a base to recrystallize a fraction of the boehmite that may be diluted in a peptizing agent.

- ***Granulation***

The alumina powder is granulated and introduced in a tilted rotating pan with alumina seeds (bigger grains) and a binder (which can be water). The alumina powder agglomerates around the seeds until a deformed spherical solid is formed and falls by gravity to the bottom of the pan. The geometry and the size distribution of solid obtained by this method are very difficult to control.

The shaped boehmite element has then to be dried and calcinated, thereby creating the final porous network of interest.

### **2.3. Alumina porous structure**

The porous structure of the alumina (topology), its textural properties (specific surface, specific pore volume, and pore size distribution) and its mechanical properties depend on:

1. The morphology and the size of the elementary crystallites.
2. The architectural arrangement in space of the different levels of porosity created by elementary crystallites, aggregates, and agglomerates.
3. The presence of an artificial pore-forming agent.

The morphology of the crystallites automatically expresses a specific surface-to-volume ratio. The commonly reported morphologies are fibrillary, oval, spherical, or orthorhombic plates (Figure 6).

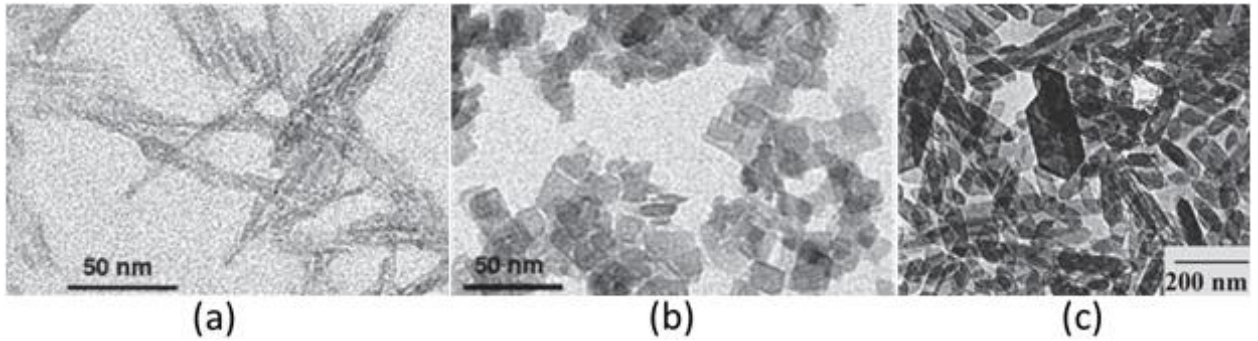


Figure 6. TEM of different morphologies of alumina elementary platelets. (a) Fibrillar (Chiche et al. 2008) (b) Orthorhombic (Chiche et al. 2008) (c) Hexagonal (Santos et al. 1996).

The morphology of the boehmite crystals and their spatial organization are the result of physicochemical, mechanical, and thermodynamic parameters of the synthesis, such as pH, viscosity, ionic strength, agitation, temperature, and pressure during the synthesis, shaping, drying, and calcination (gamma-alumina). Numerous computational and experimental studies have been developed over the years to understand the link between the properties of the shaped gamma-alumina and the different variables involved during its synthesis.

As already mentioned, the porosity of the network is represented at three different scales, one associated with the spaces between the elementary crystallites conforming to the aggregates, a second one associated with the spaces between the aggregates, and a third one associated with the spaces between the agglomerates (Figure 7).

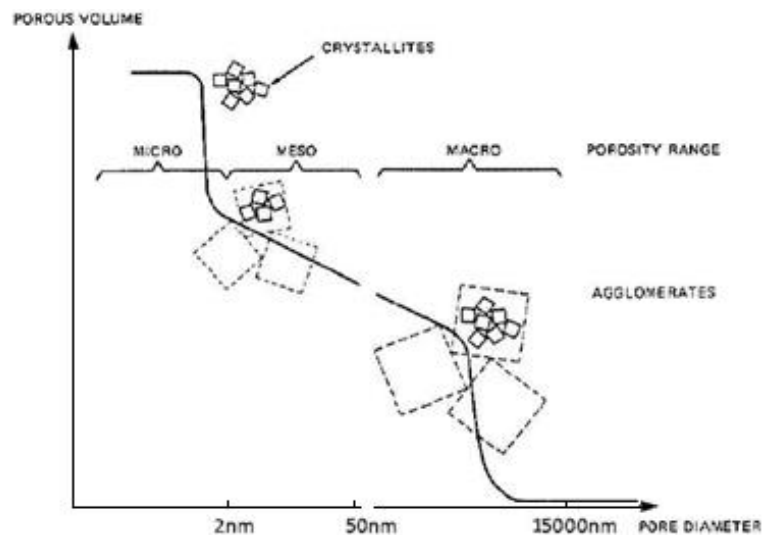


Figure 7. Schematic distribution of pore volume distribution (Dadyburjor 1988).

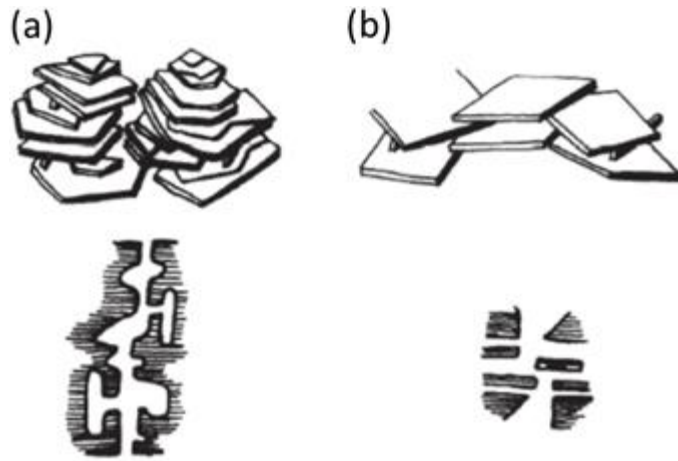


Figure 8. Influence of the orientation of aggregates on the porous structure: (a) oriented particles; (b) non-oriented particles (Kotanigawa et al. 1981).

The resultant pore network is disordered with mono or bi-dispersed porosity and has been the subject of numerous research studies linked to hierarchical structures. As would be expected, the orientation of the aggregate will also influence the architecture of the porous structure (Figure 8). Naturally, these studies influence the nature of any possible computational model.

## 2.4. Classification of pore structure models

Modeling the porous structure of a material is very useful to understand how a particular phenomenon at the pore scale influences the macro-scale. Since 1950, it has been attempted to understand how different phenomena such as adsorption, absorption, chemical reactions, mass transfer, heat transfer, momentum transfer, and growing of micro-organisms at porous scale affect macro-properties. All those phenomena are present in a vast range of domains of important industrial interest such as fuel-cells (El Hannach et al. 2014), chemical reactors (Ye et al. 2017; Gheorghiu and Coppens 2004; Ye et al. 2019a), absorbers, Carbon Capture and Storage (Li et al. 2006), Enhanced Oil Recovery (EOR) and bio-remediation (Ezeuko et al. 2011).

In a general manner, a mathematical model serves to imitate the behavior of a particular system and how good it is depends on what is intended to be obtained from the model (Coppens and Bhatt 2017). The models of porous materials can be classified according to various criteria.

A first classification is based on a distinction between continuous or discrete representations:

- *Continuum models* express a particular property of a system state as a smooth function of a position and/or a time coordinate, to guarantee continuity in the

relation that has been established. The continuum models for porous structures do not account explicitly for their local topology, even if this is an important textural property for the transport inside the porous material. The topology of the system encloses the connectivity of the network, and it can also be a function of time. Continuum models use effective parameters to account indirectly for different phenomena that occur at the porous scale. These effective parameters usually come from empirical correlations and are constrained to be representative of the evaluated system. This means that if there is a change in the topology of the material (for example) the effective parameters of the model will be no longer valid.

- In *discrete models* or *heterogeneous models*, the solid phase and the fluid phase are considered separately.

A second classification is described in the *Handbook of Porous Solids* (Schüth 2002b, 2002b, p. 208) and focuses on the generation process of the models:

- *Mimetic simulation methods* are based on the idea that, by representing the synthesis process of the material and mimicking it with a simulation model, one can obtain a simulated material that matches the measured properties of the material.
- *Reconstruction methods* directly create a numerical representation of the porous material that matches its measured properties, without considering the synthesis process of the material.

A third classification is based on the scale(s) under consideration. Models for porous structures can contemplate the atomic scale, the micro/mesoscopic scale, and the macroscopic scale:

- In *atomic-scale models*, the atoms are the smallest discretely modeled units and are placed in space considering the atomic structure of the material and the force fields around them (Figure 9). This approach contributes to study the interactions between a fluid phase and the solid structure. The drawback of this approach resides in the calculation time necessary for the minimum number of atoms (a representative volume element, or RVE) required in (heterogeneous) disordered solids in order to obtain results that represent the textural and surface properties of the material. However, atomic-scale methods are very useful to study confinement effects and to better understand phenomena such as capillary adsorption in pores of different materials, sizes, and shapes.
- For the *micro-mesoscopic scale*, coarse-grained models are used. In these models, the atoms are no longer distinguished in the solid structure, so the solid is considered to be homogeneous below the microscopic scale. These models are

discrete models, and, for their construction, they can focus either on the solid itself or on the void space.

- *Macroscopic modeling* relies on porous solids pseudo continuum models. These are used to model transport phenomena and chemical kinetics within catalyst pellets implicitly considering the pore network influence through a tortuosity factor.

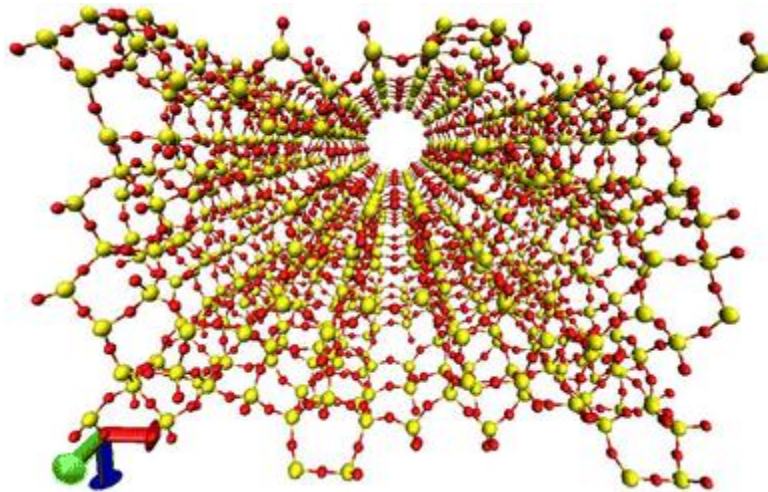


Figure 9: Atomistic perspective of ZSM-5; silicon atoms are in yellow, oxygen atoms in red (Newsome et al. 2014).

A fourth classification is based on a distinction between solid models and void models:

- The *solid-focused models* or *grain-based models* use agglomerations of solid Euclidean forms to recreate the porous structure of the material. They can also use irregular solid objects when image reconstruction techniques are used (as explained below).
- The *void space-focused models* use agglomerations of Euclidean forms that represent the void. It can be said that it is like carving the void in the solid. To do so, regular and irregular lattices of different nature are used to account for the connectivity between the pores. In this category enter the pore network models.

The last remark concerns the effect of the dimensional behavior of the model. A system is called isotropic if its intensive properties behave statistically in the same way in any direction. If not, the system is considered anisotropic. However, observing an identical statistical behavior also depends on the length scale. If we isolate a small portion of our system delimited by a cubic cell, we will probably need to increase the size of this characteristic cell until observing an isotropic behavior. A cell at this point can be considered as a discrete point with properties equivalent to volume average properties of the points enclosed by the cube. If the volume of the cell keeps increasing, an anisotropic behavior can

arise again. It is convenient to ensure that the properties at the length scale of the model are isotropic to avoid the use of tensors.

### **2.4.1. Heterogeneous models**

Generally speaking, a heterogeneous model is designed to create a discrete statistically representative structure. These structures can be:

- Lattice-based or pore network models: Regular and irregular lattices of different nature are used to account for textural and topological properties.
- Grain-based models: Random or ordered packing of solids are used, considering or not the packing process.
- Models obtained from image reconstruction methods.
- 2D mapped structure-based models: Scanning information in 2D is used to make a reconstruction of solid accompanied by extrapolation algorithms (Hannaoui et al. 2015).
- 3D mapped structure-based models: Scanning information in 3D is used to make a reconstruction of solid (Figure 10).

#### ***2.4.1.1. Image reconstruction methods***

These models use as input information the images obtained by tomography and microscopy. The image reconstruction methods are also called pore network extraction models. The main problem of these methods is the difficulty to obtain global and non-local representative properties. When the total structure is not directly mapped, these methods fail in predicting long-range connectivity (Xiong et al. 2016). Also, at the low scales, they are limited by the highest resolution that can be reached with the image characterization techniques. Image reconstruction methods can be classified in:

- Statistical Reconstruction from 2D scanning information: By using morphological descriptors, it is possible to statistically reconstruct a 3D representation of the solid by starting from 2D images (Hannaoui et al. 2015).
- Direct-Mapping Models: 3D scanning information is used to reconstruct the full topology of the solid obtaining a 1 to 1 spatial representation of the system. The two more common algorithms for extracting the porous network of a digital binarized volume are the medial axis algorithm and the maximal ball algorithm. One of the particular problems of this kind of model is the criterion to identify the pores in very heterogeneous systems (Figure 10).

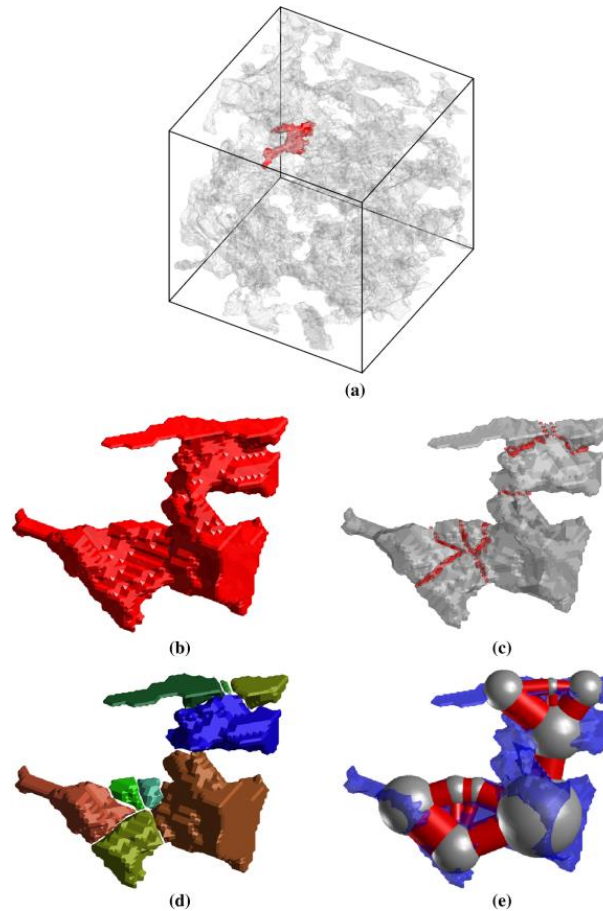


Figure 10: Extraction of Hollington sandstone pore network using watershed segmentation algorithm: (a) the region of interest within the porous body (cube size: 840 microns); (b) Connected body of isolated pores; (c) breaking down the structure with watershed algorithm; (d) labeling the detected pores with different colors; (e) Putting the spheres and tubes inside the geometry representing the pores and throats, respectively (Baychev et al. 2019).

### 2.4.2. Grain-Based Models

In this kind of model, Euclidean solids are used to simulate the agglomeration of the elementary particles or aggregates of the material in order to reproduce the porous structure. The models created using this method can be mimetic (diagenetic) or reconstructive. This kind of model is abundant in the literature (MacMullin R. B. and Muccini 1956; Aste et al. 2004; Silbert et al. 2002; Sasloglou et al. 2000; Kansal et al. 2002; Beckman 1990). Grain-based models are used to represent a stack of catalysts or supports within reactors, absorbers, filters, crystallizers, driers, and distillation columns to simulate the hydrodynamics of the system. They have been proven to be useful for the reconstruction of porous media related to soil modeling for bioremediation, oil recovery, water permeation, and geological evolution.

In mimetic models, the departure point of structural transformation is also associated with Euclidean objects, which, due to its regular geometry, makes it easy to model force field interactions and phenomena such as aggregation or peptization.

However, these models become less convenient when they are not able to reflect the heterogeneities of the pore matrix. Also, the final morphology of the void channels is generally highly irregular, which complicates the accurate resolution of the transport equations inside the void space. This is not convenient for a system with large representative volume elements because it requires high calculation times to perform a simulation.

### 2.4.3. Pore Network models

Even if all the aforementioned methods attempt to model the pore network of the material, the term pore network model is usually reserved to lattice-based structures into which the pores are represented with Euclidean solids connecting the nodes of the lattice. This kind of organization allows also building hierarchical structures.

Some examples present in the literature are hybrids of different approaches. Except by direct mapping models, the pore structures built are expected to statistically reproduce the properties of the actual porous network.

A more detailed literature review of pore network models will be given in section 2.6.

## 2.5. Porous structure experimental characterization techniques

The characterization of porous structures involves several properties of interest that reach the field of topology and stereology. The simplest properties are porosity, surface area, volume, and pore size distribution. Increasing the level of detail, it is also possible to study the pore shapes, their mean curvature, the surface roughness, the structural correlations within the solid matrix, and the topology. Some common techniques are shown in Table 2.

Table 2. Conventional characterization techniques for porous solids.

		Technique	Resolution
BULK TECHNIQUES	}	Physical gas adsorption	0.5 nm
		Mercury intrusion porosimetry	4 nm
3D IMAGING RECONSTRUCTION	}	Focused Ion Beam SEM	0.01 $\mu$ m
		X-ray Micro Tomography	1 $\mu$ m (Hard-rays)/0.01 $\mu$ m (Soft X-rays)
		Electron Tomography	0.001 $\mu$ m
		Magnetic Resonance Imaging	1-10 $\mu$ m
		Scattering Techniques	1 nm

Using different characterization techniques, it is possible to get direct or indirect insights into the material's textural properties. In this section, we will provide more information on techniques that are used in this work.

#### **2.5.1.1. *X-ray computed micro-tomography***

It provides 2D and 3D images of the topology of the solid. It is a non-destructive technique (Coles 1999; Hamamoto et al. 2016; Schlüter et al. 2014; Blunt et al. 2013; Ketcham and Carlson 2001).

#### **2.5.1.2. *Focused Ion Beam (FIB) couple with Scanning Electron Microscope (SEM)***

SEM is a microscopic technique that provides 2D images of the surface of a solid. Coupling a focused ion beam allows eroding layer by layer the sample's surface. The 3D volume is reconstructed by piling the SEM images of each slice (Wirth 2009; Keller et al. 2013; Uchic et al. 2007).

#### **2.5.1.3. *Nuclear Magnetic Resonance-Relaxometry***

NMR relaxometry allows measuring the pore size distribution of a sample and the auto-diffusion coefficient of a species. The measurement is based on the random movement of the molecules and the energy released by them due to relaxing after being excited by an energy source (Mohnke 2014; Javed et al. 2019).

#### **2.5.1.4. *Nuclear Magnetic Resonance-Cryoporometry***

This technique is based on the shift in the solid-liquid phase transition temperature of a chemical probe due to the solid-liquid interface curvature. At the beginning, the liquid phase is imbibed into the solid, and then solidification and melting of the probe are performed. As the sample is frozen or melted, the intensity of the Nuclear Magnetic Resonance (NMR) signal associated with the liquid phase quantity is recorded. Finally, one obtains characteristic curves representing the amount of liquid as a function of the temperature. The sensitivity of the temperature sensor and the right choice of the relaxation filter parameter are crucial and can limit the technique. The thermodynamic model on which is based the data treatment is the Gibb-Thomson equilibrium equation (Mitchell et al. 2008). Freezing and melting temperatures depend on the pore size and the surface-to-volume ratio, which evolves along the phase change process. The hysteresis between the melting and the freezing temperature is commonly associated with metastable states of the fluid under confinement. A difference in the solid-liquid interface mean radius of curvature between freezing and melting can also explain this hysteresis. In the case of a cylindrical pore for example, the melting proceeds radially while freezing occurs according to the pore axis. In order to avoid random heterogeneous freezing, a common practice is to generate a

solid phase layer surrounding the sample. This layer acts as a nucleation seed during the process and gets the freezing temperature closer to the equilibrium temperature (Mitchell et al. 2008; Petrov and Furó 2009). The freezing temperature can also be constrained by the absence of nucleation solid phase, preventing the solid phase formation and creating a metastable state (Petrov and Furó 2009). As there is a broad pore size distribution in disordered interconnected porous material, the freezing step can be topologically dependent, or as stated by Petrov architecturally dependent (Petrov and Furó 2009). On the surface of the pore remains a very thin layer ( $\approx \text{\AA}$ ) of liquid, even after the homogeneous freezing step. Its thickness depends on the temperature and nature of the material and is called the pre-molten layer or plastic ice (Dash et al. 2006; Li and Somorjai 2007; Schreiber et al. 2001).

Several attempts to model the cryoporometry characterization technique are described in the literature pursuing understanding the phase change under confinement phenomena and improving the interpretation of the results. For example, Kondrashova (Kondrashova and Valiullin 2013) used a lattice-fluid model to study how freezing and melting proceed in disordered mesoporous materials. Enniful presented a study that models cryoporometry by using a serially connected pore model (Enniful et al. 2019). In this model, the authors consider an advancing solid phase front for the freezing step and proposed to model advanced melting by including a constant factor to the Gibb-Thomson equation. Perkins used percolation analysis to simulate the advancing of the solid phase front phenomena and confirming the pore blocking effects by PFG NMR (Perkins et al. 2008).

#### **2.5.1.5. Mercury porosimetry**

Mercury porosimetry is used to characterize meso- and macro-porous materials. The technique relies on the resistance shown by a liquid with very high surface tension (non-wettable liquid) to penetrate in a confined medium. The pressure that needs to be applied to the fluid so that it penetrates in a pore of a determined characteristic length can be determined by the Washburn equation. The latter is a mechanical equilibrium equation that can easily be derived from the Young-Laplace equation by making a balance of forces. The applied pressure is inversely proportional to the pore size. The effective measurement range is between 4 nm and 200  $\mu\text{m}$  corresponding to pressures in the range between 4000 bar to 0.5 bar, respectively. By increasing and decreasing the applied pressure, mercury intrusion and extrusion occurs, the variation of the mercury volume present within the sample being measured.

For the analysis of the results, the assumption of a cylindrical pore geometry is widely used. This assumption allows relating the pore size to the applied pressure. Then, to each pore size must be associated a volume to get the intrusion and extrusion characteristic curves.

This characterization technique is well documented by Allen and Lowell (Allen 1990; Lowell and Shields 1991). The sample is first degassed and then immersed in mercury. By increasing its pressure, the front of mercury advances, penetrating pores according to a percolation process (Kaufmann 2010). Some difficulties can occur to assign a volume to a given pore size. As a matter of fact, due to the random location of pores of different sizes, wider pores can be further beyond the front where narrower pores have been penetrated at a certain pressure, which means that the volume of intruded mercury accounted at higher pressures will be accounted as mercury intruded into narrower pores. Naturally, this can be thought of as pore blocking. Once the final pressure is reached, it is decreased to start an extrusion process. During the intrusion, the mercury is in compression, while during the extrusion the mercury is in tension. For the analysis of the experimental results, a correction must be applied to consider the compressibility of mercury according to the pressure.

Experimentally, there is a hysteresis between the intrusion and extrusion curve that can again be related to pore blocking phenomena, as in the case of the intrusion, but also to a change in contact angle and/or mean radius of curvature between the solid and the fluid. In the model commonly used for the analysis of results, the intrusion angle and extrusion angle are considered equal and constant. This is considered to be reasonable in the domain of oxides. However, various authors have proposed models in which the angles of intrusion and extrusion are different or even variable along the characterization (Kaufmann et al. 2009). This also applies to the surface tension of the mercury.

At the end of the test, there is a volume of mercury retained in the porous material after extrusion. The retention volume of mercury is generally proposed to be related to a jump of potential (Moore and Slobod 2013; Mohanty et al. 2013), which can be simply explained as a situation in which there is mercury trapped in a pore or ensemble of pores surrounded by empty pores that are smaller. This means that these full pores are at a lower potential than their neighboring pores and that additional energy should be provided to the system to drain the mercury that is trapped inside.

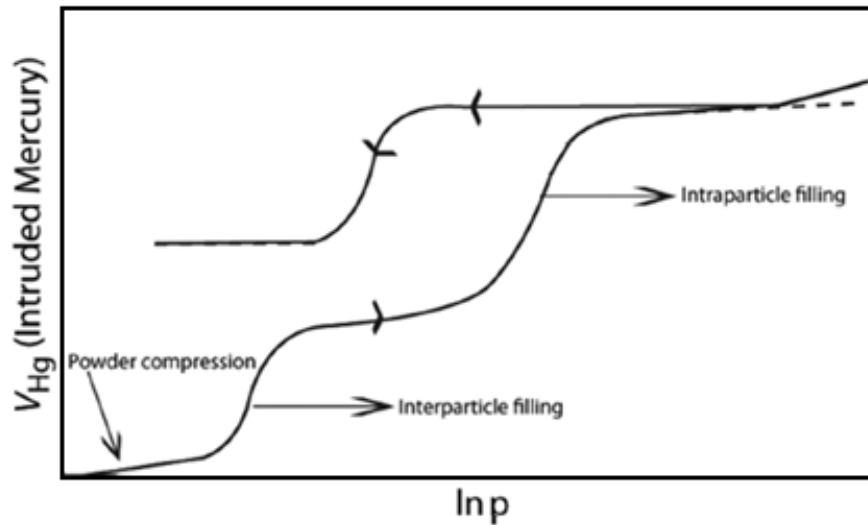


Figure 11. Intrusion/Extrusion Mercury Porosimetry typical curve (modified). (Rouquerol et al. 2011).

On the intrusion curve, well-defined zones can be identified (Figure 11) for a porous medium made of an agglomeration of porous particles. The first one corresponds to lower pressures and represents the interparticle filling region.

Due to the high hydrostatic pressures involved in the test, the solid is subject to plastic deformation and rupture caused by compression. As a result, it is necessary to be cautious if information from the extrusion curve is to be used.

A significant number of authors have proposed simulations for this characterization technique (Tsakiroglou and Payatakes 1991; Lapidus et al. 2007; Mohanty and Scriven 1987; Murray et al. 1999a). The first attempt to use a pore network model to reproduce mercury porosimetry characteristic curves was performed by Mann in 1980, assigning the pore size distribution by trial and error (Mann and Golshan 1981; Mann et al. 1981).

#### **2.5.1.6. Nitrogen adsorption and desorption**

Nitrogen sorption relies on capillary condensation phenomena and is useful to characterize micro- (down to 0.5nm) and mesoporous solids (rigorously speaking, it is a liquefaction process). First, the porous sample is heated under vacuum to eliminate any trace surface adsorbed species. Subsequently, it is submitted to an ultra-high vacuum into a sealed vessel where nitrogen is then injected at its boiling point. Nitrogen starts to adsorb on the pore walls due to physical interactions. A layer of molecules is formed, and it thickens as the pressure increases. When the pressure is high enough, sudden condensation happens within the core, i.e. the free remaining volume, of the pore (Figure 12).

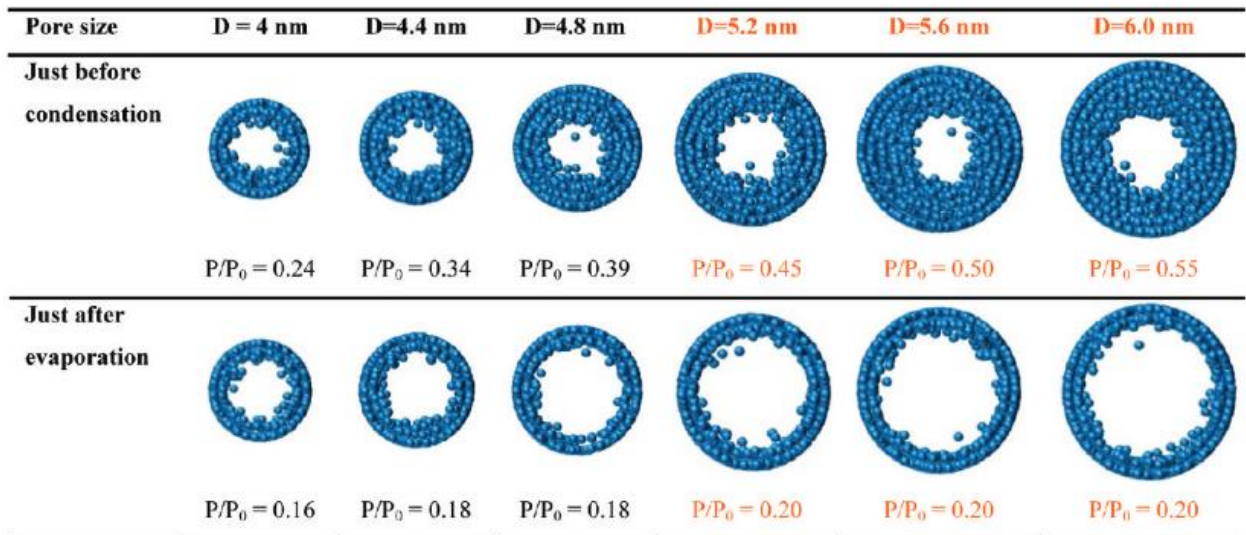


Figure 12. Simulation snapshots of argon particles in graphitic cylindrical pores at 87.3 K before condensation and after evaporation (Nguyen et al. 2011).

The quantity of nitrogen present within the sample being measured, an experimental curve that relates the pressure to the amount of nitrogen adsorbed is obtained. This curve is called nitrogen adsorption isotherm. At the end of the adsorption process, the pressure is decreased to get a desorption isotherm by the same principle. When the two isotherms are plotted, it is possible to observe in some cases a hysteresis loop. The shape of the isotherm and the hysteresis loop provide qualitative information about the topology of the porous structure. There exist classifications that allow the user to make inferences about the kind of structure and topology of solid according to the shape of the isotherm. The more cited classifications are IUPAC's and Rouquerol's (Figure 13) (Rouquerol et al. 2014a; Rouquerol et al. 2011). Different pore architectures generate different characteristic loops.

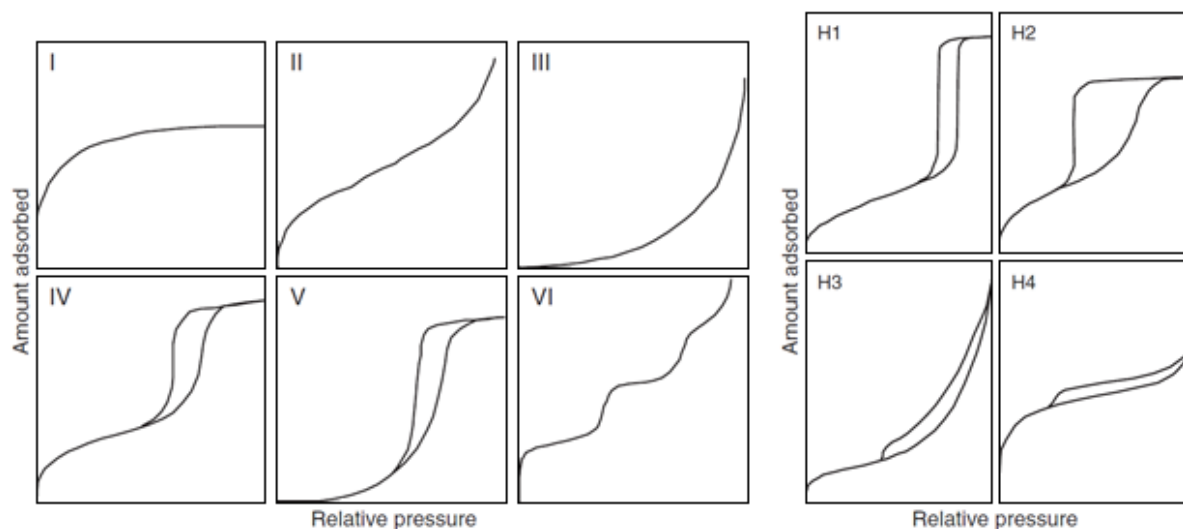


Figure 13. Isotherm and hysteresis loop classification (Rouquerol et al. 2014b).

Several authors (Rodrigues et al. 1989; Sing 1985; Rouquerol et al. 2014a; Rouquerol et al. 2011) explain why nitrogen sorption continues to be one of the most used characterization techniques for the characterization of the textural properties of porous solids. Among them, it is worth mentioning that the technique is cheap, technologically simple, widely used (useful for comparison), and that the thickness of the adsorbed nitrogen multilayer is largely insensitive to differences in the adsorbent particle size or surface structure.

There exists theoretical evidence (Nguyen et al. 2011; Gelb and Gubbins 1999; Bruschi et al. 2015; Zeng et al. 2017) suggesting that the adsorption and desorption branches are affected by the pore size, the pore length, the pore shape, the type of pores end, and the surface adsorption strength. These parameters could affect the shape of the liquid nitrogen meniscus, influencing the capillary forces and the critical density of the core before condensation/evaporation (Nguyen et al. 2011).

The sorption hysteresis loop is generally considered to be related to the textural properties of the structure, topology, surface strength, and tensile strength. Usually, the surface strength and tensile strength are neglected: the surface strength is considered to be low since there is no chemical interaction of nitrogen with the surface, and the tensile strength is considered to be very high (rigid pores), respectively.

By using theoretical and empirical models to interpret the nitrogen sorption curves, pore size distribution, pore-volume, surface area, and porosity are estimated from sorption experiments. BET, BJH and BdB (Broekhoff 1967; Brunauer et al. 1938; Barrett et al. 1951) are some common examples of models used for the interpretation of the results.

Regarding computational modeling, adsorption in mesoporous materials is generally displayed as a phenomenon mainly influenced by capillary forces. Capillary forces will influence the sorption pressure of the nitrogen as a function of the textural properties of the material (pore size and pore shape). The classic approach to represent the phenomenon is through the modified Kelvin equation (Cohan 1944; Zhang et al. 2006). The modified Kelvin equation considers the variation of the thickness of the adsorbed layer of nitrogen before the sudden phase transition within the pore core. There exist different models based on thermodynamics and statistical dynamics with some empirical components to model the thickness of the layer ( $t$ ) as a function of the pressure (Figure 14). A very interesting study about the influence of different statistical thickness models on the sorption isotherms was made by Šolcová in 2006 (Šolcová et al. 2006).

$$\begin{aligned}
 \text{Halsey} \quad t &= \frac{0.354}{5 \frac{1}{3} - \ln(P/P_0)} \\
 \text{Harkins-Jura} \quad t &= \frac{13.99}{(0.034 - \log(P/P_0))^{0.5}} \\
 \text{Micromeritics} \quad t &= \frac{0.599}{(-\log(P/P_0))^{0.399}} \\
 \text{deBoer} \quad 0 &= \log(P/P_0) - 0.1682 \exp(-1.137t) + \frac{0.1611}{t^2}
 \end{aligned}$$

Figure 14. Examples of statistical thickness models.

For adsorption, the modified Kelvin equation allows to directly relate the relative pressure to the pore size. The adsorption process of the gas is supposed to be unconstrained by the topology of the structure.

For desorption, however, the pressure of the pore at which nitrogen in the pore desorbs is determined by the combined effect of the capillary forces and the topology, i.e. according to its location within the network. The topology of the structure can cause pore-blocking promoting a vapor-phase percolation phenomenon. Indeed, during the desorption step, the nitrogen vaporization can be delayed due to the topology of the material, creating a metastable state. Even if the desorption pressure for the pore is reached, the liquid phase needs to be in contact with the vapor phase to be able to desorb. Figure 15 represents a system of three pores A, B, and C in series open at both ends. A and C have a smaller radius than B. Assuming a cylindrical geometry, the desorption pressure of A and C is lower than that of B. This means that the nitrogen contained in B is constrained and cannot desorb until A or C is evacuated. Consequently, the phase change pressure of pore B will be lower than during adsorption.

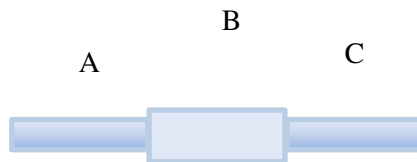


Figure 15. Representation of three pores in a row.

Another common methodology for nitrogen sorption is the generation of scanning curves or scanning desorption isotherms. A scanning curve is represented by an adsorption branch obtained from a solid that is not totally filled with condensed nitrogen (relative pressure <1). The relative pressure at which the desorption starts will determine which pores are filled with condensed nitrogen (not just with adsorbed nitrogen). Scanning curves allow to

obtain a qualitative interpretation of the structure and topology, to make inferences about the existence of possible hierarchical architectures, combining the experimental information with other characterization techniques (Cimino et al. 2013; Hitchcock et al. 2014; Rigby et al. 2017).

## **2.6. Pore Network Models: state of the art**

Pore network models are used in a great number of applications in different domains related to porous media. Adsorption, dissolution, precipitation (Peter Matthews et al. 1996), biomass growth (Ezeuko et al. 2011; Daigle et al. 2015), permeability studies through soils, rock, and shales (Huang et al. 2016; Song et al. 2020; Spearing and Matthews 1991; Bultreys et al. 2016), chemical reaction (Adloo et al. 2019), mass transfer (Rosen 1976) and lyophilization (Attari Moghaddam et al. 2018) are some of the domains in which this kind of models is used. Using a pore network model, it is possible to simulate different phenomena and heterogeneities at the micro- and mesoscopic scale; some examples are phase exchange, non-Newtonian displacement, non-Darcy flow, slippage, interfacial transport, non-viscous effects, and reactive transport.

Because pore network models are used in so many different scientific domains, there is no unified terminology for their description. Usually, the “centers” can be called nodes, sites, pore bodies, pore sites, or just pores; while the connections between them are called bonds, throats, or just pores. In what follows, referring to the vocabulary used in graph theory, we will use the term “nodes” for the centers, and the term “edges” for the connections. The term “pore” will refer to an object to which dimensions can be assigned: it can occupy a node position or an edge position.

Pore network models provide significant advantages among which it is worth mentioning:

- They represent a length scale above the atomic scale up to the macro scale. The first consideration means that it is possible to simplify the elemental surface chemistry characteristic of the material, which offers the possibility of considering representative clusters of the microscopic and the mesoscopic scale in shorter calculation times. Such a model allows simulating reaction kinetics, diffusion, and permeability at the micro/mesoscale. As affirmed by Xiong, the lower scale limit of the pore network is determined by the governing equations and the upper scale by the computational power (Xiong, Baychev et Jivkov 2016).
- They allow modeling local and global heterogeneities of the material.
- It is possible to get rid of the tortuosity. Tortuosity is defined by Keil as an ill-defined correction factor, affirming that the relation between the geometry of the structure and the parameter was not clear at all (Keil 1999), thereby supporting Rosen who defined it as a fudge factor (Rosen 1976).

The main characteristics of a pore network are:

- **Pore geometry.** The geometry used to represent the void space is relevant for mass transfer considerations and the resolution of transport equations along the network. The pores usually have regular geometries such as cylinders, spheres, and cubes. Irregular geometries are usually associated with the representations constructed from image techniques information. The pore wall can be also smooth or rough. The existence of sharp edges can be useful to model bi-phasic flow, for example. The selected geometry will condition the maximum Surface/Volume ratio of the network and the number of parameters to set (Figure 16).
- **Characteristic dimensions of the pore.** The selected geometry will determine the number of characteristic sizes or parameters to set. For example, a spherical geometry has just one characteristic dimension (radius); a cylindrical geometry has two characteristic dimensions (radius and length); a rectangular parallelepiped has three characteristic lengths (two sides sizes and its length) (Figure 16).
- **Assignment of the characteristic dimension(s) to the pores.** This is also characteristic of different models. In the simplest case, the characteristic dimensions are constant. If at least one of them obeys a particular statistical distribution, there is more than one way to perform the assignment.
- **Nodes and edges.** Different geometries and characteristics can be assigned to these elements. For example, nodes can be assigned to be zero-volume, while pores in the edge position have volume. Alternatively, a volume can be assigned to pores in the node positions, while zero-volume is considered for the pores on edges. As the latter create a resistance to mass transfer, in this case, the accumulation and resistive properties of the network are described separately. The definition of these features will affect the average coordination number, the range of reproducible textural properties, the mass transfer process, the complexity level of the equations to be solved.
- **Connectivity.** Connectivity is a very important parameter in a porous material. It represents the number of edges connected to a node. This parameter influences permeability, mass transfer coefficients, and textural properties of the network. The average connectivity of the network's nodes can be fixed at the beginning of the construction of the network, but it is also possible to make it dependent on the pore existence probability used during the creation of the pores along the network. It is also possible to use connectivity probability density functions for the network. Another way is to eliminate nodes or edges randomly until the desired connectivity is reached.
- **Architecture and level of correlation.** The pore network can have several pore classes coming from different pore size distributions and pore existence probabilities. Those can be placed on different lattices along the network. The pore classes can be independent in terms of pore size. However, it is also possible to

generate more complex networks into which the different levels of porosity are also correlated.

A lot of studies mention the importance of the distribution of the pore sizes, volume, and morphologies along with the network (Blunt et al. 1992; Knackstedt et al. 1998; Øren 2002; G. Jerauld et al. 1984; Hollewand and Gladden 1995; Valvatne and Blunt 2004; Sahimi et al. 1990; Raouf and Hassanizadeh 2010; Meyers and Liapis 1999).



Figure 16. Examples of regular transversal pore sections.

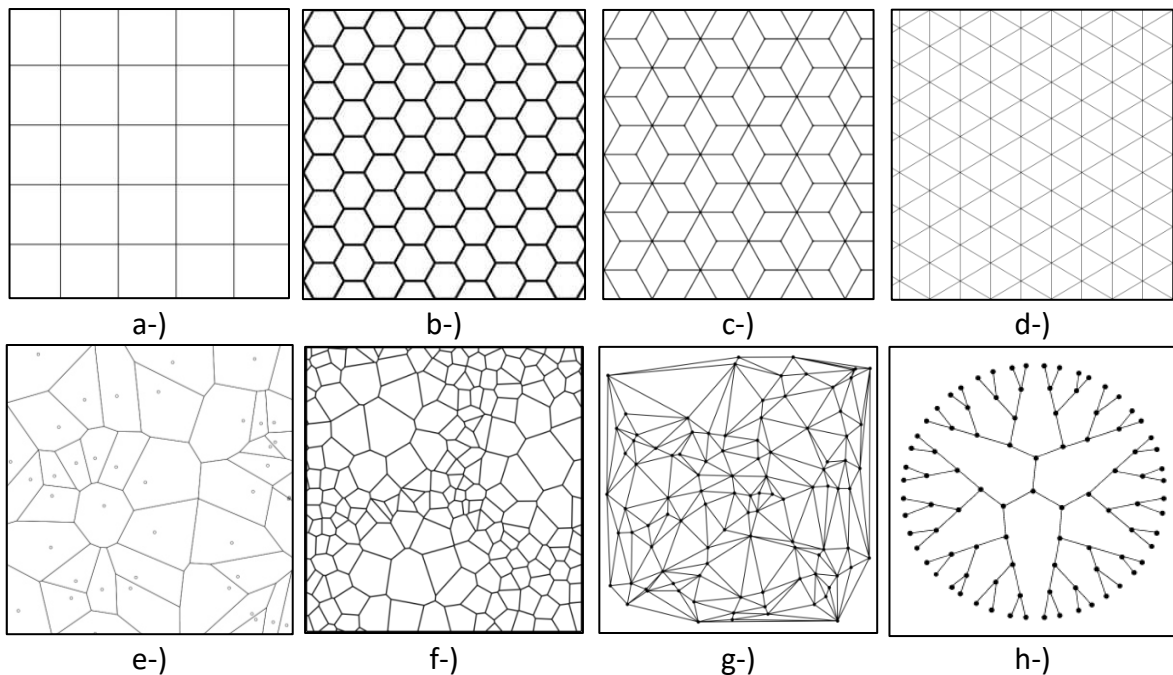


Figure 17. Different lattice examples. a-) Square, b-) Single hexagonal, c-) Double hexagonal, d-) Triple hexagonal, e-) Voronoi-Dirichlet, f-) Voronoi tessellation, g-) Delaunay tessellation, h-) Bethe tree.

Another element to pay attention to in a pore network model is the kind of **lattice** used since it will influence the connectivity and the topology (Figure 17). The elemental classification for lattices is relative to their organization. A lattice can be regular or irregular. In a regular lattice, the nodes are displayed with short or long-range order, a constant and

well-defined pattern. Since his first work, Fatt (Fatt 1956a) showed and compared several kinds of lattices. Naturally, a lattice can be displayed in two or three dimensions. There exist some more elaborated lattices as the Bethe lattice (Beeckman and Froment 1979; Beeckman and Froment 1980), the Voronoi lattice (Voronoi 1908), and the Delaunay lattice. The latter is a combination of Voronoi polygons with a Dirichlet tessellation. This kind of tessellation produces spatially correlated random networks (Tranter et al. 2018). The Bethe lattice does not have closed loops. Figure 18 shows an example of a pore network model based on a regular square lattice with spherical pores on the node locations and cylindrical pores on the edge locations.

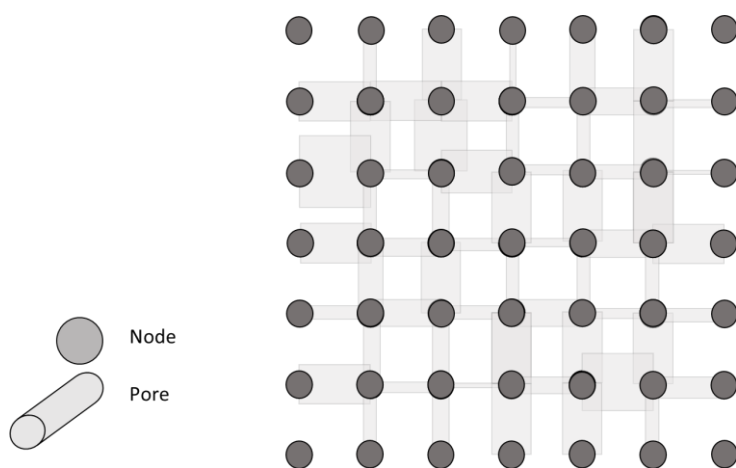


Figure 18. 2D Cylinders and spheres regular square lattice pore network representation.

The pioneer of pore network models is Fatt in 1956. At that time, there were two main common models used to describe the permeability through a material: the bundle of tubes model described for diffusion and reaction by Wheeler (Wheeler 1951) and the sphere packs. According to Fatt, even if the bundle of tubes models allows making rigorous derivations of properties, it fails to correctly represent the porous material in terms of flow isotropy. On the other hand, the sphere pack prevented the derivation of an accurate description of flow through the interstices due to the complexity of the geometry of the voids. He hypothesized that, if the two models were combined to represent the pore space seen in sphere pack model, it would then be possible to create a network on which exact flow calculations could be made (Fatt 1956a). Decades after this statement, this idea would be sustained by Gladden, who reiterated that by representing the pore space with pores of idealized geometry, the equations of diffusion and reaction can be easily solved (Hollewand and Gladden 1992).

However, for a long time, the bundle of tubes model has still been around along with some modifications but with the same limitations, as in the work by Wakao and Smith for a hierarchical network representation of alumina (Wakao and Smith 1962) or in the work by Mann and Thompson for zeolites (Mann and Thomson 1987). Johnson and Steward offered

a solution to the lack of pore connectivity in the bundle of tubes model by creating the cross-linked capillary model (Figure 19) used for model diffusion through a porous media (Johnson and Stewart 1965; Feng and Stewart 1973).



Figure 19. Cross-linked capillary model representation (Feng and Stewart 1973).

In 1981, Mann used a stochastic pore network model in order to simulate mercury porosimetry and also coking (Mann and Golshan 1981). At that time, he claimed to use some sort of version of invasion percolation previously developed for oil entrapment, but he did not explain the methodology. Some years after, he was the first author along with Sharratt in publishing an extensive study relating diffusion and reaction to the pore network properties (Sharratt and Mann 1987).

Mohanty and Lin (Mohanty 1981; Lin and Cohen 1982) were the first to develop an explicit methodology to map material onto an equivalent structure of interconnected pore bodies. Mohanty argued in his Ph.D. thesis how transport and reaction are influenced by the morphological state of the porous media and formulated the problem of lack of sufficient information for the analysis of such phenomena coming from macroscopic measures “which often provide the essential but not sufficient information” – he said. Mohanty sustained the need for a microscopic approach arguing about the multiphase flow dependency upon microscopic connectivity, which had been at the time recently demonstrated by several researchers (Larson et al. 1981; Dullien 1979).

In 1991, Gladden used two pore network models to study diffusion and reaction in a spherical-shaped catalyst. In both models, the edges are modeled as cylinders (Hollewand and Gladden 1991). The pellet is modeled as a cube. Two of the parallel faces of the cube are set as the surface of the material and the other 4 perpendicular faces are periodic boundaries. The first model uses a regular cubic lattice in which connectivity is varied by eliminating randomly nodes along the network. In the second case, the authors did not use a lattice but distributed the nodes randomly within the cube. The nodes were connected through pores that were assigned along the network until the desired connectivity was reached. The diameter of the edge was randomly assigned from a given pore size distribution. For the selected simulation conditions, the tortuosity calculated for regular and irregular networks are significantly different. It was also observed that the sensitivity of

tortuosity to the pore size distribution and the connectivity decreased as the connectivity increased. To understand the relation between the irregular and regular networks, this research group published new research in 1992 characterizing the networks by percolation and finite-size scaling theories (Figure 20). They concluded their work by saying that the critical exponents that were found are independent of the topology and the connectivity, but only dependent on the system dimensionality (Hollewand and Gladden 1992). Also, they confirmed that the differences in percolation threshold on both types of pore networks were significant but disappeared for very high connectivities ( $Z=14$ ). The authors also advised against using uncorrelated pore size distributions for the different levels of porosity. They already suggested that the topology and the connectivity may have an important role in the diffusion and diffusion-reaction properties of the network. This work changed the paradigm impelled by the results shown by Jerauld (G. Jerauld et al. 1984), in which there was no difference between the percolation properties obtained from a regular network and from an irregular network assembled on a Voronoi lattice, both having the same coordination number. However, this still remains a controversial topic.

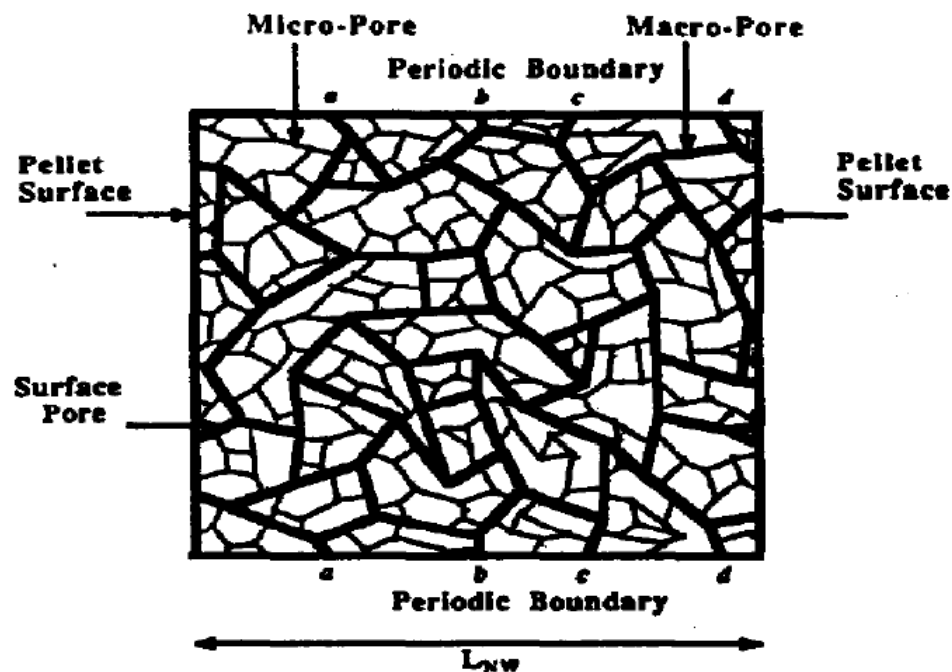


Figure 20. 2D representation of the hierarchical pore network used by Gladden in 1992 (Hollewand and Gladden 1992).

Spearing and Matthews developed a pore network baptized as the Pore-Cor model (and recently rebaptized PoreXpert) for representing a Clashach sandstone (Spearing and Matthews 1991). In their work, they chose a cubic geometry for the nodes and cylinders for the edges (Figure 21). The size of each cubic node depended on the maximum size of the cylindrical edges arriving on the node. This allowed them to avoid the overlap between

pores. At the same time, this structure allowed them to correlate the node-edge geometries and to use an experimental throat/pore diameter correlation for the same material. They verified the pore size distribution by using a mercury intrusion simulation and compare the geometric surface area to the BET area. To adjust the model's BET area, they considered a rough surface on the pore walls, adding roughness parameters to adjust the model.

In 1995, Satik and Yortsos proposed a cubic network lattice to study the effect of the temperature on sorption isotherms using as a case study the flow in a geothermal field (Satik, C. 1995). The lattice was assembled using cylinders and spheres, representing edges and nodes, respectively. The diameters of the edges were randomly assigned using three different pore size distributions. The rules used for modeling the sorption phenomenon were those established and explained by Yortsos who considered pore-blocking phenomena, the topology, and the thermodynamic stability of the system (Parlar and Yortsos 1988, 1989). Keil used the same kind of network to study diffusion and reaction in porous material using a pore size distribution coming from experimental nitrogen sorption (Keil 1999).

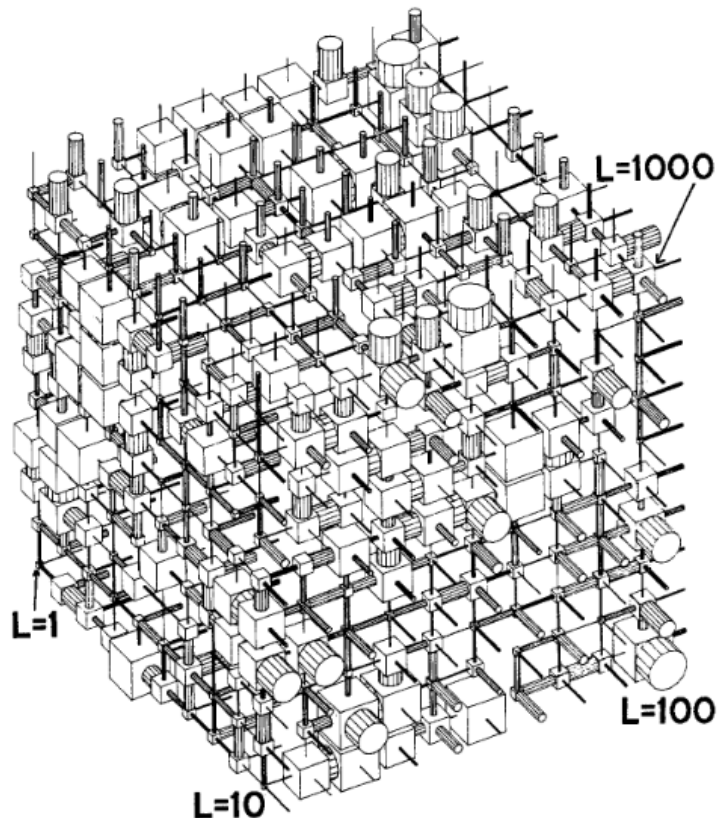


Figure 21. 3D representation of the pore network used by Spearing and Matthews in 1991 (Spearing and Matthews 1991).

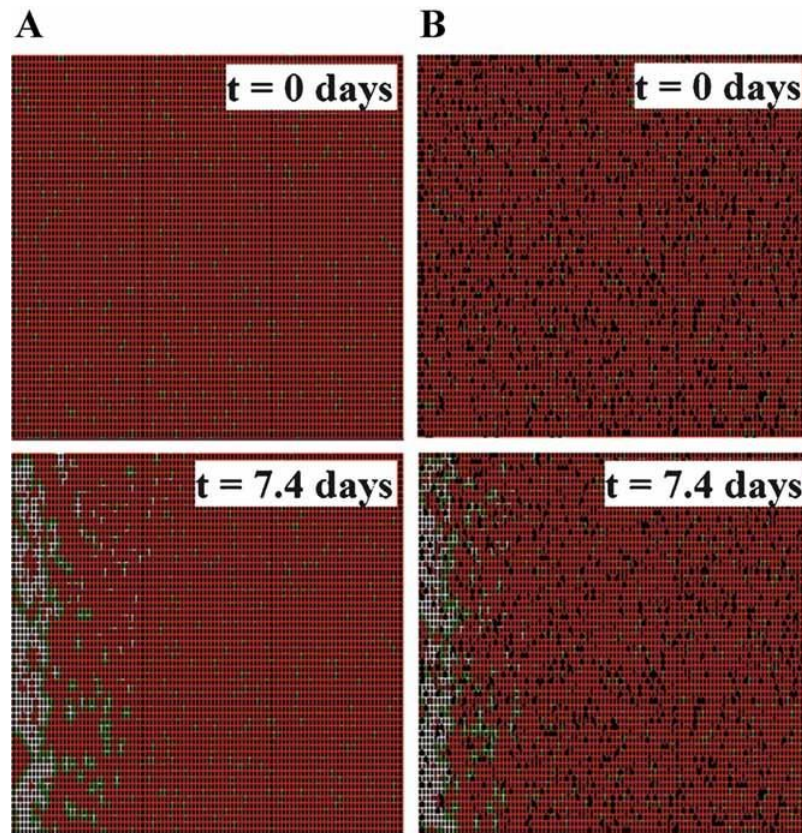


Figure 22. Pore-network modeling of biofilm evolution in porous media. (Ezeuko et al. 2011)

In 2002, Gladden published two very interesting studies in which capillary condensation was considered along with diffusion and reaction in a pore network (Wood and Gladden 2002; Wood et al. 2002). They discussed the insights of the effect of Thiele modulus and the pore network parameters on diffusion. In this work, they used a random pore network model based on their previous work (Hollewand and Gladden 1992) and on the work of Sharratt and Mann (Sharratt and Mann 1987).

In the last decade, pore network models have also been used for studying biofilm evolution in porous media (Figure 22). In these studies, the influence of the support on the biofilms is tested and new bioreactor models are proposed.

Pore network models can have a limited predictive capacity “because some characteristic features of the pore space are missing” (Blunt 2001), as in the Fisher and Celia model to predict permeability based on capillary pressure measurements (Fischer and Celia 1999). In the same review, Blunt stated that a spatially correlated disordered network was required to make more accurate predictions. With spatially correlated networks, Blunt was enclosing the effect of the topology, thereby reaffirming Gladden’s conclusions (Hollewand and Gladden 1995).

In 2002, Moore studied the effect of pore structure, randomness, and pore size on effective diffusivity using different kinds of regular and random lattices (Mezedur et al. 2002). Here, the creation of the pores is based on an average porosity, which can be directly related to a probability of existence, while in previous works, the porosity or the connectivity was met by randomly eliminating nodes or edges of the network.

The Dual Site-Bond Model (DSBM) is a pore network modeling approach was developed by Mayagoitia (Cruz et al. 1989; Mayagoitia et al. 1996; Mayagoitia et al. 1997). Like the Pore-Cor model, the authors use a regular square 2D lattice or a regular cubic 3D lattice, in which nodes are represented by spheres and edges by cylinders (Figure 23). They use a constrained Markovian process to assign of a size characteristic to each pore, in which the radius of the spherical pore located on the node needs to be larger than the radii of all cylindrical edges arriving on the node to avoid the overlap between pores. In contrast to other pore network models, the algorithm does not draw a new pore size, but it iteratively swaps the sizes of two randomly selected nodes or two randomly selected edges until all geometrical constraints are satisfied. This methodology provides a potential to the nodes and edges to restrict the way into the network is created. It can be used to create pore networks with different scales of correlated porosity by creating new probability density functions that change dynamically as a result of the interaction between the probability density functions of the two scales. It is also possible to statistically consider overlaps between the geometrical representation of the pores or avoid overlapping by setting local size constraints (Montiel et al. 2019). For example, it is possible to consider the adsorption energy distribution as a potential and to build and an energetically consistent structure (Riccardo et al. 1993).

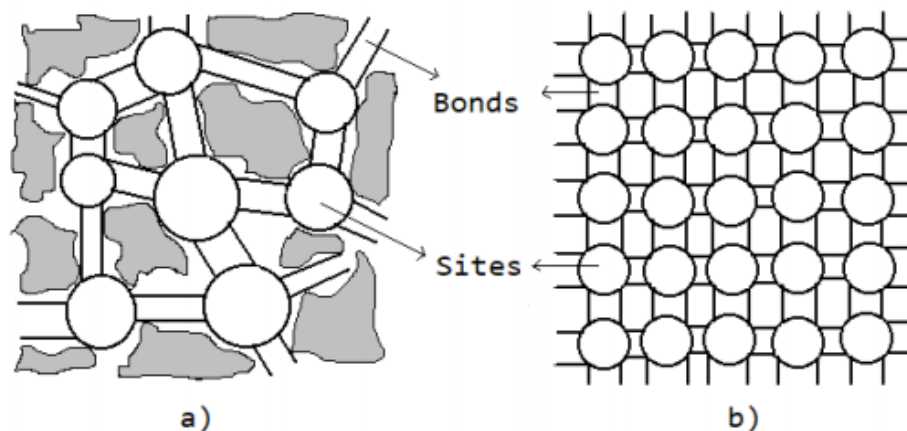


Figure 23. Dual site-bond network representation (Montiel et al. 2019). a-) Representation of the real media. b-) Pore network.

Armatas and Pomonis used a Monte Carlo semi-random dual-site-bond model (DSBM) to study the porous characteristics of functionalized silica (Armatas and Pomonis 2004). This

kind of pore network model uses as input the pore size distribution obtained by nitrogen sorption porosimetry and the specific surface area calculated by BET analysis. The length of the edges is constant. The pore networks are generated according to a probability of existence. The generation of the network starts by increasing the probability of existence until the backbone of the network is constructed as soon as the percolation threshold is reached. The edges that are part of the backbone are considered to be macropores, and no volume is assigned to them under the hypothesis that the BET analysis does not account for macropore volume since the quantity of nitrogen adsorbed within them is negligible. The rest of the network is built starting from the backbone until the BET surface is reached. Again, the nodes must have a radius higher than the biggest edge connected to them. The method is called semi-random because the smaller edges are set to be closer to the external surface of the network. Nitrogen sorption is simulated within the network. The position of the edges is then varied randomly to obtain an isotherm that agrees with the experimentally measured one. In 2006, Armatas published additional work using the same pore network and studying the combined effect of variation of the pore size distribution, tortuosity, and connectivity on diffusive transport parameters. However, this time, instead of varying randomly the edges of the network to generate a particular nitrogen isotherm, he fitted the topology of the structure to a pore connectivity distribution using a Monte Carlo method (Armatas 2006). These different approaches indicate different ways of distributing the volume along with the network and different ways to generate hierarchical networks.

In 1981, Androutsopoulos (Mann et al. 1981; Androutsopoulos and Salmas 2000b; Androutsopoulos and Salmas 2000a; Ammus et al. 1987) created a pore model called Corrugated Pore Structure Model (CPSM). This model is an upgrade of the bundle of tubes model and has similarities with the specular model developed by Foster (Foster and Butt 1966) (Figure 24). This is a statistical numerical method that models the pore structure as cylindrical pores of different diameters connected in series. The model has been adapted for nitrogen sorption, mercury intrusion, and deactivation due to carbon lay down (Androutsopoulos and Salmas 2000a; Androutsopoulos and Salmas 2000b; Ammus et al. 1987). However, the biggest disadvantage of the model lies in a limited concept of connectivity that makes impossible the simulation of a real percolation process, thereby requiring to use artificial parameters for fitting. For example, for nitrogen sorption, the two angles used to define the curvature of the liquid-vapor interphase are freely varied to fit the model. Based on CPSM, a tortuosity predicting model has been also created (Salmas and Androutsopoulos 2001). However, the lack of a real representation of the connectivity makes the model predict very high tortuosity values (Armatas and Pomonis 2004).

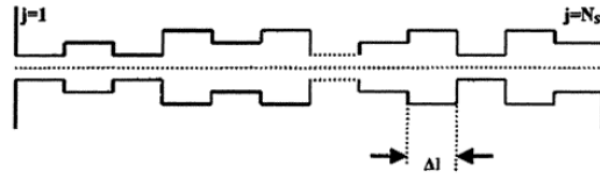


Figure 24. Graphical representation of a corrugated pore structure model (CPSM) (Androutsopoulos and Salmas 2000a).

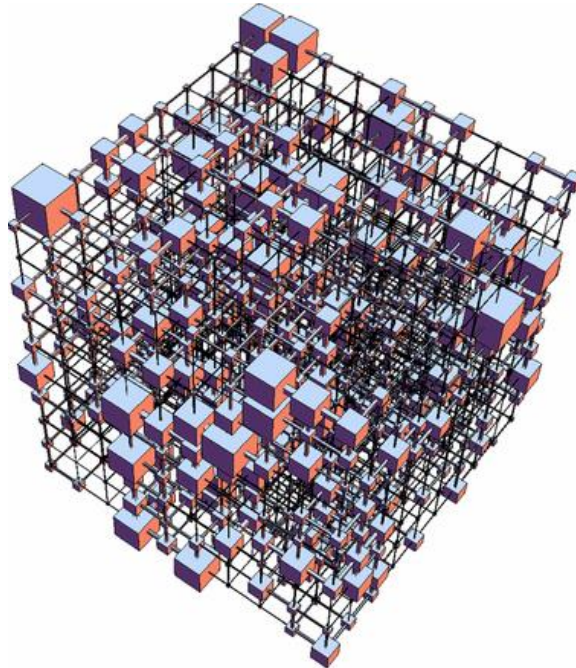


Figure 25. Huang pore network representation (Huang et al. 2016).

In 2016, Huang (Huang et al. 2016) used a pore network to model a two-phase shale matrix flow. The pore geometry was rectangular for the edges and cubic for the nodes (Figure 25). The authors assumed that only the edges would offer a resistance to the flow, but without having volume, while the nodes possess volume, but do not offer a resistance to the flow. The edge length was considered as constant, and the node inscribed diameter was randomly assigned according to a given pore size distribution.

Xie worked on a pore-network model including viscous coupling effects using direct simulation by the lattice Boltzmann method (Xie et al. 2017) based on the network adapted by Blunt (Valvatne and Blunt 2004) (Figure 26).

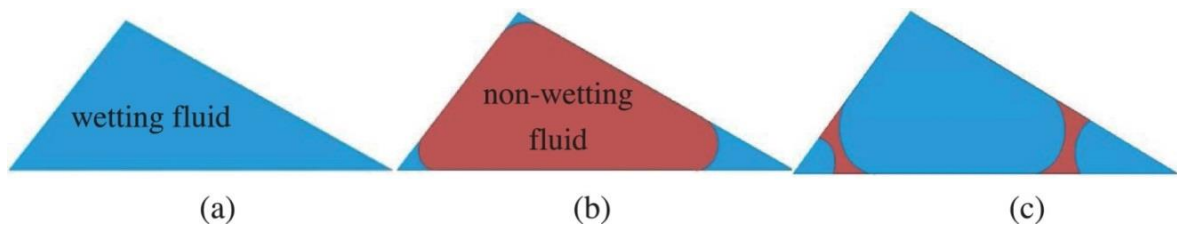


Figure 26. Different fluid configurations for biphasic flow in a pore from the network. (Xie et al. 2017)

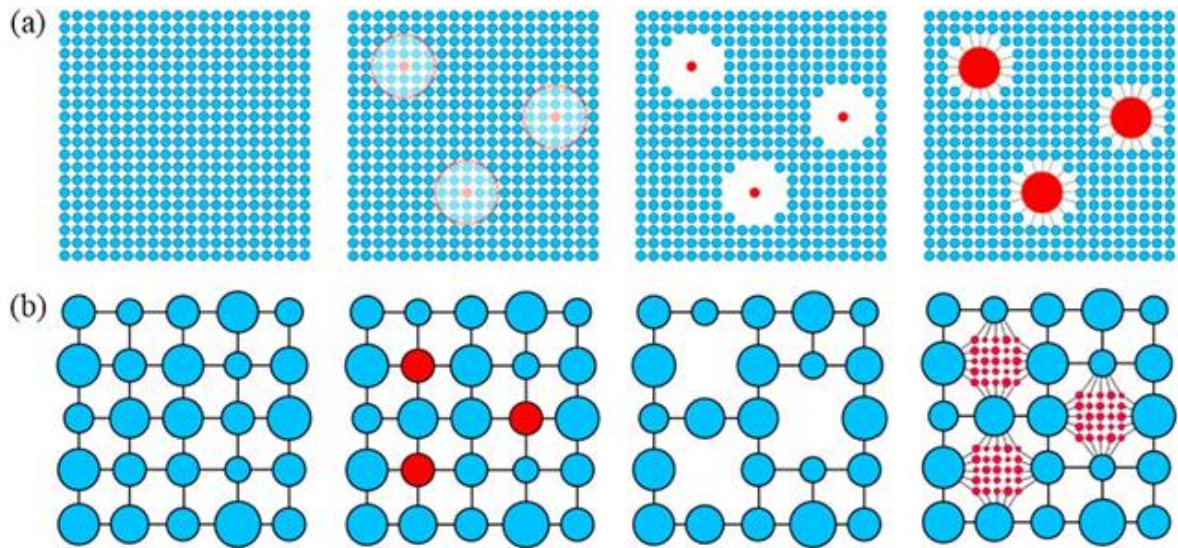


Figure 27. Sadeghi's model: (a) Bottom-up approach (b) Top-down approach (Sadeghi et al. 2017).

In 2017, Sadeghi studied the influence of hierarchical structures on mass transfer by doing a sensitivity analysis of a new pore network model approach (Sadeghi et al. 2017). In his adaptation, two approaches are defined, which he called the bottom-up and the top-down approach (Figure 27). The approaches look to create a hierarchical structure using different strategies. The node geometry is spherical, while the edges are cylindrical. The edge length is constrained by the radius of the nodes and the node spacing. There are always two levels of porosity (defined as A and B). In the bottom-up approach, the network is assembled using the smallest level of porosity (A); some nodes are selected randomly and the perimeter that surrounds it is substituted by a spherical pore of level B. The top-down approach is a simple inversion of this methodology: the network is created by using the largest level of porosity (B), and some of these nodes are selected randomly and replaced by a set of smaller nodes (A). He did not specify the strategy for the assignment of the diameters of different pore levels.

Probability functions can be applied to the networks to adjust pore densities to create porosity gradients. Tranter used two different pore size distributions for the generation of a network. Defining different pore size distributions along different directions allowed them to decrease the pore-density at the top and bottom surfaces of the domain, creating larger pores (Tranter et al. 2018). This is intended to simulate experimental porosity gradients.

Ye developed an algorithm for generating a pore network with an arbitrary external surface shape (Ye et al. 2017) (Figure 28). This methodology allows varying the external border conditions for mass transfer simulations, i.e. the ratio of external to internal pores.

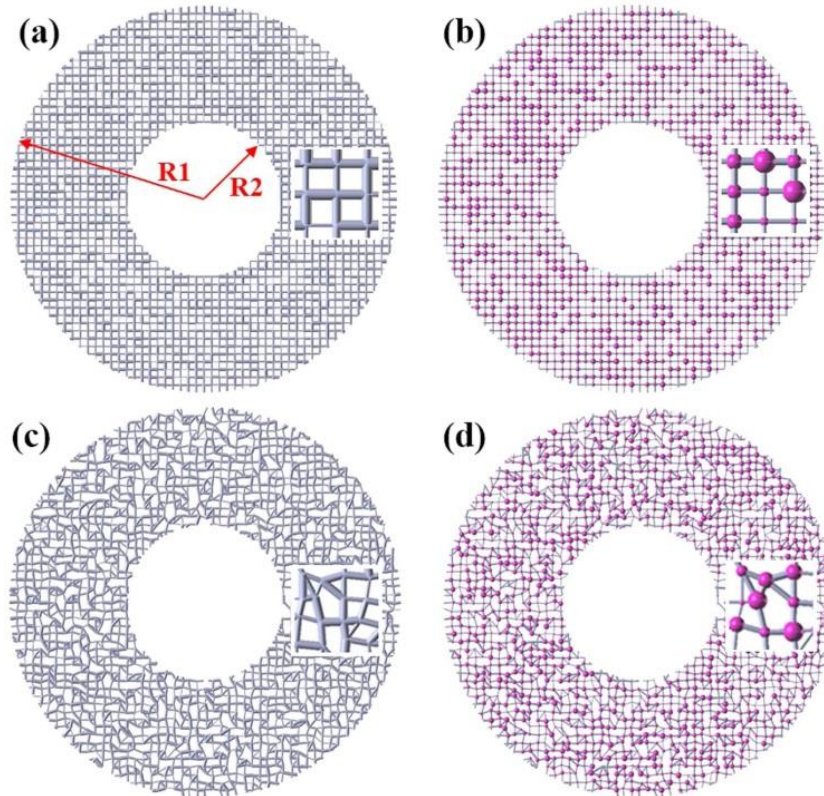


Figure 28. Four different kinds of pore networks with one-holed ring border conditions. (a) A regular network of cylindrical pores (b) Regular network of cylindrical and spherical pores (c) Irregular network of cylindrical pores (d) Irregular network of cylindrical and spherical pores (Ye et al. 2017)

## **Chapter 3: Pore Network Model Generation**

### **3.1. Introduction**

This chapter describes the pore network model that was implemented to model gamma alumina. In the next section of this chapter, a general description of the pore network model structure is given. Section 3 describes each input variable used for the pore network generation, while section 4 explains the generation algorithm of the pore network step by step. In the fifth section, the minimum network dimension and the minimum number of simulations required to limit the variance on the calculated properties is discussed. In the sixth section, an analysis of the influence of the input parameters on the geometric textural properties of the network is presented. The seventh section details the percolation algorithm used to characterize the network and the selected binary heap algorithm. In the last sections, a topological and architectural analysis of the network is performed.

### **3.2. Pore Network Model (PNM)**

The pore network model that we propose is created through a discrete reconstruction method based on a stochastic algorithm that starts from an initial lattice, or graph, made of nodes and edges. At the end of the pore network generation process, hollow cylinders will occupy a fraction of the edges, while the remaining nodes can be either zero-volume nodes (i.e., the nodes do not play any physical role) or be occupied by hollow spheres with a physical influence in the model. It is possible to create a pore network in 1D, 2D, or 3D. Generated pore networks can have a fixed size or can be periodic along one or several axes.

The characteristics of the initial lattice define the maximum connectivity of the network, i.e. the initial number of edges of each given node. At the end of the pore network generation process, this corresponds to the maximum number of pores that can be connected to a given node. The lattice can either be regular, with a fixed spacing between the nodes, or irregular, by creating random displacements of the nodes in the lattice. Hence, the length of the pores located on the edges will either be constant (in regular lattices), or variable.

Different features provide heterogeneity to the digital structures in order to obtain not only a good representation of the textural properties but also a good representation of the topology of the network. With the developed pore network generation tool, it is possible to use several pore size distributions in the same network, which allows the construction of hierarchical structures, i.e. networks with different porosity levels. The porosity of each porosity level of the network is controlled by a threshold value defined as the pore existence probability (PEP). Each porosity level can have its own PEP. The intertwining of the various

porosity levels can also be varied by modifying the grid spacing between the different pore levels, thereby adding complexity to the final network.

The pore network generation tool uses a Monte Carlo algorithm that works as follows. At a given node, an edge to a “neighboring” node is selected, and a random number is drawn and compared to the pore existence probability threshold in order to evaluate whether a pore is to be created or not. If a pore is to be created on this edge, its pore diameter is randomly drawn from a user defined pore size distribution. By repeating this procedure for each edge, each node will be connected to a number of pores that ranges from 0 (non-existing node) and the maximum connectivity number. After generating the network, inaccessible pores are removed.

### 3.3. Input variables of the pore network model

#### 3.3.1. Network size and dimensions

The network dimensions are defined according to 3 parameters that will define the network volume:

- **Directions.** The edges can be created in 1 direction ( $\vec{X}$ ), 2 directions ( $\vec{X}, \vec{Y}$ ) or 3 directions ( $\vec{X}, \vec{Y}, \vec{Z}$ ).
- **Number of nodes** along each direction  $N_{\vec{X}}, N_{\vec{Y}}, N_{\vec{Z}}$ .
- **Node spacing.**

The total number of nodes is given by:

$$N_T = N_{\vec{X}} * N_{\vec{Y}} * N_{\vec{Z}}$$

Equation 1. Total number of nodes

By defining the number of nodes in each direction, the algorithm detects which are the direction throughout the edges will be created. If in a given direction, the number of nodes is equal one, the corresponding direction is removed.

The maximum initial total number of edges can be estimated as:

$$N_T Edges = N_T nodes * \frac{Z_{max}}{2}$$

Equation 2. Maximum number of pores (estimation)

The node spacing defines the initial distance between two adjacent nodes along an axis. In the current version of the pore network generation model, the initial distance between two

adjacent nodes is the same in each direction. This initial grid of nodes is equidistant in all directions.

### 3.3.2. Grid distortion

In order to allow for more random structure, this initial grid of nodes can be distorted by defining a grid distortion parameter. The grid distortion parameter represents the maximum distance that a node can be randomly relocated in each direction from its original position. If the grid distortion is zero, the edge length along each axis will be constant. The grid distortion parameter should not exceed the initial node spacing in order to avoid overlapping between nodes in each direction. Graphically, the node can be relocated to any position within the purple zone showed in Figure 29.

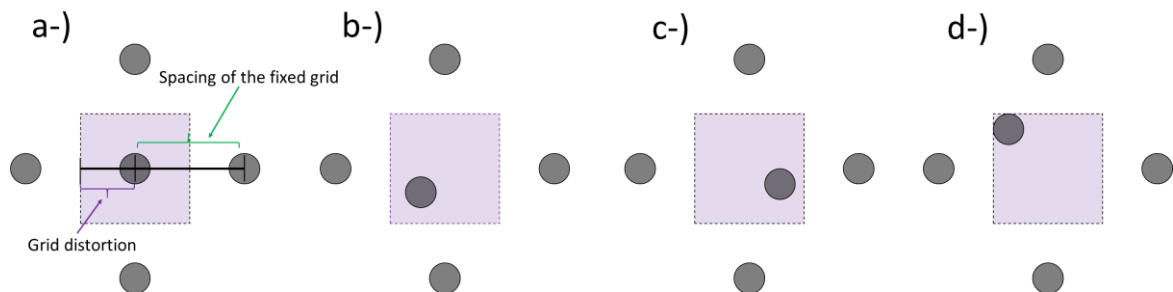


Figure 29. Random relocations for a node when grid distortion is activated. Figure a represents the original state of the system without distortion. Figures b, c and d represent different possible random relocations for one of the nodes.

The use of grid distortion will create networks with varying pore lengths. In the model developed here, this factor does not influence on average the spatial volume distribution. Thus, it does not have an important impact on the textural properties of the digital solid, and apparently, it does not influence the topology either (See sensitivity analysis for nitrogen). The reason is that, as the grid distortion is implemented, the pore length distribution will approximately follow a triangular distribution and will be homogeneously distributed in the space (Figure 30). Both characteristics are a consequence of the random nature of the process for the relocation of the nodes.

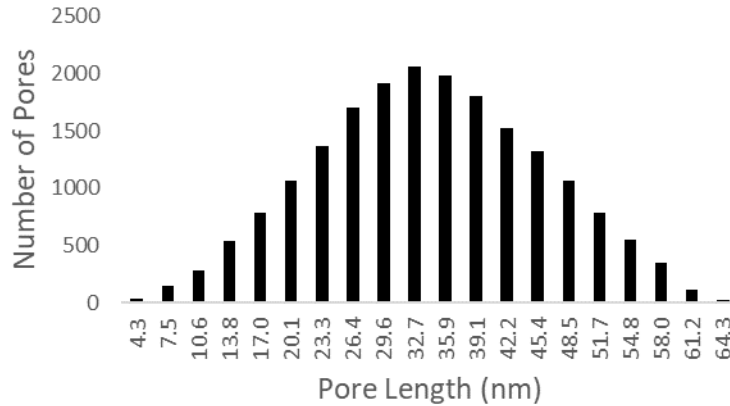


Figure 30. Pore length distribution for a 2D pore network with a spacing of the fixed grid equal to 30 nm and a Grid distortion equal to 30 nm.

### 3.3.3. Network lattice and connectivity pattern

The network lattice defines the connectivity pattern between the grid points. Hence, the lattice used for the pore network generation sets the maximum connectivity in the network. The connectivity pattern is represented by the directions of a unitary cell (Figure 31).

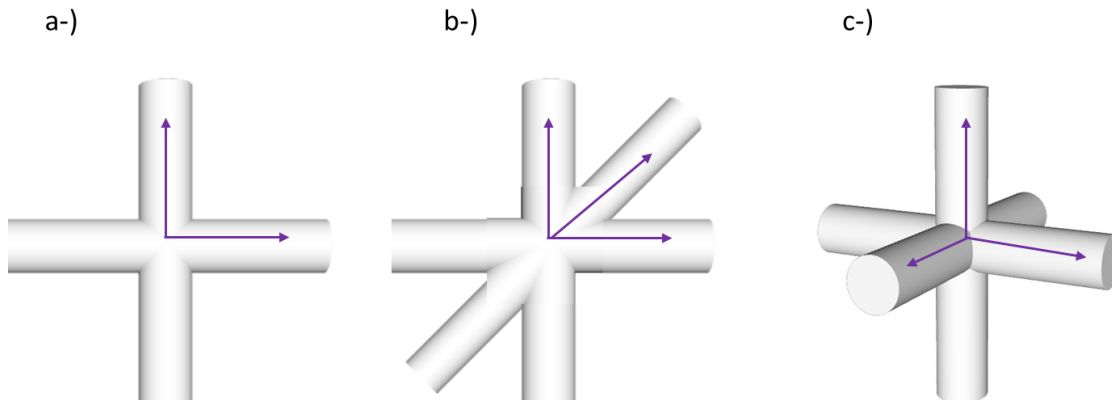


Figure 31. Different lattice representations and their unitary vectors. a-) Square lattice, maximum connectivity equal to 4 ( $Z_{max}=4$ ). b-) Triangular lattice, maximum connectivity equal to 6 ( $Z_{max}=6$ ). c-) Cubic lattice, maximum connectivity equal to 6 ( $Z_{max}=6$ ).

In this work, the connectivity is defined taking the node as reference. In the lattice, the maximum connectivity of a node is the number of edges connected to a node. As the algorithm is currently configured, it is possible to create a network with a maximum connectivity of up to 18. Once the algorithm has built the pore network by placing pores on edges, the actual connectivity of a node will become the number of pores connected to that node.

In the current version, the pore network generation tool is limited to using the same kind of lattice for all the pore populations on each porosity level.

### 3.3.4. Periodicity

The pore network can be periodic along one or several dimensions. This property is useful to create pore networks models that will be used for mass diffusion simulations. In a periodic network, an edge will connect the last available node of a row of a series of nodes along an axis to the first node on the same row (Figure 32).

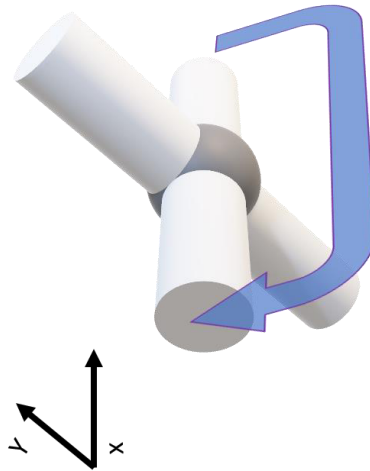


Figure 32. Example of a network with periodicity in the X-direction.

### 3.3.5. Pore populations

The term “pore population” will be used to describe a group of pores on the edges of the graph with common characteristics, such as the pore existence probability and the pore size distribution. The term “pore level” will be used for hierarchical structures with 2 or more different pore populations, i.e. with pore size distributions that represent different size scales, for example micropores, mesopores, and macropores.

The number of pore populations of the network needs to be specified first. For each pore population, a Pore Existence Probability (PEP) threshold, a grid spacing, and a pore size distribution needs to be defined.

Each pore population has its own Pore Existence Probability (PEP) threshold. This threshold defines the probability of adding a pore of an edge position. For each edge of the lattice, a random number is generated (range 0-1). A pore is created, that is to say, it is placed on the corresponding edge, only if the random number is below the PEP. Thus, if the PEP is equal to 1, all the edges of the initial lattice will be occupied.

The grid spacing is a key parameter of the model. The grid spacing is the recurrence of the pore population in each dimension. Figure 33a is generated with one population with a grid spacing equal to 1 and a PEP of 1. All the rows and columns are filled with pores. Figure 33b

is generated using the same population but with a grid spacing equal to 5 in each direction ( $\vec{X}, \vec{Y}$ ). Figure 33d shows the same population with a grid spacing equal to 5 but implementing a triangular lattice. In both cases, the free edges can be occupied by another pore population. Figure 33c shows the same initial lattice as in Figure 33b with two populations.

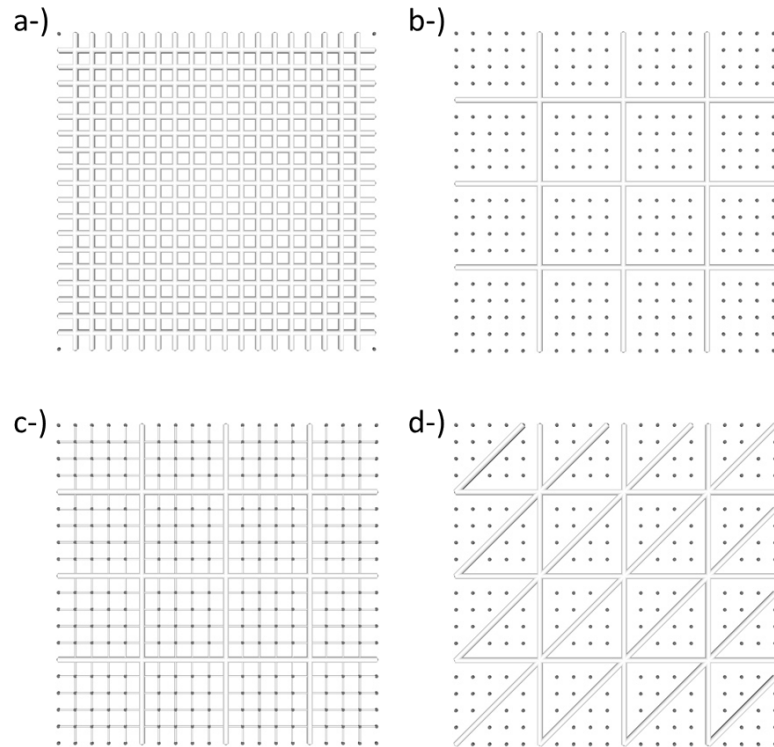


Figure 33. Pore networks with different grid spacings: a-) One population, grid spacing equal to 1. b-) One population, grid spacing equal to 5. c-) Two populations, grid spacing of population 1 equal to 5, grid spacing of population 2 equal to 1. d-) One population, grid spacing equal to 5 (triangular lattice).

There is an order in which the populations should be inserted. They should be specified starting from the population with the highest grid spacing to the one with the lowest grid spacing. The reason is that the algorithm will not allocate edges for just one population. Let's consider Figure 33c: population 1 has the largest diameter and it has a grid spacing equal to 5, while population 2 has the smallest diameter and a grid spacing of 1. The pore network generation algorithm will first create population 1 and then population 2. As population 2 has a grid spacing of 1, the generation algorithm will create pores on all the free edges. If population 2 is created first, the results would look like Figure 34. The algorithm will create first the population with the grid spacing equal to 1 and a PEP of 1. Hence, when the population with the grid spacing equal to 5 is to be created, there are no longer free edges available.

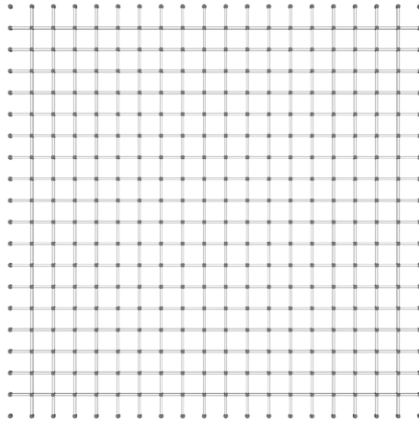


Figure 34. Wrong representation of a pore network with 2 different pore populations.

Figure 35 gives another example of the effect of grid spacing. In this example, a first population with a grid spacing equal to 4 and a second one with a grid spacing equal to 2 exist. As 4 is a multiple of 2, then the population with a grid spacing of 2 will have fewer available lines to occupy.

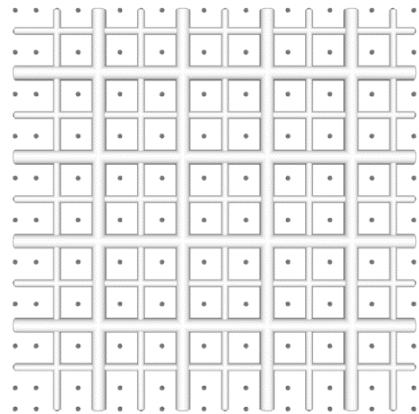


Figure 35. Network with two pore populations. Population 1 has a grid spacing equal to 4 and population 2 has a grid spacing equal to 2.

The use of multiple populations and of grid spacing allows providing a greater heterogeneity to the network and allows to fully use the capacity of the lattice to create void space. Let's consider the same case of Figure 35, but this time, the PEP of population 1 (biggest diameter) is set to 0.6. Since population 2 has a PEP equal to 1, it will fill the free spots left by the pores of the population 1 that do not exist. The result is shown in Figure 36.

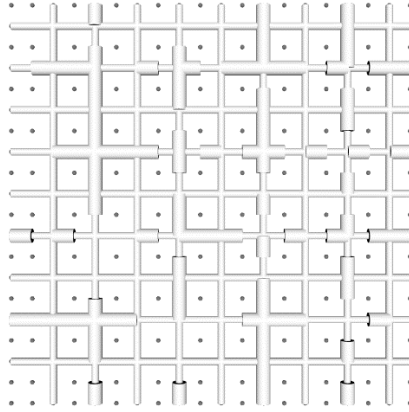


Figure 36. Network with two pore populations. Population 1 has a grid spacing equal to 4 and a PEP equal to 0.6. Population 2 has a grid spacing equal to 2 and a PEP equal to 1.

For each pore population, the pore size distribution information is provided in terms of its cumulative distribution function (CDF). The first parameter to be specified is the number of points that will be used to describe the cumulative pore size distribution. The input CFD must start at a cumulated probability equal to 0 and must end at a cumulated probability equal to 1.

### 3.3.6. Skeletal density

The skeletal density of the material, in our case of gamma-alumina, is an important parameter to be specified. This is an experimental value and is needed to calculate the total mass of the digital network.

## 3.4. Pore network construction

### 3.4.1. Generation of the grid of nodes

The nodes are the smallest unit of the network and serve as reference point for the implementation of the lattice.

All the information of the network is stored in multidimensional arrays. The first element created for the network generation is the set of nodes. The spatial coordinates of the nodes for the initial grid are first calculated considering the user-specified node spacing of the grid. If the grid distortion is different from zero, the node is relocated (Equation 3). The new position of the node is given by the distorted coordinates:

$$\begin{aligned}x &= x + (\text{rand} - 1/2) * \text{Ldistort} \\y &= y + (\text{rand} - 1/2) * \text{Ldistort} \\z &= z + (\text{rand} - 1/2) * \text{Ldistort}\end{aligned}$$

Equation 3. Node news coordinates after distortion.

where  $L_{distort}$  is the grid distortion,  $rand$  is a random number between 0 and 1, and  $x,y,z$  are the cartesian coordinates of the nodes

Once the coordinates of the nodes are calculated, they are numbered or labeled. The labeling sequence for the nodes is illustrated in Figure 37 for a 2D and a 3D network.

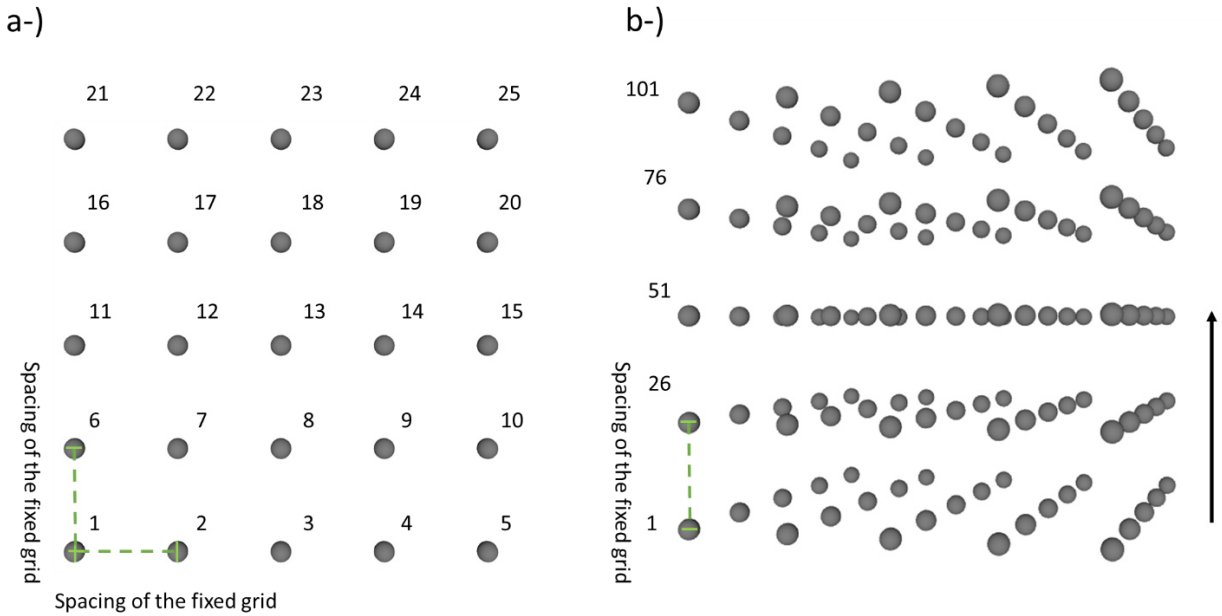


Figure 37. Labelling sequence for nodes a-) 2D network b-) 3D network.

### 3.4.2. Generation of pores on the edges

The algorithm will create the pores, node by node, fulfilling the lattice pattern given as an input. The nodes are swiped in the order indicated by their labels. Figure 38 illustrates the creation and labelling sequence for the pores. For each node, all the edges are explored one by one. Before creating the pore, a random number is generated. If this number, whose range is amid 0 and 1, is lower than the PEP threshold, then the pore is created.

Figure 38 shows a labeling example with a triangular pattern. The external pores cannot be connected between them in non-periodic networks: this is the case of the first 8 pores. Pores 9, 10, and 11 are created in the same order of the generation unit vectors on the right side of Figure 38.

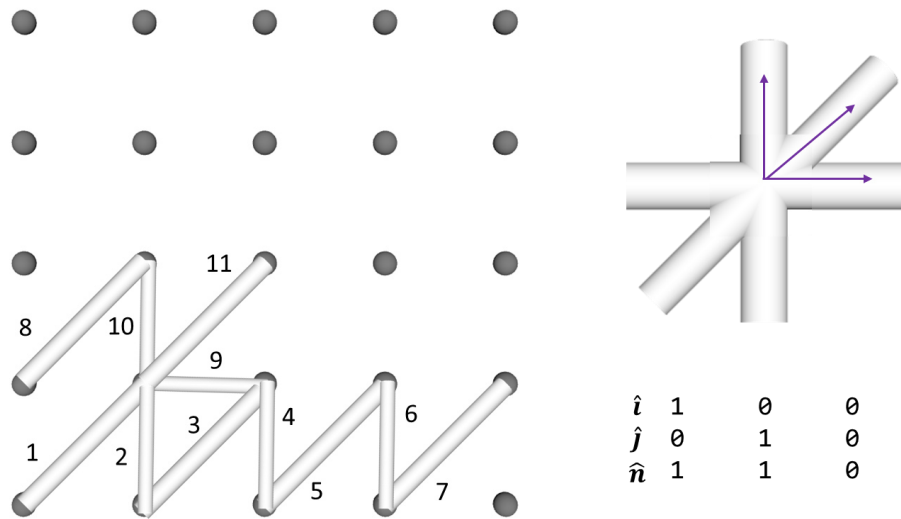


Figure 38. Labelling sequence process for pores in a network with PEP=1

If the network is periodic in the X-direction, then the external nodes of the Y-direction will be connected by pores. Similarly, if the network is periodic in the Y-direction then the external nodes of the X-direction will be connected by pores (Figure 39).

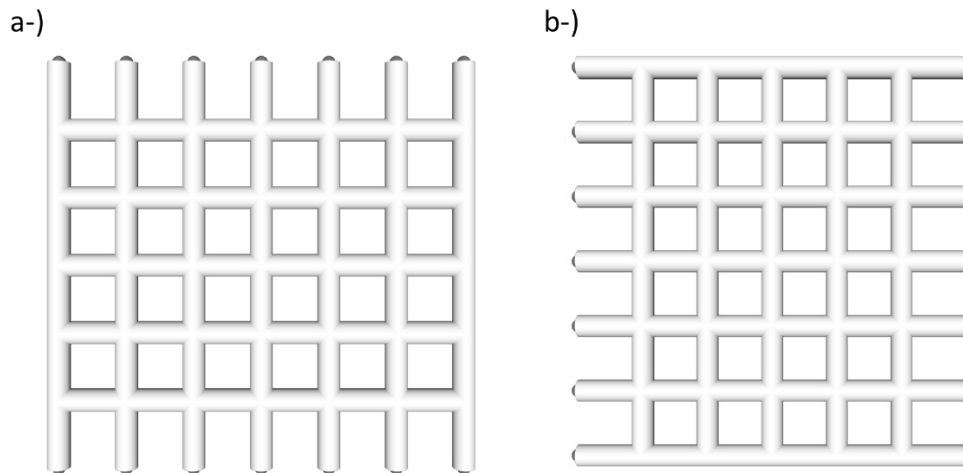


Figure 39. Periodic networks: a-) Periodic network in the X-direction. b-) Periodic network in the Y direction.

When a pore is created, dimensional information is required. Although various pore geometries could be used (Figure 16), in the current version of the pore network generation tool, the pores located on the edges of the graph are represented by smooth cylinders. Hence, two dimensions are required, and a length and a diameter are attributed to the ore when it is created. The pore length will depend on the distance between the two nodes the pore is connecting. For the diameter, a random number will be generated between 0 and 1. This random number is considered as the cumulative distribution value of the diameter to assign. If the value is between two points of the CDF of the pore size distribution, a linear interpolation is computed to find the corresponding diameter.

### 3.4.3. Generation of pores on the nodes

Once all edges have been explored, and all pores located on edges have been attributed, the algorithm will scan all nodes to add additional void space, if requested by the user. By default, the pore network will be created with nodes that do not have any physical property and just provide a reference framework. However, the pore network generation tool also allows creating pore networks with nodes that provide additional void volume to the network (Figure 40). The radius of the hollow sphere located on the node will be equal to the minimum radius that is needed to avoid overlapping of pores located on the edges of the node. This will often involve the radius of the biggest pore connected to the node. If a triangular lattice is used, diagonal pores also have to be considered for the calculation of the minimum sphere radii to avoid pore overlapping.

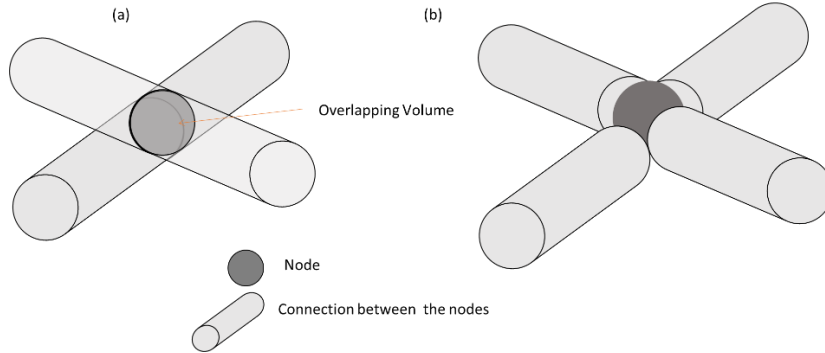


Figure 40. 2D Schematic representation of an elementary system node-pore for a square lattice with PEP equal to 1. (a) The porous space is just represented by the cylinders (pores on edges). (b) The porous space is represented by the cylinders (pores on edges) and by the spheres (pores on nodes).

### 3.4.4. Calculation of geometrical textural properties

Once the pore network model is fully generated, the geometrical textural properties are calculated using the information coming from the digital network. These properties are the pore volume, surface area, porosity, and connectivity. The total volume of the network is defined as the void volume (pores) plus the solid volume. The total volume is calculated according to Equation 4 using the coordinates of the nodes.

$$V_N = (x_{N_{\bar{X}}} - x_1) * (y_{(N_{\bar{X}} * N_{\bar{Y}} - N_{\bar{X}} + 1)} - y_1) * (z_{(N_T - N_{\bar{X}} * N_{\bar{Y}} + 1)} - z_1)$$

Equation 4. Total volume of the network

The total mass can be calculated using the total volume of the network and knowing the structural density of the material:

$$M_T = V_N * \rho_{material}$$

Equation 5. Pore network total mass

The porosity, surface area and pore volume are calculated adding the individual properties of each pore. With zero-volume nodes, the geometrical textural properties are calculated from the dimensions of the hollow cylinders.

$$\varepsilon = \frac{\sum_{i=1}^{N_{pores}} \pi * \frac{d_i^2}{4} * l}{V_N}$$

Equation 6. Digital solid porosity.

$$S_{geom}(m^2 * g^{-1}) = \frac{\sum_{i=1}^{N_{pores}} \pi * d_i * l}{\rho_{Al203} * V_N * (1 - \varepsilon)}$$

Equation 7. Digital solid specific pores surface area.

$$v_{p\_geom}(m^3 * g^{-1}) = \frac{\sum_{i=1}^{N_{pores}} \pi * \frac{d_i^2}{4} * l}{\rho_{Al203} * V_N * (1 - \varepsilon)}$$

Equation 8. Digital solid specific pores volume.

It is possible to simplify these equations for a scenario with zero-volume nodes in which the diameter and length of the pores can be considered as constant. For these conditions, textural properties can be approximated as described in Equation 9, Equation 10, and Equation 11:

$$\varepsilon = \frac{\frac{Z_{max}}{2} * PEP * \pi * \frac{D_p^2}{4}}{L_p^2}$$

Equation 9. Digital solid porosity approximation.

$$S_{geom}(m^2 * g^{-1}) = \frac{\frac{Z_{max}}{2} * PEP * \pi * D_p}{\rho_{Al203} * \left( L_p^2 - \frac{Z_{max}}{2} * P * \pi * \frac{D_p^2}{4} \right)}$$

Equation 10. Digital solid specific pores surface area approximation.

$$v_{p\_geom}(m^3 * g^{-1}) = \frac{\frac{Z_{max}}{2} * PEP * \pi * \frac{D_p^2}{4}}{\rho_{Al203} * \left( L_p^2 - \frac{Z_{max}}{2} * P * \pi * \frac{D_p^2}{4} \right)}$$

Equation 11. Digital solid specific pores volume approximation.

### 3.4.5. Output files with the network structural information

There are two main files that contain the information of the pore network structure. The first one is called connectivity matrix. It is a table that reports the connectivity of the node, i.e. the actual number of the pores connected to it, the labels of the pores, and whether the pore is an external pore or not (Table 3). The second relevant file is called Pore dimensions and Connections (Table 4). This file reports the length and diameter of each pore. It also reports to which nodes the pore is connected. Additionally, a third output file called node coordinates contains the metric coordinates of all the nodes. Knowing the metric coordinates of the nodes is possible to create computer-aided design files (CAD) to graphically represent the pore network.

Table 3. Connectivity matrix

Node	Z	Connected pores				CF
1	0	0	0	0	0	-2
2	1	1	0	0	0	-2
3	0	0	0	0	0	-2
4	1	2	0	0	0	-2
5	4	-1	-2	3	4	0
6	1	-3	0	0	0	-2
7	0	0	0	0	0	-2
8	1	-4	0	0	0	-2
9	0	0	0	0	0	-2

Table 4. Pore dimensions and connections

Pore	Length	Diameter	Node1	Node2
1	3.00E-08	1.00E-08	2	5
2	3.00E-08	1.00E-08	4	5
3	3.00E-08	1.00E-08	5	6
4	3.00E-08	1.00E-08	5	8

As can be seen in Table 3, the pore label in the connectivity matrix has an algebraic sign. This sign provides information about the position of the pore relative to the node. If the pore is connected to the node by the left side or from the downside, then it has a negative sign. If the pore is connected to the node from the top side or the right side, then it will have a positive sign (Figure 41).

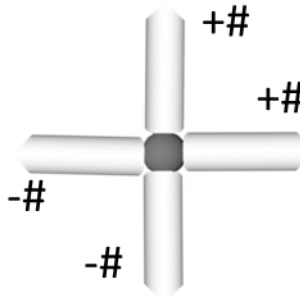


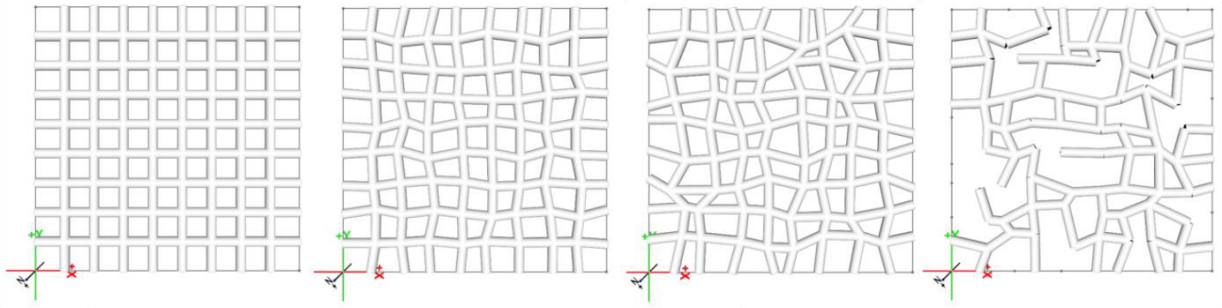
Figure 41. Pore label algebraic sign

The connectivity matrix includes a parameter designed as CF. This parameter has two functions. The first one is to mark the external nodes. The second function is to indicate the entrance and the exit of the network for a simulation that involves diffusion in a semi-infinite plate. If the CF parameters of a node is not equal to zero ( $CF \neq 0$ ), then the node is an external node. If the CF is negative ( $CF < 0$ ), it means that these nodes are the entrance of the network. If the CF is positive ( $CF > 0$ ), it means that these nodes represent the exit of the network.

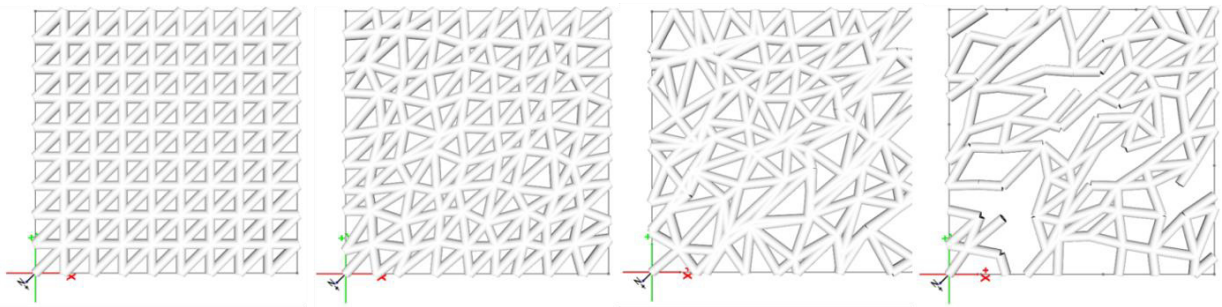
#### 3.4.6. Some examples of generated pore networks

Examples of simple 2D configurations that can be created using the pore network generation program are shown in Figure 42. Figure 43 shows examples of more complex networks. These complex networks are created using different pore size distributions and different pore existence probabilities.

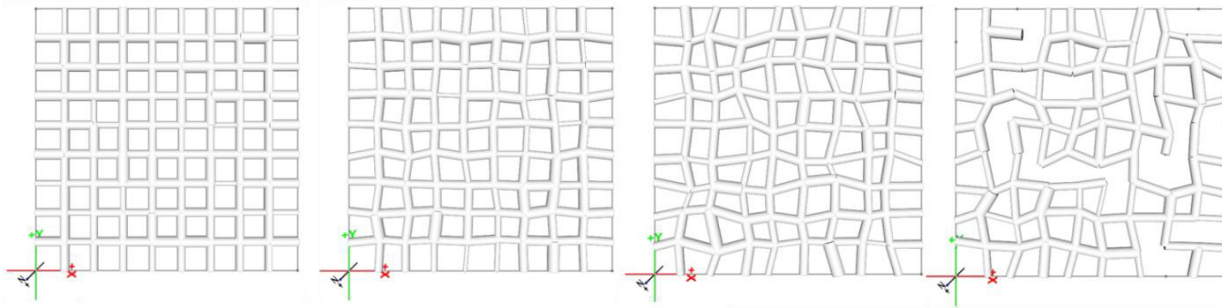
### 2D Square Networks



### 2D Triangular Networks



### 2D Square Networks + Pore Size Distribution



### 2D Square Hierarchical Networks

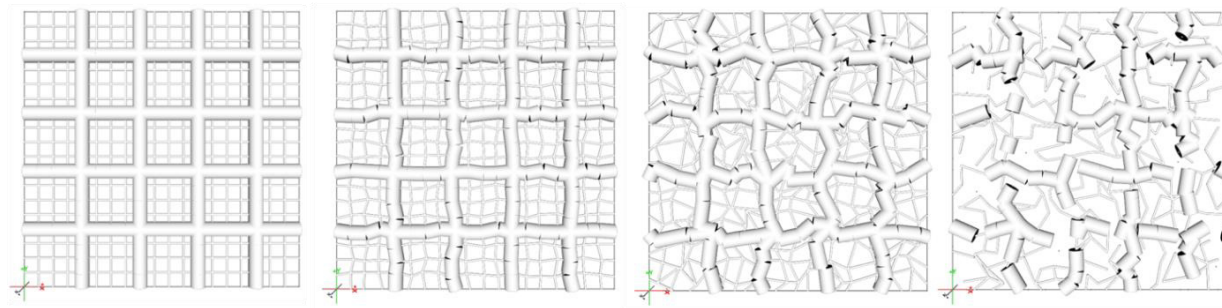


Figure 42. Example of different possible 2D configurations generated by the program. In every row, the degree of distortion is increased from left to right. The Pore Existence Probability (PEP) is lower than 1 in every last case.

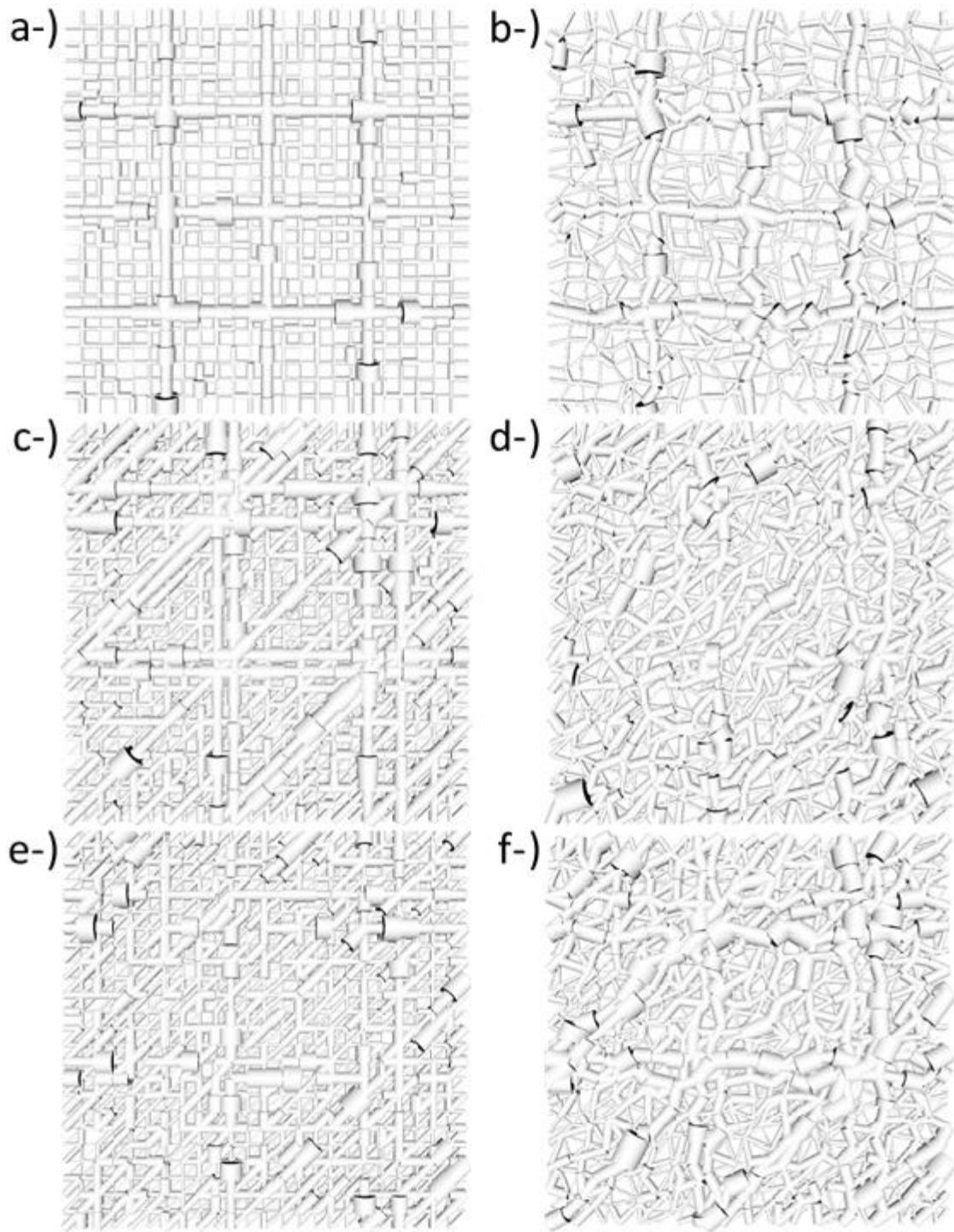


Figure 43. Transversal section of 6 different pore networks: a-) Regular pore network created with 2 different pore size distributions, a grid spacing equal to 6 for the second population, and PEP 1. b-) Distorted pore network created with 2 different pore size distributions, a grid spacing equal to 6 for the second population, and PEP 1. c-) Regular pore network created with 5 different pore size distributions and PEP 1 for all the populations. d-) Distorted Pore network created with 5 different pore size distributions and PEP 1 for all the populations. e-) Regular pore network created with 5 different pore size distributions and PEP 0.5 for the population of pores with higher diameter. f-) Distorted pore network created with 5 different pore size distributions and PEP 0.5 for the population of pores with higher diameter.

### **3.4.7. Conclusions**

As a rule, a model is good if it can represent the required characteristic of a system. The selected pore network model representation and network generation tool have multiple advantages:

- The lattice-based stochastic generation tool is extremely efficient, with low memory requirements and low computational requirements.
- A regular pore geometry is used, thereby simplifying the phase equilibrium and flow models that can be implemented in the network. This decreases the calculation time per unit of simulated volume and allows simulating bigger portions of the solid or more complex phenomena with reasonable execution times.
- The use of several pore populations allows the creation of more complex architectures.
- When different pore populations are implemented at the same time, the volume density distribution becomes heterogeneous when compared with simpler architectures with the same dimension.

As each model has its limitations, here is a list on features that could be improved in the future:

- The initial node spacing is equidistant along each axis.
- A single lattice is used for all pore populations.
- The shape of the pores is regular (cylindrical for pores on edges, spherical for pores on nodes).
- The model does not consider wall roughness in the pores.
- The maximum possible values for the solid textural properties are limited by the Surface to Volume ratio of the pore geometry (e.g., of hollow cylinders).
- The intertwining of various pore populations is regular throughout the pore network.
- The pore existence probability threshold is constant throughout the pore network.

### **3.5. Pore network minimum size and minimum number of generations**

Each time the pore network construction algorithm is executed, a different pore network is generated. Indeed, due to the stochastic nature of the generation process, a generated pore network is a random structure as a whole, and so will be its textural properties. In what follows, the word generation is referred to the action of generating a pore network. In the following sections, the variability of the output results will be investigated.

### 3.5.1. Minimum size of the pore network

For given values of the input parameters, a large number of pore networks can be generated, each having its own textural properties. One can then calculate the mean value, standard deviation and relative deviation of each of these textural properties (Equation 12, Equation 13 and Equation 14).

$$\overline{prop} = \frac{1}{N_p} \sum_{i=1}^{N_p} prop_i$$

Equation 12. Textural property average value.

$$\sigma_{prop} = \sqrt{\frac{1}{N_p - 1} \sum_{i=1}^{N_p} (prop_i - \overline{prop})^2}$$

Equation 13. Textural property standard deviation.

$$\%r\_error_{prop} = 100 * \frac{\sigma_{prop}}{\overline{prop}}$$

Equation 14. Textural property relative error.

Due to the stochastic nature of the pore network generation process, the average values of the textural properties and their standard deviations vary with the dimension of the network and the number of network generations. To find the minimum network size, different input parameter combinations for different pore network dimensions were tested as a function of the number of nodes. 1000 network generations were performed for each configuration. An example is shown in Figure 44, in which the network generations were performed using the following parameters:  $Z_{max}=6$ ,  $PEP=0.5$ ,  $PSD=60 \pm 10$  nm,  $L=300$  nm.

Each point represents, for 1000 network generations, the average value of the textural property, the maximum value obtained, its minimum value, and the relative deviation of the average value. In general, when the dimension of the network increases, the relative deviation decreases, the average value reaches a plateau, and the maximum and minimum values are closer to the average one.

The objective of the sensitivity analysis is to select the minimum network dimension in such a way that a single network generation provides representative results for all textural properties, i.e. even if the generated network corresponds to an extremum value, its properties do not deviate significantly from the average over a large number of network generations. This minimum network dimension is chosen so as to obtain a relative deviation

lower than 5% of the average textural property relative to the plateau for all the textural properties (Figure 44).

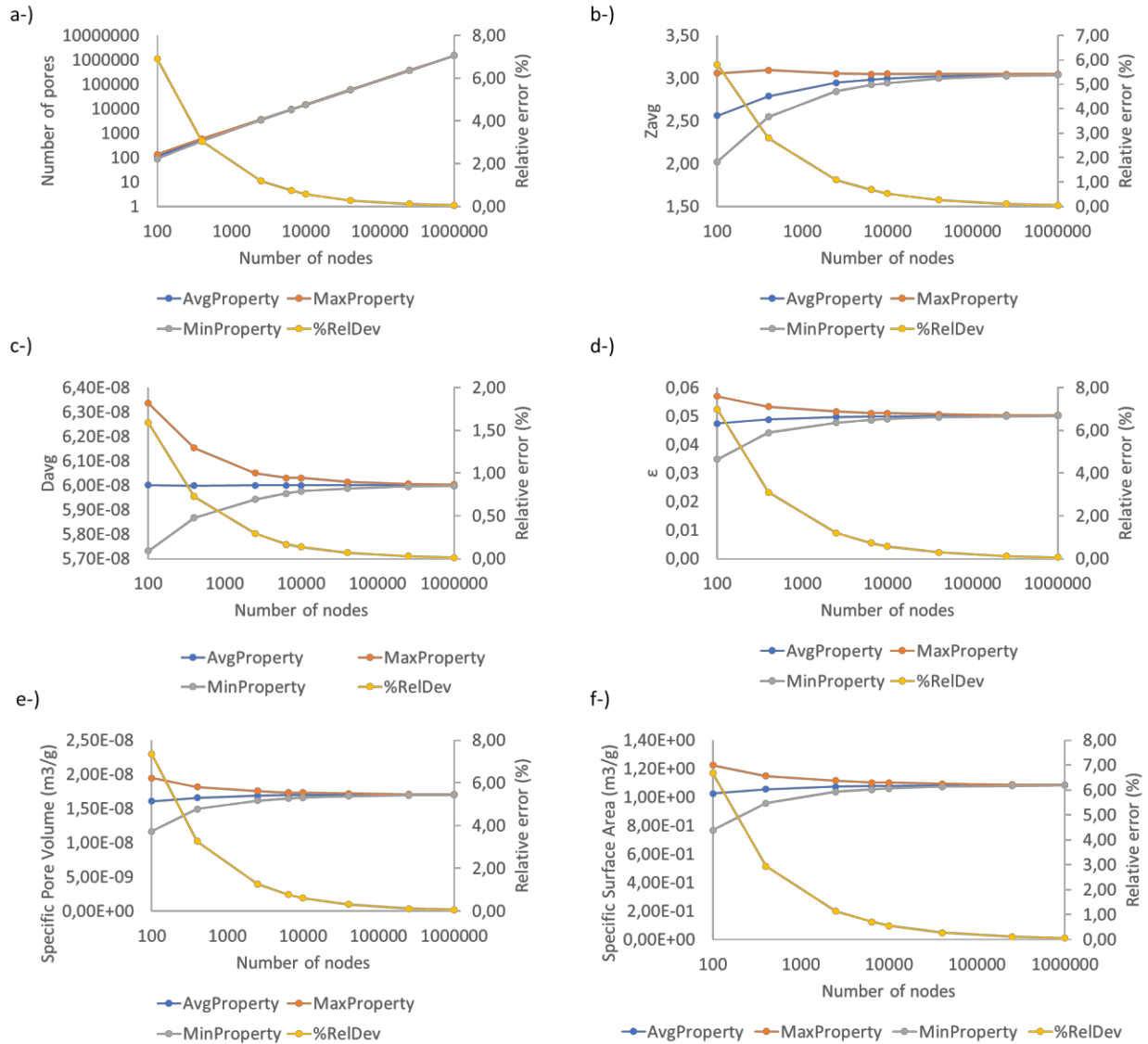


Figure 44. Textural properties for different network sizes (Triangular lattice,  $Z_{max}=6$ , PEP=0.5, PSD=60 ± 10 nm, L=300 nm): a-) Number of pores. b-) Average connectivity. c-) Average diameter. d-) Porosity. e-) Specific pore volume. f-) Specific surface area.

It is relevant to observe that when the maximum connectivity increases, the minimum dimension does not vary (case 1 and 2 in Table 5). In 1.1.1.1.Appendix B it is possible to observe that for the same dimension, as the connectivity increases, the relative deviation of all textural properties decreases. This is simply related to the higher number of pores present in the model due to the higher maximum connectivity, which improves the

representativity of each sample. Due to the same reason, when the pore existence probability is reduced, it will be necessary to increase the minimum dimension of the network to reach a standard deviation under 5% for all the textural properties (cases 1,3, and 5 in Table 5). A lower Pore Existence Probability means that a lower number of pores are present in the network. A broader pore size distribution also requires a higher minimum dimension as indicated by cases 4, 5, and 6 in Table 5.

Table 5. Minimum pore network dimension as a function of the pore network model input parameters

Case	$Z_{max}$	$D_{avg}$ (nm)	Dev (nm)	PEP	Dimension
1	4	60	$\pm 10$	0.5	50x50
2	6	60	$\pm 10$	0.5	50x50
3	6	60	$\pm 10$	0.1	200x200
4	6	60	$\pm 5$	1	10x10
5	6	60	$\pm 10$	1	20x20
6	6	60	$\pm 15$	1	20x20

### 3.5.2. Minimum number of network generations

Different input parameter combinations were tested in order to find the minimum number of generations to be performed. For each configuration, 1000 network generations were done. Figure 45 shows an example for a pore network created using the following parameters: Triangular lattice, 50x50 nodes,  $Z_{max}=6$ , PEP=0.5, PSD=60  $\pm$  10 nm, L=300 nm.

For all parameters represented in Figure 45, the relative deviation stays under 5%. A minimum number of 30 generations was considered sufficient for a broad range of different parameters combinations (See 1.1.1.1.Appendix B )

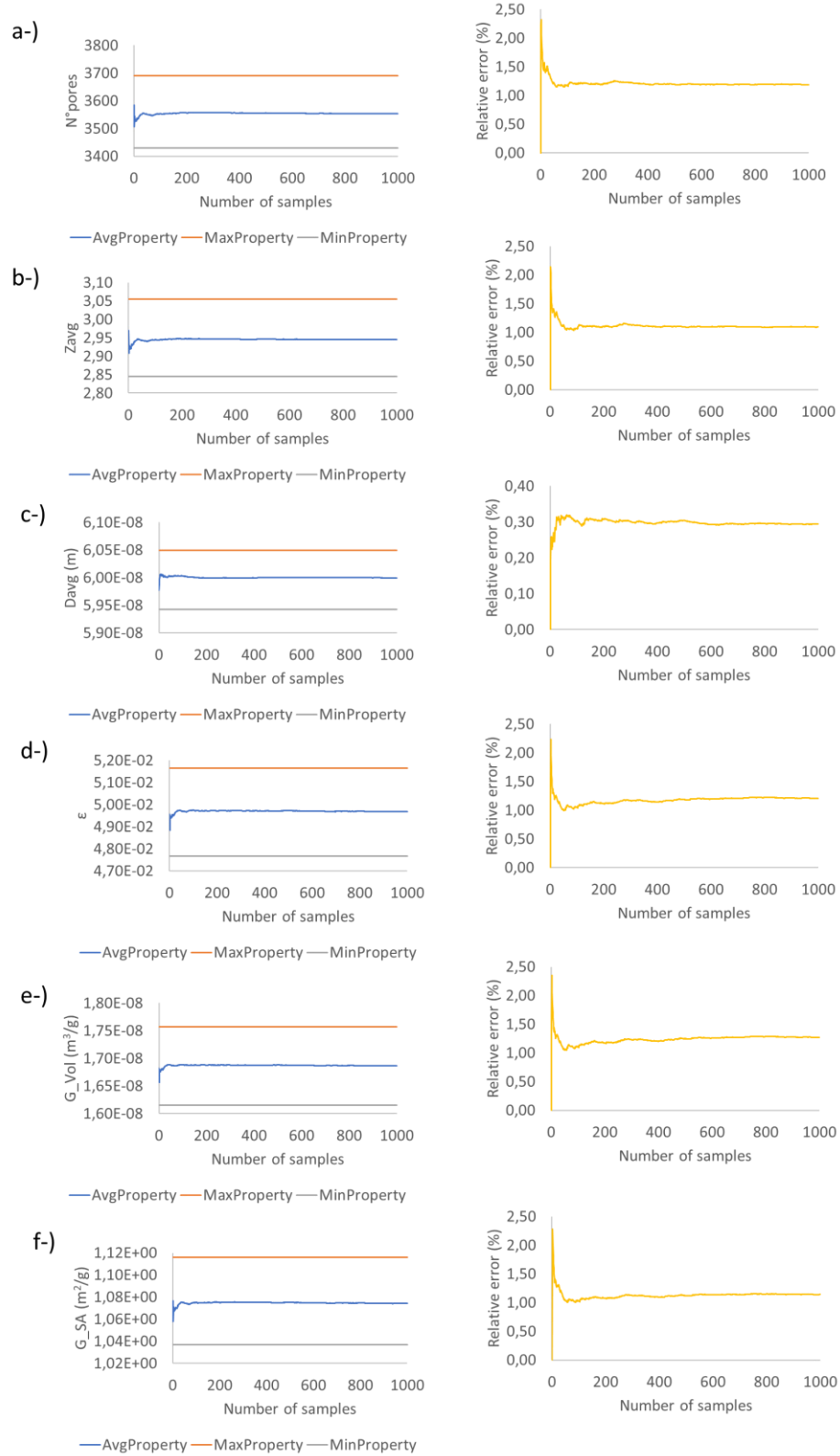


Figure 45. Average textural properties as a function of the number of generations (Triangular lattice,  $Z_{max}=6$ , PEP=0.5, PSD= $60 \pm 10$  nm, L=300 nm): a-) Number of pores. b-) Average connectivity. c-) Average diameter. d-) Porosity. e-) Specific pore volume. f-) Specific surface area.

### 3.6. Sensitivity study on the average textural properties

The influence of the pore network generation input parameters on the porosity, the specific surface area, and the specific volume was tested, the obtained results are the average from 30 different generation processes. For the 2D and 3D networks, standard size of 100x100 nodes and 50x50x50 nodes were imposed. For a fixed network size and a variation in an input parameter that increases the number of pores will naturally increase the porosity, the specific surface area, and the pore volume. For example, such is the case when the maximum connectivity increases (Figure 46a, Figure 47a, Figure 48a) or the pore existence probability increases (Figure 46b, Figure 47b, Figure 48b). An increment in the average pore size will increase the porosity, the specific pore volume, and the specific surface area of the network (Figure 46c, Figure 47c, Figure 48c). For a monomodal network, a broader pore size distribution will increase the porosity and the pore volume of the network (Figure 46d, Figure 47d) but it will not have an important effect on the specific surface area (Figure 48d). All three textural properties are very sensitive to pore length. Shorter pores will allow obtaining higher porosities, increasing the specific properties.

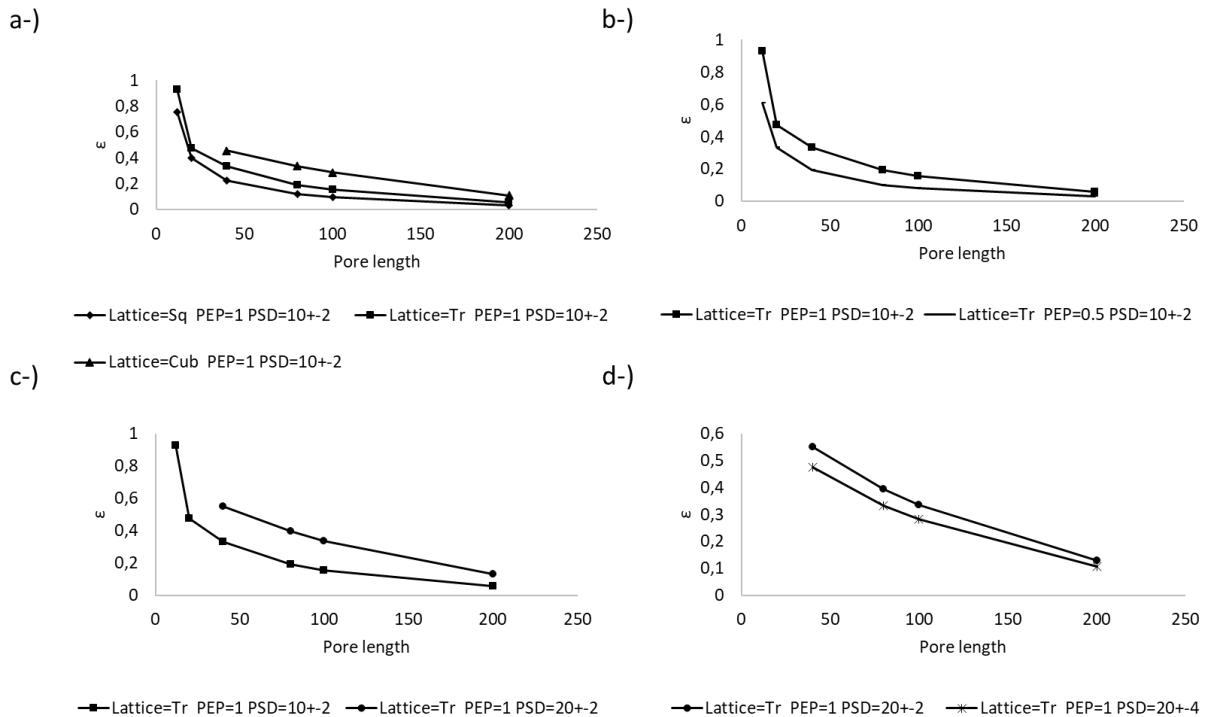


Figure 46. Porosity for different pore network input configurations. a-) Lattice b-) Pore existence probability c-) Average size of the Pore Size Distribution d-) PSD deviation.

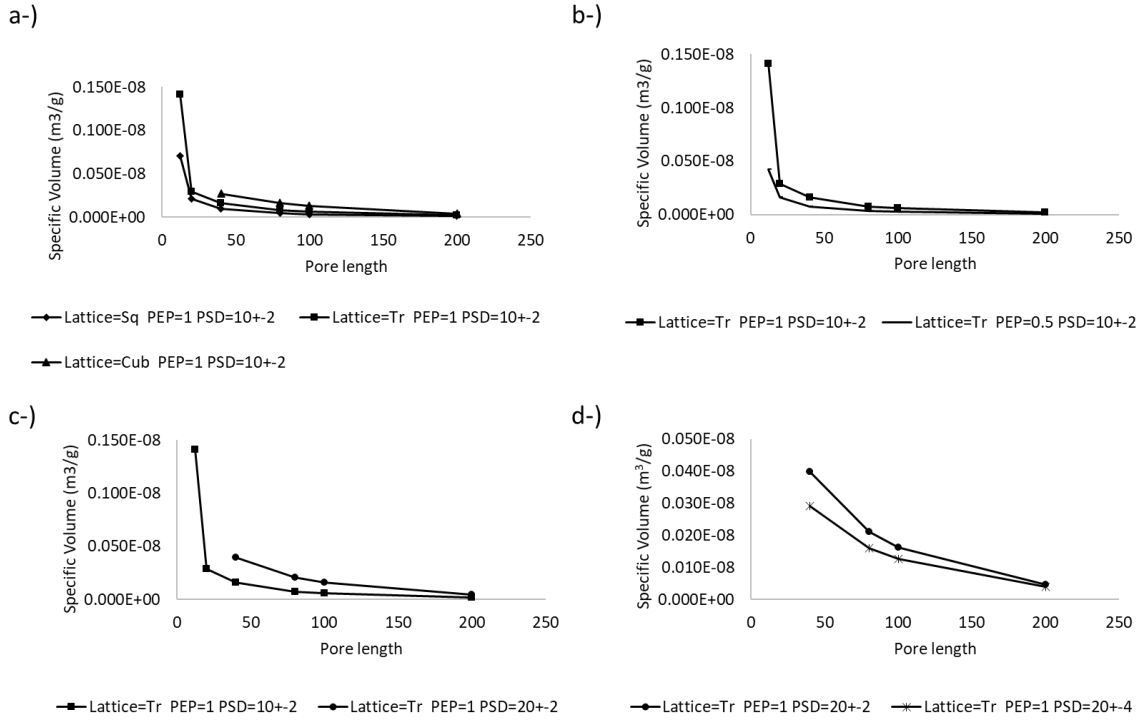


Figure 47. Specific pore volume for different pore network input configurations. a-) Lattice b-) Pore existence probability. c-) Average size of the Pore Size Distribution. d-) PSD deviation.

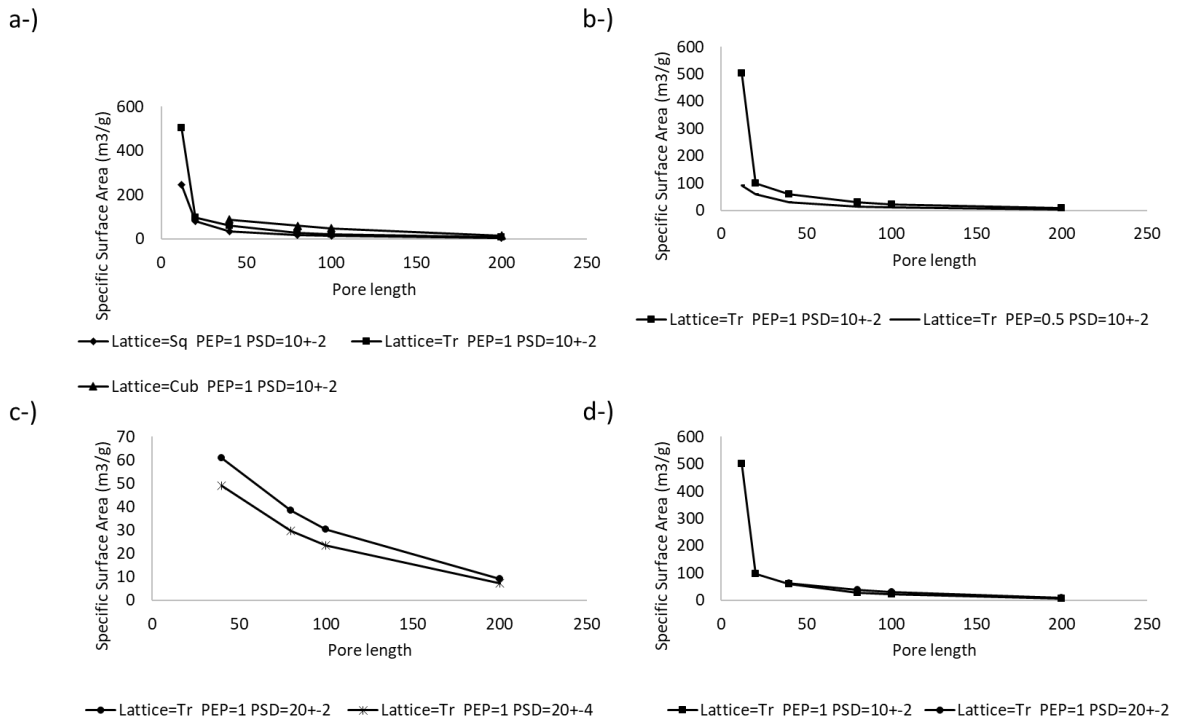


Figure 48. Specific surface area for different pore network input configurations. a-) Lattice b-) Pore existence probability. c-) Average size of the Pore Size Distribution d-) PSD deviation.

### 3.7. Percolation algorithm

In this Ph.D. thesis, three static characterization techniques will be simulated. In nitrogen sorption and cryoporometry, the phase change is associated to the diameter of the pore, but also to the environment of the pore within the network. In the case of the mercury porosimetry, the mercury intrusion in a pore depends on the pore diameter, but also its environment within the network. This phenomenon, i.e. the impact of the local environment on the phase change or the intrusion behavior in a pore, is often called pore blocking effect, pore shielding effect or pore hindering.

#### 3.7.1. Pore Blocking Phenomenon

The pore blocking phenomenon will first be described for mercury intrusion. In mercury porosimetry, thermodynamic equations relate a state of the pore with a given diameter to the pressure. Given an intrusion pressure, the Laplace-Young equation serves to calculate an equilibrium pore diameter above which the mercury can intrude into a pore. However, the intrusion process has to start from the external surface of the structure. When mercury penetrates in a porous structure, it will do this first, i.e. at the lower pressures, through the pores with a large diameter. However, if a large pore is not directly connected to the external surface but surrounded by smaller pores, mercury cannot enter the large pore unless the smaller pores are already filled by mercury, i.e. at higher pressures. This phenomenon is known as pore shielding, pore hindering, or pore blocking, because the smaller pores hinder the access of mercury to these large pores.

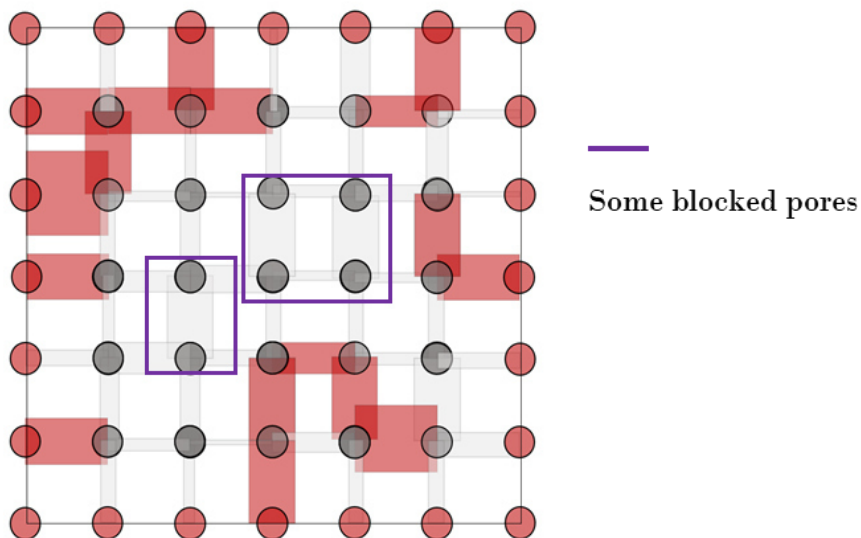


Figure 49. Pore blocking phenomenon in a 2D pore network during mercury intrusion. Mercury is colored in red.

Such a situation is illustrated in Figure 49. At the pressure represented in this image, the pores in the violet rectangles are large pores that, according to the Laplace-Young equation, should already be filled with mercury, just as their counterparts connected to the external surface. However, due to the fact that all their neighboring pores are smaller, these smaller pores block the access of mercury to the larger pores.

A similar phenomenon happens during desorption of nitrogen. Again, the thermodynamic equations relate a state of the pore with a given diameter to the pressure. For a given relative pressure, the Kelvin-Cohan equation serves to calculate an equilibrium pore diameter above which the nitrogen can desorb from a pore. Starting from a pore network completely filled with adsorbed nitrogen, the desorption process has to start from the external surface of the structure. When the relative pressure decreases, the pores with a large diameter will start to empty first. However, if a large pore is not directly connected to the external surface but surrounded by smaller pores, liquid nitrogen cannot desorb unless the smaller pores are already empty, thereby providing a pathway to the external surface. In such a case, nitrogen vaporization will be delayed, maintaining the liquid nitrogen in a metastable state. Again, this phenomenon is called pore shielding, pore hindering, or pore blocking, because the smaller pores block the desorption of the liquid nitrogen from these large pores.

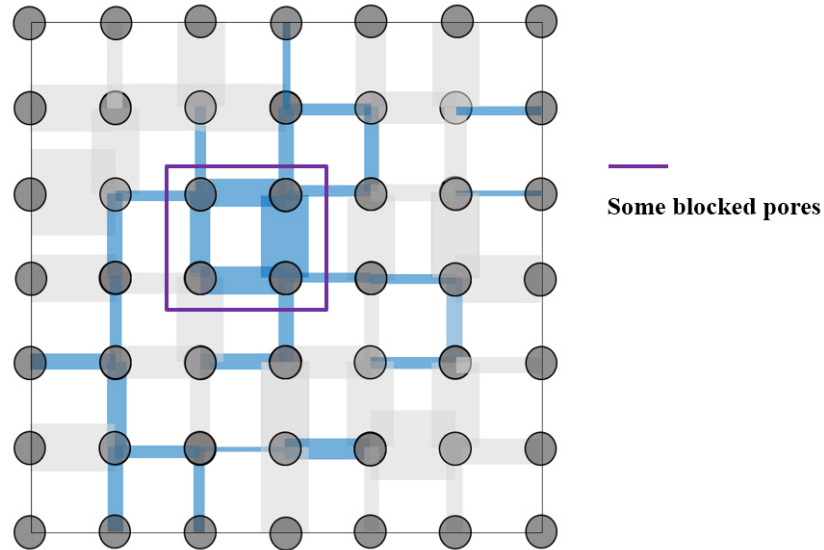


Figure 50. Pore blocking phenomenon in a 2D pore network during nitrogen desorption. Adsorbed liquid nitrogen is colored in blue.

Such a situation is illustrated in Figure 50. At the relative pressure represented in this image, the pores in the violet rectangles are large pores that, according to the Kelvin-Cohan equation, should already be empty, just as their counterparts connected to the external

surface. However, due to the fact that all their neighboring pores are smaller and still filled with liquid, these smaller pores block the desorption of nitrogen from the larger pores.

A similar phenomenon also happens during cryoporometry. The Gibbs-Thomson equation gives the solid-liquid equilibrium temperature as a function of the solid-liquid interface mean radius of curvature. During the freezing step, heterogeneous freezing of the liquid within the pore proceeds through the propagation of the ice front in the axial direction of the pore. Hence, as the freezing process has to start from the external surface, the liquid in a large pore can only freeze when connected to the external surface. However, if a large pore is not directly connected to the external surface but surrounded by smaller pores, freezing of the liquid in the large pore cannot occur unless the smaller pores are already frozen, i.e. at lower temperatures. In such a case, freezing will be delayed, maintaining the liquid in a metastable state. Once again, this phenomenon is called pore shielding, pore hindering, or pore blocking.

As discussed above, all three techniques therefore require accounting for the position of the pore in the network by determining at which conditions each pore has access to the external surface. To model such pore blocking phenomena, a percolation algorithm is required. The scope of such a percolation algorithm is to model the effect of the position and environment of the pore within the network. As explained above, such an algorithm needs to analyze a pore network and define the percolation order of a fluid inside the pore network. Finally, the general percolation algorithm will need to be adapted in order to be applicable to the three characterization techniques.

### **3.7.2. Existing Invasion Percolation Algorithms**

Wilkinson's algorithm was conceived to follow the path taken by an invading phase through a porous structure. Conceptually, there are two phases, one that is already within the pore structure (the defending phase) and another one that is slowly displacing the first one (the invading phase). Invasion Percolation therefore models slow quasi-static fluid invasion in porous media. Related algorithms have been used for multiple applications associated with percolation through soil, reservoirs, catalysts, supports, and membranes. Wilkinson's algorithm used the Kopelman algorithm to sort the pore of the network (Hoshen and Kopelman 1976). In 1999, Sheppard improved the speed of the search algorithm but did not explicitly publish the computational algorithm used (Sheppard et al. 1999). To the best of our knowledge, the most recent mathematical improvements made to the invasion percolation algorithm were published by Masson and Pride (Masson and Pride 2014). In their publication, they proposed to sort a priority list that contains the characteristic size of the pores using a binary tree, which in this case is a max binary heap with a top-down approach. They proved that this algorithm is even faster than the one proposed by

Sheppard. However, in their paper, they only discussed the mathematics but did not show explicitly how they integrated the max heap into Wilkinson's algorithm. In the next section, we show how the invasion percolation algorithm originally devised by Wilkinson (Wilkinson D., Willemsen J. 1983) can be adapted to our case. The algorithm we propose is called the triggering diameter algorithm.

### 3.7.3. The triggering diameter algorithm

The algorithm aims at finding the percolation order of a fluid inside the pore network. In the case of nitrogen sorption, the percolation order is important during the desorption process. Indeed, desorption does not necessarily occur at the relative pressure given by the Kelvin-Cohan equation but will occur at a lower pressure if smaller pores block the direct connection of this pore to the external surface. The invasion percolation algorithm needs to determine the desorption pressure for each pore considering its position within the network, i.e. the pressure at which this pressure can desorb. However, instead of storing the desorption pressure of each pore, an equivalent diameter corresponding to the desorption pressure will be stored. The diameter that corresponds to the desorption pressure will be called the desorption triggering diameter. Analogously, in mercury intrusion, the intrusion triggering diameter found by the algorithm corresponds to the real intrusion pressure of the mercury within the pore considering its location within the network. For cryoporometry, the freezing triggering diameter calculated using the algorithm is the diameter that corresponds to the freezing temperature according to the location the pore occupies in the network.

Figure 51 graphically describes the process of finding the percolation order. It lists all the algorithmic rules that will be explained in detail later. The algorithm first finds all the pores connected to the surface of the network (Figure 51a). Since these pores are in contact with the exterior, it assigns to these pores a triggering diameter equal to its real diameter (dark blue). This image is depicted in Figure 51b. The algorithm then creates a list in which the pores are ordered from the biggest diameter to the smallest diameter. Then, exploration of the network starts from the first pore on this priority list (Guide Pore). The pores connected to the guide pore are going to be added to the list in a position that corresponds to their triggering diameter. If the diameter of the connected pore is lower than the diameter of the guide pore, its triggering diameter will be equal to its own diameter. On the contrary, if its diameter is larger than the diameter of the guide pore, the triggering diameter assigned to the connected pore will be equal to the triggering diameter of the guide pore. The newly added pores are colored dark blue in Figure 51c. Since the effect of the guide pore has now been propagated to the underlying pores, the guide pore is removed from the priority list.

It is now colored orange in Figure 51c, and the next largest pore becomes the new guide pore. The exploration continues until the priority list is empty, as shown in Figure 51d.

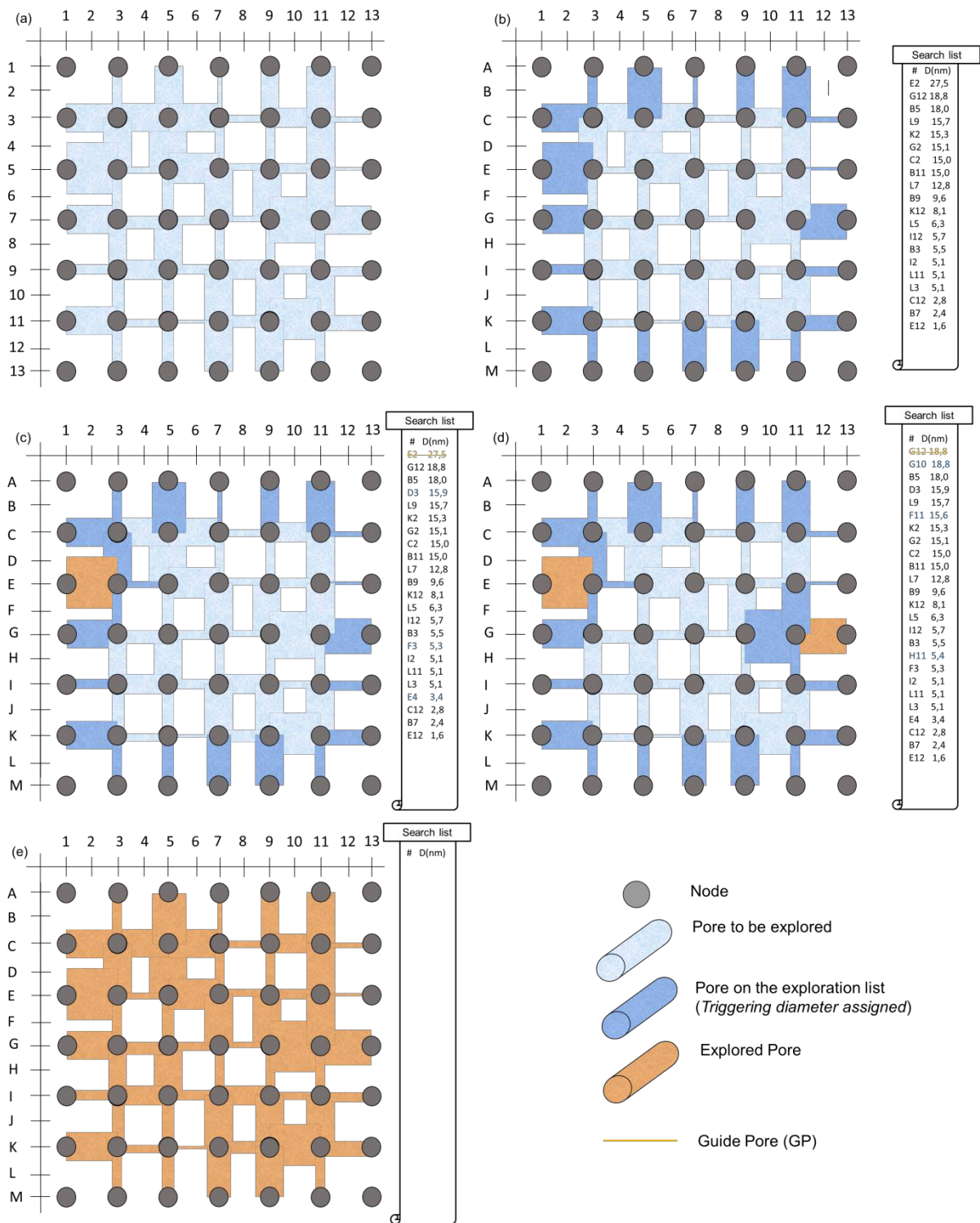


Figure 51. Triggering Diameter Algorithm Example. a) Non explored network. b) External pores identified. c) Exploration of the network. d) Exploration of the network. e) Completely explored network.

The Invasion Percolation (IP) algorithm that is proposed in this work was adapted from the work of Wilkinson and Willemsen (Wilkinson D., Willemsen J. 1983) and the improvement proposed by Masson and Pride (Masson and Pride 2014).

This triggering diameter algorithm uses five different lists: *external\_pores*, *visited\_nodes*, *visited\_pores*, *searchlist*, and *connectmatrix*. The first four are indexed lists. The last one is a matrix that contains the information on the pore network (section 3.4.5).

There are six main rules on which the algorithm is based:

- The triggering diameter is assigned only once to each pore. There is no overwriting of the triggering diameter.
- A pore can be added to the *searchlist* only once.
- A node can be visited only once.
- The pore picked up from the *searchlist* must always be the pore with the biggest diameter on the list (priority rule).
- The triggering diameter of the external pores corresponds to the actual pore diameter.
- Upon initialization, the *searchlist* must contain all external pores (boundary conditions).

First, the external nodes and the external pores of the network are identified and listed in *visited\_nodes* and *external\_pores* respectively (Figure 51a). The external pores are the initial input for *searchlist*. For each pore, its label and diameter are saved into this list. After sorting *searchlist*, the pore on the list with the biggest diameter is picked up and it will be called **guide pore** for didactic purposes. Two nodes are connected to the guide pore, but one of them has already been visited and saved in *visited\_nodes*. With this information, the node that has not yet been visited can be identified. The connectivity of this new node is explored to identify the pores connected to the guide pore using *connectmatrix*. The newly identified pores will be added to *searchlist*, but first, its triggering diameter will be assigned by comparison with the guide pore. We will call the two following rules assignment rules.

- i) If the diameter of the pore is smaller than the triggering diameter of the guide pore, the pore conserves its original diameter as triggering diameter.
- ii) If the diameter of the pore is bigger than the triggering diameter of the guide pore, the pore adopts the guide pore's triggering diameter as its triggering diameter.

Then, the pores are added to *searchlist* and *visited\_pores*. At the same time, the node is saved in the *visited\_nodes* list. The guide pore is removed from *searchlist*, and a new guide pore is selected. This process is repeated until *searchlist* has been emptied, which means

that a triggering diameter was assigned to all the non-isolated pores (pores that can be accessed from the surface).

Let's consider an example in order to explain the principle of the algorithm. Figure 51a represents a network in which no pore has yet been assigned a triggering diameter. In Figure 51b, the external pores have been identified, their triggering diameters are assigned, since for external pores the triggering diameter is equal to the actual diameter, and the pores are stored in *searchlist*. Figure 51c depicts the selection of a guide pore (the biggest diameter in *searchlist*) and the assignation of a triggering diameter to the pores connected to it. The guide pore is eliminated from *searchlist* and one of the pores to which it is connected is taken as guide pore (Figure 51d). In Figure 51e, all pores have been explored.

A general algorithm flow chart for the assignation of the triggering diameter is shown in Figure 52. For ordering hierarchically the search list, binary heaps are used. Sorting, adding, and eliminating elements from the list is handled using the binary heaps (Section 3.7.4).

It is important to note that:

- Any risk of infinite loops is mitigated by not considering pores with an already assigned triggering diameter (*visited\_pores*).
- Due to the randomness of the pore network generation process, and as in the real material, some isolated clusters of pores are not connected to the surface. Due to the logic used to explore the network, the algorithm never walks through those pores, saving time.
- The full analysis of the pore network is completed with only one sweep.

The three key points of the general algorithm are:

- The algorithm initializes *searchlist* with the external pores.
- The pore selected as the guide pore is the one with the biggest diameter in *searchlist* (priority).
- The assignation rules.

The first point means that the algorithm explores the network starting from its exit points, the surface nodes. Combined with the second point, this means that the best possible option is always studied. For example, if the biggest pore of the network is in the middle of the network if that pore is not yet in the search list, it means that for sure it is surrounded by smaller pores and blocked by them.

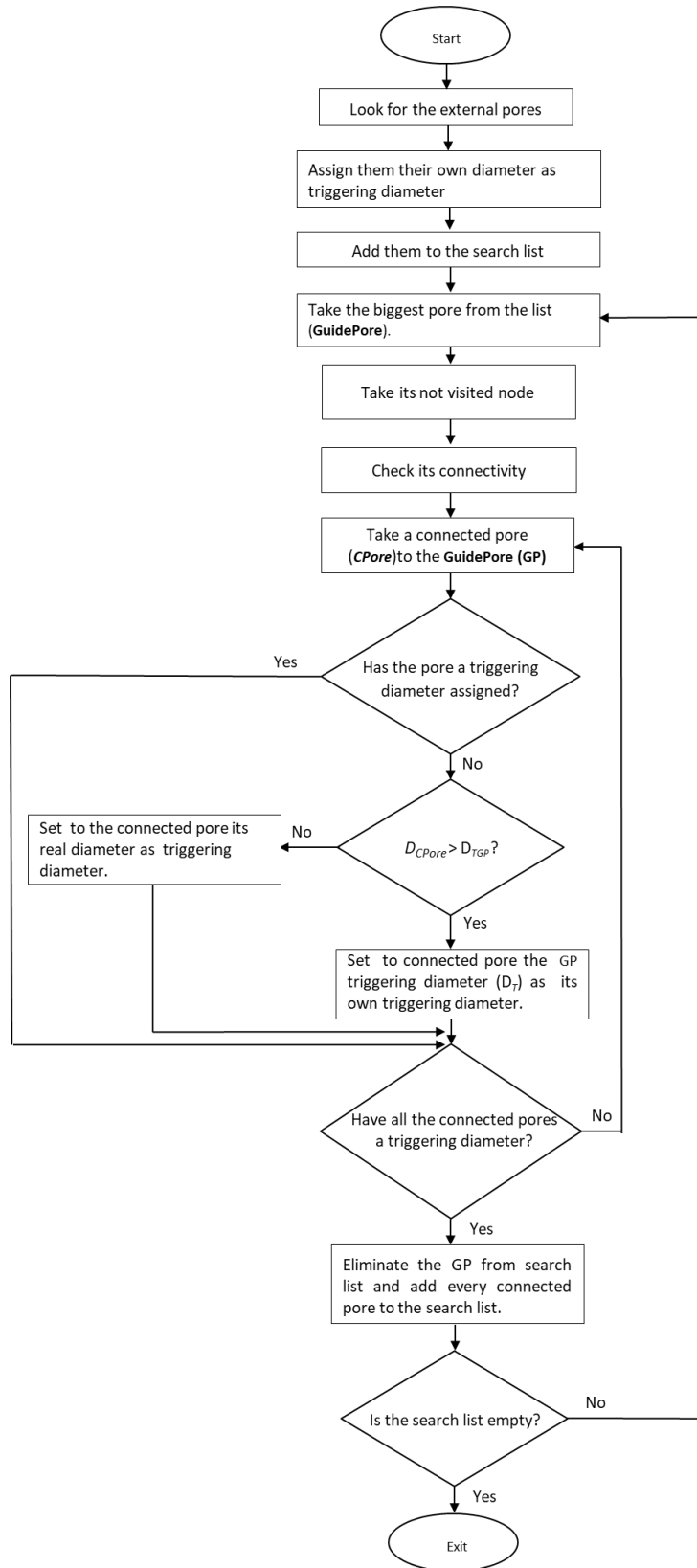


Figure 52. Triggering diameter algorithm flow diagram.

In the triggering diameter algorithm described above, the list of pores is always ordered from the biggest diameter to the smallest diameter. This is due to the fact, during nitrogen desorption, the largest pores will empty first. The same pore diameter order is needed for mercury intrusion and for the advancing ice front during the freezing step of cryoporometry. However, for mercury extrusion, the algorithm needs to be slightly modified because the list of pores now needs to be ordered from the smallest diameter to the largest diameter.

#### 3.7.4. Binary Heap Algorithms

The triggering diameter algorithm can only work correctly if the search list contains the priority queue, i.e. if it is always sorted from the biggest to the smallest diameters. But sorting a list of numbers is a computationally intensive task. Also, the exploration list *searchlist* is constantly refreshed. It is a list for which there are very specific needs:

- 1- The guide pore, which represents an element with the highest diameter (or lowest diameter, in the case of mercury intrusion), needs to be **identified** in every iteration.
- 2- There are **addition operations**, every time a pore is added to the list.
- 3- There are **extraction operations**, every time a guide pore is removed from the list.

This basically means that the elements in the list should be ordered at least N times for a pore network of N elements (if there are no isolated pores). The algorithm time used to handle such a sorted list could easily represent more than 60% of the execution time of the complete algorithm.

The selection of the right computational algorithms to model the physical phenomena and to store and handle the network's information is very important to limit the execution time. In computer science, a priority queue can be efficiently implemented in a heap. This is a tree-based data structure that satisfies the so-called heap property: in a Max-Heap, the value of any given node is smaller than or equal to the value of its parent node. Hence, the node at the top of the heap contains the highest value, has no parent, and is called the root node. In a Min-Heap, the value of any given node is larger than or equal to the value of its parent node. Hence, the top of the heap now contains the lowest value of all data. A binary heap is heap structure in which a parent node can have at most two children. A heap is a maximally efficient useful data structure when it is necessary to repeatedly remove the object with the highest (or lowest) priority, or when insertions need to be interspersed with removals of the root node.

Figure 53 represents the kind of two-dimensional array [R] used for the dynamic *searchlist*. It has two columns. In the first one are written the labels of the pores, and in the second

one, the pore diameter. For the heap, the value, which is always compared for the operation within the heap, is the diameter, representing the key value to sort the priority queue.

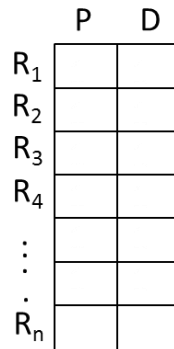


Figure 53. Two-dimensional array for the dynamic list

As mentioned before, Masson proposed a top-down binary heap approach in order to decrease considerably the time used for ordering the elements of the list and finding a value of interest (Masson and Pride 2014). In our case, we propose to use a max-heap in the top-down approach (and the min-heap in the bottom-up approach, in the case of mercury intrusion). The following paragraphs explain the logic of these approaches and how each characterization technique can be implemented in a more convenient manner.

The first to be described is the Max-Heap algorithm. It consists of an array of elements for which the root node contains the element with the maximum value. This algorithm has an execution time of  $O[N \log(N)]$  and can be segmented in several operations (Cormen et al.). This data structure can be represented graphically as a tree with nodes having maximum of two children each (Figure 54). This binary tree structure allows rearranging the element elements easily without sorting the full array. The operations that are required for this are the *addition* and *elimination* operations.

The *addition* operation (Figure 55) allows adding new elements to the list. The new element is placed at the first empty position ( $i_n$ ) of two-dimensional array  $[R]$  and its value compared with the diameter corresponding to  $i_n/2$  position, which following the common jargon for data structures will be called the parent of the  $i_n$  position. If the diameter of the parent is lower than the diameter of the added element, both elements swap their positions. The operation finishes when the element has arrived at the top position or the value of the diameter of its parent is higher.

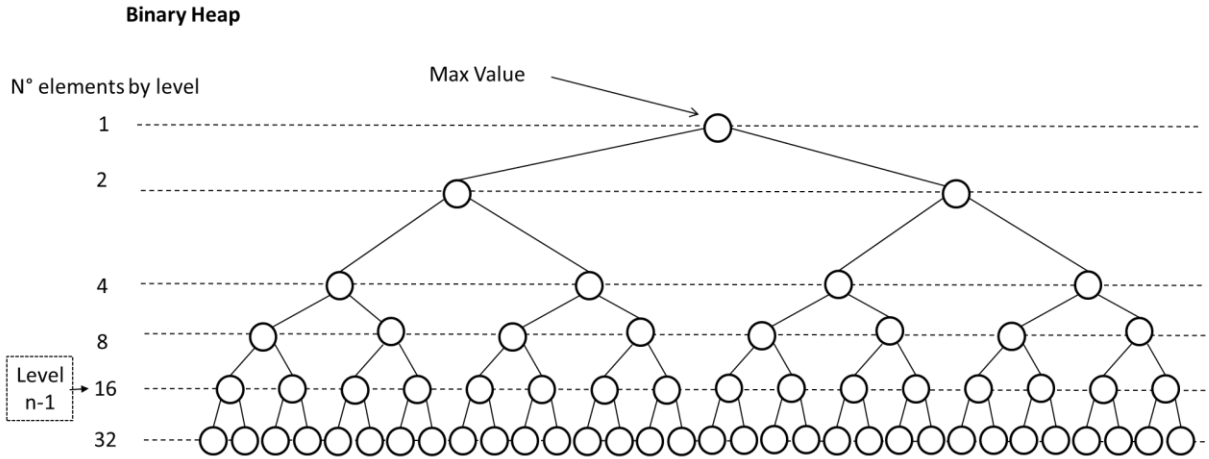


Figure 54. Algorithm Flowchart. Max Heap: Elimination Operation

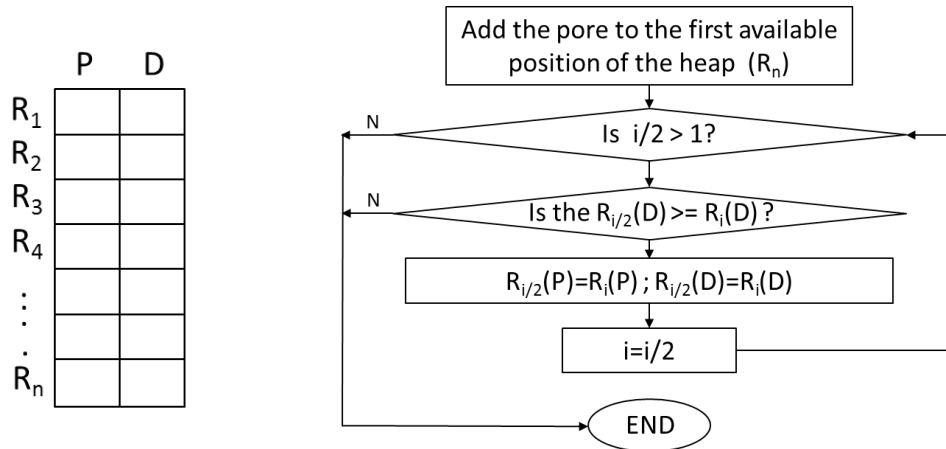


Figure 55. Algorithm Flowchart. Max Heap: Addition Operation

The *elimination* operation consists of the elimination of the top element of the array, the promotion of one of its two children to the top position and in consequence displacing upwards the elements of the array without leaving empty spaces along (Figure 56). In order to keep the tree balanced and not leaving empty spaces, once the floor of one of the two branches of the tree is reached, the resultant empty space is filled with the last value of the array.

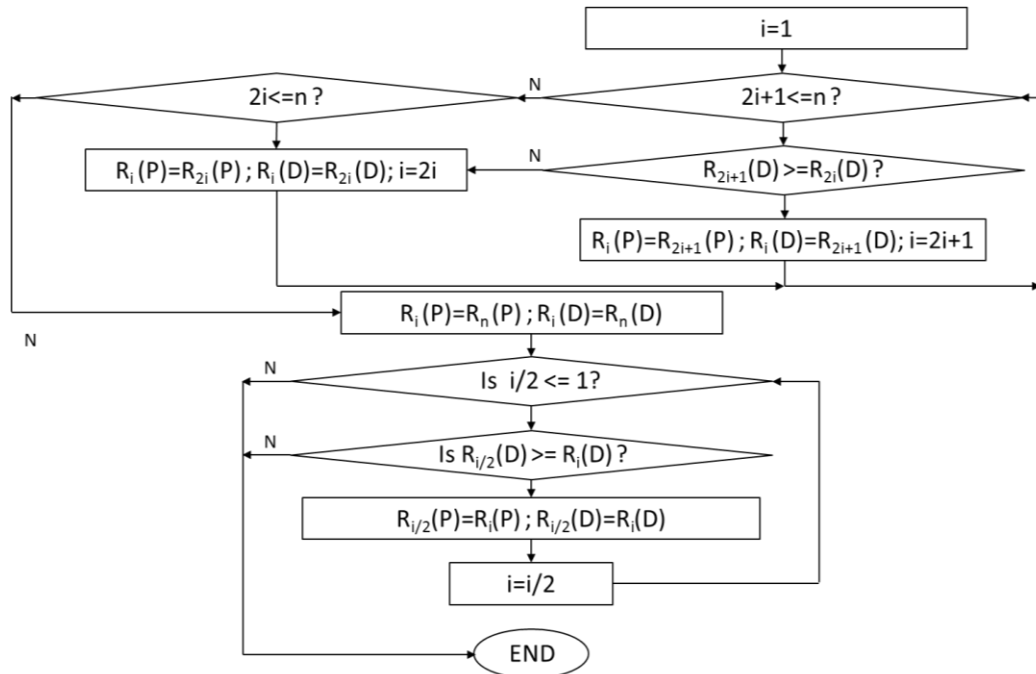


Figure 56. Algorithm Flowchart. Max Heap: Elimination Operation

The Max-Heap algorithm is used for the **desorption isotherm algorithm**, the **intrusion curve algorithm**, and the **advancing ice front for the freezing algorithm**, into which it is necessary to follow a priority sequence starting from the higher value represented by the higher pore diameter which is dynamically changing as the network is explored.

The Min-Heap algorithm consists of the same procedure but placing at the top the value with the lowest possible value. In this way, the array is going from the lowest value (stored in the root node) to higher (bottom) values. This kind of algorithm is used for the **extrusion curve algorithm**. For this case, the bottom-up approach can be used to easily transform a Max-Heap to a Min-Heap. It allows sorting the list by starting at the  $n-1$  level of the tree (Figure 57). Every element is compared with all its family offspring, and the comparison stops when the  $2*i$  position does not exist. Its utility resides in using the same initial array built for the dynamic search list in the desorption isotherm algorithm (or in any of the other two algorithms) to create a Min-Heap to be used for the extrusion curve algorithm.

The contrast between the top-down and bottom-up algorithms lies in the starting state of the values that compose the array. If the values to build the array (search list) are known a priori and there is no need to add new elements to it, the best option is the bottom-up approach. The advantage of this approach resides in performing a heap sort of the array from the bottom starting from level  $n-1$ , thus saving the need of sorting half of the elements in the array. However, making this every time a new element is added ends up being more expensive in terms of number of operations. Its counterpart is used when the array is

initially empty and new elements need to be dynamically added, which means sorting  $n$  times a logarithmic number of elements with respect to the total size in the worst case.

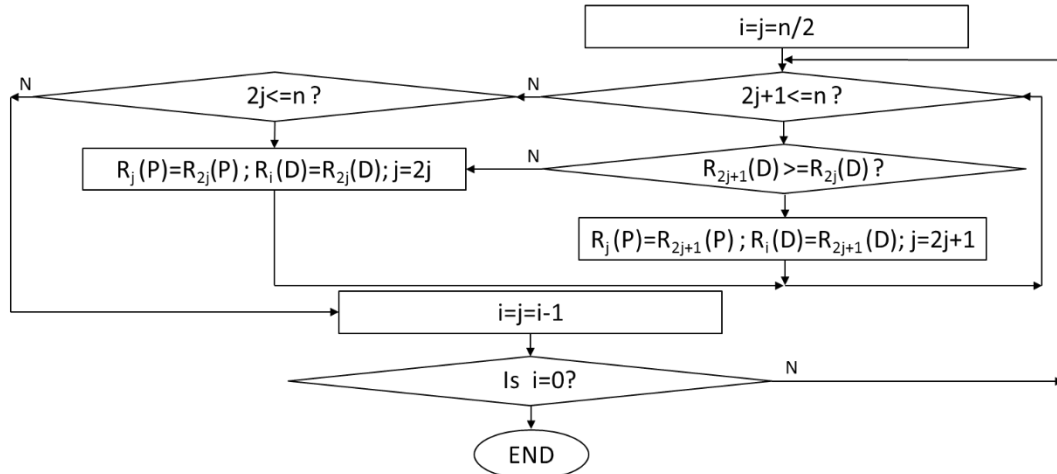


Figure 57. Algorithm Flowchart. Max Heap: Bottom-Up Approach

### 3.8. Topological analysis of the pore network model

There are three relevant characteristics of the pore network:

- The topological map.
- The percolation map.
- The volume distribution.

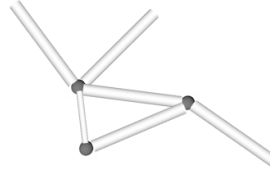
The topology of the network represents how the pores are interconnected. In the case of the present pore network models, the topology is defined by the connectivity distribution of the network. Such a connectivity distribution is impacted by changing the lattice of the network (affecting the maximum connectivity) or the pore existence probability (PEP) (creating a connectivity distribution).

The percolation map represents the percolation order of the network. It is represented by the order in which some fluid would enter the network starting from the pores in contact with the surface and always from the biggest to the lowest diameter. The percolation map is a function of the topological map and the diameter of the pores.

The volume distribution on the network is a function of the diameter of the pore and the pore length. It is related to the capacitance of the network and is a fundamental parameter for volume processes.

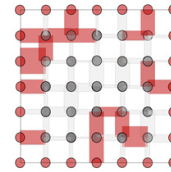
### Topologic map

Lattice  
Pore existence probability



### Percolation map

Topologic Map  
Pore size distribution



### Void Volume distribution

Pore size distribution  
Pore length distribution

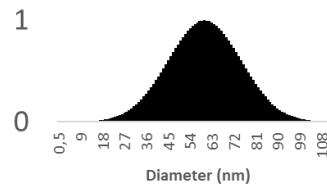


Figure 58. Variables that influences the topology, percolation and volume distribution of the network

Before performing a sensitivity analysis on the topology of the network, percolation spectra and several other variables will be defined first.

A percolation spectrum shows how an observed variable will change when the network is being explored. Such a spectrum is created using the percolation list obtained from the percolation algorithm described in section 3.7. The percolation list contains the order in which a liquid would percolate through the network using as only the criterion the pore diameter and its position in the network (percolation order). The percolation spectrum plots an observed variable as a function of the fraction of explored pores. The fraction of explored pores  $fe$  is defined in Equation 15, where  $n_{exp}$  represents the number of explored pores from the list.

$$fe = \frac{n_{exp}}{\text{Total number of pores in the list}}$$

Equation 15. Explored fraction

A first observed variable is the Cumulated Pore Volume Fraction (CPVF), which is given in Equation 16. This term represents the sum of the pore volume of explored fraction from the list divided by the total pore volume in the list ( $Vp_{tl}$ ).

$$CVPF = \sum_{i=1}^{n_{exp}} \frac{V_{p,i}}{Vp_{tl}}$$

Equation 16. Cumulated Pore Volume Fraction (CVPF)

A second observed variable is the Cumulated Average Diameter (CAD) defined by Equation 17. This corresponds to the average pore diameter of the fraction explored and is calculated as the sum of the pore diameter of explored fraction from the list divided by the number of explored pores.

$$CAD = \sum_{i=1}^{n_{exp}} \frac{D_{p_i}}{n_{exp}}$$

Equation 17. Cumulated Average Diameter (CAD)

The two variables above can also be clustered into classes. Each class will represent the pores contained in each 1% of the exploration list (meaning 1% of  $fe$ ).

The CVPF by Class (CVPF\_C) is defined in Equation 18 as the average diameter of the pores for each 1% of the explored fraction  $fe$ , where  $np\_class$  represents the number of pores in this class.

$$CVPF\_C = \sum_{j=1}^{np\_class} \frac{V_{p_i}}{np\_class}$$

Equation 18. CVPF by class (CVPF\_C)

The Average Diameter by Class (ADC) is defined in Equation 19 as the average diameter of the pores for each 1% of the explored fraction  $fe$ , where  $np\_class$  represents the number of pores in this class.

$$ADC = \sum_{j=1}^{np\_class} \frac{D_{p_j}}{np\_class}$$

Equation 19. Average Diameter by class (ADC)

For an ideal case of a network with pores of equal diameter, all percolation spectra will show a horizontal line, i.e. the spectra are completely uniform. As an example, since 1% of CVPF would correspond exactly to 1% of explored fraction, we will find a horizontal line that intersects the y-axis in  $CVPF/fe = 1$ .

### 3.8.1. Effect of the maximum connectivity

Figure 59 compares the spectra of three different structures with the same pore size distribution: the first structure is a bundle of parallel non-interconnected pores ( $Z_{max}=1$ ), the second structure is a pore network that uses a square lattice with a maximum connectivity of 4 ( $Z_{max}=4$ ); the third structure is a pore network based on a triangular lattice

with a maximum connectivity of 6 ( $Z_{\max}=6$ ). In a bundle of parallel non-interconnected pores, the connectivity is always equal to 1. As all pores are in contact with the external surface in this case, percolation phenomena do not affect the network.

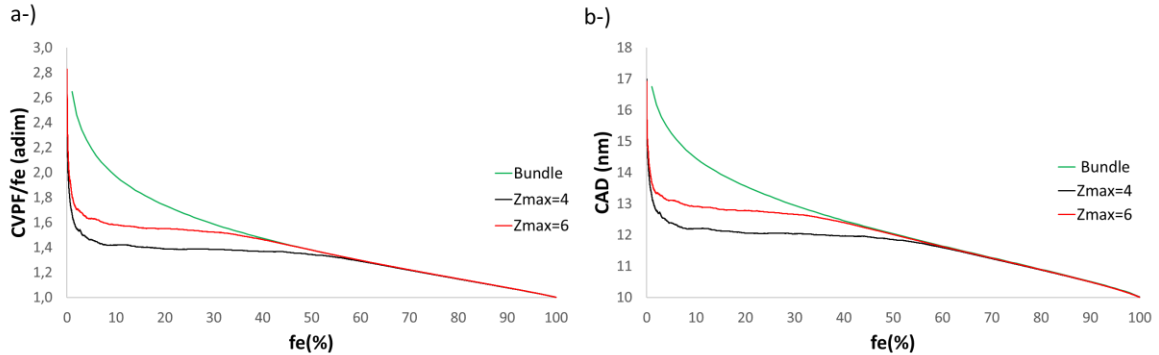


Figure 59. Effect of the **maximum** connectivity on the topological map. a-) Percolation spectra of a square pore network compared with the percolation spectra of a triangular network. b-) Average diameter for the spectra of figure a.

In Figure 59a, the spectra start at their highest point, meaning that the first pores to be explored are big pores close to the external surface. The bundle of tubes spectrum shows an ideal case that is not affected by the percolation order. The spectra for the maximum network of connectivity 6 and 4 consistently draw away from the bundle of tubes curve. This means that smaller pores, belonging to the left branch of the pore size distribution, need to be explored first in order to be able to access the larger pores in this  $fe$  section. This behavior is also observed in Figure 59b. For a  $fe$  lower than 40 %, the average diameter CAD of the explored pores is the highest for the bundle of pores and, for the same pore size distribution, the average diameter decreases when the average connectivity is lower, due to the fact that the pores with a diameter above the average will be relegated to lower positions in the list.

On the spectra in Figure 59, there is a region where the CAD value is almost constant. It corresponds to the range  $fe \approx 2\% - 40\%$  in the case of  $Z_{\max}=6$ . The region in the spectra implies that the average diameter of the explored fraction remains close to constant. This is confirmed by Figure 60, which shows the Average Diameter by Class (ADC) as a function of the explored fraction  $fe$ . At values for  $fe$  below 30% to 40%, the average explored diameter per class (ADC) is almost constant lower in the case of the interconnected pore networks.

For high values of  $fe$ , above 45% for  $Z_{\max}=6$  and above 65% for  $Z_{\max}=4$ , the spectra become identical to the bundle of pores network. This indicates that pore shielding becomes much less important for the smaller pores. For the small pores in the network, the topology is no longer relevant since they always seem to be a pathway to the external surface.

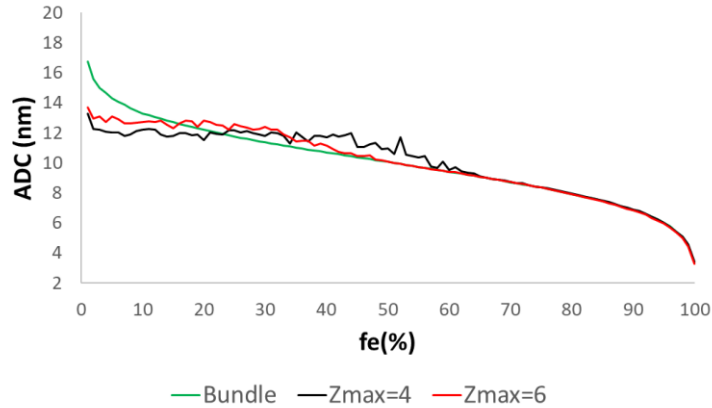


Figure 60. Average Diameter by class (ADC) as a function of fe.

As the length of the pores in this comparison is constant, the CVPF\_C spectrum in Figure 61 follows the same trend as the ADC spectrum in Figure 60.

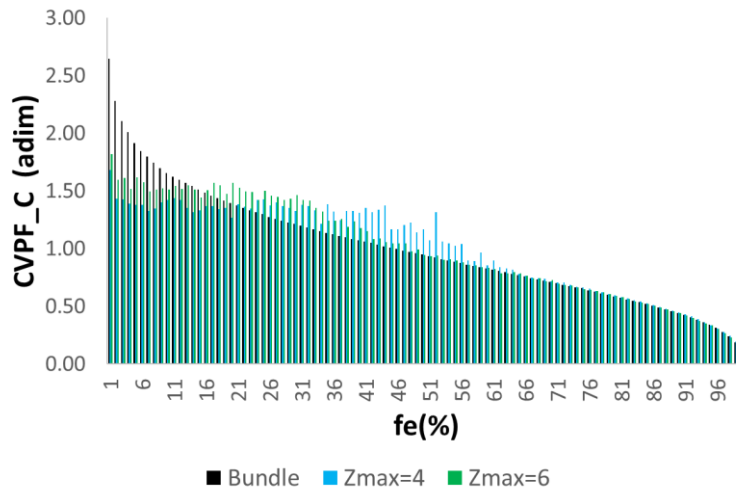


Figure 61. CVPF by class (CVPF\_C) as a function of fe.

In conclusion, the higher the connectivity, the less relevant is the topology of the network when the percolation phenomena need to be evaluated. A high connectivity influences the percolation map by improving the connections of large pores to the external surface. Depending on the maximum connectivity and the pore network organization, a different fraction of the network will not be influenced by the percolation order.

### 3.8.2. Effect of the pore existence probability

The pore existence probability (PEP) influences the topological map because it influences the connectivity. Using a PEP lower than 1 will create a connectivity distribution. Given the random nature of the pore generation algorithm, the connectivity distribution will follow a gaussian trend that can be skewed to the right or the left according to the value of the PEP. The distribution at PEP 0.5 is Gaussian. For PEP lower than 0.5, the distribution is skewed to

the left and, as the PEP increases above 0.5, the shape is progressively skewed to the right (Figure 62).

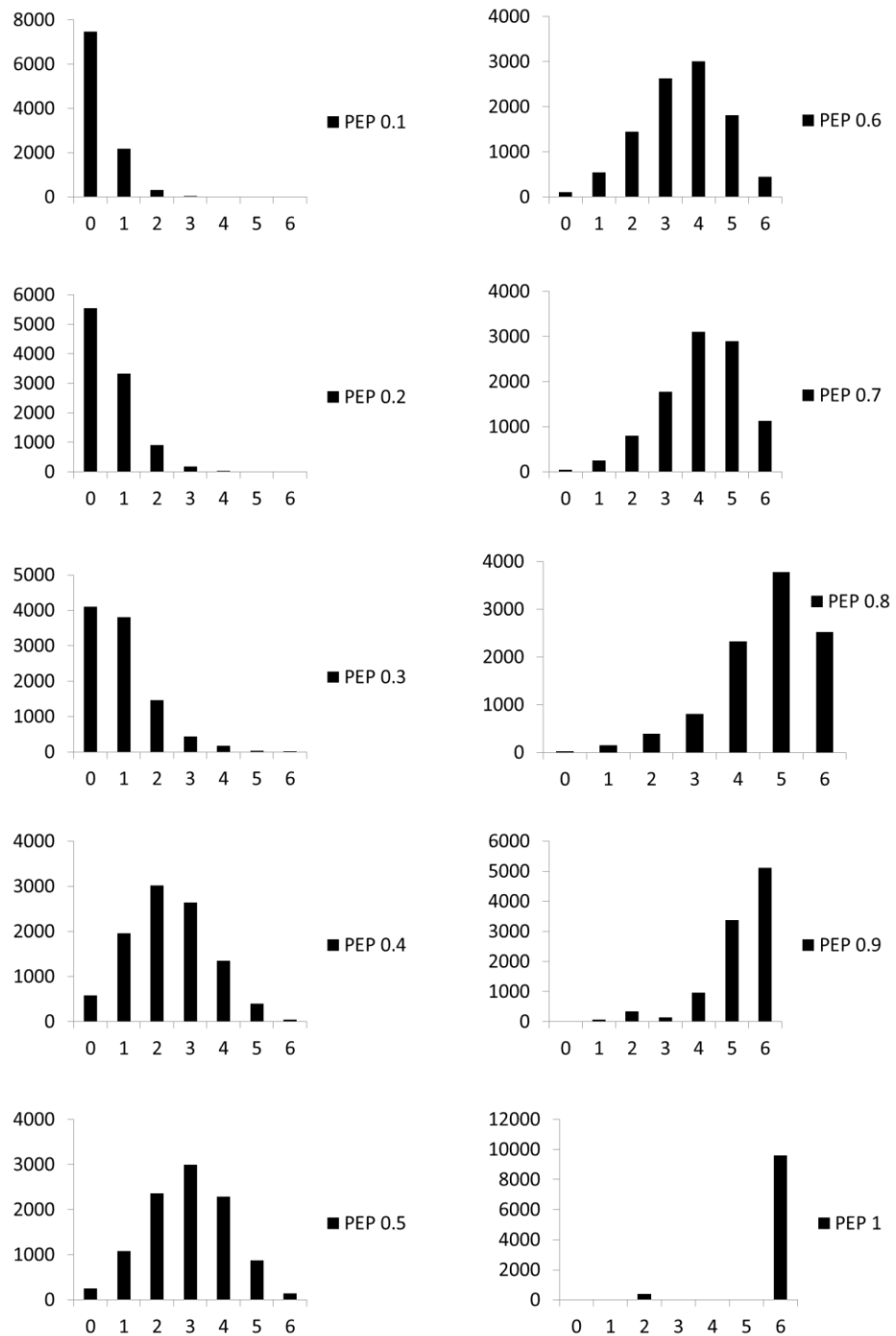


Figure 62. Number connectivity distribution for a triangular network ( $Z_{max}=6$ )

Figure 63 contains the percolation spectra for two triangular pore networks with two different PEP. One network was created using a PEP=1 and a second network was created with a PEP=0.5. Due to the use of PEP=0.5 the network has connectivity distribution. For

PEP=0.5, the average connectivity is equal to 3 ( $Z=3$ ), different from the case of PEP=1 when the connectivity is the same in all the network (except by the external nodes) and equal to 6 ( $Z=6$ ). The use of a PEP of 0.5 changes considerably the topological map, making about 80 % of the network sensitive to the percolation map instead of just the 40% ( $Z=6$ ).

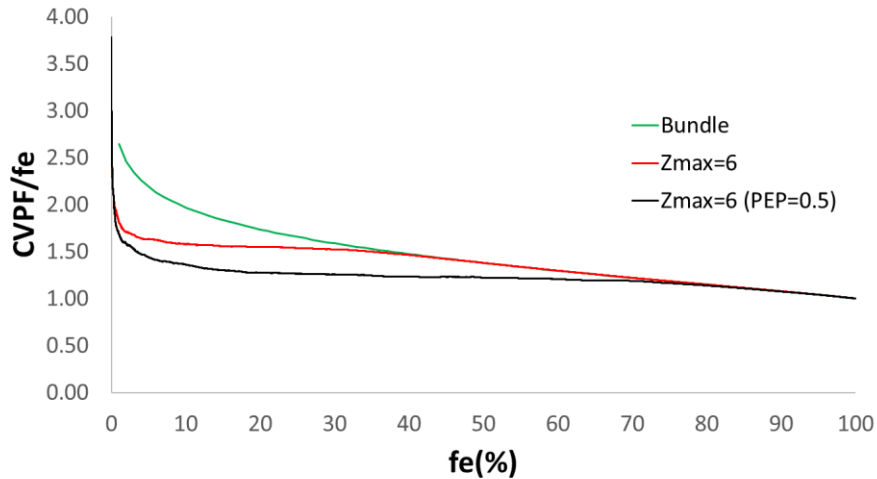


Figure 63. Effect of the connectivity on the topological map

### 3.8.3. Effect of the Pore Size Distribution

The percolation map is also affected by the pore size distribution. In the case of gaussian pore size distribution, it is not affected by the average value of the distribution but by the standard deviation. A higher standard deviation leads to a more important fraction of the network influenced by the percolation map. Figure 64 compares the ADC for different pore size distributions that have the same average and different standard variance. For each pore size distribution, an interconnected pore network (dotted line) and the ideal case, a bundle of pores (continuous line), are compared. A higher standard deviation for the pore size distribution produces a higher relative deviation between the ADC for the interconnected pore network and its ideal case. For the pore size distribution that corresponds to  $10 \pm 2.5$  nm, the difference between the pore network and its ideal case is the highest at  $fe = 50\%$ . A high standard deviation in Gaussian distribution indicates long tails. Longer tails increase the percentage of the pore influenced by the percolation order.

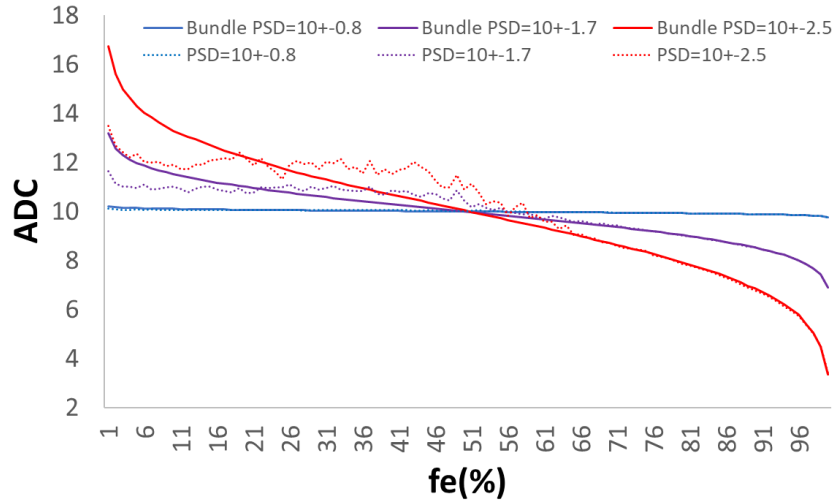


Figure 64. Influence of the pores size distribution on the percolation map.

### 3.8.4. Effect of multiple populations

When several populations are used, the topology of the network is influenced by the PEP of each population. In addition to the connectivity distribution of the network, the connectivity distribution by population becomes relevant.

When only one pore population is implemented and the PEP is lower than 1, isolated group of pores can exist. The term isolated is reserved to pores that are not connected to the external surface, either directly or through other pores belonging to the same pore population. Figure 65 represents an example of such pore domains. The highlighted regions in green show some examples of them.

These isolated groups of pores belonging to one population will be considered as pore domains. The access to these pore domains will be ruled by the pores of the population that surrounds them, as shown in Figure 66.

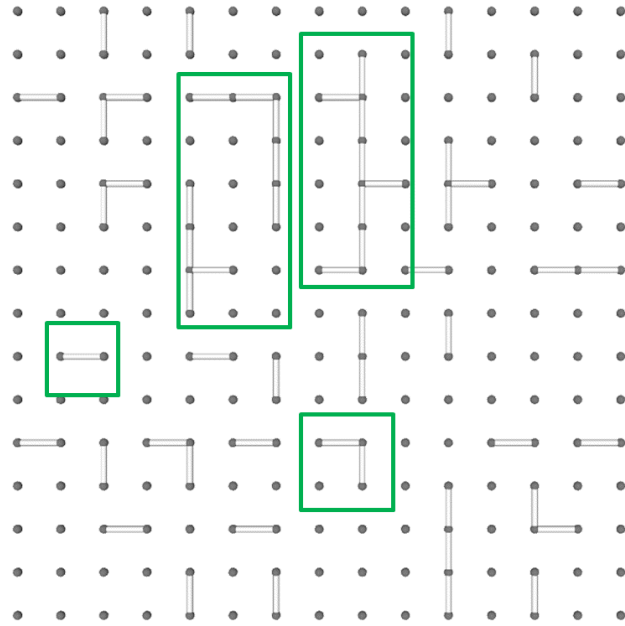


Figure 65. Pore network with a PEP=0.2: The green rectangles enclose examples of pore domains.

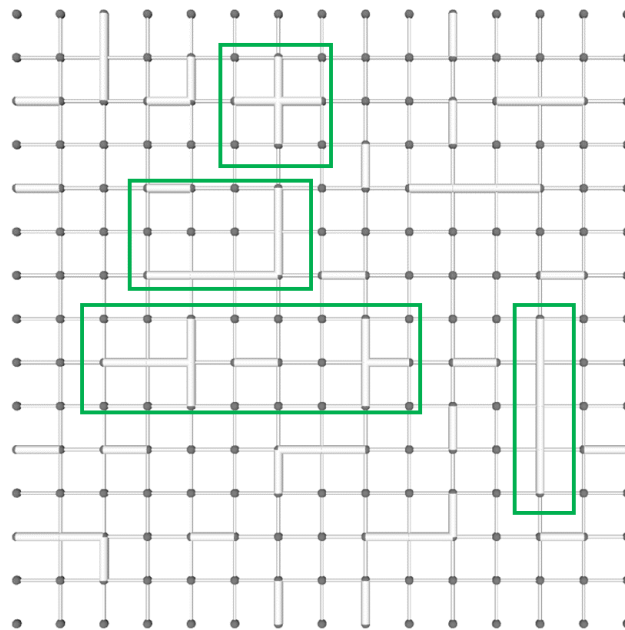


Figure 66. Pore network with two different populations: Population 1, PE=0.2; Population 2, PEP=1. The green rectangles enclose examples of pore domains.

These domains can have different topology, size distribution, volumetric density and represent a different fraction of the total porosity represented by the population. All these parameters are mainly influenced by the PEP. As the PEP decreases, the pore volume represented by these pore domains (relative to the full network) will change following a gaussian trend. At the same time, the pore volume represented by them relative to their population will increase, meaning that a smaller fraction of this population is in contact with

the external surface when the PEP decreases. Figure 67 shows the number of pores represented by the domains relative to the total number of pores of the population. For this test, a network with a triangular lattice, constant diameter and constant length was used.

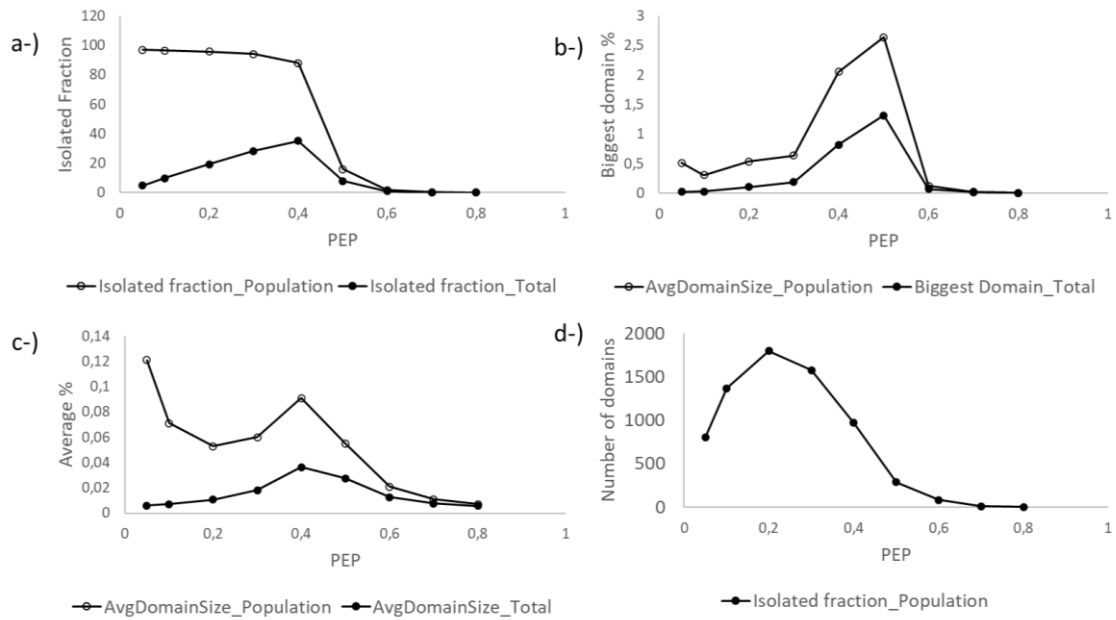


Figure 67. Domain sensitivity to PEP. a-) Isolated pore fraction of the population. b-) Biggest domain in the pore network calculated as pores percentage. c-) Average pore percentage in each domain of the population. d-) Quantity of population domains (trend).

The average size of the domains shown in Figure 67c represents the percentage of pores contained in each domain. It is important to note that the size of these domains has a high dispersion (relative to PEP) that corresponds to the Gaussian maximum in 0.4-0.5 (Figure 68). It can be concluded from Figure 67c and Figure 67d that lower PEP creates a higher number of domains of smaller size. The biggest domains that can be created exist at PEP of 0.5. However, the conclusion needs to be analyzed with care given the dispersion shown in Figure 68. Big domains are far from the average number of pores for each domain and are extreme values. According to the pore volume fraction set as target for the population, the desired domain size, and the acceptable fraction of the population that can be connected to the external surface, the PEP range of 0.2-0.4 and 0.4-0.6 should be used (Figure 67c). Both ranges have similar sensitivity in terms of the number of domains and domain size. However, they differ in the fraction of the population connected to the external surface (without crossing other domains) and the total pore volume fraction that they represent.

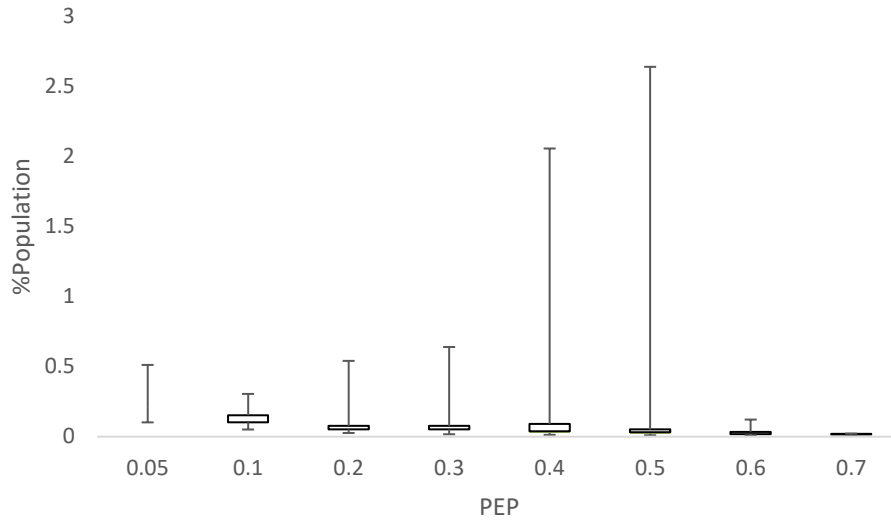


Figure 68. Domain size (calculated as fraction of the total number of pores in the population) as a function of PEP.

These domains can be created using several populations and 1 dominant population that will fill all the spaces left by the populations used for the domains. It is also possible to create bigger domains of the same population. To do so, it is possible for example to declare 2 populations with the same pore size distribution and different grid spacings (See section 3.3.5) and then declare a third population that will dominate the 2 first ones in terms of percolation.

Two examples will be analyzed using two different populations in the same network to illustrate how a second population can influence the percolation order of the domain. The results for these two examples are shown in Figure 69 and Figure 70. The pore fractions (%Pores Pop #) and pore volume fractions (%Vp Pop #) contained in each population are given in Table 6. Each population has a unique pore diameter (no pore size distribution is used). Population 1 has a grid spacing equal to 2 and population 2 has a grid spacing equal to 1.

Table 6. Pore volume percentage represented by different populations

Case	Pop1	PEP_Pop1	Pop2	PEP_Pop2	%Pores Pop1	%Pores Pop2	%Vp Pop1	%Vp Pop2
1	20	0.1	40	1	5.0	95.0	1.3	98.7
	20	0.5	40	1	24.7	75.3	7.6	92.4
	20	1	40	1	50.0	50.0	20.0	80.0
2	40	1	20	0.1	5.1	94.9	17.7	82.3
	40	1	20	0.5	25.1	74.9	57.3	42.7
	40	1	20	1	50.0	50.0	80.0	20.0

In case 1, population 1 is represented by pores of 20 nm and population 2 is represented by pore of 40 nm. Three different networks with a squared lattice and different PEP for population 1 are compared. It is important to remark the effect of the pore diameter of each population. If the PEP is equal for both populations, the number of pores for each population will be the same, however, the population with the highest pore diameter will represent the highest pore volume fraction (Table 6). The pore size of each population will also influence the percolation maps according to their spatial coordinates and its grid spacing (Section 3.3.5).

Figure 69 represents the cumulated pore volume explored for each population as a function of the explored fraction ( $f_e$ ) for case 1. In this graph, an average constant slope refers to the constant average pore size. Population 1 is represented by pores of 20 nm and population 2 is represented by pores of 40 nm. Each slope variation corresponds to a change in the population that dominates the percolation. In the second column of Figure 69, the associated connectivity distribution by population is shown. Even if the maximum connectivity is defined by the lattice, the use of two different pore populations will create a connectivity distribution by population that will influence the topology map and then the percolation list. Still, the total maximum connectivity remains the same, a lower connectivity by population increases the influence of the percolation map. This connectivity distribution by population shows how many pores of a certain population are connected to one node. When the connectivity is equal to zero ( $Z=0$ ), it means the number of nodes that are not connected to any pore.

In Figure 69a there is no interaction between population 1 and population 2. Despite the PEP of population 1, even if several domains are formed, its exploration is not blocked by population 2 because its diameter is smaller than the diameter of population 2. In Figure 69a before the exploration of population 1, all the pores belonging to population 2 are already explored. Most of the nodes do not have pores from population 1 connected to them. This population is present with a maximum of 2 pores by each node. The most common pores that are connected to nodes are those from population 2 (percentage %).

Figure 69 shows how, as the PEP of population 1 grows, the connectivity distribution by population passes from having specular symmetry to become symmetrical. This leads to total modification of the topological map.

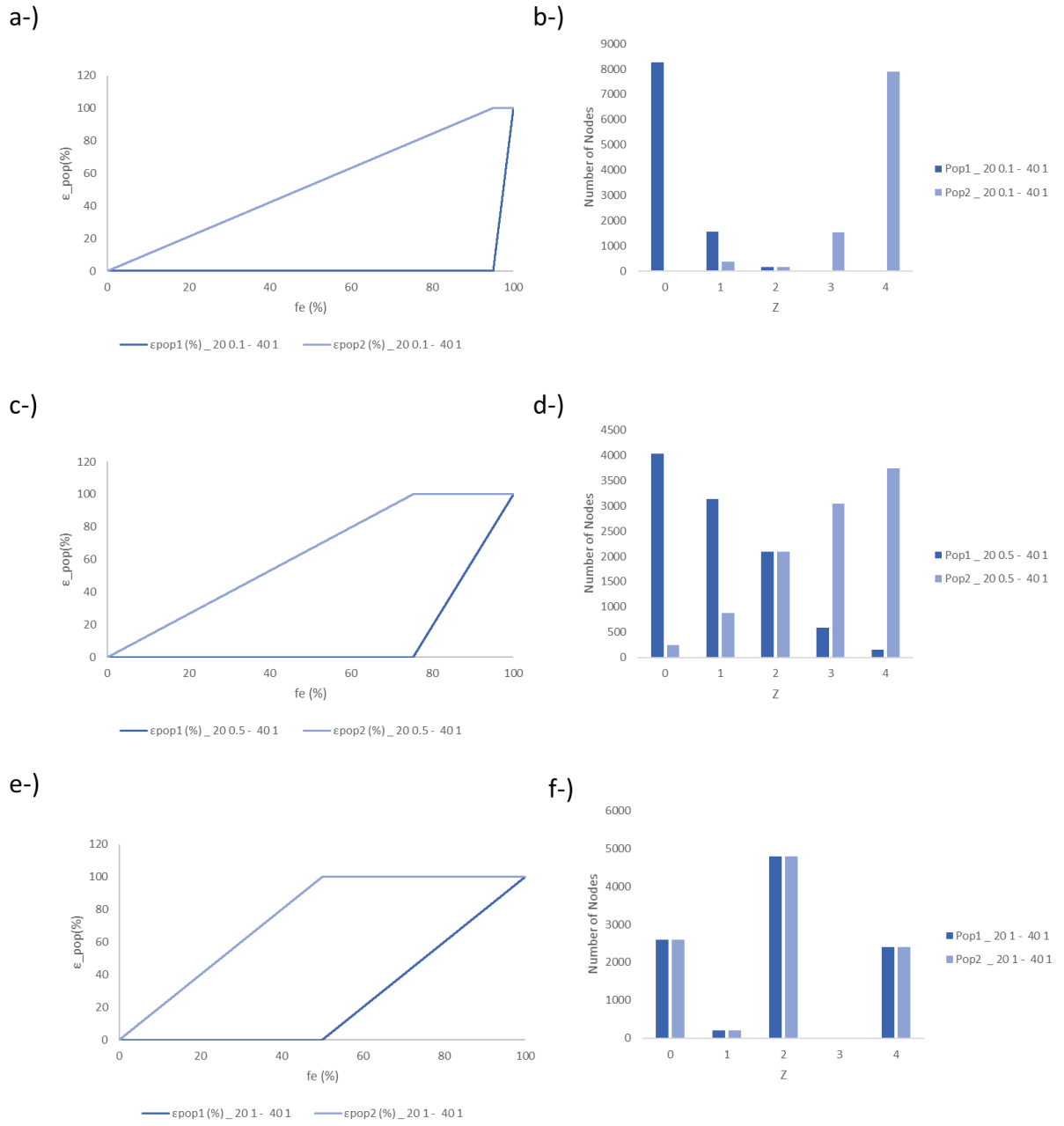


Figure 69. Cumulated explored percentage by population as a function of  $fe$  and pore connectivity distribution by population: a-) Population 1 – PEP=0.1, Population 2 – PEP=1; b-) Population 1 – PEP=0.5, Population 2 – PEP=1; Population 1 – PEP=1, c-) Population 2 – PEP=1

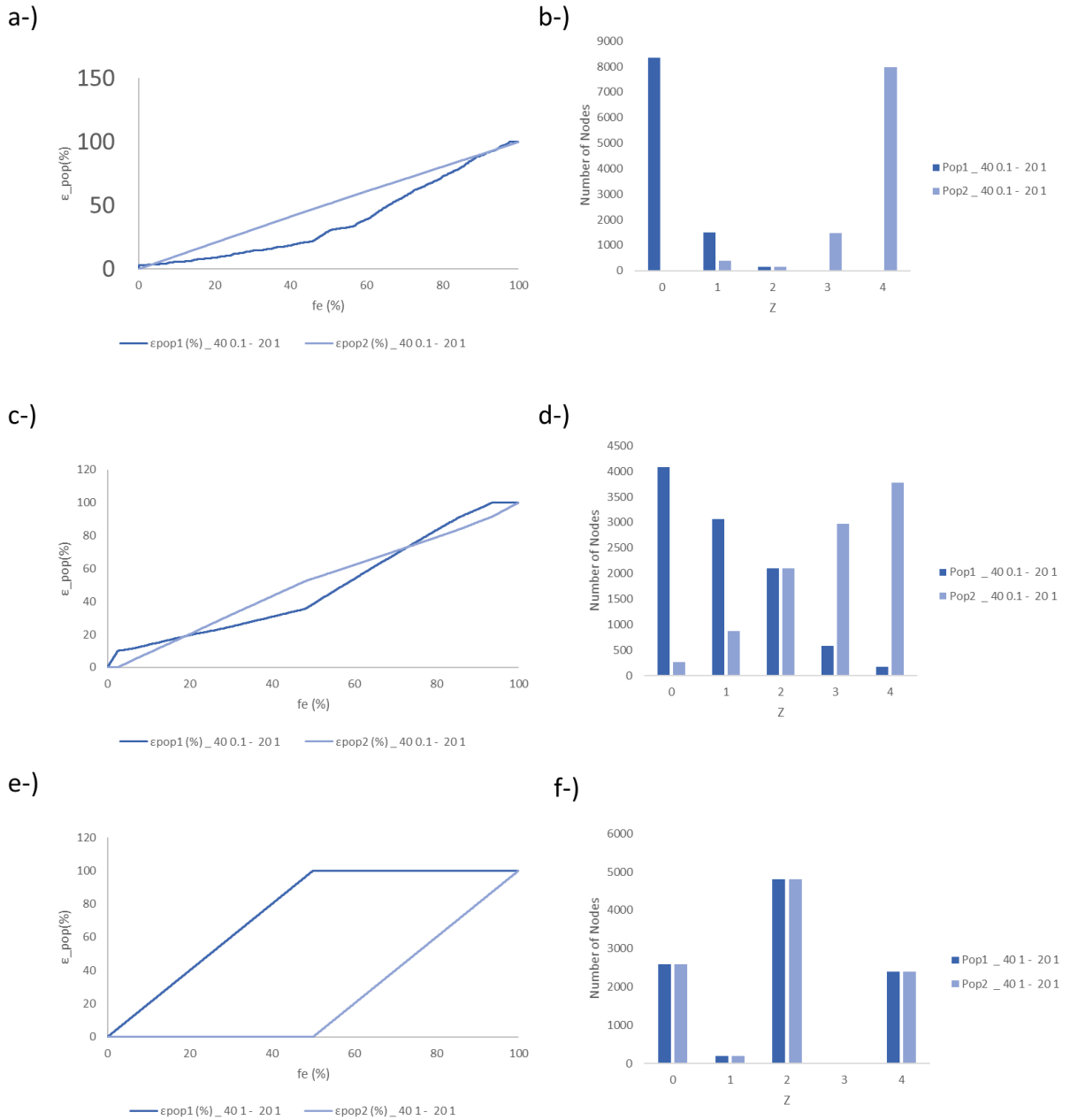


Figure 70. Cumulated explored percentage by population as a function of fe and pore connectivity distribution by population: a-) Population 1 – PEP=0.1, Population 2 – PEP=1; b-) Population 1 – PEP=0.5, Population 2 – PEP=1; c-) Population 1 – PEP=1, Population 2 – PEP=1. Inverse to the population configuration used in Figure 69.

In case 2, population 1 is represented by pores of 40 nm, and population 2 is represented by pores of 20 nm (inverse of case 1). In this case, Figure 70a shows the interaction between the 2 populations. Population 1 is explored at a constant rate, while population 1 is explored at different rates highlighted by the slope change. There are at least 4 different slope changes. This indicates that population 1 was segregated into 4 different effective domains.

Figure 70c depicts the case for PEP of population 1 equal to 0.5. In this case, the pore volume fraction represented by population 1 is bigger than the one represented by population 2 (Table 6). The number of pores for both populations is the same. In this case, the exploration rate of population 2 is affected by population 1. There are still 4 rate changes. However, at each change in the exploration rate of population 1, the exploration rate of population 2 changes too. In this case, a higher number of pores from population 1 are not constrained by population 2 and it dominates the exploration at the beginning of the percolation list. Finally, Figure 70d shows the case in which the two populations have a PEP equal to 1. In this case, as already mentioned before, despite the position of the population or the grid spacing, the populations do not interact with one another. If pore size distributions that overlap in their tails had been used for the 2 populations, an interaction would exist.

Figure 70 again shows how, as the PEP of population 1 grows, the connectivity distribution by population passes from having specular symmetry to become symmetrical. This leads to total modification of the topological map.

### 3.9. Tortuosity of the pore network

A parametric study was performed to analyze the influence of the input parameters on the tortuosity factor of the network. A sufficient number of simulations was executed for each case in order to obtain a relative error lower than 10%. The dimension of the network used for the analysis was fixed to 50x50. The simulation time is sufficiently long to reach the stationary state of the system. The diffusion simulation time step ( $\Delta t_{step}$ ) was fixed at  $4.16 \cdot 10^{-9}$  s.

#### 3.9.1. Diffusion simulation methodology and tortuosity factor estimation.

The first and second Fick laws are used to simulate diffusion into each pore of the network. The 1D material balance within each pore associated to the Fick model is represented in Equation 20.

$$J_i = -D_m \frac{\partial C_{ip}}{\partial l}$$

Equation 20. Fick first diffusion law

Boundary conditions at each end of the pore depend on the position and the type of node the pore is connected to (Table 7). For external nodes, the concentration is considered as constant, and a Dirichlet boundary condition is imposed. For the internal nodes connected to just one pore (blind pore), a Neumann boundary condition is implemented. For internal nodes linked to more than one pore, a Kirchhoff's flow boundary condition is used. This

means that the concentration at the extreme of the pores connected to the same node must be the same.

Table 7. Boundary conditions

Node type	Border condition
External node	$C_{ip} = C_{ext} \quad t \geq 0$
Internal node (blind pore)	$\frac{dc_i}{dl} = 0 \quad l = L_p$
Internal node	$\sum_0^Z J_{i,n} S_{p,n} = 0$

The network was spatially discretized using the orthogonal collocation method (Villadsen and Stewart 1967). For the resolution of the resulting algebro-differential equation system the DASPAK routine was employed (van Keken et al. 1995).

A semi-infinite pore network, representing an infinite plate, was used. Two orthogonal directions are periodic, while in the third direction boundaries represent the entrance and the exit of the network. A similar element was presented before by Gladden in 1991 (Hollewand and Gladden 1991). For the calculation of the tortuosity factor, a methodology like the one presented by Ruthven is implemented (Helfferich 1985). At steady state, the molar flow at the exit of the network can be calculated as the addition of the molar flows coming out of each individual pore which is connected to the external nodes of the exit face of the infinite plate (Equation 21).

$$J_i = -\frac{\sum J_{ip} S_p}{\sum S_p}$$

Equation 21. Molar flux at the outlet of the network

The effective diffusion coefficient can be calculated assuming that the structure can be modelled in a higher length scale as a unique straight fluid macropore, where the concentration difference is measured between the inlet and the outlet of the 3D periodic network (Equation 22).

$$J_i = -D_{eff} \frac{\Delta C_i}{L_N}$$

Equation 22. Flux throughout the network thickness.

The length  $L_N$  represents the linear distance between the two non-periodic faces of the plate, while  $\Delta C_i$  is the concentration difference between the inlet and the outlet size of the

3D periodic network. Finally, by definition, the tortuosity can be calculated using the Equation 23.

$$\tau = \frac{D_m}{D_{eff}}$$

Equation 23. Tortuosity

### 3.9.2. Influence of the pore network generation parameters on tortuosity

#### 3.9.2.1. Influence of the Pore Existence Probability

The input conditions used for the simulations are presented in Table 8.

Table 8. Conditions used to analyze the influence of PEP on the tortuosity factor

Input parameters	
PEP (-)	Variable
Pore Length (nm)	40
Avg. Diameter (nm)	20
PSD St.Dev. (nm)	20
Z <sub>max</sub> (-)	6
Grid Distortion (%)	0

As shown in Figure 71, a decrease in the pore existence probability causes an increase in the tortuosity of the system. A lower PEP increases the average length travelled by the chemical species to reach the exit of the semi-infinite network.

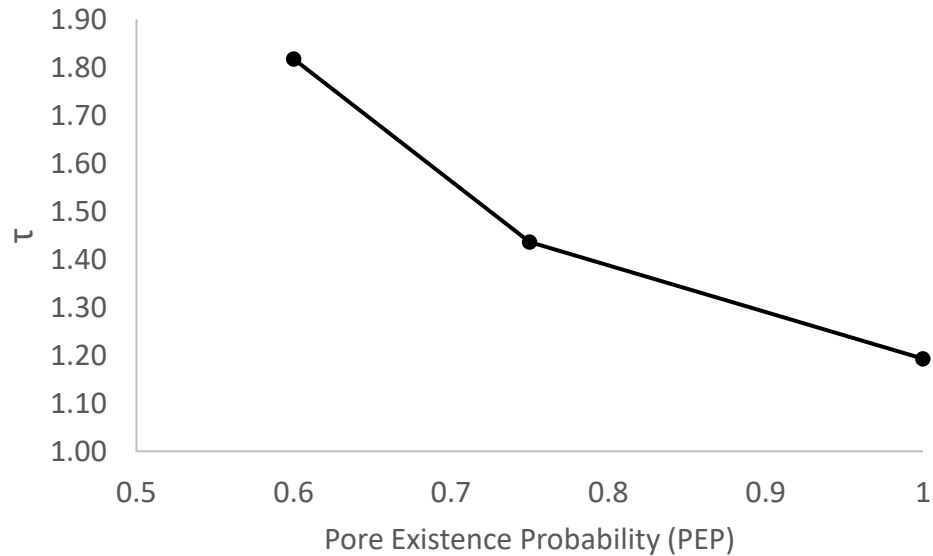


Figure 71. Variation of the tortuosity as a function of the PEP.

### 3.9.2.2. Influence of the average diameter

The input conditions used for the simulations are presented in Table 9.

Table 9. Conditions used to analyze the influence of average diameter of a gaussian PSD on the tortuosity factor

Input parameters	
PEP (-)	0.75
Pore Length (nm)	40
Avg. Diameter (nm)	Variable
PSD St.Dev. (nm)	2
Z <sub>max</sub> (-)	6
Grid Distortion (%)	0

As shown in Figure 72, a lower PSD average diameter increases the tortuosity. This observation is coherent if the system is analyzed in terms of the resistance to diffusion (Equation 24). As the diameter increases, the resistance to diffusion decreases.

$$R_i = \frac{L_p}{\pi * R_p^2 D_m}$$

Equation 24. Mass transfer resistance

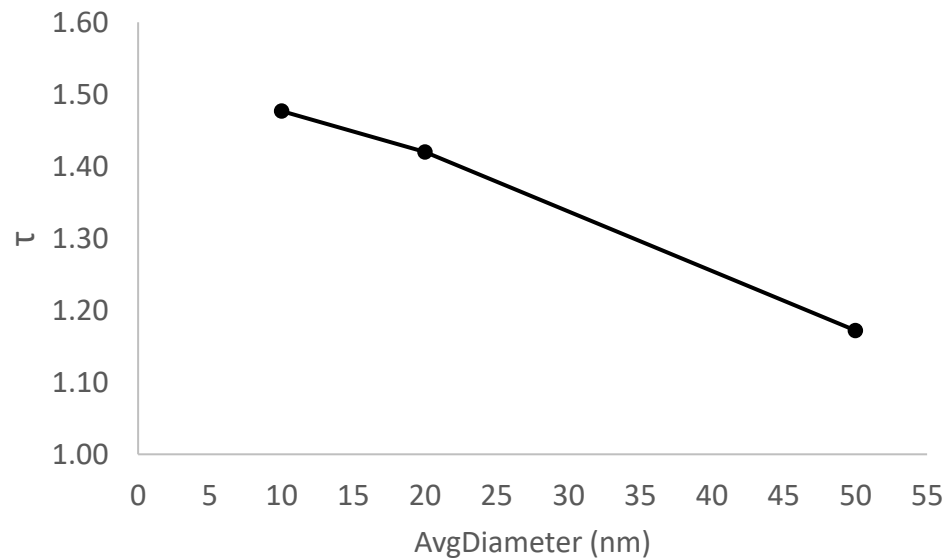


Figure 72. Variation of the tortuosity as a function of the pore average diameter.

### 3.9.2.3. Influence of the PSD standard deviation

The input conditions used for the simulations are presented in Table 10.

Table 10. Conditions used to analyze the influence of the standard deviation of gaussian PSD on the tortuosity factor

Input parameters	
PEP (-)	0.75
Pore Length (nm)	40
Avg. Diameter (nm)	20
PSD St.Dev. (nm)	Variable
Z <sub>max</sub> (-)	6
Grid Distortion (%)	0

As shown in Figure 73, an increase of the PSD standard deviation causes a small increase in the tortuosity of the system. As discussed in section 3.8.3, the PSD standard deviation influences the percolation map of the system. A higher PSD standard deviation will cause an increase in fraction of pores affected by pore blocking. This means that in the diffusion case, the fluid could face a more complex system of resistances. These results are in agreement with the conclusion of Gladden (Hollewand and Gladden 1992).

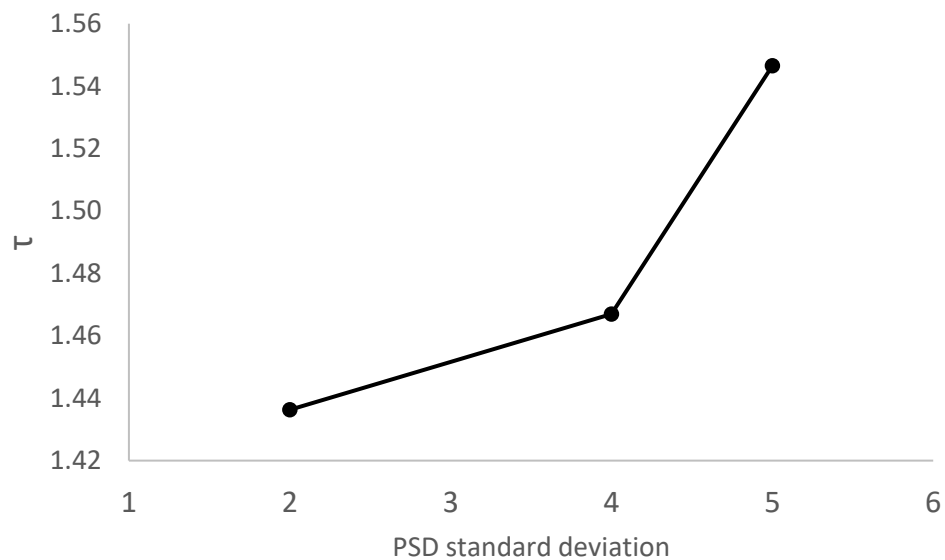


Figure 73. Variation of the tortuosity as a function of the PSD standard deviation.

### 3.9.2.4. Influence of the pore length

The input conditions used for the simulations are presented in Table 11.

Table 11. Conditions used to analyze the influence of the length on the tortuosity factor.

Input parameters	
PEP (-)	0.75
Pore Length (nm)	Variable
Avg. Diameter (nm)	10
PSD St.Dev. (nm)	2
Z <sub>max</sub> (-)	6
Grid Distortion (%)	0

As shown in Figure 74, a variation of the pore length in a network in which all the pores have the same pore length has no effect on the tortuosity of the system. In this pore network model, an increase of the pore network length causes a proportional increase of the network size and in the characteristic time of the network. These results imply that the tortuosity of a pellet could be simulated using very long pores to extrapolate the size of the system to the macroscopic scale as proposed by Coppens (Ye et al. 2017). It should be mentioned that the textural properties will of course be different.

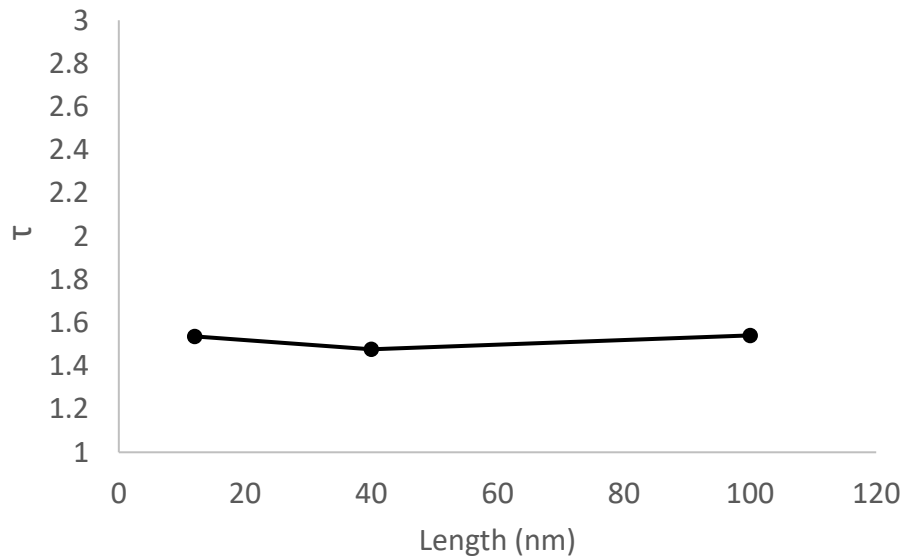


Figure 74. Variation of the tortuosity as a function of the pore length.

### 3.9.2.5. *Influence of the grid distortion*

The input conditions used for the simulations are presented in Table 12.

Table 12. Conditions used to analyze the influence of length distortion on the tortuosity factor

<b>Input parameters</b>	
PEP (-)	Variable
Pore Length (nm)	100
Avg. Diameter (nm)	10
PSD St.Dev. (nm)	2
Z <sub>max</sub> (-)	6
Grid Distortion (%)	Variable

As shown in Figure 75, an increase in the distortion percentage causes a small increase on the tortuosity of the system. The distortion of the network in this model generates a gaussian length distribution (Figure 30). However, the pore length apparently has no influence on the tortuosity factor. It is possible that the increase of the tortuosity factor is due to the fact that the distortion is emphasizing the effect of the PSD standard deviation.

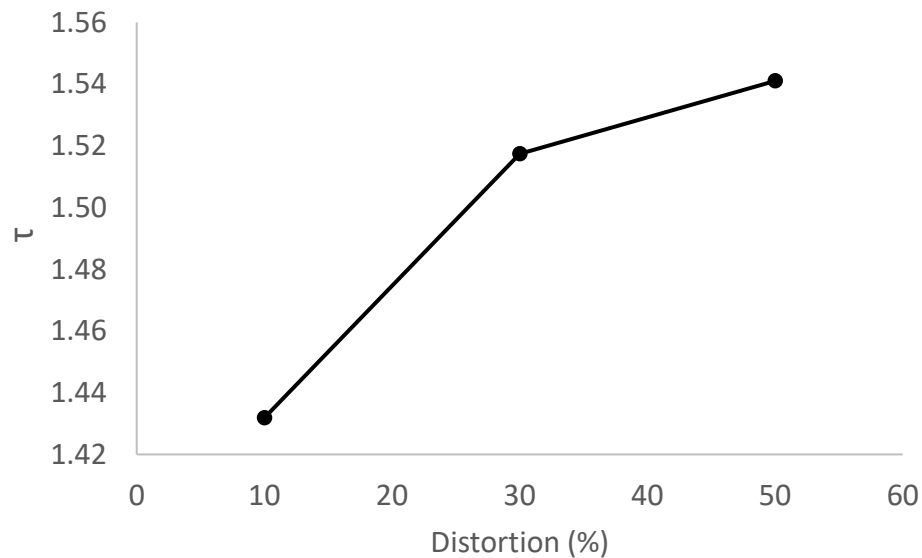


Figure 75. Variation of the tortuosity as a function of the grid distortion.

### 3.9.2.6. *Influence of multiple domains*

The constant input conditions used for the simulations are presented in Table 13, where two pore populations are defined.

Table 13. Conditions used to analyze the influence of different PEP in a hierarchical network on the tortuosity factor

Input parameters	
PEP (-)	Variable
Pore Length (nm)	10
Avg. Diam. Pop 1 (nm)	15
Avg. Diam. Pop 2 (nm)	5
PSD St.Dev. Pop 1 (nm)	2
PSD St.Dev. Pop 2 (nm)	2
$Z_{max}$ (-)	6
Grid Distortion (%)	0

Having multiple domains located in random positions into a hierarchical architecture will have an influence on the tortuosity factor (see section 3.8). Figure 76 shows a parabolic evolution of the tortuosity factor as a function of the pore existence probability of the first population. When Figure 76 is confronted to the parametric analysis of PEP for hierarchical networks (or domains) in Figure 67, it seems that there exists a correlation between the number of clusters (or domains) and the tortuosity factor. The highest tortuosity value corresponds to the PEP that generates the highest number of clusters.

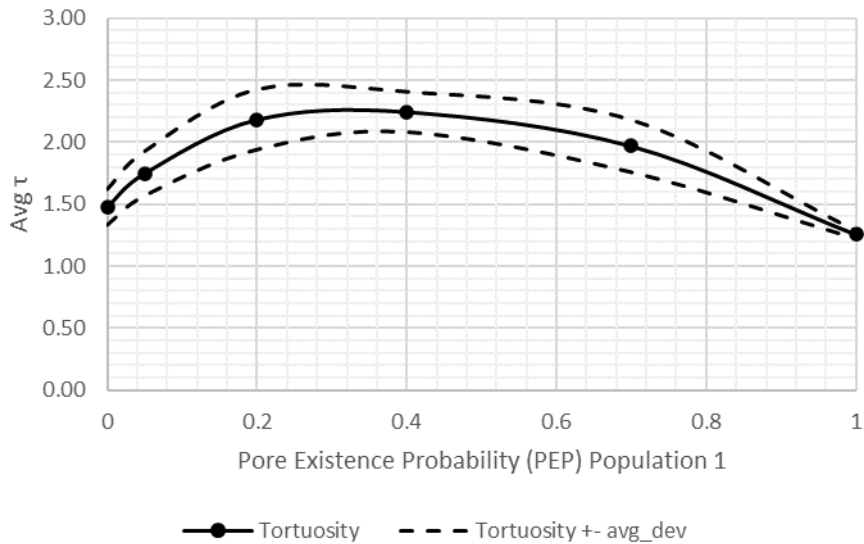


Figure 76. Variation of the tortuosity as a function of the PEP of the population 1.

This is line with experimental results for hierarchical gamma aluminas in which the porosity is concentrated into the grains instead of being concentrated into the matrix. When the tortuosity measured by PFG-NMR was compared against the tortuosity of hierarchical gamma alumina in which the porosity is concentrated into the matrix, it was found that the tortuosity is higher for the first case (Figure 77 and Figure 78).

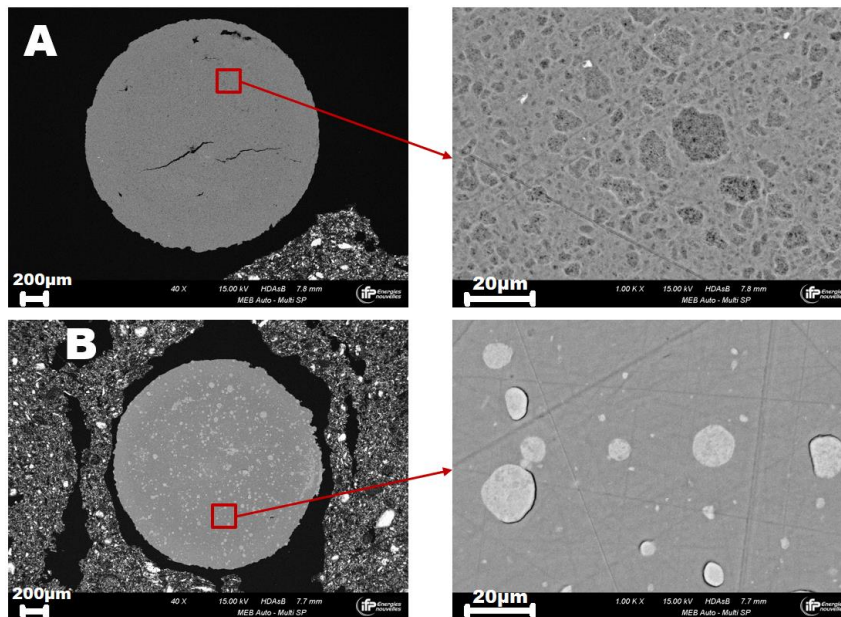


Figure 77. SEM microscopies for two gamma alumina's A and B (Głowska 2021)

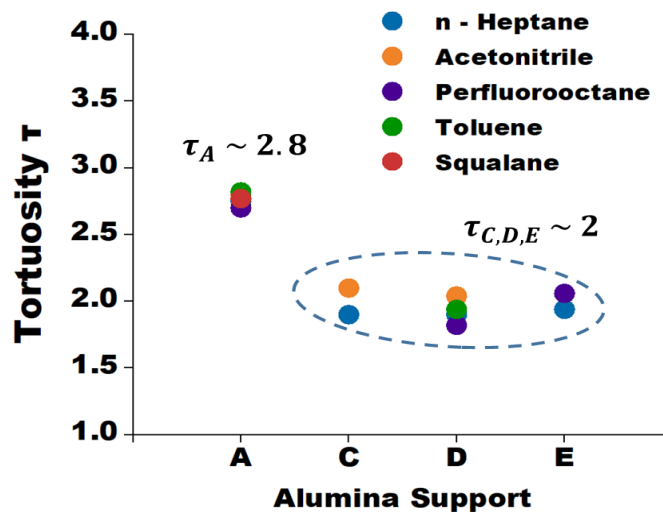


Figure 78. PFG NMR tortuosity measurements for 5 gamma alumina's A, B, C, D and E (Głowska 2021)

### 3.10. Conclusion

In this chapter, the pore network model implemented was discussed in detail. The flexibility of the model and its versatile features were illustrated. 2D and 3D networks can be created using one or several pore populations that have independent characteristics: pore size distribution and pore existence probability. The network can be regular or distorted as shown in section 3.3. In the model, the maximum connectivity can be easily varied by implementing different lattices. The interaction between the different pore populations

and the variation of the pore network generation parameters can produce complex outputs such as pore connectivity distributions and pore volume distribution by population. The implementation of a percolation algorithm using advanced strategies such as heap structures significantly increases the simulation speed.

A topological analysis was carried out in order to better understand the influence of the different network generation parameters the network's architecture. It was argued how the topological maps are affected by the lattice and the pore existence probability, how the percolation map is affected by the topological map and the pore size distribution, and how the pore volume distribution is affected by the pore size distribution and the pore length distribution. The fact that a fraction of the pores is not influenced by percolation phenomena is an interesting conclusion of this section. This fraction depends on the maximum connectivity of the network and the pore existence probability.

The interaction between several pore populations was also studied. The populations can hinder each other according to their grid spacing and their pore size distribution. The volume represented by each population is a key variable. The effect of the percolation map on volume processes is significantly influenced by the pore volume fraction allocated to each population. This is result relevant to understand the role of pore blocking effect when techniques such as nitrogen sorption are to be simulated. Controlling the size and the dispersion of the domains could improve importantly the quality of the model. These descriptors can be useful to characterize hierarchical gamma aluminas.

The existence of pore domains of different populations, their number, and their dispersion in the network strongly influence the effective diffusion coefficient. This is in line with experimental observations. This analysis proves the relevance of using multiple populations and pore domains to model the network architecture of gamma aluminas.

## Chapter 4: Simulating textural characterization techniques

### 4.1. Introduction

Generating structures that match structural descriptors of a real porous material is an important task. For disordered porous material, the randomness of the structure is an important factor to consider and sometimes the existing characterization techniques only provide limited information about the structure. The lack of information is due to constraints of the techniques, to the low accuracy of the interpretation models or to a lack of understanding of the phenomena occurring during the characterization experiments. Interpretation of the results coming from different techniques can be time-consuming and sometimes contradictory.

Direct simulation of the phenomena on which the experimental characterization technique is based can help to get a better interpretation of the results. Studying the validity of the assumptions used for the interpretation of the raw data and the calculation of specific properties such as surface area, pore volume, and pore size distribution is a way to do this. By doing this, it should be possible to create a more accurate digital representation of the material and a statistically representative computational structure (Schüth 2002a). It could be also possible to extrapolate results, identify new relevant descriptors, and finally optimize the structure with a specific goal.

In this chapter, we will describe the models that we have developed for the simulation of the characteristic curves obtained by Nitrogen Sorption (NS), Mercury Porosimetry (MP), and Cryo-Porosimetry (CP).

Several authors have worked on the numerical modeling of these characteristics curves: some of them using computationally expensive methods coming from molecular dynamics or DFT (Wongkoblap et al. 2011; Bruschi et al. 2015; Gelb and Gubbins 1999; Do et al. 2010; López-Ramón et al. 1997; Gavalda et al. 2002), others through statistical methods such as percolation theory (Seaton 1991; Daigle et al. 2015; Murray et al. 1998, 1999a; Liu et al. 1993; Cimino et al. 2013), and the last group using equations and models based on capillary phenomena (Mehmani and Prodanović 2014; Meyers et al. 2001; Tian and Daigle 2018; Rojas et al. 2002; Satik. C. 1995; Wang et al. 2018). To match the digital structure with the structure of the material, an important amount of computational time must be invested depending on the number of parameters of the model. It is therefore critical to create algorithms capable of getting accurate results in a minimum time. Recent interesting research proposes to combine the information provided by different porous solid characterization techniques (digital and experimental) to characterize the topology of the solid (Cimino et al. 2013; Rigby et al. 2017; Hitchcock et al. 2014).

## 4.2. Methodology

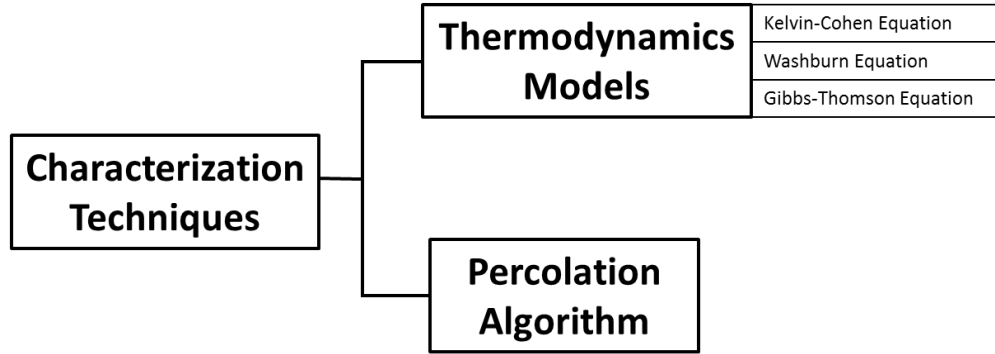


Figure 79. Elements of the algorithm for the characterization techniques simulations.

The models that we propose are based on the pore networks that are generated by using the stochastic generation algorithm described in Chapter 3.

The simulation of each characterization technique has two fundamental parts (Figure 79). The first one is the thermodynamic or mechanical equilibrium model that relates the input experimental variable to the size of the pores. The second one corresponds to the pore blocking phenomena and how they affect penetration and exit, or the phase change of the fluid used for the characterization. The percolation algorithm that we have developed in section 3.7 will be used to deal with this situation.

## 4.3. Nitrogen sorption simulation

### 4.3.1. Thermodynamic Model

The Kelvin-Cohan (KC) equation (Equation 25) represents the pressure of the vapor-liquid equilibrium in a confined medium as a function of the liquid-vapor interface mean curvature at a given temperature. This equation has well-known limitations, especially below the 5 nm diameter threshold (Zhang et al. 2006).

To model the vapor-liquid equilibrium in confined media, the Kelvin-Cohan equation is used along with the Harkin-Jura statistical thickness equation (Equation 26) that gives the thickness of a layer of adsorbed nitrogen on the pore's surface. This layer reduces the size of the empty part of the pore and hence the mean curvature of the liquid-vapor interface.

$$\frac{P_v}{P_o} = \exp\left(\frac{\sigma_{lg} * V_{lm}}{RT} * \left(\frac{1}{r_1(t)} + \frac{1}{r_2(t)}\right)\right)$$

Equation 25. Kelvin-Cohan equation as a function of two curvature radii.

$$t = \frac{13.99}{0.034 - \log_{10} \left( \frac{Pv}{P_0} \right)^{\frac{1}{2}}}$$

Equation 26. Harkins-Jura Statistical thickness equation (with  $t$  in angstrom).

If  $r_p$  is the radius of a given cylindrical pore, the size  $r_{eq}$  to be accounted for is given by:

$$r_{eq} = r_p - t$$

The following assumptions are taken:

- The pores are rigid, cylindrical, and open at both ends.
- During the increasing pressure step, sorption mechanism starts with the adsorption of the nitrogen on the pore wall followed by sudden liquefaction. For a given pressure, liquefaction occurs in pores the radius of which being given by the KC equilibrium (Equation 25) with:

$$\frac{1}{r_1(t)} + \frac{1}{r_2(t)} = \frac{1}{r_{eq}}$$

- During the decreasing pressure step, the liquid nitrogen needs to be in contact with the vapor phase to evaporate. In this case, a pore blocking phenomenon occurs, and a triggering diameter has to be assigned to each pore of the network. In a pore whose diameter is equal to the triggering diameter, the evaporation occurs axially according to the equilibrium KC equation. In this case, the liquid-vapor interface is spherical, and the mean radius of curvature is:

$$\frac{1}{r_1(t)} + \frac{1}{r_2(t)} = \frac{2}{r_{eq}}$$

Once all the liquid nitrogen is vaporized, desorption occurs on the pore wall.

#### 4.3.2. Triggering diameter assignment for decreasing pressure step

Even if the equilibrium pressure in a given pore is reached, the liquid phase needs to be in contact with the gas phase to be able to vaporize. In Figure 80, a simple example is represented by considering three cylindrical pores in series: *A*, *B*, and *C*. All the three pores are open at both ends and *A* and *C* are in contact with gas. *C* has the smallest radius, *A* has an intermediate radius, and *B* has the largest radius. This means that the vaporization equilibrium pressure in pore *B* is higher than in pores *A* and *C*. The liquid nitrogen contained in *B* cannot vaporize until there is a connection to the surrounding gas, i.e. until the liquid nitrogen contained by *A* is vaporized. We will say that vaporization in pore *B* is triggered by

vaporization in pore *A*. The vaporization pressure in pore *B* will therefore be out of equilibrium and lower than during a non-blocked liquefaction process.

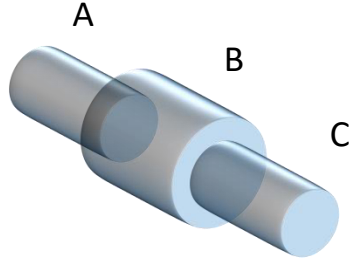


Figure 80. Representation of an example network of three pores.

The triggering diameter of pore *B* represents the critical diameter at which vaporization of nitrogen contained in pore *B* will take place. Hence, in the case of Figure 80, the triggering diameter of pore *B* is equal to the diameter of pore *A*.

The attribution of the vaporization triggering diameter to each pore is performed by using the dedicated generic algorithm described in section 3.7.

#### 4.3.3. Nitrogen volume calculation

The simulation starts from a relative pressure equal to zero. As the pressure increase, the nitrogen penetration process occurs in two steps: layer formation and full condensation. It is therefore necessary to establish a liquefaction criterion for the cumulated volume of liquid nitrogen (Equation 27).

$$D_p > D_{eq} - 2t$$

Equation 27. Liquefaction criteria

If the diameter of the pore ( $D_p$ ) is higher than the Kelvin-Cohan equilibrium diameter ( $D_{eq} - 2t$ ) for a given relative pressure, then the adsorbed volume  $V_p$  in this particular pore at the current pressure is equal to the volume of nitrogen in the adsorbed layer:

$$V_{N_2} = \pi * L_p * (D_p - t) * t$$

Equation 28. Total adsorbed volume as a function of the adsorbed layer thickness.

Otherwise, it is considered that pore is full of liquid, and its volume is given by:

$$V_{N_2} = \frac{\pi}{4} * l * D_p^2$$

Equation 29. Total liquid volume within the pore

For the decreasing pressure step, as the pore blocking phenomena exist, the procedure is the same, but the vaporization triggering diameter ( $D_T$ ) of the pore instead of the actual diameter ( $D_p$ ) is used in the comparison against the Kelvin-Cohan equilibrium diameter ( $D_{eq\_n-2t}$ ) for a given pressure step. For the calculation of the cumulated volume, the easiest way to do it is to count the liquid volume in the same way as for adsorption: from the lowest relative pressure to higher relative pressures. Doing it in the higher-to-lower relative pressure direction would imply using more criteria to correctly attribute the volume of the core that desorbs abruptly once the metastable state is broken.

#### 4.3.4. Characteristic curve generation

Finally, in pseudo-code, the simulation code can be written as follows:

```

Generate Pore Network Model
Find desorption triggering diameter for each pore
FOR Prelative= 0 to 1
  FOR pore=1, Npores
    Calculate the quantity of nitrogen inside the pore (Equation 27,
    Equation 28 and Equation 29) using the actual diameter (for adsorption)
    or the triggering diameter (for desorption)
  END FOR
END FOR
Print

```

First, the pore network is generated. Secondly, the desorption triggering diameter is found. Thirdly, the relative pressure is varied from 0 to 1. At each pressure step the quantity of nitrogen within each pore is calculated. Finally, the characteristic curve is printed.

#### 4.3.5. Scanning curves

By adapting the full Nitrogen Sorption algorithm, it is also possible to simulate scanning curves that are sensitive to pore blocking phenomena. The thermodynamic phenomena remain the same. However, there are slight changes in the input used for triggering diameter algorithm and the curve generation. A scanning curve is represented by an adsorption branch obtained from a solid that is not totally filled with condensed nitrogen (relative pressure < 1). The relative pressure at which the desorption starts will determine the number of pores filled with condensed nitrogen (not just with adsorbed nitrogen). This pressure will be called target pressure.

The target pressure will determine how to change the input of the triggering diameter. Using the Kelvin-Cohan equation it is possible to determine the critical diameter for the target pressure. In the connectivity matrix, the diameters that are superior to the critical value will be substituted by 1 (or any value bigger than the biggest pore diameter of the network). Then, triggering diameter assignment algorithm will be executed. Once the task is finished, the original diameter of all the pores with a modified diameter will be restored.

At the same time, for these pores also, their original diameter will be assigned as their triggering diameter.

There are two reasons to assign a diameter equal to 1 to the pores with diameter higher than the critical diameter at the target pressure. The first one is that the nitrogen adsorbed in these pores will not block the desorption of the nitrogen condensed in smaller pores. The second reason is to transport the critical diameter information to the more inner pores (see assignation rule ii) in section 3.7.3). A graphical depiction is shown in Figure 81. The three pores are explored from the right to the left. In Figure 81b, the nitrogen adsorbed in the pore 2 does not block the nitrogen condensed in pore 3. When the pore 2 takes the triggering diameter of pore 1 as his own, the pore 3 can take it too.

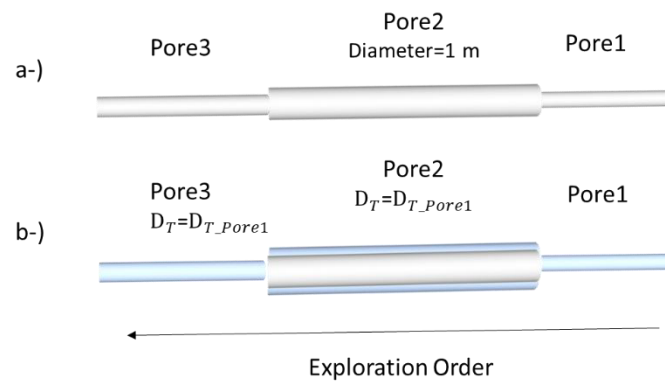


Figure 81. Scanning curves input change logic. a-) Array of three pores in which the pore 2 has a diameter superior to the critical diameter for the target pressure. b-) Case a with nitrogen condensed in pores 1 and 3.

As mentioned before, the original diameter of all the pores with corrected diameter of 1 will be restored. For these pores, their original diameter will also be assigned as their triggering diameter. This will allow to create the characteristic curve. The use of the true diameter of the pore over the critical value is important to quantify the quantity of adsorbed nitrogen in these pores.

The critical diameter at the target pressure is calculated assuming that the meniscus is described by a cylindrical geometry. If the meniscus of the pore has a geometry different than the one used for the adsorption (ex. cylindrical for the adsorption and spherical for desorption), a discrimination needs to be made for pores with a diameter higher the critical diameter (modified diameter for the triggering diameter algorithm). In the criteria described in Equation 27,  $D_{eq}$  must be calculated using Equation 25 for a cylindrical meniscus. For the pore in which nitrogen condensed,  $D_{eq}$  must be calculated using Equation 25 for a spherical meniscus. The process is summarized in Figure 82.

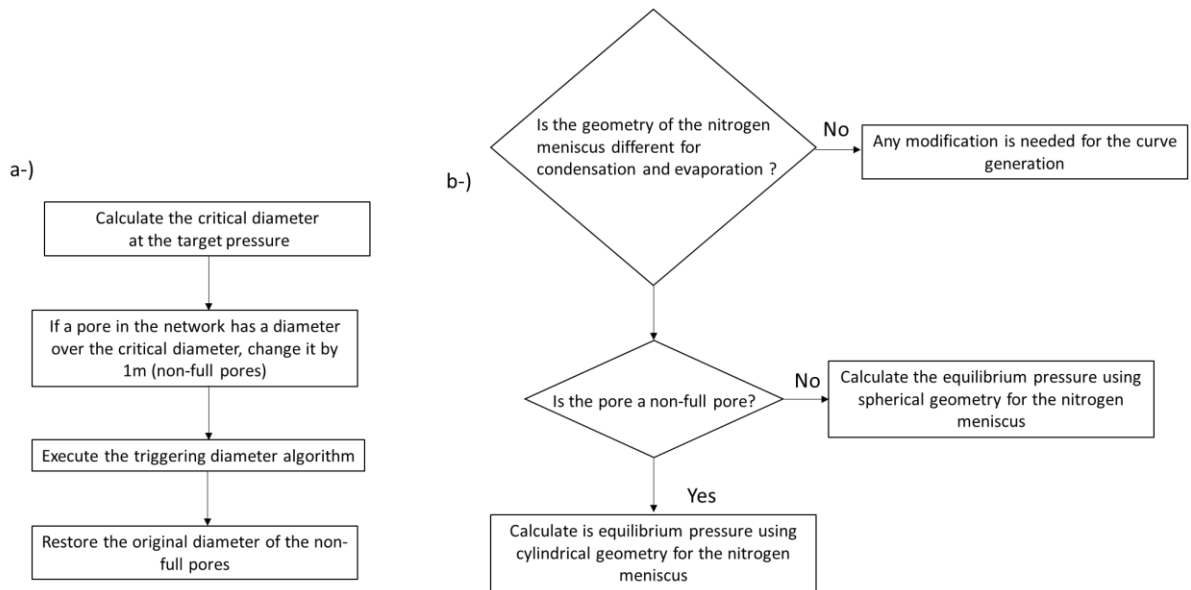


Figure 82. Modification on the nitrogen simulation algorithm for the scanning curves simulation: a-) Modifications for the input of the triggering diameter algorithm. B-) Modification for the characteristic curves.

The use of the spherical cap to describe the meniscus of a pore has for consequence a reduction in the desorption pressure for pore of the same diameter. This means that if this geometry is also used for pores with an equilibrium pressure over the target pressure, the model will quantify evaporation at lower relative pressure.

The procedure is repeated for each scanning curve as described in Figure 83.

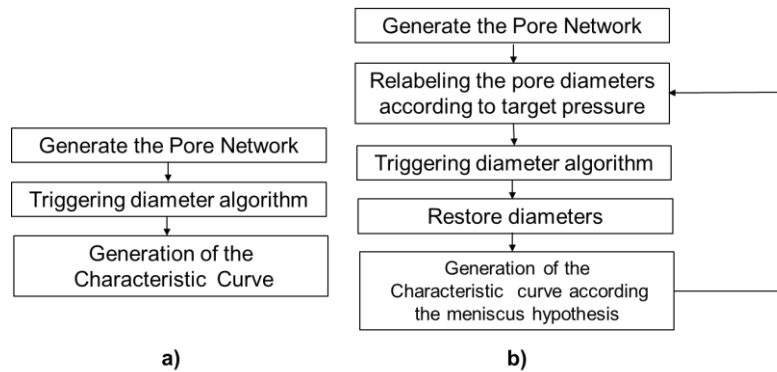


Figure 83. Algorithm's modification for scanning curves: a-) General sequence of the integrated algorithm. b-) Adaptation for the generation of the scanning curves.

#### 4.3.6. Brunauer, Emmett Teller (BET) surface area

The calculation of the BET area follows the methodology described by (Rouquerol et al. 2014b). Initially, all the isotherm points belonging to the relative pressure range between 0

and 0.15 are considered to adjust the BET curve (Equation 30). If the intercept is negative ( $\frac{1}{n_m C} < 0$ ), then the upper limit of the range is reduced. This procedure is repeated until  $\frac{1}{n_m C} > 0$ .

$$\frac{1}{n_a \left( \frac{P}{P_0} - 1 \right)} = \frac{1}{n_m C} + \frac{C - 1}{n_m C} * \left( \frac{P}{P_0} \right)$$

Equation 30. BET model for to calculate the specific surface area of a porous solid.

Once the capacity of the monolayer is obtained ( $n_m$ ), knowing the average cross-sectional area occupied by each molecule of nitrogen ( $\sigma$  [m<sup>2</sup>/molecule]), it is possible to calculate the specific area of the solid (m<sup>2</sup>/g) using Equation 31:

$$S_{BET} = n_m * N_{Avogadro} * \sigma$$

Equation 31. Specific surface area calculation using the monolayer capacity obtained from the BET equation.

#### 4.3.7. BJH Pore Size Distribution

The calculation of the pore size distribution using the method of Barret, Joyner and Halenda (BJH) is computed using the methodology described in detail by Lowell and Shields (Lowell and Shields 1991). The methodology is based on the evaluation of the change of nitrogen volume in liquid state between two relative pressures in the section of the isotherm that is occupied by the hysteresis loop. The total pore volume occupied by the change of liquid nitrogen volume at each pressure step is calculated as:

$$V_{T_{Pstep}} = \left( \frac{\overline{r_{p_{Pstep}}}}{\overline{r_{k_{Pstep}}}} \right)^2 \left[ \Delta V_{liq} - \left( \Delta t \sum_{j=2}^{j=Pstep} S_j \right) \right]$$

Equation 32. Total pore volume occupies by the change of liquid nitrogen volume

All the averages in Equation 32 are calculated using the quantities that corresponds to Pstep and (Pstep-1).  $\Delta V_{liq}$  is the change of nitrogen volume in liquid state.  $\overline{r_{p_{Pstep}}}$  is the average pore radius. For each relative pressure step, the pore radius is calculated as:

$$r_p = r_k + t$$

Equation 33. Pore critical pore radius

$r_k$  is the Kelvin radius calculated using Equation 25.  $\Delta t$  represents the difference in statistical thickness of the adsorbed nitrogen layer. Finally,  $\sum_2^{Pstep} S_j$  represents the

cumulated area of the pore walls quantified up until the pressure steps under consideration. The surface area for each pressure step is calculated as:

$$S_{Pstep} = 2 \frac{V_{TPstep}}{r_{pPstep}}$$

Equation 34. Exposed wall pore surface area at each pressure steps

## 4.4. Mercury Intrusion Porosimetry

### 4.4.1. Mechanical model

Mercury intrusion can be considered as a mechanical process, modelled here by the Laplace-Young equation. Again, there are two important components to model and link: the triggering diameter algorithm, which allows to find the pressure at which mercury intrudes in every pore considering pore blocking, and the mechanical/thermodynamic model represented by Laplace-Young equation (Equation 35), which sets the pressure at which the mercury intrudes in a pore based on purely *mechanical/thermodynamic* considerations.

$$P = \frac{-4 * \sigma_{LV} * \cos \theta}{D_{eq,m}}$$

Equation 35. Laplace-Young equation

To search for the intrusion diameter, the following assumptions made are:

- The Laplace-Young equation is applicable over the complete pore size distribution range.
- The shape of the meniscus is always considered as hemispherical.
- The intrusion angle is constant and air-mercury surface tension are constant.
- The material is not deformable under stress.
- The mercury is not compressible.
- The pores are cylindrical.
- Pore blocking phenomena are present and fully associated with the topology of the pore network.
- The effect of gravity is negligible compared to the capillary forces.

In this case, the simulation will only model the intraparticle intrusion. The system is considered to be in equilibrium at every pressure step.

#### 4.4.2. Triggering diameter assignment adaptation

In this case, the triggering diameter represents the critical diameter at which the intrusion of mercury will take place.

The percolation algorithm for mercury intrusion is identical to the percolation algorithm for nitrogen desorption (section 3.7). The following assignment rules are used:

- i) If the diameter of the pore is smaller than the intrusion triggering diameter of the guide pore, the pore conserves its original diameter as intrusion triggering diameter.
- ii) If the diameter of the pore is bigger than the intrusion triggering diameter of the guide pore, the pore adopts the guide pore's intrusion triggering diameter as its own intrusion triggering diameter.

However, the percolation algorithm for the extrusion is different. The assignment rules change due to two reasons:

- The pores from which the mercury extrudes first are the smallest pores, which means that pores causing pore blocking are now the bigger pores.
- There needs to exist a continuum path of pores filled by mercury connecting a specific pore to the external bulk of mercury to allow the extrusion of this pore.

In this case, the exploration of the network for identifying the trapped zones can be easily done exploring the network from the external pores. The extrusion process can be modelled with a similar algorithm as for the other characterization techniques with slightly modification on the logic.

#### 4.4.3. Mercury volume calculation

The simulation starts with pressure equal to the atmospheric pressure. If the intrusion triggering diameter of the pore is lower than the *equilibrium diameter* ( $D_{eq\_m}$ ) for a given pressure, then mercury does not intrude into the pore and has a null contribution to the total intruded volume at that step. Otherwise, the intrusion process is modeled as if it happens in one single step: the mercury has totally intruded into the pore and contributes to the volume increase with the volume of this pore as given by Equation 36.

$$V_{Hg} = \frac{\pi}{4} * l * D_p^2$$

Equation 36. Total intruded/extruded volume within/from the pore

#### 4.4.4. Characteristic curve generation

Finally, in pseudo-code, the simulation code can be written as follows:

```
Generate Pore Network Model
Find intrusion triggering diameter for each pore
FOR Prelative= 0 to 420MPa
  FOR pore=1, Npores
    Calculate the quantity of mercury intruded using Equation 36
  END FOR
END FOR
Print
```

First, the pore network is generated. Secondly, the intrusion triggering diameter is determined. Thirdly, the relative pressure is varied from 0 to 420 MPa. At each pressure step, the quantity of mercury within each pore is calculated. Finally, the characteristic curve is printed.

### 4.5. Cryoporometry

#### 4.5.1. Thermodynamic Model

To model the liquid-solid equilibrium in the confined media, Strange's simplification based on the Gibbs–Thomson equation is used along with the Liljeblad pre-molten layer data obtained from <sup>2</sup>H-NMR experiments on porous silica imbibed with deuterium (Liljeblad et al. 2016; Strange et al. 1993). The Gibbs-Thomson equation gives the solid-liquid equilibrium temperature as a function of the mean radius of curvature of the solid-liquid interface, the solid phase being in the concave part of the interface. For this simulation, the thicknesses of the pre-molten layer  $t_i$  during freezing and melting are considered to be equal.

$$\Delta T_i = T_i - T^\circ = -\frac{2 * k}{D_{eq\_c}}$$

Equation 37. Strange's simplification of the Gibbs–Thomson equation

$$t_i = -0.452 * Ln(\Delta T_i) + 1.7704$$

Equation 38. Pre-molten layer equation based obtained from Liljeblad experiments ( $t_i$  in angström).

During the freezing step, the porous media is considered to be surrounded by a layer of bulk ice prior to the freezing step according to the experimental operating conditions. The heterogeneous freezing of the liquid within the pore is carried out by propagation of the ice front in the axial direction of the pore and is only hindered by the pore size. The liquid

considered for the simulation is ultrapure water. The homogenous freezing temperature of the water is set to be 233 K (Enniful et al. 2019; Mascotto et al. 2017).

The following assumptions are made for our model:

- The Gibbs-Thompson equation is applicable over the complete pore size distribution range.
- The properties of the confined water are assumed to be the same as those of the bulk water and to be independent of the temperature.
- The properties of the material are considered to be independent of the temperature (no dilatation).
- Pore blocking phenomena are present and fully associated with the topology of the pore network.

#### 4.5.2. Triggering diameter assignment adaptation

The triggering algorithm is applied to the freezing branch. The advancing of the freezing front proceeds as for the desorption process in nitrogen desorption, but instead of considering a desorption triggering diameter, a freezing triggering diameter is considered (section 3.7).

#### 4.5.3. Frozen volume calculation

The simulation starts from the temperature equal to the freezing condition of the liquid in the bulk. If the freezing triggering diameter of the pore is lower than the Gibbs-Thompson equilibrium diameter ( $D_{eq,c}$ ) for a given temperature, then the ice front does not advance through it and has a null contribution on the decrease of the total volume of liquid at that step. Otherwise, the advancing of the frozen front occurs in a single step, and the reduction in volume at liquid state is equal to:

$$V_{H2O} = \frac{\pi}{4} * l * (D_p - t_l)^2$$

Equation 39. Total volume of frozen liquid within the pore

In Equation 39,  $t_l$  represents the thickness of the pre-molten layer. For the melting, the same logic is applied, but the diameter is the actual diameter of the pore, since the melting is not considered to be constrained by pore blocking.

#### 4.5.4. Characteristic curve generation

Finally, in pseudo-code, the simulation code can be written as follows:

```

Generate Pore Network Model
Find freezing triggering intrusion diameter for each pore
FOR T = 273 to 233K
  FOR pore=1,Npores
    Calculate the volume of ice using Equation 39
  END FOR
END FOR
Print

```

First, the pore network is generated. Secondly, the freezing triggering diameter is found. Thirdly, the temperature is varied from 273 K to 233 K. At each temperature step, the frozen volume is calculated. Finally, the characteristic curve is printed.

#### 4.6. Case Study

Two different kinds of pore networks were used for the case study. In the first case, the pores are connected to zero-volume nodes, and only the pores located on the connections between the nodes represent the total pore space; in the second case, the nodes have a volume, and the total pore space is the sum of the volume of all pores and all nodes (Figure 84). Due to the stochastic nature of the network generation process, 30 simulations were performed for every test case to obtain a low standard deviation for the network's average textural properties (Section 3.5). The results are presented as the average of every set. The simulation was carried out on a Dell desktop computer with a 3.5 GHz Intel Xeon E5 CPU and 16GB of RAM.

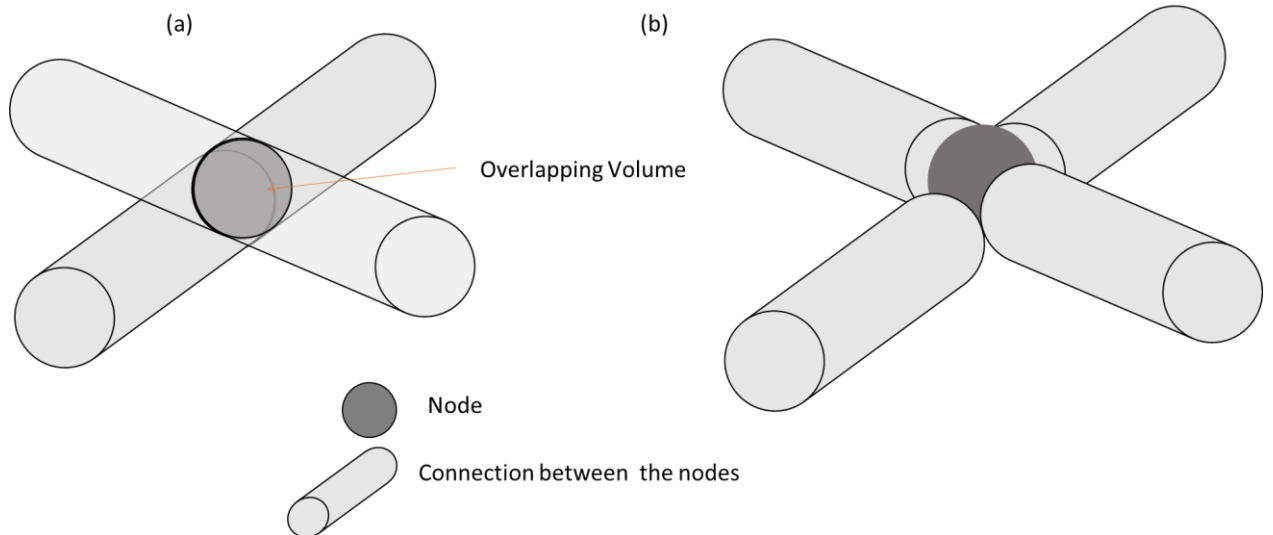


Figure 84. 2D Schematic representation of an elementary system node-pore for a square lattice with PEP equal to 1. (a) The porous space is represented by the cylinders (pores) and the spheres (nodes). (b) The porous space is represented by the cylinders only (pores).

### 4.6.1. Network Parameters

A pore size distribution generated from a Gaussian distribution centered at 10 nm and with a standard deviation equal to 2 nm was employed. To verify the consistency, the output pore size distribution of the generated network was analyzed, and its consistency was proven. The comparison between input and output in terms of the cumulative distribution function is shown in Figure 85.

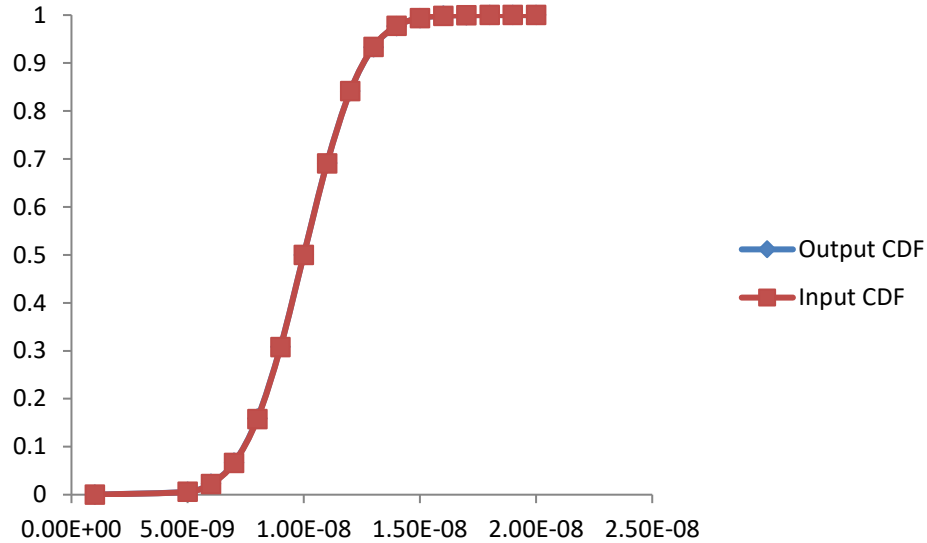


Figure 85. Comparison between the input and output CDF.

### 4.6.2. Execution Time

In order to test how the execution time of the algorithm evolves with the size of the network, six cubic lattice networks of different sizes were generated. The pore existence probability (PEP) was set to 1. The results are shown in Figure 86 and Figure 87 with execution time in function of the total number of pores. As the size of the network increase, the time required for the execution increases as well. The execution times for all three algorithms exhibits approximately the same trend. All algorithm execution times proceeds with an  $O[N \log(N)]$  time. The mercury porosimetry algorithm is slightly faster, not because the min-heap algorithm is faster, but since the breakup consideration makes a list of active pores considerably shorter, a significant number of pores do not need to be explored, thereby considerably reducing the execution time. The time for the network with nodes as porous space is not considered superior to the first case because it treats the nodes as pores. This is equivalent to an increase of about 16% the number of the pore to explore, and hence an increase in execution time.

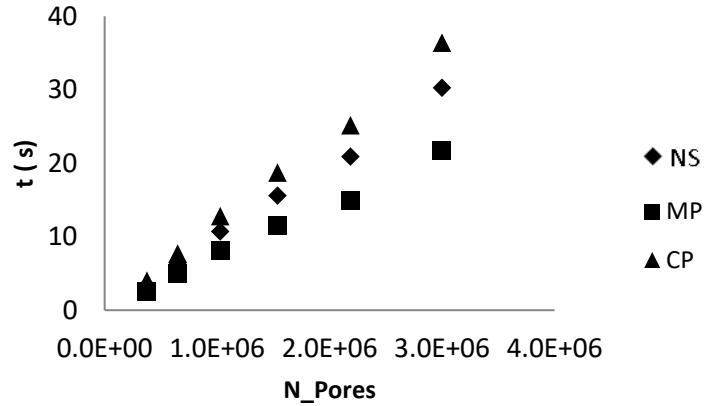


Figure 86. Effect of the network size on the algorithm's execution time for nodes with zero volume.

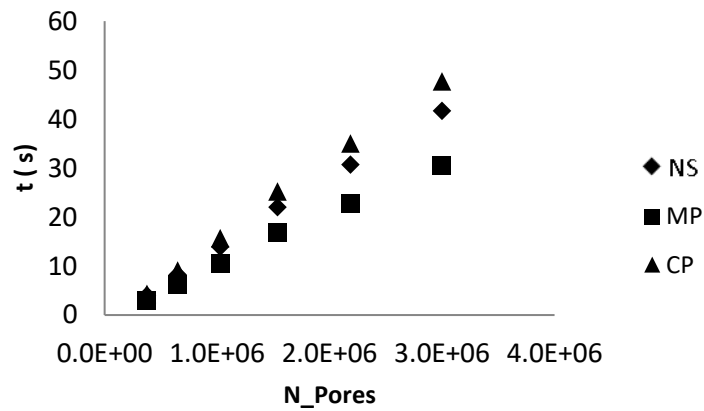


Figure 87. Effect of the network size on the algorithm's execution time for nodes with volume.

### 4.6.3. Connectivity Effect

To test the connectivity effect, six cubic lattice networks were generated. Networks with different average connectivities were generated by changing the pore existence probability, but also the dimension of the network in order to maintain constant (on average) the total number of pores. The number of pores was set to  $3.5E+05$ . The result is shown in Figure 88 and Figure 89 with the execution times as function of the average connectivity. The execution time is not significantly affected by connectivity. It is far from being a relevant factor influencing the execution time at low connectivity.

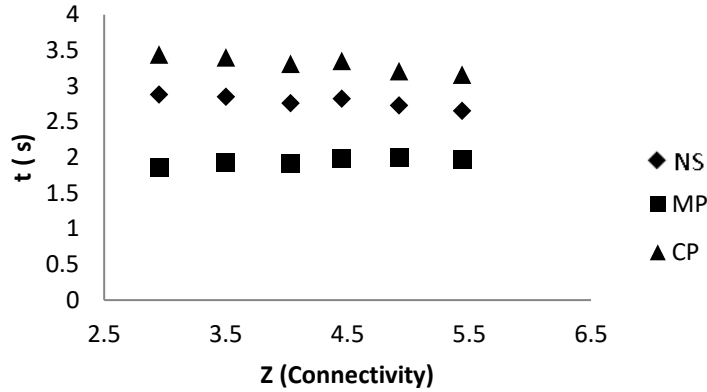


Figure 88. Effect of the connectivity on the algorithm’s execution time for nodes with zero volume.

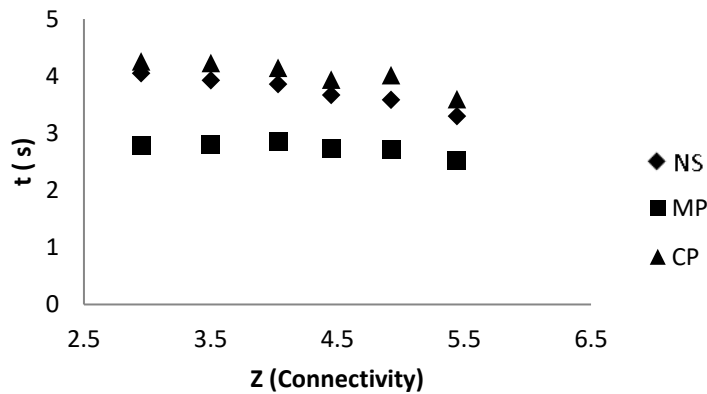


Figure 89. Effect of the connectivity on the algorithm’s execution time for nodes with volume.

#### 4.6.4. Execution time to generate a network with low variability

In section 3.5, we studied the minimum required network size for different pore existence probabilities and lattice patterns in 2D and 3D in order to obtain textural properties with low variability. The execution times of the algorithm for those practical cases was also stored and are shown in Table 14 to Table 17. As expected, the required time is very low and opens the door to more ambitious applications of the digital characterization of pore network models.

Table 14. Execution time for the minimum required size of the network for NS.

Dimensions	2D				3D			
	Zmax=4 (square)	t(s)	Zmax=6 (Triangular)	t(s)	Zmax=6 (Cubic)	t(s)	Zmax=8 (tetrahedral)	t(s)
P=0.5	100x100	0.06	100x100	0.09	20x20x20	0.06	30x30x30	0.33
P=0.7	100x100	0.09	100x100	0.13	20x20x20	0.09	80x80x80	16.76
P=0.9	50x50	0.03	200x200	0.72	40x40x40	1.20	-	-

Table 15. Execution time for the minimum required size of the network for MP.

Dimensions Connectivity/Lattice	2D				3D			
	Zmax=4 (square)	t(s)	Zmax=6 (Triangular)	t(s)	Zmax=6 (Cubic)	t(s)	Zmax=8 (tetrahedral)	t(s)
P=0.5	100x100	0.02	100x100	0.06	20x20x20	0.04	30x30x30	0.25
P=0.7	100x100	0.06	100x100	0.09	20x20x20	0.07	80x80x80	12.13
P=0.9	50x50	0.02	200x200	0.51	40x40x40	0.93	-	

Table 16. Execution time for the minimum required size of the network for CP.

Dimensions Connectivity/Lattice	2D				3D			
	Zmax=4 (square)	t(s)	Zmax=6 (Triangular)	t(s)	Zmax=6 (Cubic)	t(s)	Zmax=8 (tetrahedral)	t(s)
P=0.5	100x100	0.07	100x100	0.10	20x20x20	0.06	30x30x30	0.40
P=0.7	100x100	0.10	100x100	0.15	20x20x20	0.10	80x80x80	19.83
P=0.9	50x50	0.03	200x200	0.85	40x40x40	1.40	-	

In order to make a simple comparison in terms of final execution time using the max-heaps algorithm vs. the common sorting algorithm used by default in FORTRAN, the execution times for the same cases are shown in Table 17.

Table 17. Execution time for the minimum required size of the network for NS by using the Fortran 90 sorting algorithm.

Dimensions Connectivity/Lattice	2D				3D			
	Zmax=4 (square)	t(s)	Zmax=6 (Triangular)	t(s)	Zmax=6 (Cubic)	t(s)	Zmax=8 (tetrahedral)	t(s)
P=0.5	100x100	1.97	100x100	7.37	20x20x20	2.63	30x30x30	64.49
P=0.7	100x100	5.12	100x100	16.56	20x20x20	6.89	80x80x80	19 h 42min
P=0.9	50x50	0.56	200x200	395.24	40x40x40	757.91	-	

#### 4.6.5. Characteristic Curves

For the characterization of the network in this case study, zero-volume nodes have been used, and only the connections between the nodes represent the porous space (Figure 84). The pore size distribution employed to assemble the network is the same used in section 4.6.1.

The characteristic curves of the three characterization techniques are shown in Figure 90 to Figure 92. All simulated curves correspond qualitatively to typically observed experimental curves. The input used for the generation of the network were: cubic geometry-lattice of dimension 50x50x50, PEP equal to 0.75, and pore size distribution generated by using a Gaussian distribution centered at 10 nm and with a standard deviation equal to 2 nm. The average connectivity of the resulting network was equal to 4.20.

The isotherm observed in Figure 90 is the result associated with the parameters given above. There is a hysteresis loop as a consequence of the pore blocking phenomena and

the difference of curvature of the meniscus between adsorption and desorption considered in the KC equation. The isotherm qualitatively corresponds to a type IV isotherm (according to IUPAC classification) with hysteresis loop closing at about 0.42 (Rouquerol et al. 2014a).

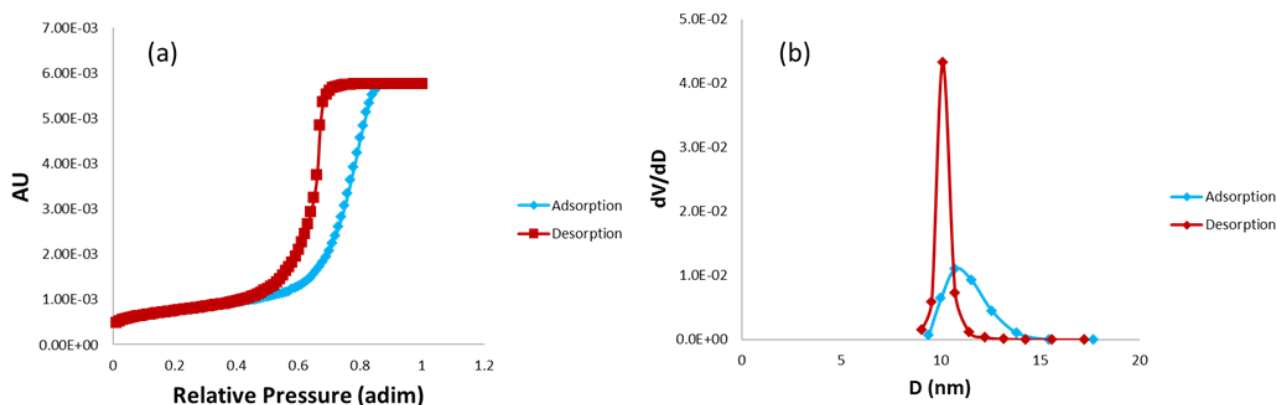


Figure 90. Nitrogen sorption simulation output: a) Numerical Nitrogen Isotherm. b) Calculated BJH Pore Size Distribution (Both branches)

The intrusion/extrusion curves in Figure 91 show similar behavior to experimental curves with a retention volume of about 40 % (Kaufmann 2010). In this characteristic curve intrusion and extrusion, branches are influenced by the pore blocking phenomena.

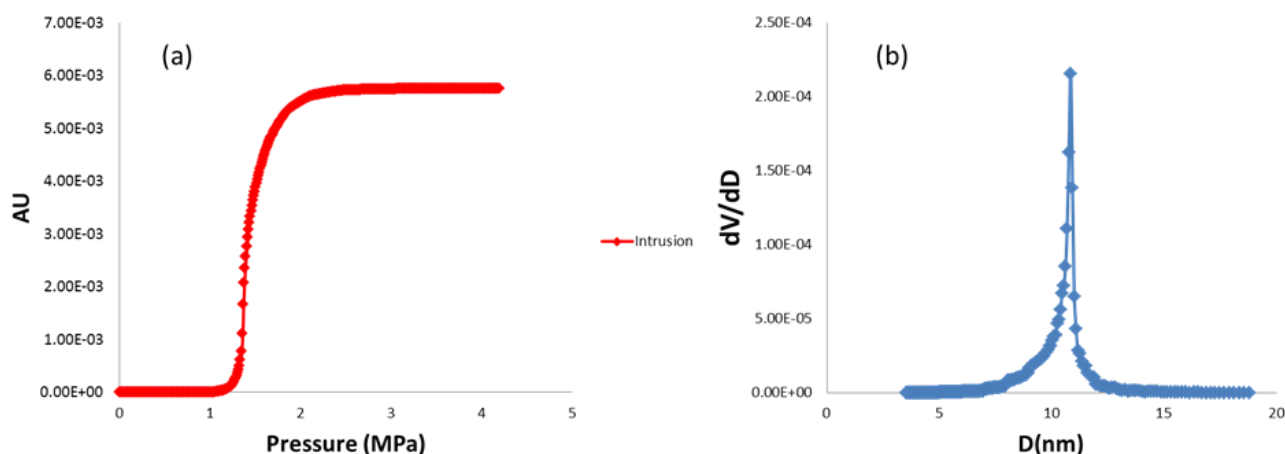


Figure 91. Mercury intrusion simulation output: a) Numerical Intrusion/Extrusion Curve. b) Calculated Pore Size Distribution (Intrusion branch).

Last but not least, the freezing/melting curves in Figure 92 show a classical hysteresis loop, qualitatively similar to experimental curves shown by Hitchcock and coworkers (Hitchcock et al. 2011). The loop closes above 233 K as expected due to the minimum pore size. The freezing branch is affected by the advancing ice front consideration and hence by the

topology of the structure. In all three cases, the starting and closing volumes coincide for both branches.

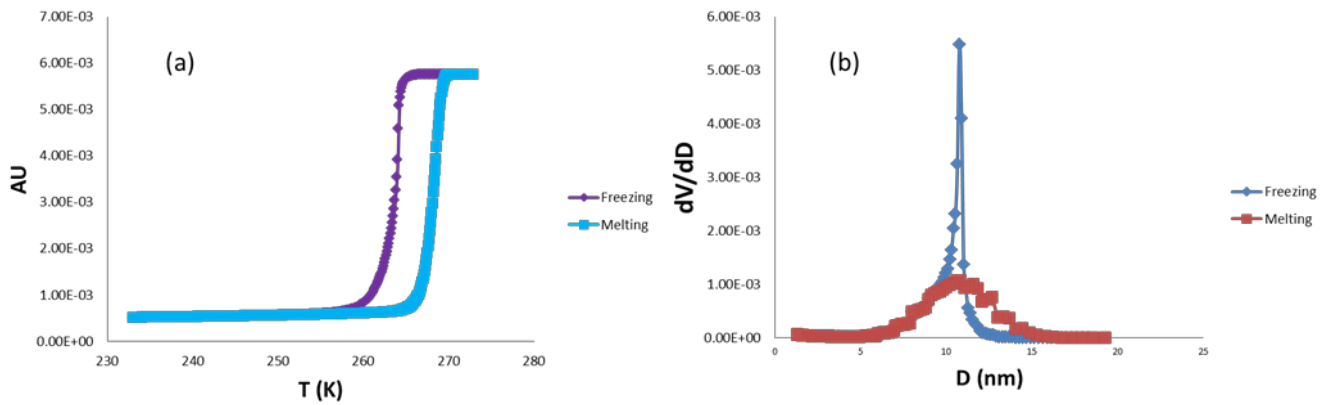


Figure 92. Cryoporometry simulation output: a) Numerical Freezing/Melting Curve. b) Calculated Pore Size Distribution (Both branches)

Figure 90 to Figure 92 also show the pore size distributions back-calculated from the simulated numerical experiments. As can be seen, the back-calculated pore size distribution is very close to the actual one for mercury porosimetry and for the freezing branch of the cryoporometry. Significant differences are found for the back-calculated BJH pore size distribution from the nitrogen adsorption isotherm.

Finally, Figure 93 provides an example of the scanning curves obtained for this sample.

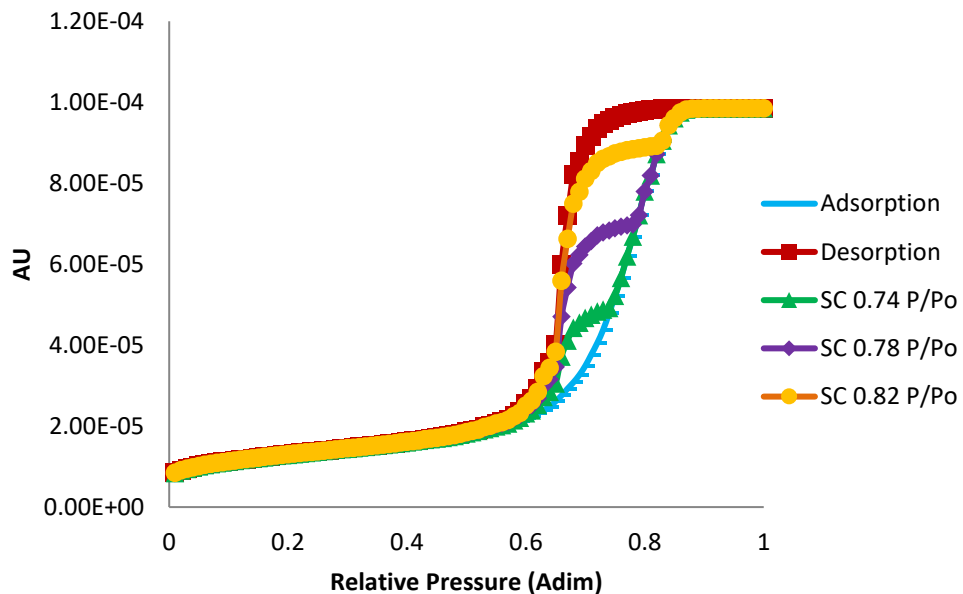


Figure 93. Nitrogen sorption simulation output: Scanning Curves

## 4.7. Conclusions

A fast algorithm for the characterization of a digital pore network was developed and adapted to three different porosimetry techniques. The algorithm can also easily be adapted to other porosimetry characterization techniques such as thermoporometry. Pore blocking phenomena and thermodynamic or mechanical equilibrium were considered to determine a triggering diameter for each pore through the network.

The algorithm was optimized by using a Max-Heap / Min-Heap sorting technique as a tool for handling the search list. A time execution test for the nitrogen sorption algorithm and an octahedral lattice of about 2 million pores required 6.7 seconds using the binary heap algorithm, which is more than 20 times faster than other sorting algorithms. This shows the advantage of using the binary heaps for handling the search list as suggested by Masson (Masson and Pride 2014). The size of the network is the main parameter that affects the execution time and exhibits an  $O[N \log(N)]$  behavior.

The developed algorithms are able to reproduce qualitatively the trends of the typical curves for Nitrogen Sorption (NS), Mercury Intrusion Porosimetry (MIP), and cryoporometry (CP). A future sensitivity analysis will help to better characterize how the different input parameters influence the obtained type of characteristic curve. Adding an optimizer to this algorithm in order to match the digital characteristic curves to those of an actual porous alumina sample will allow obtaining a digital structure that not only exhibits the same macroscopic properties but that could also statistically represent the topology of the material.

## Chapter 5: Parametric sensitivity analysis for the digital characterization techniques

### 5.1. Nitrogen sorption

A nitrogen isotherm possesses several characteristic indicators that allow getting qualitative information about the textural properties of the solids and their topology. In Figure 94, an experimentally obtained isotherm of an actual alumina sample is shown, and the indicators are numbered from 1 to 6. These characteristic indicators are:

- **1) BET adsorption/desorption branch Slope.** The slope of the section of the isotherm lies in the  $P/P^0$  range 0-0.15. The magnitude of this slope and the corresponding nitrogen volume are both used to calculate the BET surface area. In this range, the nitrogen is liquefied in the micropores (diameter = 0-2 nm) and the very initial range of mesopores (diameter = 2-50 nm) (See Table 18). However, the nitrogen volume measured in this range includes also the nitrogen adsorbed in bigger pores quantified by the statistical thickness equation (Equation 26). The pores that contribute with the highest fraction of the total surface area are not necessarily the micropores of the solid structure, but the pores that exist in greatest abundance. In the pore network model, this indicator depends on the pore volume distribution and the density of the pores. The density of the pores depends on the pore existence probability (PEP), the lattice used, and the pore length.
- **2) Loop lower closure.** It indicates the end of the pore blocking effect. This provides information about the smallest pore size that is causing the liquid nitrogen retention. In some works, cavitation is reported under  $P/P^0 = 0.4$ , meaning that if there is nitrogen retention due to the pore size distribution, the liquid nitrogen in a metastable state does not need to be in contact with the external area to evaporate.
- **3) Vaporization/liquefaction branch slope change.** The slopes that can be individuated in the desorption branch are indicators of the kind of pore size distribution that constitutes the solid structure. In the case of the isotherm shown in Figure 94, there is a clear slope change. When the BJH method for the calculation of the pore size distribution is applied to the vaporization branch, a bimodal pore size distribution is obtained.
- **4) Nitrogen retention pressure range during vaporization.** This indicates the average diameter of the pores initially blocked. This retention can be also due to the change in the curvature radius of the nitrogen meniscus before evaporation. When a spherical meniscus arises in the pore, the consideration of this spherical meniscus in the Kelvin-Cohan equation reduces by half the equilibrium evaporation pressure

for a pore relative to its liquefaction pressure. This means that even if the topology and the percolation map would not have caused the liquid nitrogen retention, the nitrogen still would be retained.

- **5) Total nitrogen volume within the sample.** This represents the specific total volume present within the porous solid, it is then equivalent to the specific void volume of the structure. The void volume is mainly supplied by the pores of higher diameters.
- **6) Retained volume fraction.** It is calculated between the liquid volume at maximum relative pressure and the loop lower closure. This considers the volume fraction of the hysteresis loop. It is an indicator of the influence of the pore blocking effect.

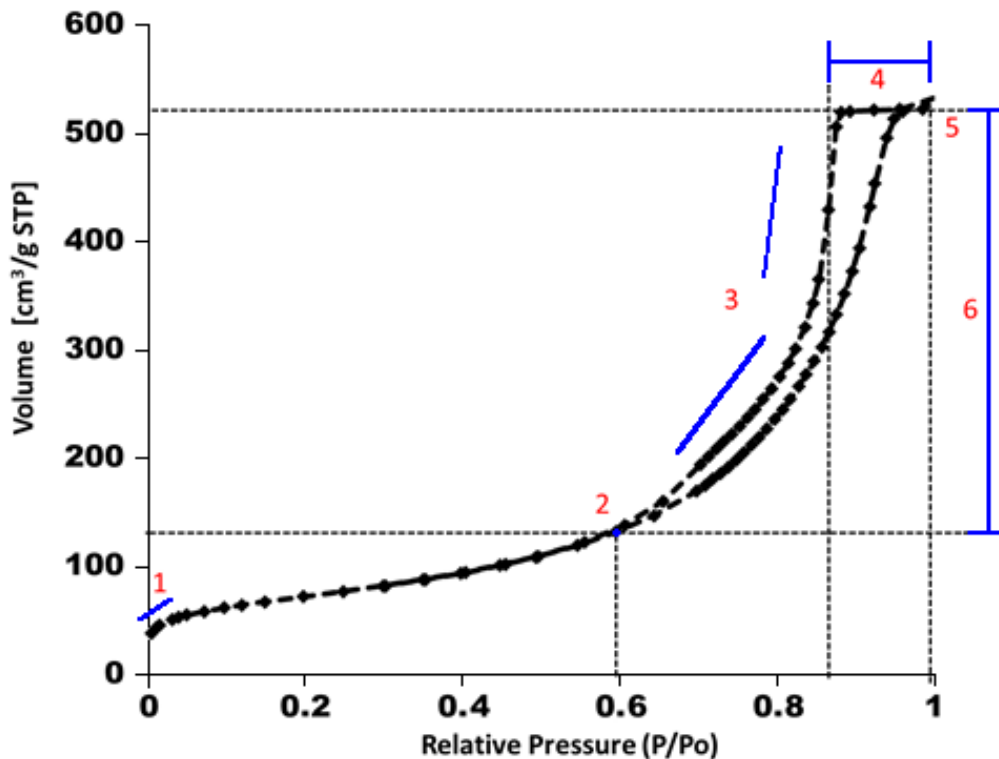
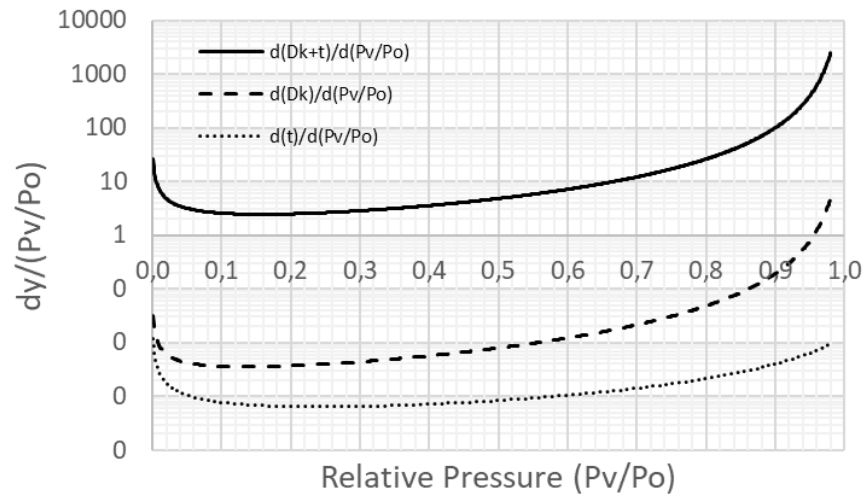


Figure 94. Major indicators on a nitrogen isotherm: 1-) BET Slope, 2-) Loop lower closure, 3) Desorption/ Adsorption slopes change, 4) Initial nitrogen retention, 5) Total adsorbed volume, 6) Retained volume fraction.

The sensitivity of the equilibrium diameter to the pressure in the Kelvin equation can be analyzed using derivatives. In Figure 95, the derivative of the diameter as a function of the pressure is represented. Also, the derivative of the Kelvin diameter (without the thickness of the adsorbed layer), and the derivative of the thickness of the adsorbed layer are presented for comparison. The sensitivity to the pressure change decreases until the  $P/P_0$  0.15, which is the BET maximum pressure. This relative pressure value corresponds to a pore diameter equal to 1.8 nm.

a-)



b-)

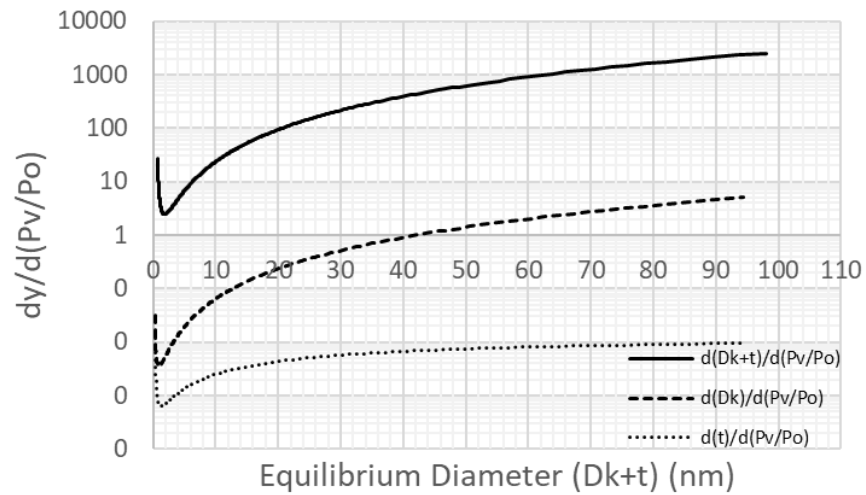


Figure 95. Analysis of the Kelvin equation and the Harkin Jura statistical thickness

It is not difficult to calculate the evolution of volume fractions in the pore that correspond to the volume adsorbed in the layer ( $f_a$ ) and to the volume of the core ( $f_c$ ), i.e. added by liquefaction. The fractions in Equation 40 are calculated for the full range of relative pressure. The results are presented in Figure 96.

$$f_a = \frac{t}{D_k + t}$$

$$f_c = \frac{D_k}{D_k + t}$$

Equation 40. Fractions that correspond to the adsorbed volume ( $f_a$ ) and liquified volume ( $f_c$ ).

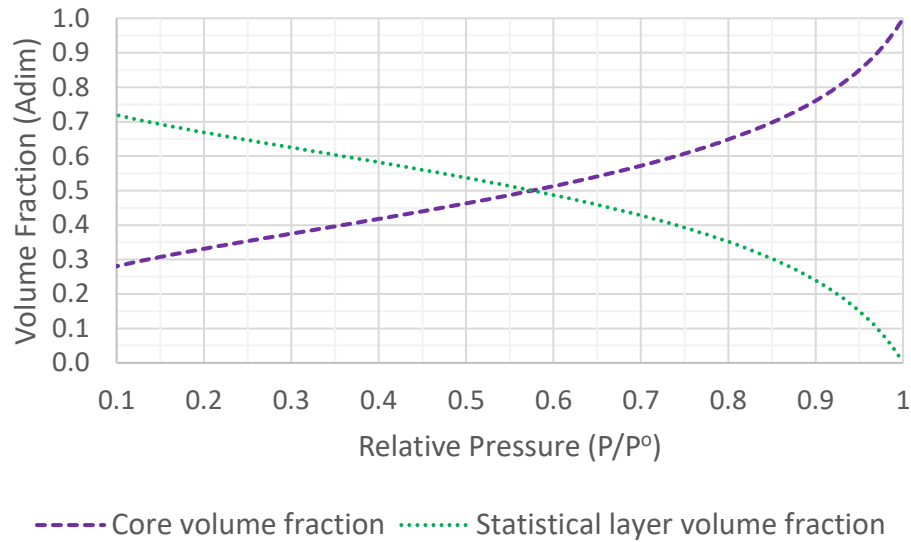


Figure 96. Core and adsorbed layer volume fraction as a function of the relative pressure using the Kelvin-Cohan for a cylindrical pore.

The adsorbed layer volume contribution is the highest until  $P/P^0 = 0.57$ , which corresponds to an equilibrium diameter equal to 4.8 nm.

After the BET zone in Figure 95, the sensitivity of the equilibrium diameter to change in the relative pressure grows at an increasing rate that eventually becomes exponential after  $P/P^0=0.91$  (See also Table 11).

Table 18. Kelvin equation relevant ranges

<b>BET Relative pressure range (0-0.15 <math>P/P^0</math>)</b>			
$P/P^0$	t (nm)	$r_k$ (nm)	$D_k+2t$ (nm)
0.15	0.40	0.50	1.80
<b>High sensitivity to relative pressure (&gt;0.91 <math>P/P^0</math>)</b>			
$P/P^0$	t (nm)	$r_k$ (nm)	$D_k+2t$ (nm)
0.91	1.32	9.05	20.74
<b>Mesopores relative pressure (0.19-0.96 <math>P/P^0</math>)</b>			
$P/P^0$	t (nm)	$r_k$ (nm)	$D_k+2t$ (nm)
0.96	1.64	23.35	50.00

For the network tested here, the default generation parameters are  $PEP=0.75$ ,  $PSD=10 \pm 2$  nm, and pore length=20 nm.

### 5.1.1. Effect of the connectivity

As seen in section 3.8.1, an increase in the connectivity of the network decreases the fraction of pores influenced by the percolation phenomena. Figure 97 shows the

comparison between the sorption isotherms simulated for two networks of maximum connectivity equal to 4 and 6 respectively. As a matter of fact, the use of higher connectivity implies that a higher number of pores are present in the generated network (in the case of our example 50% more from  $Z_{max}=4$  to  $Z_{max}=6$ ). This is only due to the generation algorithm. To facilitate the comparison, the volumes of both networks are normalized to one.

It can be seen on Figure 97 that a higher connectivity decreases the fraction of pores blocked for vaporization, reducing the nitrogen retention pressure range during vaporization (indicator 4), and decreasing the retained volume fraction (indicator 6). Consequently, the hysteresis loop closes at a higher pressure (indicator 2). The slope of the BET region (indicator 1) does not change. The adsorption branches overlap because there are no changes in the volume and distribution, since a monomodal PSD has been used to generate the network. Consequently, for both isotherms, the slope of the vaporization branch throughout the hysteresis loop and after the retention zone is almost constant.

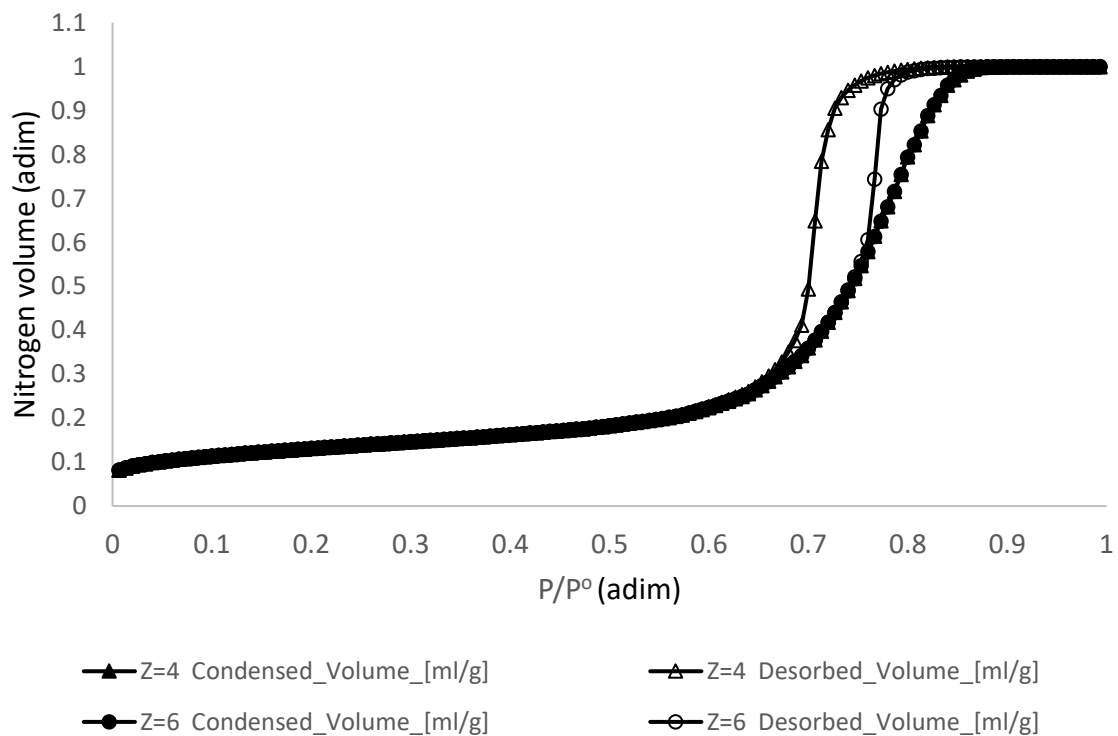


Figure 97. Effect of the connectivity on the nitrogen isotherm.

### 5.1.2. Effect of the pore existence probability (PEP)

Figure 98 presents three isotherms generated with different PEP. The total pore volume of the generated network increases if the PEP increases (indicator 5), the volume distribution being constant. Consequently, the BET slope does not vary (indicator 1) and the adsorption

branches for the normalized volume isotherms overlap. On the contrary, a decrease of the PEP increases the fraction of the pores affected by the percolation phenomena. Hence, a lower PEP causes the recession of the loop lower closure (indicator 2) and increases the initial retention volume (indicator 4).

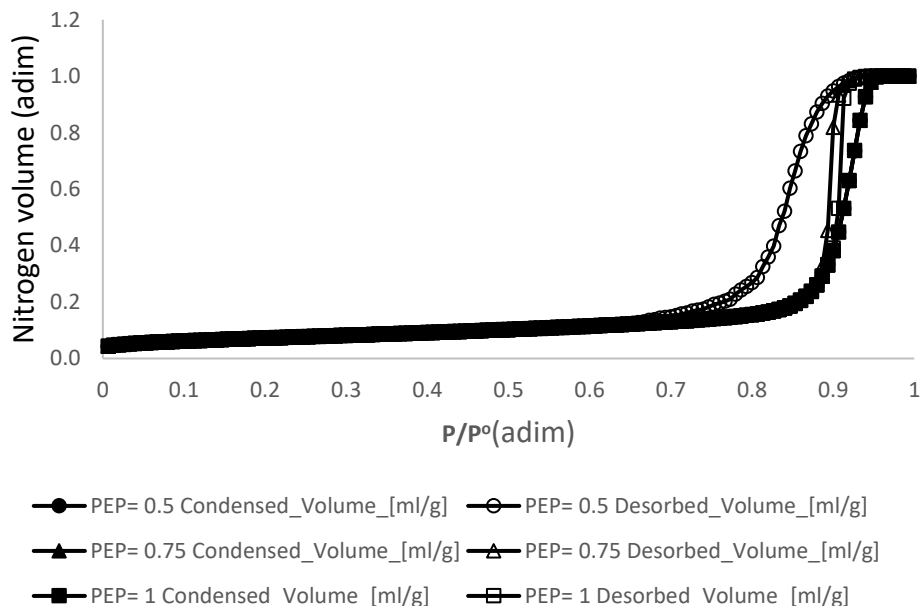


Figure 98. Effect of the pore existence probability on the nitrogen isotherm (PSD=20 ± 2 nm).

### 5.1.3. Effect of the average diameter of the pore size distribution

The simulated isotherms are influenced by the average diameter through the equilibrium relation between the applied pressure and the pore diameter as given by the Kelvin-Cohan equation. As was shown in Figure 95, the equilibrium diameter trend becomes steeper when the relative pressure increases. Three isotherms are compared in Figure 99, obtained by using three pore size distributions having the same variance but different mean values. The retention pressure range during vaporization (indicator 4) decreases when the average diameter size increases. However, the retained volume fraction (indicator 6) is the same for the three cases. The loop lower closure (indicator 2) recedes as the average diameter size become lower due to a thermodynamic effect. Indicator 3 for each vaporization branch remains constant. Looking at indicator 1, the slope of the BET region and the nitrogen adsorbed volume increase as the average diameter size decreases. This is expected due to the higher quantity of smaller pores.

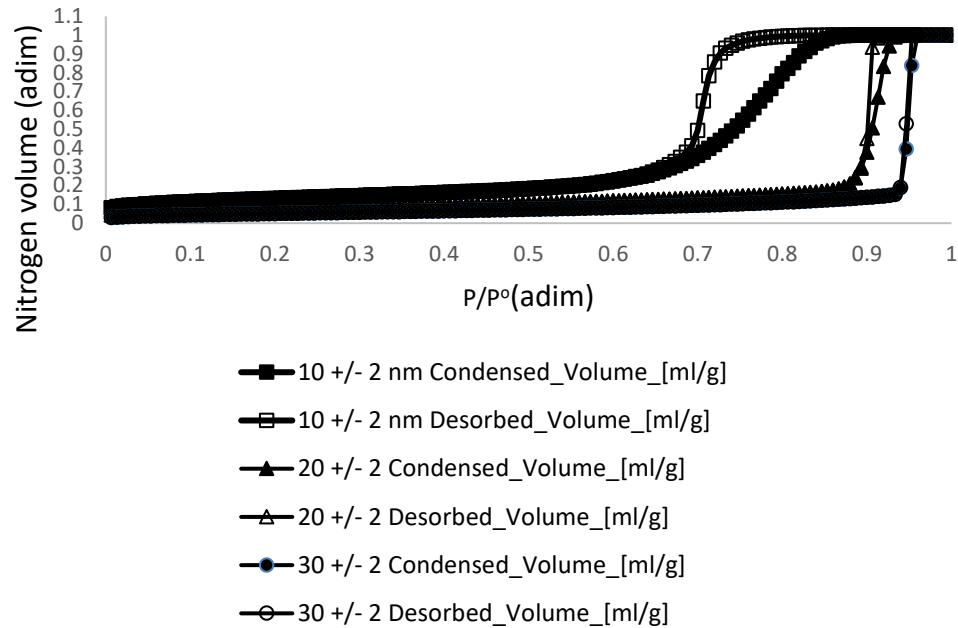


Figure 99. Effect of the average pore diameter on the nitrogen isotherm.

#### 5.1.4. Effect of the width of the pore size distribution

The width of the pore size distribution has a thermodynamic effect on the simulated isotherm and influences the percolation map of the generated network. Regarding indicator 1, a higher gaussian pore size distribution width generates a larger quantity of smaller pores, increasing the slope of the isotherm and the adsorbed volume within the BET region.

Figure 100 represents three isotherms generated with different pore size distribution widths. The existence of long tails increases the fraction of pores influenced by percolation (see section 3.8.3). Therefore, the increase of the pore size distribution width has several consequences: as smaller pores are going to block bigger pores, the loop lower closure recedes (indicator 2), and the nitrogen retention pressure range during vaporization slightly increases (indicator 4) due to the damping effect created by the big pores (right tail of the distribution) from which nitrogen freely evaporates. The total void volume increases (indicator 5) due to the existence of bigger pores. Finally, the retained volume fraction will increase (indicator 6).

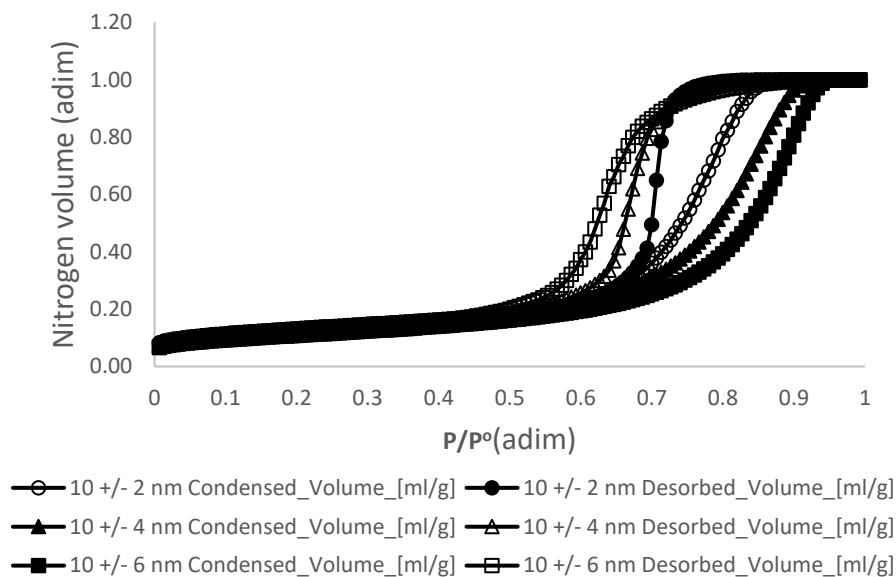


Figure 100. Effect of the pore existence probability variance on the nitrogen isotherm (PSD=10 ± st.dev.).

### 5.1.5. Summary

Table 19 summarizes the effect of different input parameters used to generate the pore network on the sorption isotherm. The connectivity and the pore existence probability are the variables that influence the topological map of the network. These input variables are both related to the fraction of pores affected by the percolation phenomena (see section 3.8.1 and 3.8.2). Both change the relative pressure at which the hysteresis loop lower closes (indicator 2) and the nitrogen retention fraction (indicator 6). However, the connectivity influences also the retention pressure range during vaporization (indicator 4). When any of those 2 input variables are changed, the trend of the nitrogen adsorption does not change. If the resultant isotherms are normalized, the adsorption branches fully overlap. As expected, the adsorption branch is independent of the topology and the network architecture.

The influence of the average diameter of the pore size distribution on indicators 1, 2, 4 and 5 is only due to the liquid-vapor equilibrium thermodynamic model. It is interesting to see that, as they have no effect on the topological and the percolation maps, it cannot influence the retained volume fraction.

The pore size distribution width changes the percolation map, increasing the fraction of the retained nitrogen volume, as expected. Unlike the maximum connectivity and the PEP (which influences the topological map), the width of the pore size distribution can also change the indicator 1 (by increasing the fraction of smaller pores). This causes a variation on the trend for the adsorption.

It can be concluded that the shape of the adsorption branch only depends on the volume distribution. This suggests that the shape of the adsorption branch of a pore network model can be fully fitted by simply adjusting the pore volume distribution. This could lead to affirm that under the present model hypothesis, an adsorption branch has a unique solution for a given pore volume distribution. The pore size distribution and the pore length distribution can therefore be adjusted in consequence.

However, to fit the desorption branch, it is necessary to consider indicators 2, 3, 4, and 6. This means that it is necessary to fit the topological map by changing the lattice (maximum connectivity), the pore existence probability (connectivity distribution), and using multiple pore size distributions (domains) if changes in indicator 3 are observed.

Once the topological map, the percolation map, and the average pore size (for the thermodynamic model) are fixed, then the isotherm can be fitted.

Indicator 3 is not changed by any of the input variables of the table because it depends on the use of more than one pore population, the grid spacing, and the PEP of each population.

Table 19. Effect of the different input variables on the sorption isotherm

Manipulated Variable	Davg (nm)	1	2	3 (desorption)	3 (adsorption)	4	5*	6	Topologic m.	Percolation m.
Max Connectivity	10	none	+	none	none/overlapping	-	+	-	Y	N
	20	none	+	none	none/overlapping	-	+	-	Y	N
	30	none	+	none	none/overlapping	-	+	-	Y	N
PEP	10	none	+	none	none/overlapping	none	+	-	Y	N
	20	none	+	none	none/overlapping	none	+	-	Y	N
	30	none	+	none	none/overlapping	none	+	-	Y	N
PSD Avg	10	-	-	none	non	-	+	none	N	N
	20	-	-	none	non	-	+	none	N	N
	30	-	-	none	non	-	+	none	N	N
PSD Dev	10	+	-	none	non	+	+	+	N	Y
	20	+	-	none	non	+	+	+	N	Y
	30	+	-	none	non	+	+	+	N	Y

\*For a volume non-normalized system.

## 5.2. Mercury porosimetry

A mercury intrusion porosimetry curve contains a few indicators that provide qualitative and quantitative information about the textural properties and the topology of the structure. These indicators are numbered from 1 to 3 in Figure 101. The mercury intrusion curve shown in this figure corresponds to the experimental characterization of an actual alumina sample. These indicators are:

- **1) Macropores range:** Mercury first occupies the inter-particle volume made of the biggest pores as well as the particles' macropores.

- **2) Main pore population filling region:** Despite a decrease in the sensitivity of the pressure to the pore size, the intrusion curve becomes steeper. When changes in slope in this steep region are observed, it is possible to infer about the existence of different pore populations or also pore blocking.
- **3) Total intruded volume:** It simply represents the pore volume of the sample accessible to mercury.

It is important to remember that digital mercury porosimetry simulation does not consider the inter-particle volume.

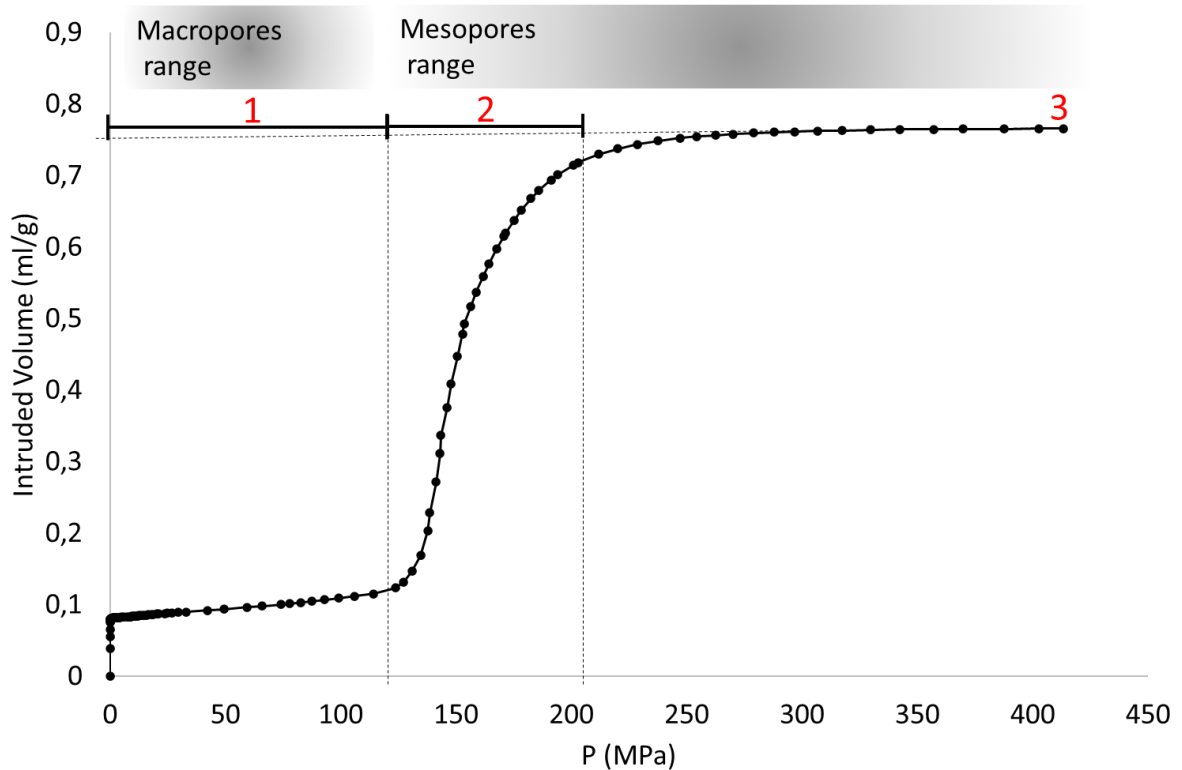


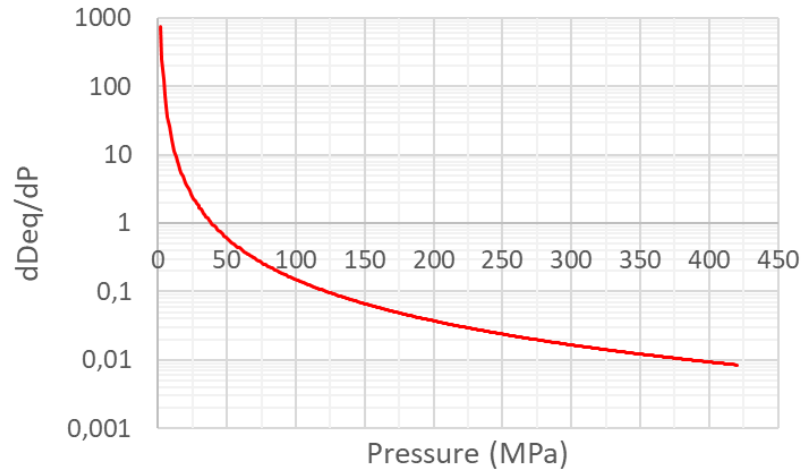
Figure 101. Major indicators on a mercury intrusion curve: 1) Inter-particle volume, 2) Main pore population filling, 3) Total intruded volume.

The sensitivity of the equilibrium diameter to the pressure in the Kelvin equation can be analyzed using derivatives. In Figure 102, the derivative of the intrusion diameter as a function of the pressure is represented. The sensitivity to the pressure change decreases as the intrusion pressure increases.

The region that corresponds to a pressure below 117.6 MPa is the most sensitive to the pressure: this is the range of the macropores. The mesopores region ( $P > 117.6$  MPa) is characterized by a lower sensitivity to the variation of the pressure. This implies that very

high pressures need to be reached to make the mercury intrude in the smallest mesopores (Table 20).

a-)



b-)

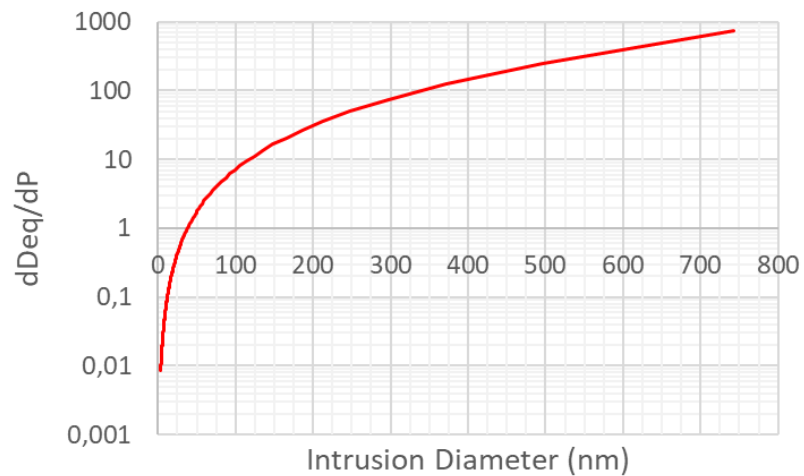


Figure 102. Washburn equation derivative

Table 20. Washburn equation relevant ranges

<b>Pore size intrusion pressure range</b>		
Pore Size	Lower Limit	Upper Limit
Micropores	none	none
Mesopores	117.6 MPa	420 MPa*
Macropores	0	117.6 MPa

\* This upper limit corresponds to a mesopore size of 4 nm

For the network here tested, the default generation parameters are PEP=0.75, PSD=10 ± 2 nm, and pore length=20 nm.

### 5.2.1. Effect of the connectivity

To facilitate the comparison, the volumes of the generated networks compared here are normalized to one. As a matter of fact, a higher connectivity implies that a higher number of pores are present in the generated network (50% higher from  $Z_{\max}=4$  to  $Z_{\max}=6$ ) leading to a higher intruded volume (Indicator 3). An increase in the average connectivity decreases the number of pores affected by the pore blocking effect. One can see in Figure 103 that the mercury intrusion is delayed for the network with the lowest connectivity. This means that the biggest pores are less connected to the external surface in this case. It is also valuable to consider how, for indicator 2 (the mesopore range), the curves are at first parallel. The curve with higher connectivity starts to be saturated first, approximately halfway of the total intruded volume. The reason is that, as the pressure increases, the size of the pores that can be intruded decreases, and thus also the volume that they can contain. However, the curve with the lower connectivity has a higher slope at the same intruded volume range, meaning the mercury is also intruding in the bigger pores that were blocked by the smaller ones. For a given pressure, the difference between the intruded volumes in both normalized curves would provide the blocked pore volume fraction relative to this pressure. However, this is only true if there is no pore blocking for the lowest connectivity.

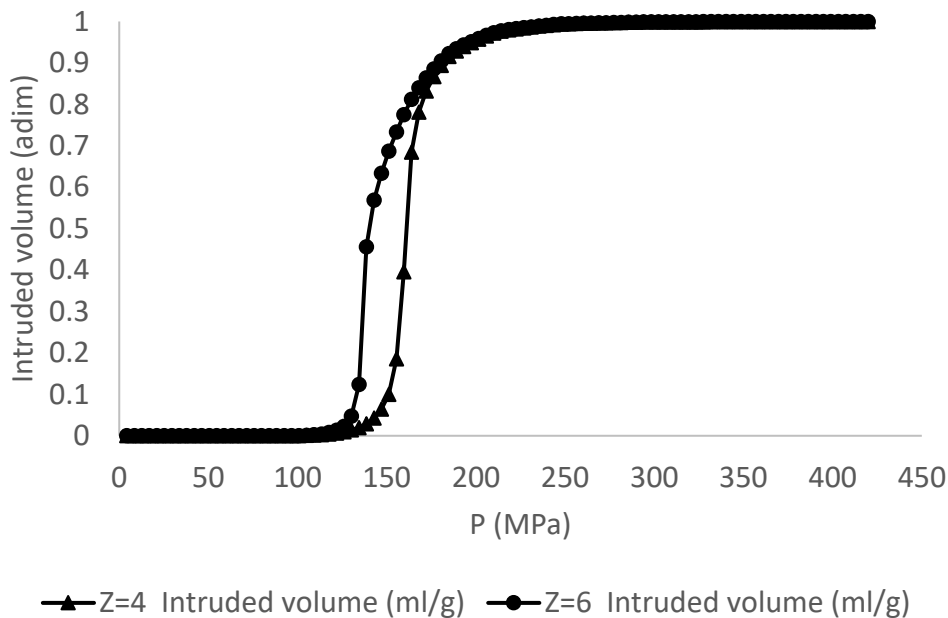


Figure 103. Effect of the connectivity on the mercury intrusion curve.

### 5.2.2. Effect of the pore existence probability (PEP)

In a mercury intrusion curve, when the pore existence probability decreases, the intrusion will start at a higher pressure, as was the case for a lower connectivity (Figure 104). As a

matter of fact, a lower pore existence probability decreases the average connectivity and changes the trend of the pore connectivity distribution (Figure 62). For the cases of a PEP equal to 1 and 0.75, the pore blocking phenomena effect is similar to the one represented in Figure 103. However, for a PEP of 0.5, the intrusion curve of Figure 104 shows a strong pore-blocking effect in which the slope of the intrusion is remarkably lower. In this case, there are multiple regions of blocked pores due to the very low connectivity, which differs from cases where there is a sudden access to one region of large pores. For a pore network with a triangular lattice and maximum connectivity of 6, the use of a PEP=0.5 produces average connectivity of about 3 (Figure 62).

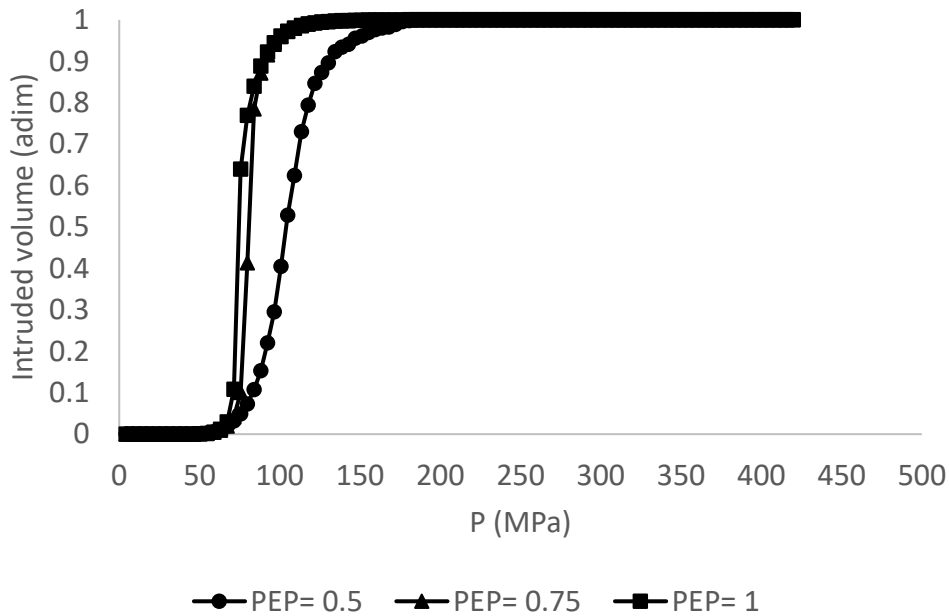


Figure 104. Effect of the pore existence probability on the mercury intrusion curve.

### 5.2.3. Effect of the average diameter of the pore size distribution

When different average diameters are used, it is possible to study the influence of the equilibrium mechanical model on the simulated intrusion process. As the average pore diameter increases, the intrusion process begins at a lower pressure and exhibits a steeper slope (Figure 105). As explained at the beginning of section 5.2, at higher pressure the sensitivity of the mechanical equilibrium model decreases (Figure 102).

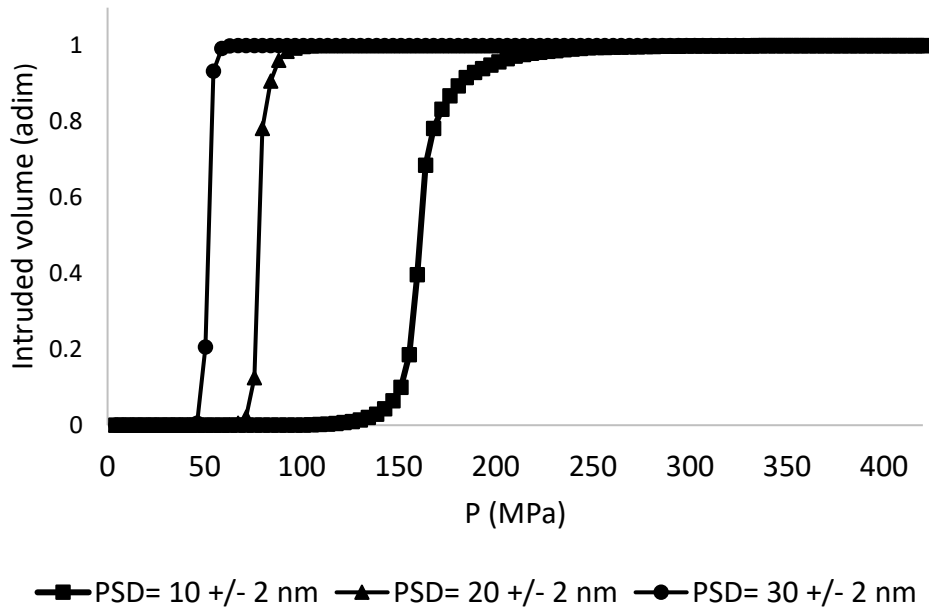


Figure 105. Effect of the average pore diameter on the mercury intrusion curve.

#### 5.2.4. Effect of the width of the pore size distribution

A broad pore size distribution increases the fraction of pores affected by pore blocking. A decrease in the width of the pore size distribution leads to a steeper intrusion occurring at a slightly lower pressure (Figure 106).

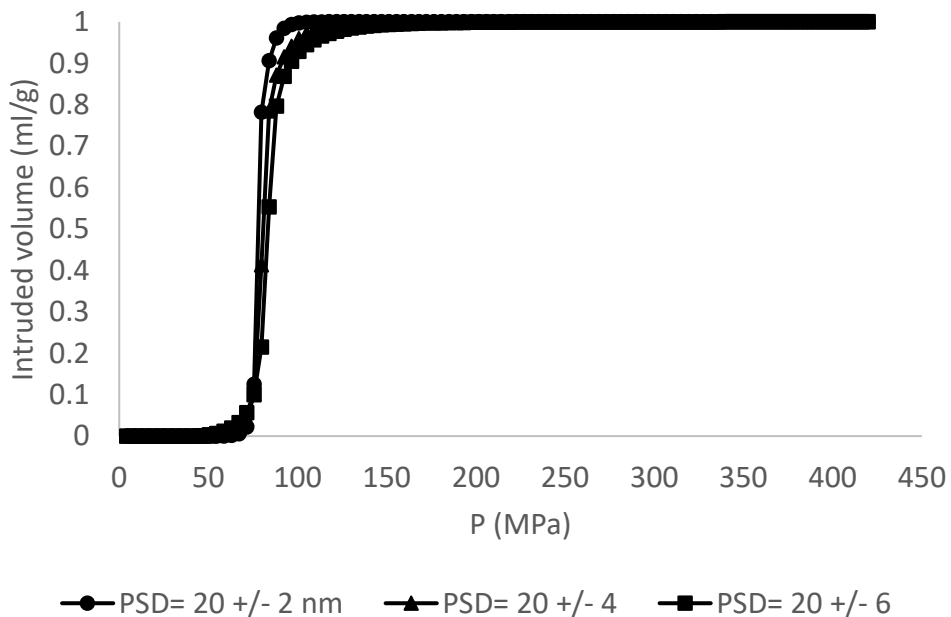


Figure 106. Effect of the width of the pore size distribution on the mercury intrusion curve

### 5.3. NMR Cryoporometry

The NMR cryoporometry characteristic curve contains different indicators that provide qualitative and quantitative information about the textural properties and topology of the porous structure. These indicators are illustrated and numbered in Figure 107.

- **1) Freezing/Melting slope change.** The slopes that can be individuated on the freezing branch are an indicator of the kind of pore size distributions that constitute the solid structure.
- **2) Total liquid volume.** This represents the specific total liquid volume that fills the porous solid. It is equivalent to the specific void volume of the structure. The void volume is mainly provided by the pores of higher diameter.
- **3) Initial water retention range.** It indicates the pore diameter of the pores initially blocked. This initial retention can be also due to the differences between the values of the cryoscopic and ebullioscopic constants.

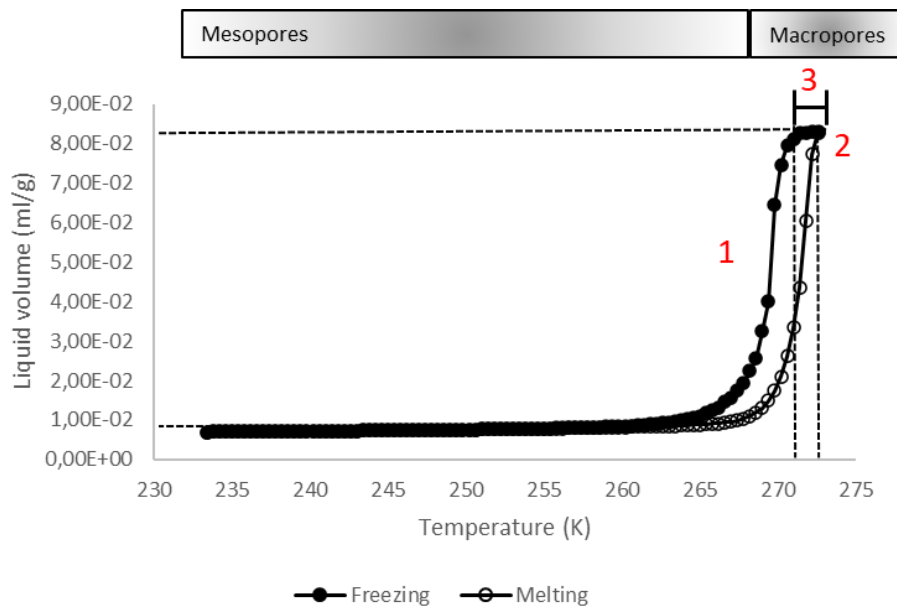


Figure 107. Major indicators on a cryoporometry curve: 1-) Freezing/Melting slope, 2-) Total liquid volume.

In Figure 108, the derivative of the equilibrium diameter as a function of the temperature is represented. Also, the derivative of the equilibrium diameter (without the thickness of the plastic ice layer) and the derivative of the thickness of the plastic ice layer are presented for comparison. The sensitivity to the temperature change decreases as the temperature increases. The macropores range is studied between 273 K and 269 K (see Table 21). The second part of the temperature range encompasses the mesopores (Figure 108b). This technique does not allow the study of the microporosity due to the homogenous freezing temperature (233K for water) (see Table 21). The influence of the plastic ice layer is

negligible for the macropores but becomes important for the mesoporous range. The thickness of this layer never exceeds 2 nm. However, as the equilibrium diameter decreases, the pore volume fraction that it occupies increases considerably. At the minimum pore size, it can surpass 50% of the volume fraction of the pore (Figure 109).

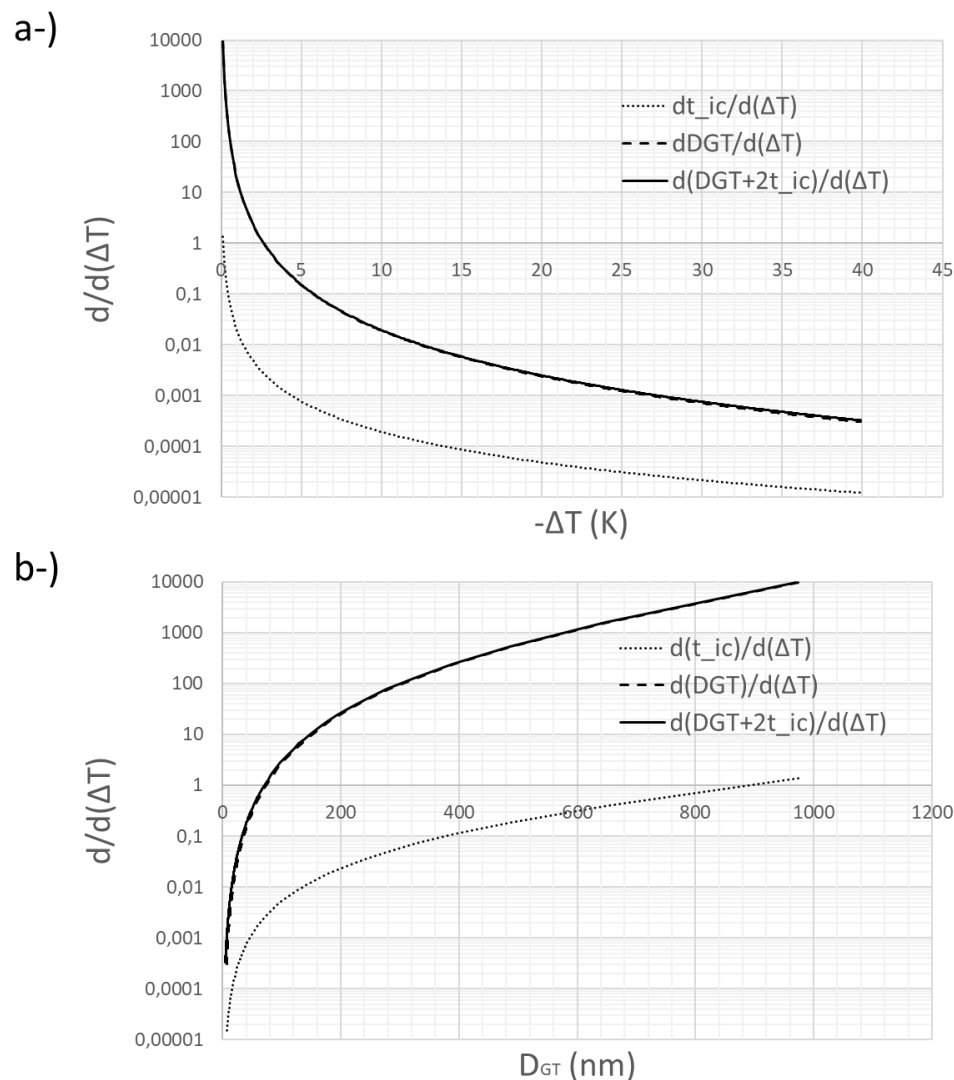


Figure 108. Gibbs-Thompson equation derivative: a-) with respect to temperature, b-) with respect to pore diameter

Table 21. Gibbs-Thompson thermodynamic model relevant ranges

T (K)	Dimensions
273-269	1940 nm - 50nm
269-233	50nm - 4.85nm

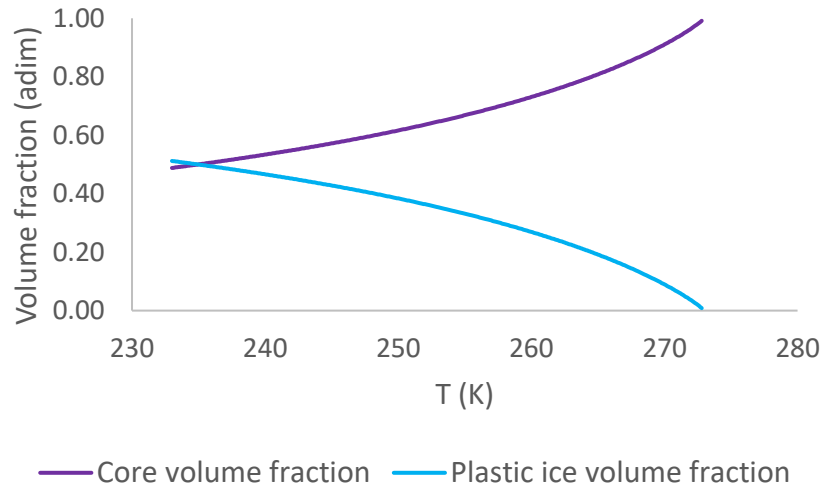


Figure 109. Core and plastic ice layer volume fraction as a function of the temperature calculated using the Gibbs-Thompson thermodynamic model.

### 5.3.1. Effect of the connectivity

Again, the curves compared are volume normalized. The connectivity of the generated network influences the topological and percolation maps, but it does not influence the volume distribution. As a result, despite the use of different lattices, the melting branches overlap in Figure 110. When the connectivity decreases, indicator 2 increases due to a larger influence of the pore blocking effect.

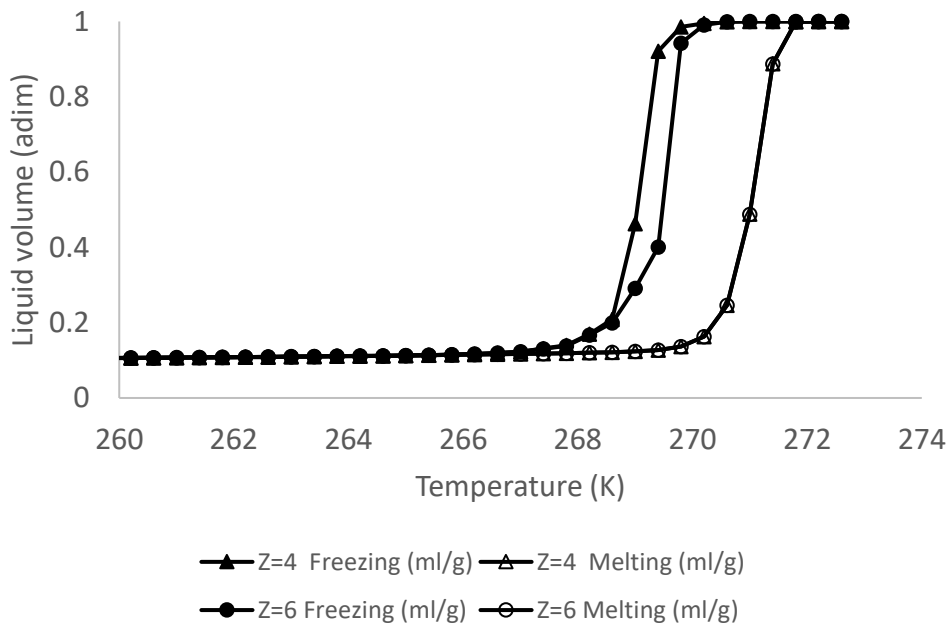


Figure 110. Effect of the connectivity on the cryoporometry curve.

### 5.3.2. Effect of the pore existence probability (PEP)

The pore existence probability influences the percolation and topological map by creating and pore connectivity distribution. It also decreases the total pore volume of the sample. Then, a lower pore existence probability will increase the fraction of pores affected by pore blocking, increasing the value of indicator 2 (Figure 111). The case of the lowest PEP in Figure 111 evidence a strong pore-blocking effect caused by the low average connectivity of the structure ( $Z_{avg}=3$ ).

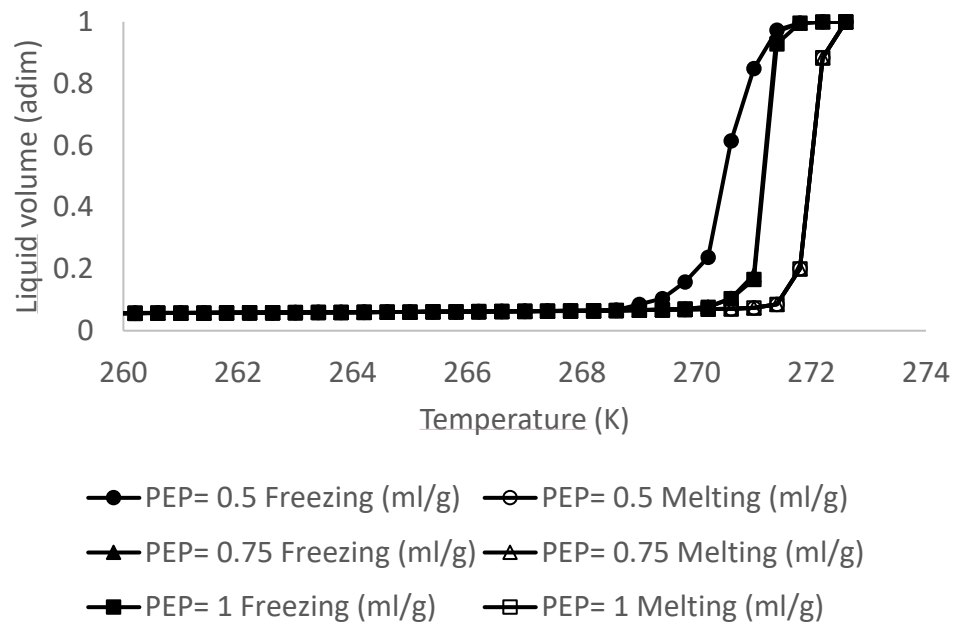


Figure 111. Effect of the pore existence probability on the cryoporometry curve.

### 5.3.3. Effect of the average diameter of the pore size distribution

The study of the average pore diameter allows studying the effect of the thermodynamic model. As for mercury porosimetry, the model is less sensitive to the lower pore sizes. In cryoporometry, low pore sizes are visible at the lower temperatures. Lower pore sizes cause more pronounced hysteresis between the fully frozen and fully melted network state (Figure 112). In Figure 112, it is also possible to observe an increase on indicator 1 for lower average pore diameters. There is also an increase of indicator 2.

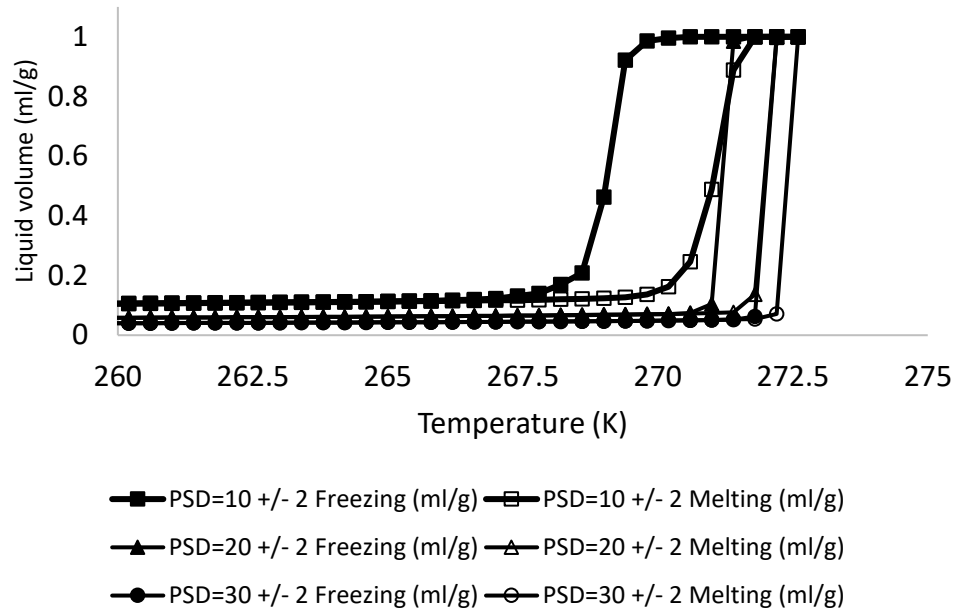


Figure 112. Effect of the average pore diameter on the cryoporometry curve.

#### 5.3.4. Effect of the width of the pore size distribution

The width of the pore size distribution changes the volume distribution, which affects the percolation map. As the width increases, the fraction of pores influenced by the pore blocking increases too. This becomes evident by observing how, in Figure 113, the indicator 3 increases as the pore size distribution variance increase too. The transitions from the total frozen to the total melted state are slower when the variance increases too.

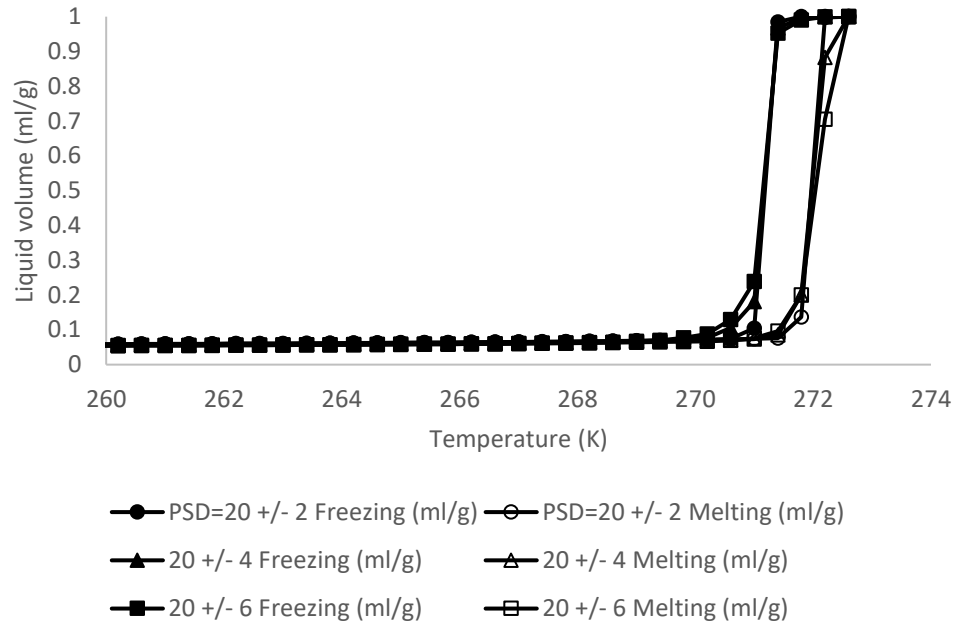


Figure 113. Effect of the width of the pore size distribution on the cryoporometry curve.

## Chapter 6: Porous model validation from porosimetry experiments

A gamma-alumina digital twin is created by means of a hierarchical pore network model. For this digital twin, nitrogen sorption is simulated, and the parameters of the pore network model are modified by means of a Particle Swarm Optimization (PSO) algorithm until both branches of the digital isotherm match those of the experimental isotherm. After parameter identification, the resulting pore network model provides a digital isotherm that is in good agreement with the experimental results. The same set of parameters also allows to predict the experimental nitrogen scanning curves. The BJH pore size distribution obtained from the digital isotherm corresponds well to the experimental one. The generated digital twin can therefore statistically represent the topology of the industrial alumina sample. Diffusion simulations on the final structure allowed to estimate the tortuosity factor of the structure. A relative error of 17 % was found.

In the first section of this chapter, the alumina sample characterization is described. In the second section, the optimized results are represented.

### 6.1. Alumina characterization

Nitrogen sorption isotherms of various gamma-aluminas were measured on the 3Flex instrument (Micromeritics). Prior to analysis, the samples were subjected to a pretreatment at 350°C during 3 hours under secondary vacuum ( $10^{-5}$  mbar). Structural properties, such as porous volume and specific surface area, were evaluated from the nitrogen adsorption isotherm with an uncertainty of 3% and 5%, respectively. For the evaluation of pores size distribution, the BJH model was used. The analysis was repeated several times on each alumina sample for measurement of desorption scanning isotherms. Each scanning curve was measured by allowing adsorption up until a fixed value of relative pressure below 1, followed by complete desorption induced through gradual decrease of pressure.

Helium pycnometry was performed on the AccuPyc 1340 apparatus (Micromeritics) to evaluate the structural density of each alumina ( $\rho_s$ ), which was further used to calculate the total porosity ( $\varepsilon_{N_2}$ ) from the porous volume provided by nitrogen adsorption according to the following expression:

$$\varepsilon_{N_2} = \frac{V_{pore}}{V_{pore} + \frac{1}{\rho_s}}$$

Equation 41. Porosity calculated through helium pycnometry

Diffusion measurements were performed by  $^1\text{H}$  PFG (Pulsed-Field Gradient)-NMR at 305 K on Avance 600MHz spectrometer (Bruker) equipped with a BBI (Double Resonance Broadband Probe) scattering probe of 5mm and a field gradient amplifier capable of producing field gradient pulses up to 50G/cm. A range of organic liquids of varying size and polarity were used for experiments (Table 22), and, for each molecule, the unrestricted molecular and effective self-diffusivity in the support was measured.

Table 22. Molecular size and dipole moment of organic liquids used for diffusion measurements

Organic liquid	Formula	Molecular radius, Å	Dipole moment, D
Acetonitrile	$\text{C}_2\text{H}_3\text{N}$	2.76	3.30
Toluene	$\text{C}_7\text{H}_8$	3.49	0.36
n-Heptane	$\text{C}_7\text{H}_{16}$	3.89	0
Squalane	$\text{C}_{30}\text{H}_{62}$	5.94	0
Perfluorooctane	$\text{C}_8\text{F}_{18}$	4.63	0

For molecular and effective self-diffusion measurement, a 13-interval stimulated echo-pulsed bipolar sequence (PGSTEBP, Bruker) was applied with the following acquisition parameters (Table 23):

Table 23. Acquisition parameters for PFG-NMR experiments

PFG-NMR parameter	Unrestricted molecular diffusion	Effective diffusion in support
Diffusion time $\Delta$ , s		0.140
Gradient pulse duration $\delta$ , s		$6 \cdot 10^{-4}$
Gyromagnetic ratio of $^1\text{H}$ $\gamma_g$ , $\text{rad} \cdot \text{s}^{-1} \cdot \text{G}^{-1}$		$2.67 \cdot 10^4$
Time between two radio-frequency pulses $\tau_e$ , s		$2.61 \cdot 10^{-3}$
Maximum gradient intensity $G$ , G/cm	26	46
Number of gradient steps	10	20

In both cases, measurements were conducted through linear variation of the gradient intensity  $G$  at a constant gradient pulse duration  $\delta$ . For the PGSTEBP sequence, the relation between signal intensity and the self-diffusion coefficient for a molecule  $D_i$  is expressed as:

$$I = \exp \left[ -(\gamma_g \delta G)^2 D_i \left( 4\Delta + 6\tau_e - \frac{2\delta}{3} \right) \right]$$

Equation 42. Model for the signal calculation using a PGSTEBP sequence

where  $D_i$  represents either the molecular  $D_m$  or effective diffusivity  $D_{eff}$ , depending on whether diffusion is measured for unconfined molecules in the bulk or within the porous solid, respectively.

Prior to PFG-NMR experiments on the studied alumina, support extrudates were dried at 120°C for 24 h in order to remove physisorbed water. Directly after pretreatment, the extrudates were soaked in each organic liquid for 10 minutes to ensure full saturation. Before analysis, extrudates were taken out from the liquids and gently rolled over blotting paper to remove excess liquid from the external extrudate surface. All measurements were performed in 5 mm NMR tubes on a single extrudate placed in a 2.5 mm capillary and the analysis was repeated on three extrudates for each studied liquid to verify the repeatability of effective diffusivity measurement.

Based on these measurements, the tortuosity factor  $\tau$  was calculated for each liquid as the ratio of the unrestricted molecular diffusivity to the effective diffusivity in alumina (Equation 23).

## 6.2. Pore network model parameter estimation

For the simulations, the final simulated isotherm is the average of the simulated characterization of 50 different 3D distorted hierarchical pore networks generated with the same input parameters. A randomly distorted cubic lattice was used for the generation of the networks. The selected lattice type fixed the maximum connectivity to 6. The experimental sorption curves were fitted using three porosity levels with three different pore size distributions (PSD 1, PSD 2, and PSD 3). Each pore size distribution has its own grid spacing and pore existence probability (PEP). The length of the pores is defined by the position of the lattice points. A cubic section of one of the pore networks is shown in Figure 114.



Figure 114. Cubic section of one of the full networks

The parameters of the pore network model were identified by using a particle swarm optimization (PSO) algorithm. The resulting pore network model provides a digital characterization isotherm in good agreement with the experimental isotherm (Figure 115). To validate the pore network model, the digital scanning curves were compared to experimental ones. Overall, for the scanning curves also a good agreement was observed (Figure 116). The final parameters for the pore network generation model are listed in Table 24.

Table 24. Estimated parameters for the pore network generation

<b>Fixed network generation parameters</b>				
Lattice Type	Dimensions	Node spacing (m)	Number of porosity levels	Skeletal density of the solid (kg/m <sup>3</sup> )
Cubic	50x50x50	3.00E-08	3	3100
<b>Estimated network generation parameters</b>				
<b>Pore Size Distribution 1</b>				
Beta Distribution $\beta=0.5$ ; $\alpha=2.4$ ; Minimum diameter = 20 nm, Maximum diameter= 60 nm				
PEP = 0.1				
Grid Spacing = 3				
<b>Pore Size Distribution 2</b>				
Beta Distribution $\beta =1$ ; $\alpha =1$ ; Minimum diameter = 1 nm, Maximum diameter= 20 nm				
PEP= 0.95				
Grid Spacing = 2				
<b>Pore Size Distribution 3</b>				
Log-Normal Distribution Average=6 nm; Standard Deviation= 3 nm				
PEP= 1				
Grid Spacing = 1				
<b>* Max number of pores = 375000</b>				

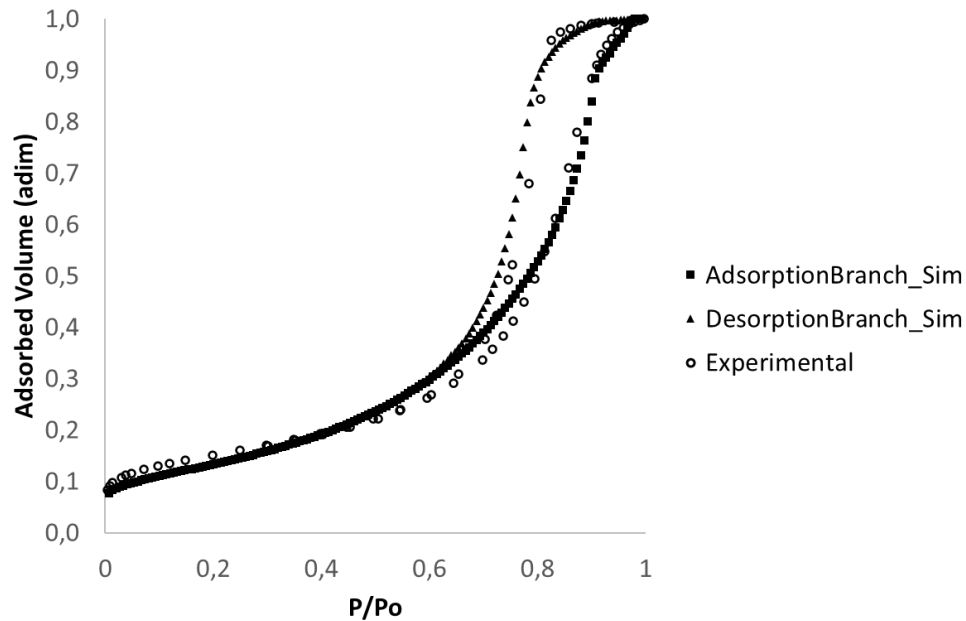


Figure 115. Experimental Isotherm compared to the simulated Isotherm

The adsorption branch is the easiest branch to fit. It allows to set the pore volume distribution of the structure. However, to fit the desorption isotherm and the scanning curves, the topology of the network plays an important role. It is computationally possible to generate pore network models with the same adsorption isotherm but with totally different desorption branches due to a different topology. This allows to infer that this could also be possible experimentally and could explain why solids with similar textural properties can have very different experimental tortuosity values.

Complex pore networks exhibit hysteresis in several classic characterization techniques (Nitrogen Sorption, Mercury Porosimetry, CryoPorometry, and ThermoPorometry). In each of them, the pore network organization has been declared to be partially responsible for this. In the particular case of Nitrogen Sorption, during the desorption stage, there is a retention of nitrogen in a metastable state within some pores. As explained above, the evaporation process is blocked by the nitrogen contained in pores with lower evaporation pressure that stand between the blocked pores and the vapor phase. This pore blocking phenomenon is related to a characteristic size effect and to how these pores are connected to each other. For complex solids as gamma-alumina, the shape of the desorption isotherm is influenced by the topology of the network, and hence it contains implicitly information about its topology. It is preferable to use the word implicitly because to relate the topology of the network to the shape of the isotherm, a model is needed. At this point, it is valid to mention also that if the desorption branch is influenced by the topology, it is then also heavily influenced by the volume distribution into space.

In a single isotherm, there are 5 characteristics that are relevant for its interpretation:

- the slope that corresponds to the BET specific surface area,
- the pressure at which the hysteresis loop closes,
- the desorption branch slope (s) in the hysteresis loop,
- the relative pressure at which the desorption starts,
- the volume of the total specific adsorbed nitrogen volume.

The BET surface area slope represents the monolayer of the nitrogen adsorbed and is mainly determined by the smallest pores. In our digital twin, PSD 3 represents mainly small mesopores with some micropores. Hence, it is this PSD that determines the BET slope. The relative pressure at which the hysteresis loop closes is influenced mainly by PSD 1 and PSD 2. PSD 2 is a uniform pore size distribution that contains pores from 1 to 20 nm. The simulated isotherm loop closes at a relative pressure of about 0.64, just as the experimental curve (Figure 115). The different slopes in the desorption branch can indicate the presence of several pore populations. In fitting this section, all three pore size distributions have an important influence. However, the maximum connectivity, the pore existence probability for each population, and the grid spacing between populations play a very significant role. Indeed, these parameters modify the architecture of the network. They have also an important influence on the relative pressure at which the desorption starts.

The parameters found for our digital twin also allow to correctly predict the scanning curves of the industrial alumina sample (Figure 116). This indicates that the digital twin is a good representation of the pore blocking effects of the network. Applying the BJH analysis to an adsorption branch indicates the most accessible pore size, but an analysis of the scanning curves allows to get information about how the pore populations are hindering each other. The scanning curves therefore provide more information about the internal organization of the network and constitute a very useful tool to computationally study the topology of the structure.

The overall pore size distribution in the pore network model contains less than 3% of pores with a pore diameter below 2 nm, representing less than 0.09 vol% of the total pore network. Figure 117 illustrates the combined input PSD of the pore network model on a volume basis. A BJH analysis was also applied to the simulated isotherm. A good agreement was found between the BJH pore size distribution calculated for the experimental sample and the pore size distribution for pores above 10 nm (Figure 117). For pores smaller than 10 nm, the deviation is more pronounced.

Using diffusion simulations, a tortuosity factor equal to 1.5 was obtained. By employing PFG-NMR on the actual sample, an experimental tortuosity factor of 1.8 was measured. The relative error between the two tortuosity factors is 17 %.

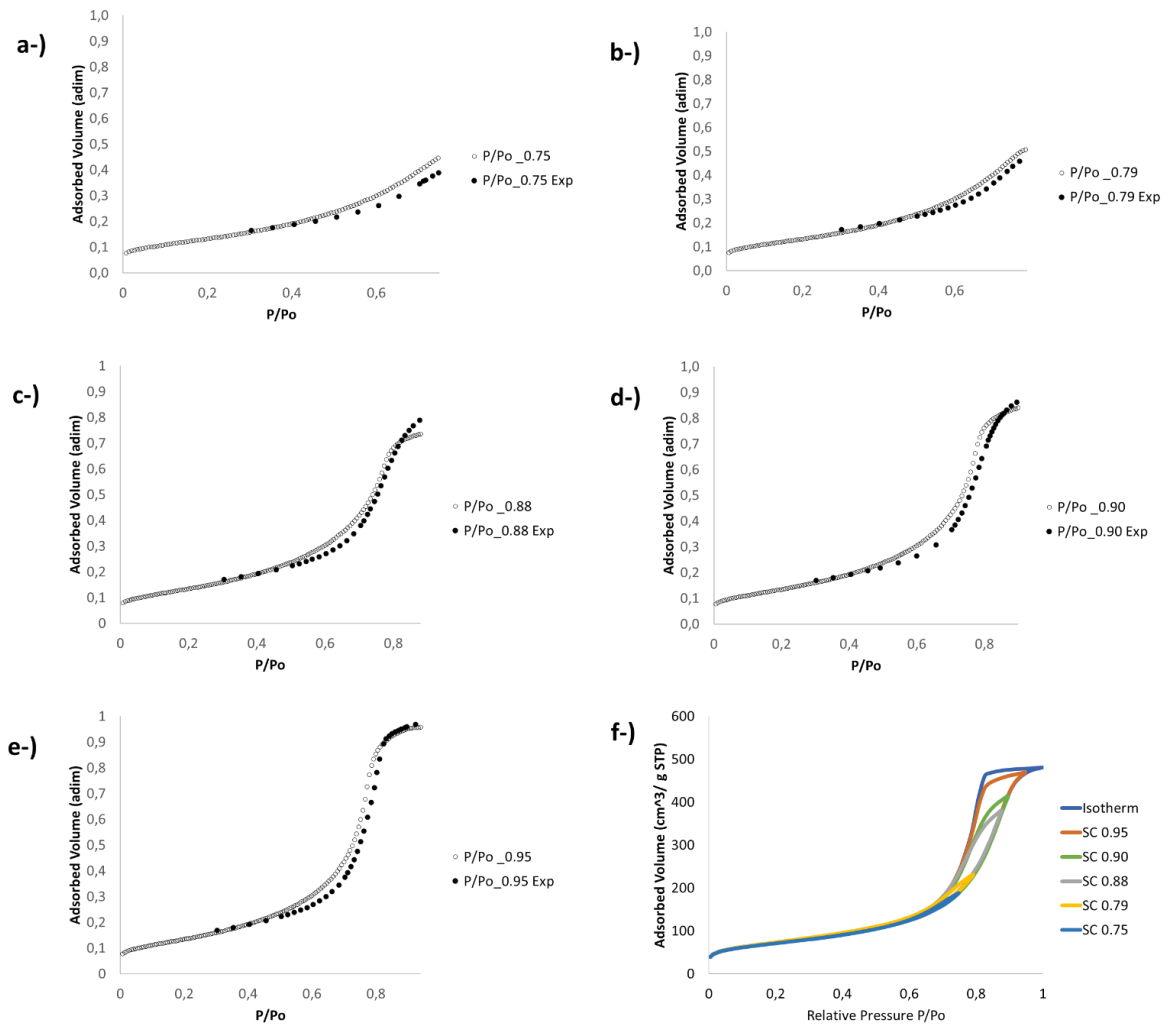


Figure 116. Experimental scanning curves compared to the simulated scanning curves: a-) Relative Pressure 0.75. b-) Relative Pressure 0.79. c-) Relative Pressure 0.88. d-) Relative Pressure 0.90. e-) Relative Pressure 0.95. f-) Experimental Scanning curves over the full experimental isotherm.

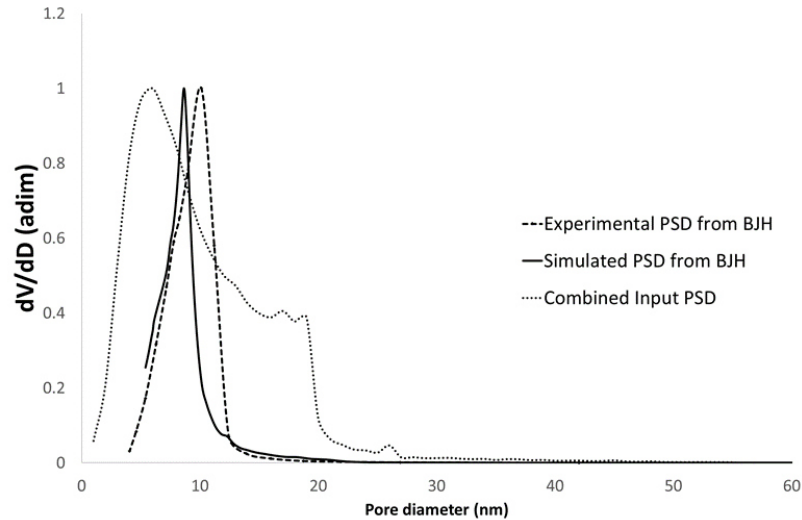


Figure 117. BJH pore size distribution obtained from the desorption branch.

### 6.3. Conclusions

A digital twin of an industrial alumina sample was created by generating a three-level hierarchical pore network model. Through parameter identification, a pore network model was obtained that provides a digital characterization isotherm in good agreement with the experimental isotherm. The same set of parameters allows to correctly predict the nitrogen scanning curves, thereby validating the digital twin. The BJH pore size distribution obtained from the desorption branch of the digital isotherm corresponds well to the experimental BJH pore size distribution for the pores above 10 nm.

For nitrogen sorption porosimetry, the adsorption isotherm mainly provides information on the pore volume distribution of the structure, but it does not allow to get a statistically representative model that reproduces the effects of the topology of the solid. However, the desorption isotherm and the scanning curves are strongly influenced by the topology of the network. It is therefore computationally possible to have various representations with the same adsorption isotherm, but with totally different desorption branches that represent different topologies. This allows us to infer that it should also be experimentally possible and could explain why solids with similar textural properties can have different experimental tortuosity values.

It should be stressed that it is not yet possible to confirm that, from a given isotherm, the attributes of the pore network structure curve can be uniquely identified. Our results point in the direction that a family of topologies can generate the same isotherms. However, the use of the scanning curves in the objective function of the optimizer could help to reduce the number of structures that can generate the same characteristic curves as a given alumina sample, and therefore restricts the possible topologies of the solid.

Using diffusion simulations on the pore network model fitted to the nitrogen sorption curves, a tortuosity factor was calculated that differs by less than 20% from the tortuosity factor measured by PFG-NMR. This illustrates how a digital twin allows to predict the tortuosity factor from readily available nitrogen porosity experiments with a reasonable accuracy.

More information on the industrial alumina sample will of course allow to generate better digital twins. Hence, the simulation tool will be extended to perform the structural optimization with an objective function that not only uses nitrogen porosimetry data, but also scanning curve, mercury porosimetry and NMR-cryoporometry simulations. In future works, further diffusion-reaction simulations could also be used to investigate and better understand the link between the topology of these solids and their tortuosity.

## Chapter 7: Simulation of PFG-NMR experiments

### 7.1. Introduction

PFG-NMR characterization technique is used to estimate the effective diffusion coefficient of porous structures. The objective of this chapter is to create a tool able to characterize pore network models. The comparison of the digital and characterization information could lead to a better understanding of the influence of the pore structure on diffusion phenomena.

Nuclear magnetic resonance (NMR) is a non-invasive technique based on the reorientation of the magnetic moment of nuclei that possess a non-null spin. The spin is reoriented by using radiofrequency applied continuously (continuous wave) or by sending it in the form of pulses (pulse methods) (Farrar and Becker 1971). In the present bibliography, we just consider pulse methods. According to Levitt (Levitt 2008) *“an NMR spectrometer is a device capable of: (i) Magnetizing the nuclear spin with a large applied magnetic field; (ii) Rotating the spin polarizations by radiofrequency pulses to produce transverse nuclear magnetization. (iii) detecting the small oscillating electric currents induced by the processing transverse spin magnetization”*.

One of the most common NMR applications is Nuclear Magnetic Resonance Imaging (MRI). MRI is used to create images of the internal sections of closed structures (e.g., the brain). The main advantage is that NMR uses a non-invasive methodology. NMR applications are not limited to medicine, but it is also employed in chemistry, physics, and engineering. In this research, the main interest lies in the applications to measure mass transfer properties. The NMR branch used to measure effective diffusion coefficients is the Pulsed Field Gradient NMR (PFG-NMR).

### 7.2. NMR Fundamentals

#### 7.2.1. The nuclear spin

The nuclear spin is an intrinsic property of elementary atomic particles such as mass or electric charge. This property has a quantum mechanics description, so it is represented by discrete energy levels defined by the nuclear spin quantum number. For fermions (electron, protons, and neutrons) it has just two possible states  $+1/2$  ( $\uparrow$ ) (the lowest energy level) or  $-1/2$  ( $\downarrow$ ) (the highest energy level). The population of the states follows the Boltzmann distribution (Equation 43).

$$\frac{N \uparrow}{N \downarrow} = e^{-\frac{\Delta E_i}{\kappa T}} = e^{-\frac{h\nu}{\kappa T}}$$

Equation 43. Boltzmann distribution

The spin provides to the particle an intrinsic kinetic and magnetic moment. The nuclei with an odd total number of proton or/and neutron have a total fractional nuclear spin and then exhibit a magnetic moment. By finding the projection of the spin energy levels on a Riemann sphere, it is possible to define the direction of the magnetic moment, obtaining a mechanic representation of the spin properties. It is impossible to know the exact state of an individual spin in a particular instant, however, it is possible to measure the probability of an ensemble of particles to be in a particular state, or according to our interest, pointing towards a direction. This is the origin of the vectorial spin model (Figure 119). Then, in quantum terms, the distribution of spins among the two energy states can be changed by providing energy to the system; in mechanic terms, the application of an external magnetic field can orient a set of the population into a particular direction generating a macroscopic magnetic moment that produces a measurable signal (Levitt 2008).

## 7.2.2. Spin Dynamics

### 7.2.2.1. The initial state

The nuclear magnetic resonance technique takes advantage of the nuclei spin properties. Not all elements have an impaired nuclear spin, but each element has at least one isotope that possesses it. For the basic experiment, the sample is placed into a homogeneous static magnetic field of known intensity  $\mathbf{B}_0$ , which is referentially pointing along the Z-axis in a Cartesian coordinate system Figure 120a. From now on let us visualize the model as the addition of the individual magnetization moments of a sufficiently big number of nuclei with spin  $\frac{1}{2}$  (by example protons as hydrogen nuclei). The total magnetic moment of the sample (generated by a part of the spin's population) precesses about the direction of  $\mathbf{B}_0$ . The precession frequency is called the Larmor frequency. It is dependent on an intrinsic property of the nuclei called the gyromagnetic ratio ( $\gamma$ ) and the magnitude of external magnetic field. The Larmor frequency is represented in Equation 44, where  $|\mathbf{B}_0|$  is intensity of the magnetic field.

$$\omega = \gamma |\mathbf{B}_0|$$

Equation 44. Larmor Equation

The spins that are precessing about Z are in the lowest energy level or  $+1/2$ . The population of spins in this level is slightly higher than the population filling the highest energy level ( $-1/2$ ) (magnetic moment pointing in the opposite direction to  $\mathbf{B}_0$ ). The net magnetic moment is pointing towards +Z and it is called equilibrium magnetization moment ( $\mathbf{M}_0$ ) that

is to say in equilibrium with the magnetic field. The segregation among the energy levels is caused by the presence of the static magnetic field and the phenomenon is called the Zeeman effect. It is important to mention that as a function of the intensity of the magnetic field the energy gap between the two levels increases (Figure 118).

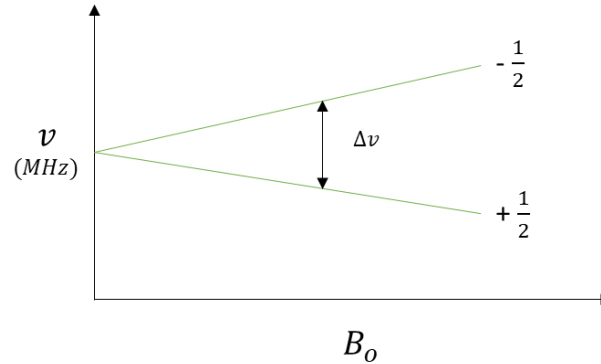


Figure 118. Proton spin energy differences (Joseph P. Hornak 1997)

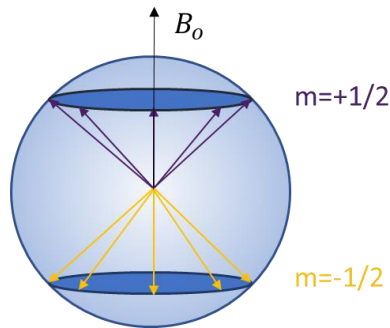


Figure 119. Vectorial representation

The energy separation between these states is small and the energy coming from thermal collisions is sufficient to take nuclei into higher energy spin states (Kaseman et al. 2020). In Equation 45 the segregation is described in terms of the Boltzmann distribution and as a function of the static magnetic field.

$$Polarization = \frac{N \uparrow}{N \uparrow + N \downarrow} = N_{Total} \frac{e^{-\frac{E_i}{\kappa T}}}{\sum_i e^{-\frac{E_i}{\kappa T}}} = \frac{h \gamma |\mathbf{B}_0|}{4 \pi \kappa T}$$

Equation 45. Fractional segregation of the two energy levels

### 7.2.2.2. The Magnetic Pulse and the T1-T2 time constants.

An alternating magnetic field  $\mathbf{B}_1$ , perpendicular to  $\mathbf{B}_0$  and with the same Larmor frequency (to send energy at the same frequency) is pulsed during the experiment according to a

selected sequence. The equivalence between energy and frequency is given by the Einstein equation (Equation 46) in which the frequency can be substituted by the Larmor frequency.

$$E = h w = h \gamma B$$

Equation 46. Relation between frequency and field strength.

A right calibrated pulse with the right intensity will equalize the energy level population. This will cause the vertical component of the total magnetic moment to cancel while the horizontal or transversal one being in the xy-plane will be measurable (Figure 120a and Figure 120b).

The static field is several orders of magnitude larger than the oscillating field. The reason why a weaker field can produce an effect on the spins that are under the effect of  $B_0$  is that  $B_1$  is resonant with the precession frequency of the spin. This means that the effect of  $B_1$  can accumulate during the radiofrequency pulse duration so that the change in the Larmor frequency can be induced after several microseconds (Levitt 2008).

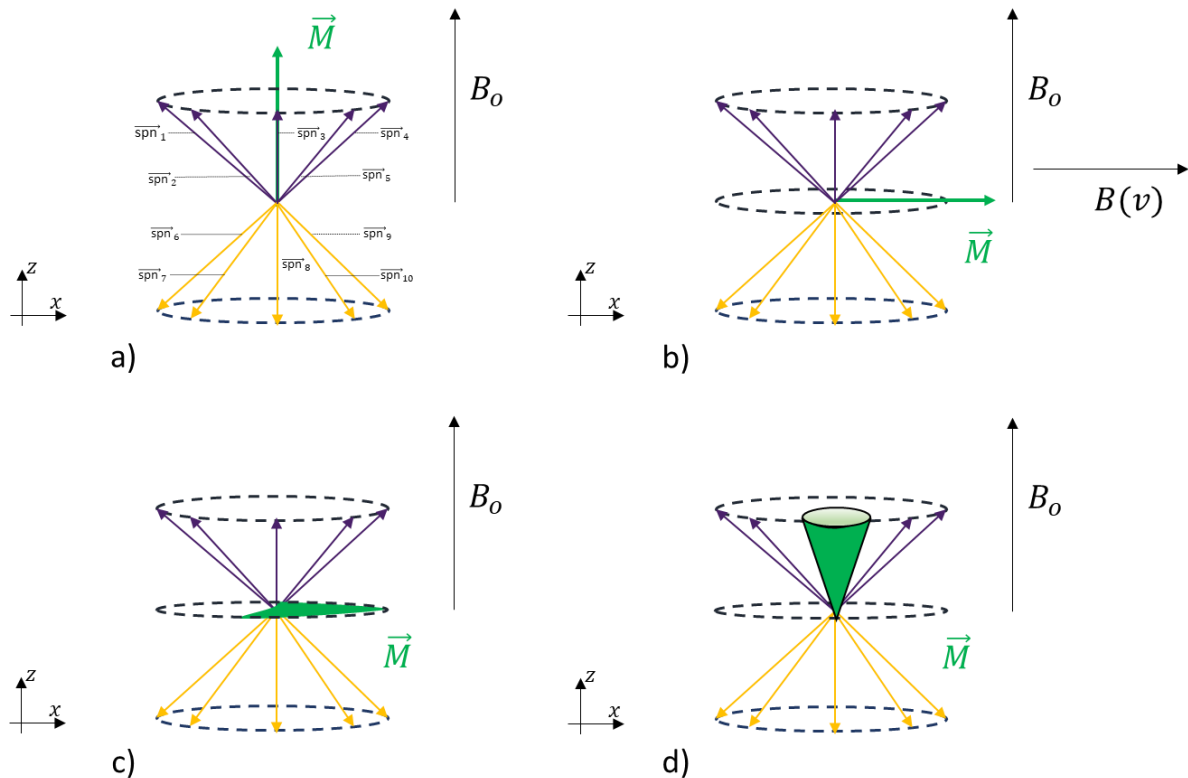


Figure 120. Magnetic moments orientations. a-) Initial state, b-) 90° degrees pulse applied, c-) Dephasing of transversal magnetization, d-) Return to the fundamental state.

It is said that the total magnetic moment has rotated 90°. In the technical jargon means that a radiofrequency pulse intense enough to make rotate the total magnetization vector by 90° has been employed (Figure 120b). After some time, the populations go back to equilibrium with its surroundings and the magnetic moment come back to its original position ( $M_0$ ) (Figure 120a) (Farrar and Becker 1971). This process is called longitudinal relaxation (Figure 120d). The time constant that describes this process is called spin-lattice relaxation time (T1). It is measured as the time that takes the magnetic moment to reach  $\left(\frac{1}{e} * 100\right)\%$  of  $M_0$  and it represents a first order relaxation process. The T1 constant is the first characteristic valuable information of the NMR technique.

To simplify the mathematical treatment of the phenomena, a rotating coordinate system is used. If we think about the trajectory that follows the total magnetization vector from the transversal plane to its original equilibrium position (or vice versa), it is easy to imagine a conical spiral due to the precession of the spins about Z. However, if the three-axis XYZ rotate at the same frequency  $\omega$  than the spins, the total magnetization is seen as stationary (assuming perfect resonance).

A second process occurs while the magnetic moment is still on the transversal plane. Let's think about it as a faster process than the T1 process. As the magnetic moments are polarized in the same direction on the transversal plane (XY), it is said that they are in resonance. This resonance corresponds to the maximum value of the transverse magnetization ( $M_{XY}$ ). As time passes, the spins start to come in equilibrium with each other, which makes them dephase by precessing at different frequencies (still in the XY plane) (Figure 120c). This causes the decay of the  $M_{XY}$  magnitude. The process is called transversal relaxation. The time constant that describes the transversal relaxation process is called spin-spin relaxation time (T2). The spin-spin relaxation phenomena are related to the spins entering equilibrium with each other. The T2 constant is the second valuable characteristic information coming from the NMR technique.

### 7.2.2.3. *Some of the sources of error in the measured signal*

Two phenomena contribute to the decay of transverse magnetization. The first one is molecular interactions (pure T2 molecular effect). The second one is the variations in  $B_0$  (inhomogeneous magnetic field effect) (Joseph P. Hornak 1997). The addition of the two effects led to a corrected T2 defined as  $T_2^*$ .

$$\frac{1}{T_2^*} = \frac{1}{T_2} + \frac{1}{T_{2\_inhomogeneous}}$$

Equation 47 T2 correction

As an interesting fact, Peter Mansfield and Paul Lauterbur won the Nobel Prize in 2003. The inhomogeneity of  $B_0$  causes heterogeneous broadening on the NMR spectra. These two researchers showed in 1972 that if the inhomogeneity was controlled, the shape of the spectra could be related to the shape of the sample and the distribution of spin within it. This opened the door to MRI and diffusion measuring techniques (as PFG-NMR).

The rotation frequency distribution depends on the temperature and viscosity of the solution. Therefore, T1 will vary as a function of temperature (Joseph P. Hornak 1997). The spins are also continuously exchanging between the lower and the higher energy level with no changes in the population distribution. These phenomena do not affect T1 but influence T2 because the phase coherence of transverse magnetization is lost during the exchange (Joseph P. Hornak 1997).

The electrons can create a local magnetic field that is opposite to the homogeneous magnetic field. This local field shields the nucleus and then changes the precession frequency which varies the frequency that needs to be sent with  $B_1$  to excite the system. Therefore, when a spectrum is generated for the identification of multiple compounds, normally a compound of reference is used for normalization.

$$\delta = (\nu - \nu_{\text{REF}}) \times 10^6 / \nu_{\text{REF}}$$

Equation 48 Chemical Shift

#### **7.2.2.4. Basic Pulse Sequence**

A radiofrequency pulse or  $B_1$  has two objectives: (i) To equalize the spin population and (ii) to create coherence meaning to put in phase the spin (to make them point into the same direction in a rotating frame). The value of the transverse component magnetization vector is measured in the direction perpendicular to the homogeneous magnetic field. The obtained signal is called Free Induction Decay (FID). It is related to the dephasing of the spins in the transversal (T2) (Figure 120c) and longitudinal (T1) direction (Figure 120d). To measure the value of the transverse component of the total magnetization vector, a coil perpendicular to the homogenous field is used. The rotating magnetic moment generates a rotating magnetic field, this rotating magnetic field creates an oscillating magnetic current that flows through the wire generating a detectable signal. The device can detect just the transverse magnetization component. The projection of the total magnetization vector on the transversal plane will evolve according to a sinusoidal curve of frequency  $\omega$  and initial amplitude proportional to  $M_0$  (Akoka S. 2002). When the total magnetization vector is in equilibrium with  $B_0$  the detected signal is equal to zero.

A suitable pulse sequence for  $B_1$  will help to improve the signal-to-noise ratio during the experiment and also to reduce the effect of possible field inhomogeneity's that influence

the measurement (due for example to Eddy's currents) (Price 1998). According to the application and the structural architecture of the sample, there is a wide choice of possibilities adapted to different cases. However, the most common sequences are the Inversion-Recovery (used to measure  $T_1$ ) and the Spin-Echo sequence (used to measure  $T_2$ ) (Figure 121).

The reason to use pulse sequences is to cast down the sources of the error in the measured signal and to comply with the assumptions made by the signal post-treatment models.

### 7.2.2.5. The Spin-Echo Experiment

Unless  $T_2 \ll T_{2\_inhomogeneous}$  (Equation 47) the contribution of  $\mathbf{B}_0$ 's inhomogeneity makes of  $T_2^*$  a bad approximation to  $T_2$  (Farrar and Becker 1971). Hahn proposed in 1950 a pulse sequence to cast down the inhomogeneity effect. The name of the pulse experiment is spin-echo (Hahn 1950).

The Spin-Echo sequence is normally used to measure  $T_2$ . It consists of a first  $90^\circ$  degrees pulse that makes rotate the total magnetization  $90^\circ$  (Figure 122a), a time interval between the first and second pulse ( $\Delta t$ ) followed by a  $180^\circ$  pulse that refocuses the total magnetization vector in the opposite direction (Figure 122c). The pulse sequence is written as  $90^\circ, \Delta t, 180^\circ$ . This sequence generates an FID signal with a characteristic shape exhibiting a first intensification of the signal due to the  $180^\circ$  pulse until a maximum and a new dephasing process on the transversal plane.

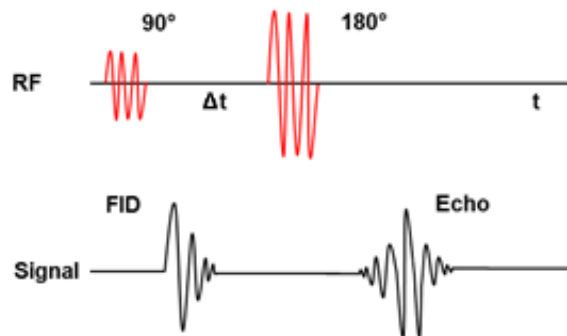


Figure 121 Spin-Echo sequence (Joseph P. Hornak 1997)

As  $\Delta t$  is bigger, the maximum value of the transversal component will decrease because of natural transversal relaxation processes (Farrar and Becker 1971). The maximum value of the echo amplitude of the transversal magnetization component is correlated with  $T_2$ . The experiment is repeated several times to get the maximum signal for several  $\Delta t$ .

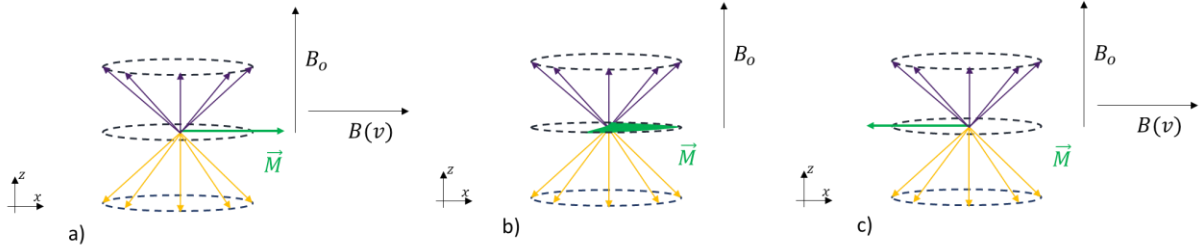


Figure 122 Vectorial model of a Spin-Echo sequence.

### 7.2.2.6. **Mathematic Model of the interactions of the magnetic fields with the spins: The Bloch equations.**

The dynamic of the macroscopic magnetization vector in presence of a static magnetic field ( $\mathbf{B}_0$ ) and an oscillating one ( $\mathbf{B}_1$ ) were first described by Bloch (Bloch 1946). The motion can be represented by the torque exerted by the homogeneous magnetic field on the spin magnetic moment as shown in Equation 49, where  $\boldsymbol{\mu}$  represents the magnetic moment of one single molecule and  $\mathbf{H}$  the homogeneous magnetic field ( $\times$  being the cross product).

$$\frac{d\boldsymbol{\mu}}{dt} = \gamma \boldsymbol{\mu} \times \mathbf{H}$$

Equation 49

Considering that the macroscopic vector  $\mathbf{M}$  represents the addition of all the individual's magnetic moments, it is possible to write:

$$\frac{d\mathbf{M}}{dt} = \gamma \mathbf{M} \times \mathbf{H}$$

Equation 50

By definition of the cross product, we obtain for each coordinate:

$$\frac{dM_x}{dt} = \gamma(M_y H_z - M_z H_y)$$

$$\frac{dM_y}{dt} = \gamma(M_z H_x - M_x H_z)$$

$$\frac{dM_z}{dt} = \gamma(M_x H_y - M_y H_x)$$

Equation 51

The term of the magnetization field includes the addition of and static and an alternating contribution of the two fields, by cancelling the non-existent contributions (e.g., the

alternating field has no static contribution) and taking into account that the alternating field is moving with the rotating frame of reference at a frequency equal to  $\omega$ :

$$H_x = H_1 \cos(\omega t), H_y = -H_1 \sin(\omega t), H_z = H_0$$

$$\frac{dM_x}{dt} = \gamma(M_y H_0 + H_1 \sin(\omega t))$$

$$\frac{dM_y}{dt} = \gamma(M_z H_1 \cos(\omega t) - M_x H_0)$$

$$\frac{dM_z}{dt} = -\gamma(M_x H_1 \sin(\omega t) - M_y H_1 \cos(\omega t))$$

Equation 52

At last, taking into account the relaxations processes, into which the transverse components go back to their null equilibrium value and the longitudinal component to  $M_0$ :

$$\frac{dM_x}{dt} = \gamma(M_y H_0 + H_1 \sin(\omega t)) - \frac{M_x}{T_2}$$

$$\frac{dM_y}{dt} = \gamma(M_z H_1 \cos(\omega t) - M_x H_0) - \frac{M_y}{T_2}$$

$$\frac{dM_z}{dt} = -\gamma(M_x H_1 \sin(\omega t) - M_y H_1 \cos(\omega t)) - \frac{M_z - M_0}{T_1}$$

Equation 53

To consider the diffusion effect, Torrey modified these equations in 1956 (Torrey 1956). The detailed deduction will not be shown here but it is available on his paper. In a simple vectorial form for isotropic diffusion, it is possible to write:

$$\frac{\partial \mathbf{M}(\mathbf{r}, t)}{\partial t} = \gamma \mathbf{M} \times \mathbf{B}(\mathbf{r}, t) - \frac{M_x \mathbf{i} + M_y \mathbf{j}}{T_2} - \frac{(M_z + M_0) \mathbf{k}}{T_1} + D \nabla^2 \mathbf{M}$$

Equation 54. Bloch-Torrey Equation

### 7.2.3. Pulsed Field Gradient (PFG)-NMR

The purpose of PFG-NMR is to measure the molecular self-diffusion coefficient. The technique covers a broad range of fields since it allows to measure the self-diffusion coefficient of species in a confined medium or effective diffusion coefficient. Vast examples exist on the study of diffusion and reaction in porous media (Keil 1999; Rieckmann and Keil 1997), nutrient transport by cells (Brownstein and Tarr 1979), oil permeation (Wilson and

Hürlimann 2006), and also the structure of materials (Imaging techniques), particularly biological tissue (Nicholson 2001).

The self-diffusion coefficient can be determined by the analysis of relaxation data (T1-T2 experiments). The differences between these two alternatives lie in the sensitivity of the relaxation experiment to rotational diffusion and the PFG's to translational diffusion (Price 1997). The first technique allows measuring molecular motion in a time scale from pico- to nanoseconds, whereas PFG measurements are performed over milliseconds. By using the Debye and the Stokes-Einstein equations the rotational diffusion coefficient determined by relaxation can be translated to the translational diffusion coefficient (Price and Hwang 1992; Blümich 1993).

PFG-NMR consists in measuring the average displacement of the molecules along one dimension. The best we can get is a displacement distribution. The challenge is how to mark the initial and the final position of the molecules.

The precession frequency of the spin is proportional to the magnitude of the surrounding magnetic field. On the other hand, the intensity of the signal is directly associated with the number of spins in resonance (same precession frequency) and phase (magnetic moment polarized in the same direction). The spins can be resonance but to lost coherence (Figure 123).

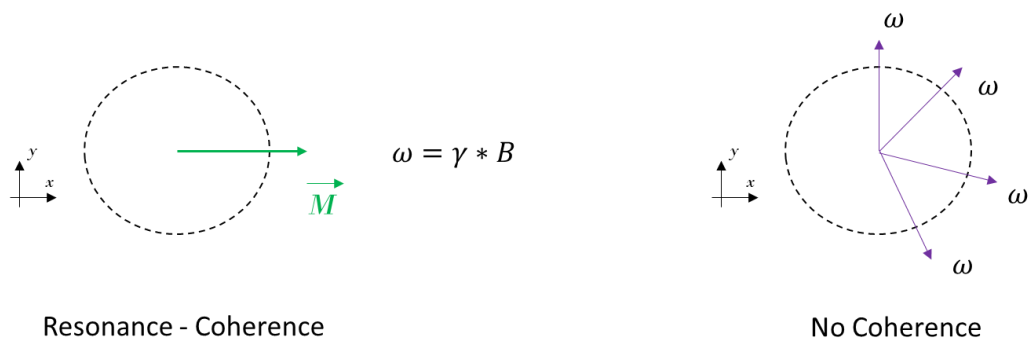


Figure 123 Spin resonance and spin coherence

For PFG-NMR as for NMR there exist a vast catalogue of pulse sequences, in this case, with different magnetic field gradients (Equation 55) echoes and spin echoes.

$$g = \nabla B_0$$

Equation 55. Magnetic field gradient (T/m)

The most basic proposed sequence is based on the Hahn spin-echo sequence adding two gradient pulses of equal intensity and duration around the 180° pulse (Figure 124). The 180° pulse not just refocuses the phase dispersion caused by the first gradient pulse but also the

chemical shifts and the frequency dispersion due to  $B_0$  inhomogeneity. This sequence is the Stejskal and Tanner pulse sequence (Stejskal and Tanner 1965).

In the pulse sequence described in Figure 124 at time zero the spins are in phase in the transversal plane (if the spins are in phase, they are also in resonance).

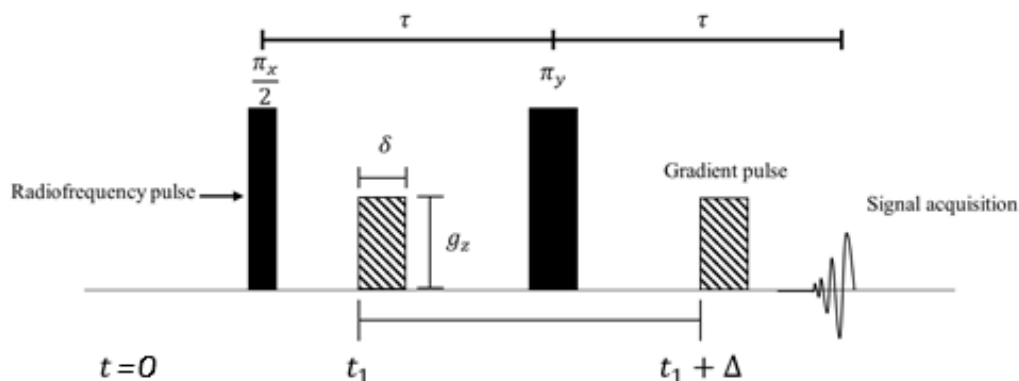


Figure 124 Stejskal and Tanner pulse sequence (Stejskal and Tanner 1965)

A magnetic field is generated. Its magnitude varies in a particular direction according to a given gradient. According to the magnitude of the magnetic field at the molecule position, the precession frequency will be different (Figure 125).

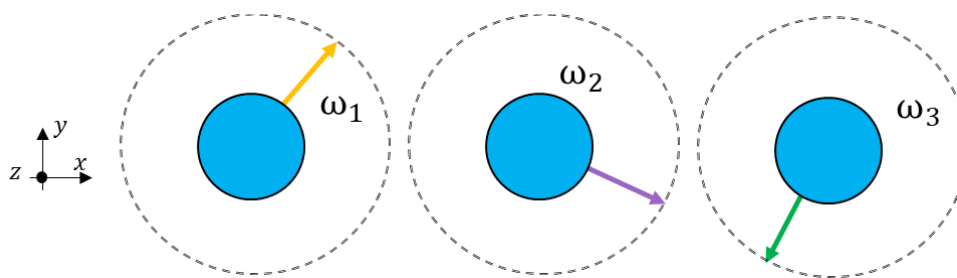


Figure 125 Spins with different Larmor Frequencies

The magnetic field gradient is established for a few milliseconds ( $\delta$ ). The Larmor frequency obtained by each molecule acts as a marker for its initial position. Then a  $180^\circ$  rf pulse is applied. This pulse rotates the magnetization around the Y-axis. It serves to invert the effect of the first gradient. The molecules are let to diffuse for a few milliseconds ( $\Delta$ ). The final position of the molecules after  $\Delta$  will be proportional to their final Larmor frequency. Finally, a gradient with the same characteristics as the first one is pulsed. This second gradient should reverse the effect of the first one. So, if the molecule was always at the same place, the maximum possible signal will be obtained. However, if it has diffused, the molecule will not recover its original Larmor frequency, and the obtained signal will be lower. So, it is possible to think about it as the quantification the phase difference or phase shift ( $\varphi$ ) (Larmor Frequency change) originated when the molecules travel in one direction. If  $\varphi$  is zero, the final and initial position of the molecules is the same (see Figure 126). The further

has travelled an ensemble of molecules, the lower will be the detected signal meaning the phase difference is higher.

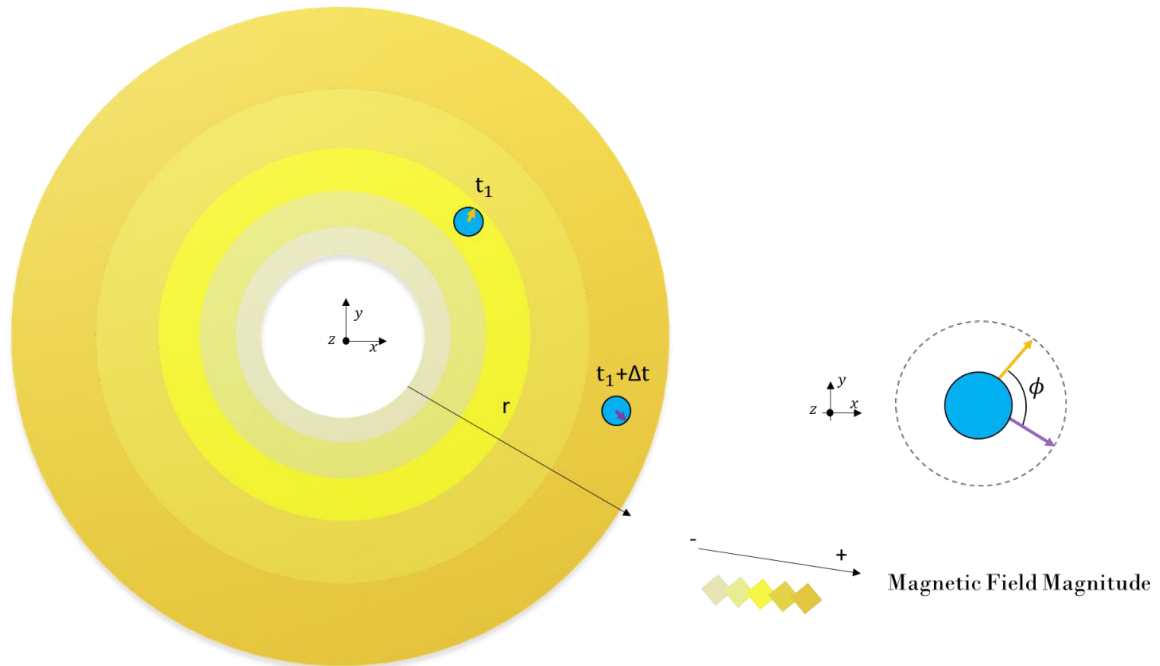


Figure 126. Phase Shift ( $\phi$ ) after diffusion process.

The further an ensemble of molecules has travelled, the lower will be the detected signal meaning the phase difference is higher (Figure 127).

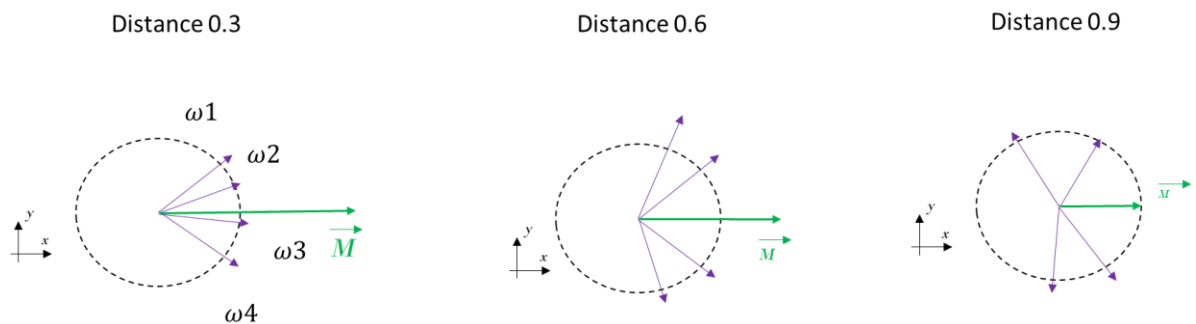


Figure 127. Progression of the magnitude of the total magnetization vector as a function of the distance. The distance is normalized in the 0-1 interval.

The experiment is repeated several times, increasing the diffusion time ( $\Delta$ ) and always saving the signal value right after the gradient pulse. At the end, a curve that relates the diffusion time with the signal intensity is obtained ( $\Psi$ ) (Figure 128). There is another

methodology in which  $\Delta$  is maintained constant and the magnitude of the magnetic gradient ( $g$ ) is varied.

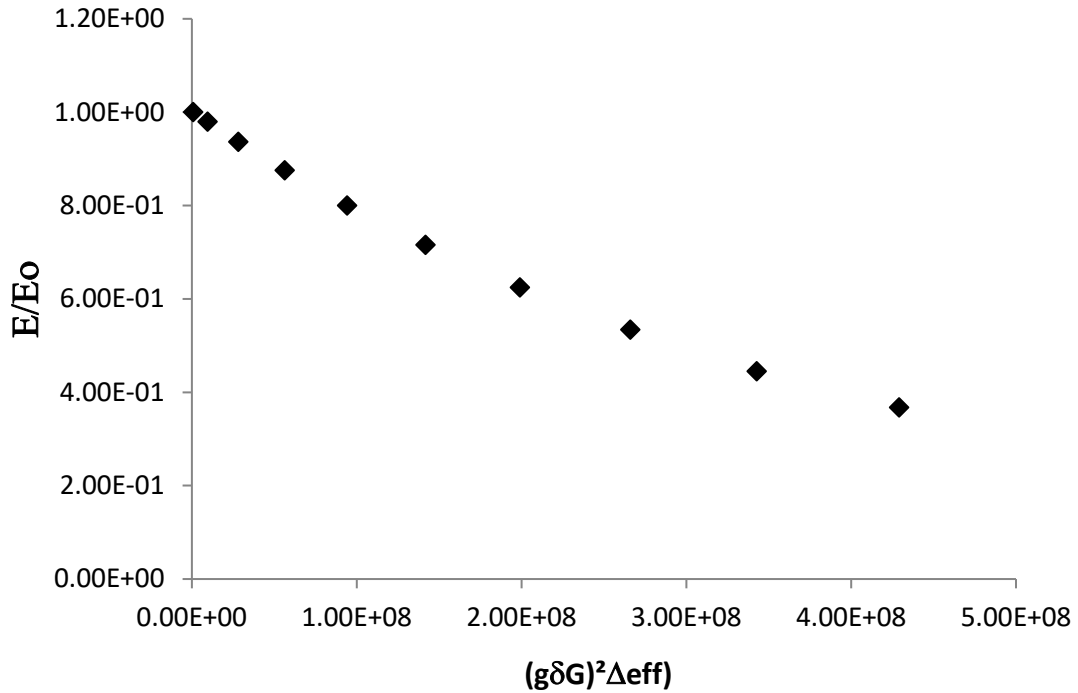


Figure 128 PFG-NMR Signal decay

### 7.2.3.1. Relation between the signal attenuation and the diffusion process

The attenuation of the signal is caused by relaxation and by diffusion. In the presence of diffusion and gradient pulses, it is possible to separate the contributions from both. In the absence of diffusion and/or gradient pulses, the signal value obtained at the end of the pulse sequence (highest peak value) is given by:

$$S(2\tau)_{g=0} = S(0) \exp\left(\frac{-2\tau}{T_2}\right)$$

Equation 56

where  $S(0)$  is the signal measured at  $t=0$  right after the  $90^\circ$  rf pulse is applied. In order to take into account the diffusion and the gradient pulses, the signal at the end of the sequence can be mathematically given by:

$$S(2\tau) = S(0) \exp\left(\frac{-2\tau}{T_2}\right) f(\delta, g, \Delta, D)$$

Equation 57

The attenuation due to the diffusion process is then given by:

$$E = \frac{S(2\tau)}{S(2\tau)_{g=0}} = f(\delta, g, \Delta, D)$$

Equation 58

where  $f(\delta, g, \Delta, D)$  is a function of the gradient pulse duration ( $\delta$ ), the gradient intensity ( $g$ ) the diffusion time ( $\Delta$ ), and the molecular diffusion coefficient ( $D$ ).

In Stejskal and Tanner pulse sequence in Figure 124 the total magnetization vector is first rotated  $90^\circ$ . Then a first gradient pulse is applied, which causes the spin to dephase. Secondly, a  $180^\circ$  rf pulse is applied, to invert the orientation to their opposite direction on the transversal plane. The molecule is diffusing during the time interval  $\Delta$ . The last step is to pulse a second gradient, identical to the first one during an equivalent time  $\delta$ . The logic of this sequence lies in the following concept: if the molecules haven't changed their position, the phase shift caused by the second gradient will be of the same magnitude than the first one leading to a null phase shift.

In this case, we are describing the gradient as a pulse of constant amplitude. According to the chosen sequence, the gradient can be time-dependent or constant.

The cumulative phase shift for a single spin in the case of a gradient pointed towards  $\mathbf{X}$  can be generally described as:

$$\Phi(t) = \gamma B_0 t + \gamma \int_0^t g(t') z(t') dt'$$

Equation 59. Phase shift as a function of the position

Where  $B_0 = |\mathbf{B}_0|$ . In this equation, the effect of field inhomogeneity is neglected. Generally, it is assumed that the transmitter of the alternating magnetic field is turned on and off so fast that the pulse function has a squared shape (Farrar and Becker 1971).

Considering the Stejskal and Tanner sequence in Figure 124, what is relevant is the net phase shift between the two gradients (Figure 126) after the time interval  $\Delta$ . The expression for the cumulative phase shift for one spin will be:

$$\begin{aligned} \phi_i(2\tau) &= \left\{ \gamma B_0 \tau + \gamma g \int_{t_1}^{t_1+\delta} x_i(t) dt \right\} - \left\{ \gamma B_0 \tau + \gamma g \int_{t_1+\Delta}^{t_1+\delta+\Delta} x_i(t') dt' \right\} \\ \phi_i(2\tau) &= \gamma g \left\{ \int_{t_1}^{t_1+\delta} x_i(t) dt - \int_{t_1+\Delta}^{t_1+\delta+\Delta} x_i(t') dt' \right\} \end{aligned}$$

Equation 60. Phase shift as a function of the position and the gradient parameters

where  $x_i$  is the position of the nuclei along the direction of the gradient.  $\delta$  is a key parameter. During the time  $\delta$  the phase shift is going to cumulate. This is reason why  $\delta$  must be equal for both gradient in the Stejskal and Tanner pulse sequence sequence.

The measurement taken from the experiment is the signal emitted by the system. Then it is needed an expression that relates the signal to the phase shift. A generic version of this equation is:

$$S(2\tau) = S(2\tau)_{g=0} \int_{-\infty}^{\infty} P(\phi, \Delta) e^{i\phi} d\phi = S(2\tau)_{g=0} \int_{-\infty}^{\infty} P(\phi, \Delta) \cos(\phi) d\phi$$

Equation 61. Signal as function of the phase shift distribution of the system

where  $P(\phi, \Delta)$  is the phase distribution function comprising the phase of all the elements of the system. By definition  $\int_{-\infty}^{\infty} P(\phi, \Delta) d\phi = 1$ .

PFM-NMR gives no information about the trajectory of a particle but about the average mean square displacement of the molecules. If the probability density function is defined as  $P(\mathbf{r}_0, \mathbf{r}_1, t)$ , it is possible to calculate the probability for a molecule to be at a position  $\mathbf{r}_1$  starting from a position  $\mathbf{r}_0$  after a time  $t$ .  $P(\mathbf{r}_0, \mathbf{r}_1, t)$  varies according to the nature of the diffusion domain. When the technique is used to measure free diffusion, meaning diffusion of particles into a non-restricted domain, it does not matter how much  $\Delta$  is increased, the means squared displacement increases linearly with  $\Delta$  and the diffusion coefficient will not change Figure 129. However, when the measurement is taken into a restrictive geometry (ex. Pores), the diffusion time  $\Delta$  becomes relevant.

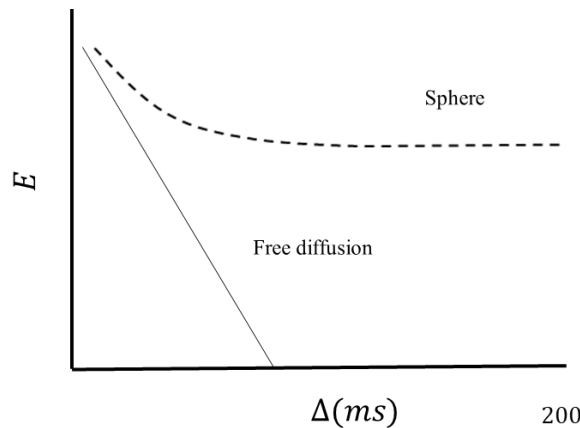


Figure 129 Signal attenuation progression comparison for free diffusion and restricted diffusion in a spherical medium.

Price proposed three different regimes for measurements in confined media based on Equation 62 comparing the diffusion time constant based on the characteristic length  $L$  of the confinement structure to the diffusion time (Price 1997).

$$\xi = \frac{D\Delta}{L^2}$$

Equation 62. Price's restricted diffusion criteria

In the case of a sphere of  $L=R$  radius for example (Figure 129), when  $\xi < 1$ , the mean square displacement increases linearly with  $\Delta$  and the diffusion coefficient is not different from the one obtained for the free diffusion regime. When  $\xi = 1$  the growth of the mean square displacement start to abandon linearity and for  $\xi > 1$  the measured diffusion coefficient will be an apparent one that is heavily influenced by the surface to volume ratio of the confined space where the mean squared displacement becomes constant and so independent from  $\Delta$  (Mitra and Sen 1992b; Mitra and Sen 1992a; Latour et al. 1993; Tycko 1994).

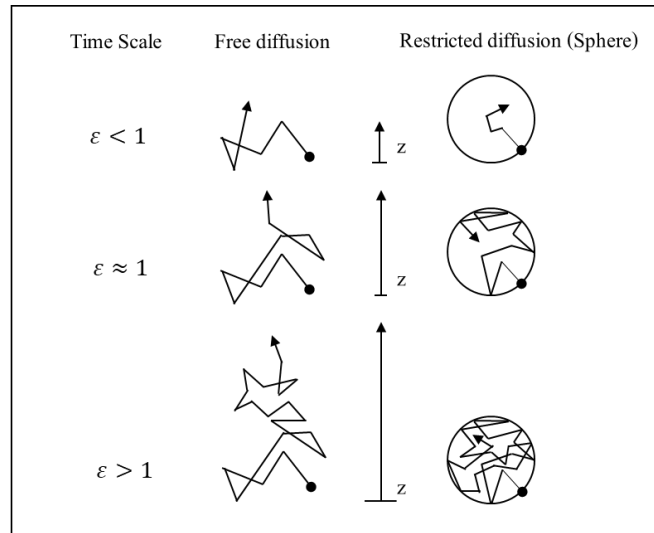


Figure 130 Restricted diffusion regimes according to Price's Criteria reference ( $\xi$  from price criteria) (Price 1997)

To get a model for the interpretation of the output signal as a function of the diffusion coefficient there are multiple paths. The rigorous deduction starting from the Bloch equation for diffusion (Equation 54) will not be shown here but can be found in (Price 1997). Generally, the experiment is done under constant  $\tau$  so can be considered constant and absorbed by  $E_0$  (Balinov et al. 1993). The model used for the interpretation of the Stejskal and Tanner pulse sequence is:

$$\ln(E/E_0) = -\frac{2\tau}{T_2} - (\gamma g \delta)^2 D \left( \Delta - \frac{\delta}{3} \right) = -(\gamma g \delta)^2 D \left( \Delta - \frac{\delta}{3} \right)$$

Equation 63. Signal attenuation model for the Stejskal and Tanner pulse sequence using a GPD approximation (see section 7.2.3.2)

### 7.2.3.2. *GPD and SPG approximations*

There are different assumptions that can be made to simplify the resolution of Equation 54. The Gaussian Phase Approximation (GPA) considers that the radial distribution function of the spins in an infinitely large system concerning an arbitrary reference time is Gaussian (Equation 64) (Joseph P. Hornak 1997; Cotts et al. 1989; Price 1998, 1997).

$$P(\mathbf{r}_0, \mathbf{r}_1, t) = (4\pi Dt)^{-\frac{3}{2}} \exp\left(-\frac{(\mathbf{r}_1 - \mathbf{r}_0)^2}{4Dt}\right)$$

Equation 64. Gaussian propagator

It is shown by Van Kampen (van Kampen 2007) that the phase distribution is also Gaussian:

$$P(\phi, 2\tau) = (2\pi \langle \phi \rangle_{av}^2)^{-\frac{1}{2}} \exp\left(\frac{-\phi^2}{2 \langle \phi \rangle_{av}^2}\right)$$

Equation 65. Phase distribution

Where  $\langle \phi \rangle_{av}^2$  is the mean-squared phase change at  $t = 2\tau$ . Finally, it leads to a result similar to the one obtained for free diffusion starting from the Bloch Equations:

$$\ln(E/E_0) = -(\gamma g \delta)^2 D \left(\Delta - \frac{\delta}{3}\right)$$

Equation 66. Signal for a GDP approximation

The short gradient pulse (SGP) approximation considers  $\delta \ll \Delta$  so there is no displacement or phase change during this time. The detailed derivation of the model is presented by Price (Price 1997). The signal attenuation at  $t = 2\tau$  is represented by Equation 67 which very similar to Equation 66 but with  $\frac{\delta}{3} \rightarrow 0$ .

$$E(g, \Delta) = \exp(-(\gamma g \delta)^2 D \Delta)$$

Equation 67. Signal for a SGP approximation

The GDP and the SGP approximations can be considered as equally valid for free diffusion, that is  $\xi < 1$  and the GDP has been proven to work well at  $\xi \gg 1$  after the time-lapse in which the original position  $r_0$  is not considered relevant anymore.

When the interest is to find an effective diffusion coefficient for restricted space, the model used for the interpretation of the result must be modified. The complexity increases exponentially from regular to complex restrictions and generally for the complex media there is no exact solution. When experimental data coming from a restricted space as a pore network is analyzed with free diffusion models, an apparent auto-diffusion coefficient is

expected (Price 1997). However, it is important to deal with the technical problems associated with these structures.

### 7.2.3.3. Existing simulation models

There are two common general approaches for the simulation of NMR. The first one is to use random walkers to diffuse through the structure which allows quantifying the phase change and by doing so, the apparent diffusion coefficient (Grebekov 2011; Grebekov et al. 2013; Balinov et al. 1993; Lin et al. 2003; Waudby and Christodoulou 2011). The second one consists of the resolution and analysis of the Bloch-derived equations with the scope of extending or improving the models for the analysis of experimental data (Lin 2018; Li et al. 2019; Ning et al. 2017). In this classification the simulations vary regarding the optimization time, the hypothesis of the models, and the type of physical restriction for the domain (Ex. catalyzt pores, adsorbents, biological tissue).

The common approach is based on the simulation of Brownian motion of spin-bearing particles confined into a physical domain with Neumann border conditions (Neuman 1974), meaning reflection on the walls. The main modules of the simulation are the Brownian motion, the physical boundaries, and the phase accumulation model. Douglas and McCall developed the method of phase accumulation for measuring diffusion in paraffin hydrocarbons (Dean C. Douglass, David W. McCall 1958).

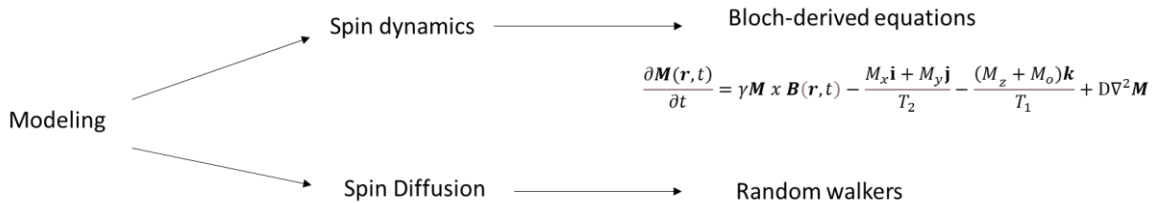


Figure 131. Simulation approaches

## 7.3. PFG-NMR experiment simulation model

In this section is described a simulator of the PFG-NMR experiment allowing to calculate the tortuosity of a digital pore network. To this end, it is necessary to compute the effective diffusion coefficient. Such coefficient will be obtained from the self-diffusion simulation of the molecules within the network. In this sense, it is necessary to simulate the spin diffusion and not the spin dynamics (see Figure 131). This will allow to obtain the signal attenuation curve associated to the transversal magnetization (see Figure 132).



**Parameters**

- NMR  $t_{\text{steps}}$
- Number of tracer pores
- Type of gradient
- Molecular Diffusion Coefficient

Figure 132. PFG-NMR simulation block diagram

In literature it is possible to find multiple researches works that simulate the auto-diffusion phenomenon based on molecular simulations (Balinov et al. 1993; Cotts et al. 1989; Grebenkov et al. 2013). To decrease the simulation time and open the door to new simulation scales, it is proposed here to simulate the auto diffusion phenomenon using the Fick’s model that is formally equivalent to Brownian motion at the molecule’s population scale.

The simulation of the PFG-NMR has two main blocks. In the diffusion block are set all the boundary equations, diffusion model, discretization and numeric solver are specified. The second block corresponds to the PFG-NMR model. The output data that comes from the diffusion block is used as the input for the PFG-NMR mathematical model.

**7.3.1. Hypothesis**

- The magnetic field inhomogeneities are neglected
- The total magnetic moment is in the transversal plane
- The interactions between the local magnetic fields created by each molecule are neglected
- The signal loss due to the particle that escape from the porous media is neglected

It is important to remark that it not necessary to model the full spin dynamics. The required magnitude is the phase shift after  $\Delta$ . Considering the hypotheses that are made, the phase shift in just dependent of the magnitude of the gradient ( $g$ ), the gradient time application ( $\delta$ ), the distance travelled by the molecule, and the gyromagnetic ratio (constant).

### 7.3.2. Methodology

The diffusion block handles each auto diffusion simulation. The diffusion block works as described in section 3.9.1. A Dirichlet boundary condition is imposed in the external work of the network.

Equation 68 quantifies the cumulative phase shift for the system. The phase change is cumulated during the application time of the gradient. One of the properties of the radiofrequency ( $\mathbf{B}_1$ ) is to allow the spin to cumulate the phase (different to the case of homogeneous magnetic field ( $\mathbf{B}_0$ )). The phase change depends also on the magnetic field gradient.

$$\phi_i(2\tau) = \left\{ \gamma g \int_{t_1}^{t_1+\delta} x_i(t) dt \right\} - \left\{ \gamma g \int_{t_1+\Delta}^{t_1+\delta+\Delta} x_i(t') dt' \right\}$$

Equation 68. Phase shift as a function of the position and the gradient parameters

If the displacement of the molecules during  $\delta$  is neglected, the phase shift can be calculated as:

$$\phi(2\tau) = \left\{ \gamma g x_o \int_{t_1}^{t_1+\delta} dt \right\} - \left\{ \gamma g x_f \int_{t_1+\Delta}^{t_1+\delta+\Delta} dt' \right\} = \gamma g \delta (x_o - x_f) = \gamma g \delta (x_o - x_f)$$

Equation 69.

where  $x_o$  and  $x_f$  represent the initial and the final X coordinate of the molecule.

For the calculation of the phase shift, the pore network is discretized using the middle coordinates of pores.

For  $t_{sim} = 0$  a gaussian concentration profile of a tracer species is set along one pore of the network. The pore is randomly chosen, and it will be denominated the tracer pore.  $x_o$  will be equal to the middle coordinate of the tracer pore ( $x_o = x_{m_{tp}}$ ). The diffusion simulation is then triggered. The final diffusion simulation time will be equal to  $\Delta$  ( $t_{sim} = \Delta$ ). A phase shift relative to each pore middle coordinate will be calculated using Equation 70, where  $x_f$  will represent the middle coordinate of each pore  $i$  different than the tracer ( $x_f = x_i$ ).

$$\phi_i = \gamma g \delta (x_{m_{tp}} - x_i)$$

Equation 70. Phase shift expression used for the pore the network characterization

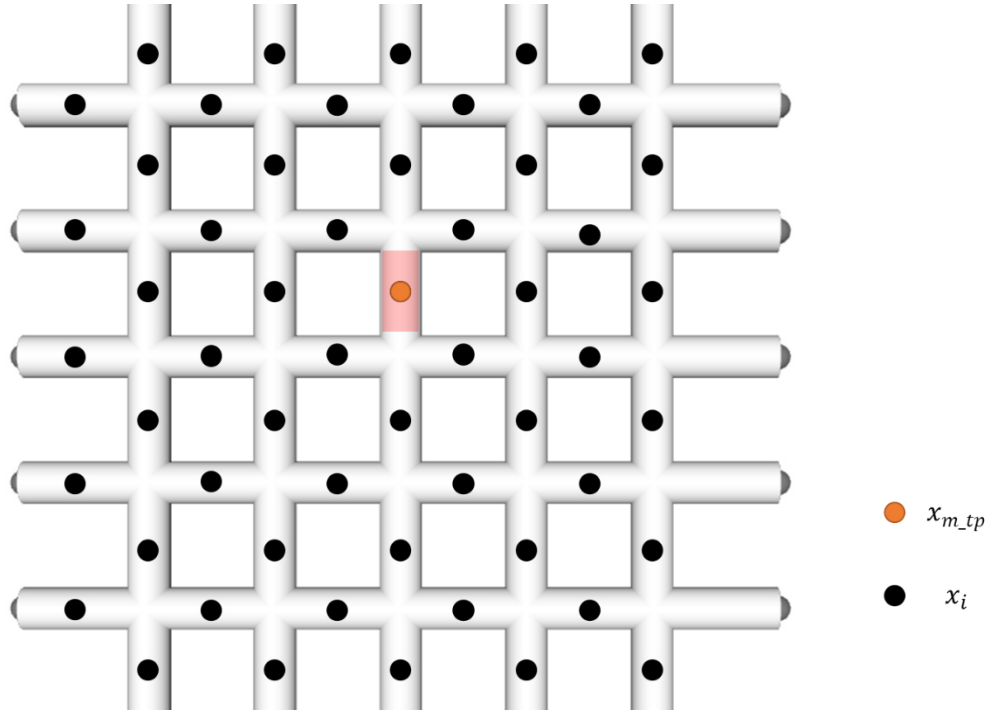


Figure 133. Post treatment discretization for the PFG NMR simulation

The total signal that corresponds to the simulation is calculated multiplying the signal generated by each phase shift by the fraction of the tracer species in the pore associated to it:

$$E_j = \sum_{i=1}^{i=N_p} \left\{ \cos(\varphi_i) \frac{S_i \int_0^{P_i L} C_A(l, \Delta) dl}{S_0 \int_0^{P_0 L} C_A(l, 0) dl} \right\}$$

Equation 71. Signal for one simulation

where  $C_A(l, 0)$  represents the molar concentration of the tracer species in the tracer pore at  $t = 0$  and  $C_A(l, \Delta)$  represent the concentration in a pore at  $t_{sim} = \Delta$ .

The initial position of the tracer will conditionate the signal obtained for each  $\Delta$ . Multiple initial simulation conditions are considered (initial tracer pores) to get a representative signal of the full pore network (Figure 134). Each tracer pore is randomly chosen. Figure 134 shows an example of three different tracer pores (pores in red).

The final signal will be then calculated as:

$$E_{\Delta} = \frac{1}{N_t} * \sum_{j=1}^{j=N_t} E_j$$

Equation 72. Average signal generated for a particular  $\Delta$  after multiple tracer simulations

where  $N_t$  represents the total number of tracer pores. A sufficiently high number of tracer pores is considered in order to get a standard deviation for the average signal lower than 5%.

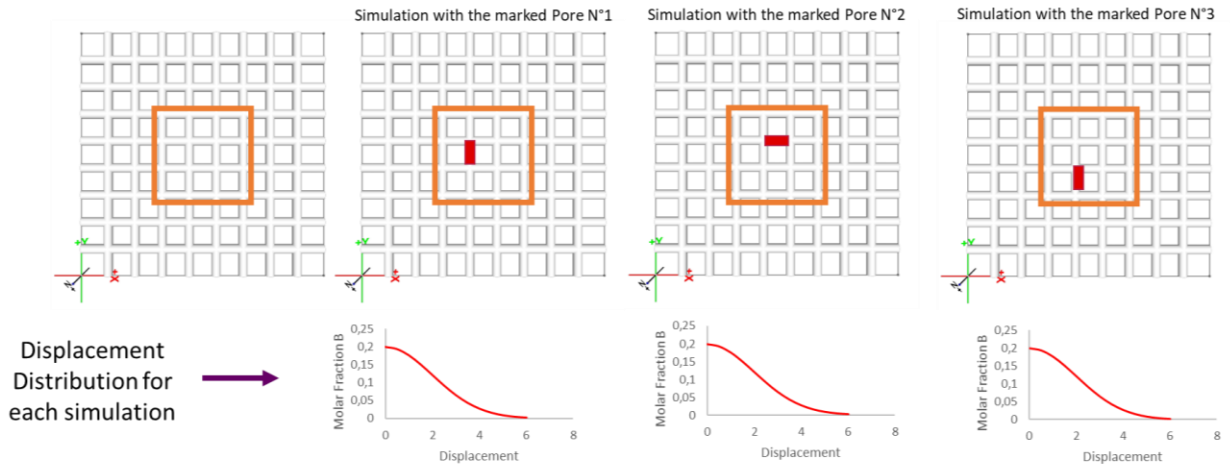


Figure 134. Tracer pores graphical representation (pores in red).

If the tracer pore is far enough from the border of the pore network, then there is no risk of losing a fraction of the tracer during the simulation. To avoid this situation the pores that can be chosen as tracer pores will be inside of a squared region called the *active zone* (Figure 135) of the network.  $L_D$  in the Equation 73 represent the diffusion distance for unrestricted diffusion calculated using the Einstein equation. The dimension  $L_{AZ}$  for the active zone is calculated using the Equation 74.  $L_{AZ}$  is imposed and the total length of the network is calculated as:

$$L_D = \sqrt{4 * \Delta * D_m}$$

Equation 73. Distance from the border of the active zone to the border of the network.

$$L_N = L_{AZ} - 2 L_D$$

Equation 74. Dimension of the network

The minimum dimension of the network if fixed to grant the representativity of the topology map, the percolation map, and the pore size distribution.

To reduce the simulation times to actions were implemented. According the with the diffusion time  $\Delta$ , a different network size is used. In each case  $L_{AZ}$  is recalculated and network size is determined. As the scope of the simulation is to measure the tortuosity, a sufficiently low diffusion coefficient is used to minimize the network size that should be used for each  $\Delta$ .

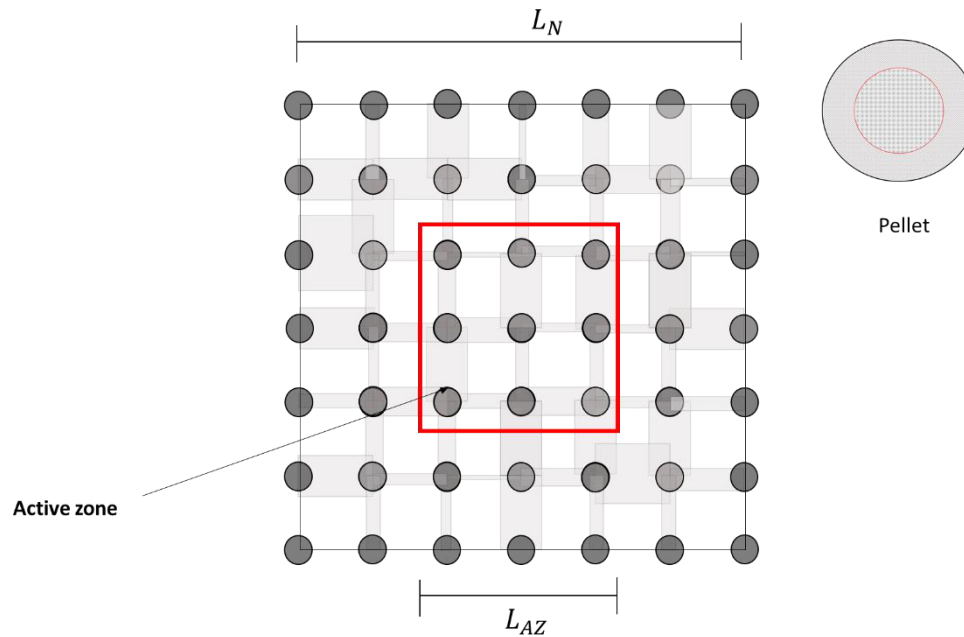


Figure 135. Active zone graphical description

Summarizing, the signal for each  $\Delta$  point is the average of the signal obtained for several tracer pores simulations. At the same time, the signal from each tracer pore is calculated considering the mol fraction of tracer in each pore at  $t_{sim} = \Delta$ . A graphical representation that illustrates the relations between the output variables is shown on Figure 136.

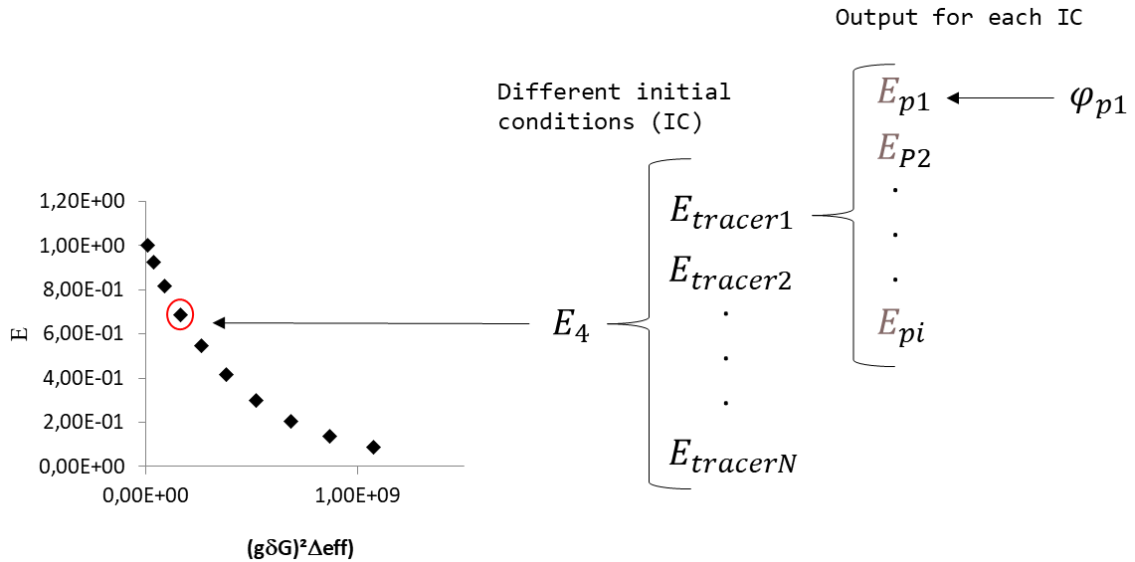


Figure 136. Simulations scheme for each  $\Delta$

This is pseudo would be written as:

```

FOR i= 1, N_measurements
  Create/ Adjust Pore Network Size
  Read the pore network
  FOR j= 1, N_tracerpores
    Choose randomly a tracer pore
    CALL diffusion simulation
    Calculate the phase shift  $\varphi$  for each pore than contains compound B
    Calculate the signal for the simulation of the tracer j
    Calculate the propagator
  END FOR
  Average the signal
  Average the propagator
END FOR
Print Results

```

## 7.4. Case study

Different pore networks were characterized using the methodology described in the last section. Table 25 specifies the parameters used for the simulation. The default parameters for the network generation were triangular lattices, 1 pore population, PEP=0.75, PSD=(10 ± 2) nm, pore length=60 nm, grid spacing=1. The  $L_{AZ}$  for the test was fixed in 1740 nm.

Table 25. Parameters used for the PFG-NMR ideal case simulation

Parameter	Value
G (T/m)	3.44
$\delta$ (s)	0.0006
$\Upsilon$ (rad/s/T)	2.67E+08
Dm(m <sup>2</sup> /s)	1,897*10 <sup>-13</sup>

In the first test, the pore existence probability for the network was varied. Figure 137 represents the attenuation curve observed for a pore network of PEP=0.71. As can be observed, the trendline passes close to zero and the correlation coefficient is 0.9998. The ratio  $\Delta/\delta$  for  $\Delta=5\text{ ms}$  is equal to 8 and to 160 for the longest used diffusion time ( $\Delta=100\text{ ms}$ ).

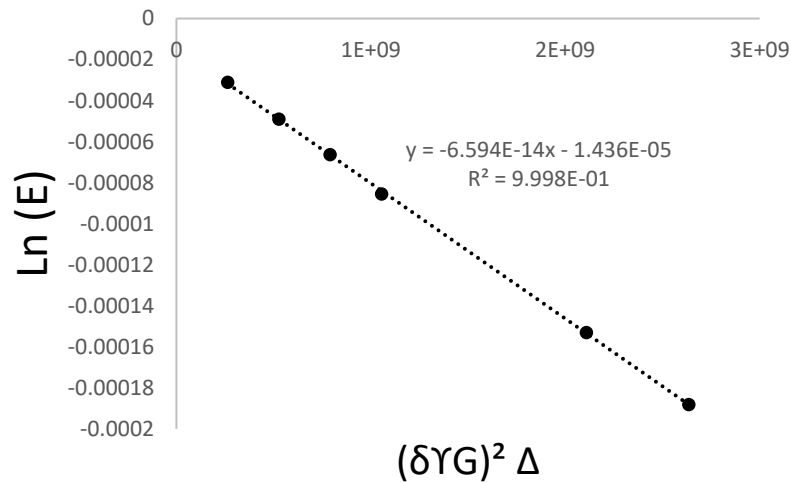


Figure 137. Attenuation curve for network of PEP=0.71

Figure 138 presents the tortuosity obtained for different PEP using the PFG-NMR simulation. The obtained tortuosity values have the right order of magnitude for gamma alumina samples. As the PEP decreases, the tortuosity increases. This trend is in agreement with the results obtained for the characterization done using the infinite plate methodology in section 3.9.

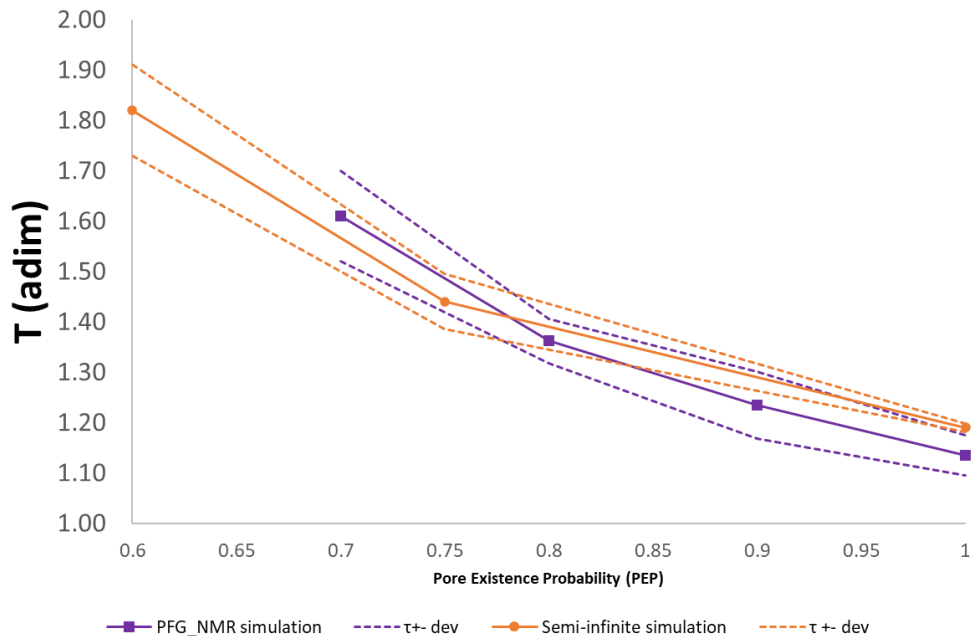


Figure 138. Tortuosity for different PEP using the PFG-NMR simulation **and the semi-infinite plate** simulation.

## 7.5. Conclusions

A fast PFG-NMR simulation method for the characterization of pore networks was developed. It is based on a Fickian diffusion simulation. The equation used for the interpretation of the results derives from the Stejskal and Tanner pulse sequence. A set of different initial conditions is used to obtain a good representation of the diffusion into the pore network.

Two simulation methods were created, in agreement with the experimental practice:

- Variation of the diffusion time  $\Delta$
- Variation of the magnitude of the magnetic field gradient ( $g$ )

The size of the generated pore network is varied according to the diffusion time  $\Delta$ . This is done to avoid mass loss and to save simulation time.

The obtained tortuosity trends are reasonable and similar to those in section 3.9. The simulation derived tortuosity values are of the same order of magnitude of the experimental values for gamma alumina.

## Chapter 8: Conclusions and Future Work

### 8.1. Conclusions

In this work, digital twins for porous gamma aluminas have been developed in order to simulate mass transfer without or with reactions. These representations are based on pore network models that are created by means of a discrete reconstruction method using a stochastic algorithm. Starting from an initial graph, or lattice, composed of nodes and edges, pores are randomly added on the structure. At the end of the pore network generation process, hollow cylinders occupy a part of the edges. The nodes can be set to have zero volume (the nodes do not play any physical role) or can be occupied by hollow spheres that create an additional pore volume in the pore network model.

The characteristics of the initial lattice set the maximum connectivity of the network, that is to say the maximum number of edges that can be connected to a given node. Different features provide heterogeneity to the digital structures to get not only a good representation of the textural properties but also a good representation of the topology of the network. The pore network generation tool can accommodate several pore size distributions in the same network, which allows the construction of hierarchical structures, i.e. networks with different porosity levels or pore populations. The porosity of each population of the network is regulated through its own existence threshold defined as the pore existence probability (PEP). The length of the pores can either be constant in regular lattices, or variable by creating random distortions in the lattice. The grid spacing between the different pore levels can also be modified, defining their intertwining. The interaction between the different pore populations and the variation of the pore network generation parameters can produce complex outputs such as pore connectivity distributions and pore volume distribution for each population. It is possible to create pore networks in 1D, 2D, or 3D. The resulting pore network can be periodic along one or several dimensions.

A topological analysis was carried out in order to better understand the influence of the different pore network generation parameters on the network's architecture. It was discussed how the topological maps are affected by the lattice and the pore existence probability, how the percolation map is affected by the topological map and the pore size distribution, and how the pore volume distribution is affected by the pore size distribution and the pore length distribution. To understand pore blocking phenomena in the network, a percolation algorithm was developed that characterizes the effect of the position and environment of each pore within the network by establishing the percolation order of the pores when a fluid enters the pore network. The implementation of the pore blocking algorithm required implementing high performance priority queues using heap structures

to drastically increase the simulation speed of such an analysis. A sensitivity analysis of percolation simulations into various pore network models showed that a fraction of the smaller pores is not influenced by the percolation phenomena. The fact that this fraction depends on the maximum connectivity of the network and on the pore existence probability is an interesting conclusion of the analysis of these simulation results.

The interaction between several pore populations was also studied. The populations can hinder each other depending on the grid spacing and their pore size distributions. The volume represented by each population is a key variable. The effect of the percolation map on volume processes is highly influenced by the pore volume fraction allocated to each population. This result is relevant to understand the role of the pore blocking effect when techniques such as pore nitrogen sorption are simulated. By controlling the size and dispersion of the domains, one can significantly improve the quality and representativity of the pore network model.

The existence of pore domains with different pore populations, their number and their dispersion in the network strongly influence the effective diffusion coefficient. This is in line with experimental observations, thus confirming the relevance of using multiple populations and pore domains to model the gamma alumina network architecture.

To fully characterize the pore network models and provide a detailed comparison of these models to experimental data, a fast algorithm was implemented for the simulation of three porosimetry techniques: Mercury Intrusion Porosimetry, Nitrogen Sorption and CryoPorometry. These characterization techniques exhibit hysteresis phenomena that can be attributed to pore blocking, resulting in percolation phenomena and thermodynamic or mechanical equilibrium hysteresis. By introducing the concept of triggering diameter, such hysteresis phenomena can be simulated on digital pore networks. The algorithm used to identify the triggering diameter of each pore in the network was optimized by using a Max-Heap / Min-Heap sorting technique as a tool for handling the search list. A time execution test for the nitrogen sorption simulation and an octahedral lattice of about 2 million pores only required 6.7 seconds using the binary heap algorithm, which is more than 20 times faster than other sorting algorithms. The size of the network is the main parameter that affects the execution time, which exhibits an  $O[N \log(N)]$  behavior.

A sensitivity analysis applied to the simulated characterization techniques helped to better characterize how the different input parameters influence the obtained characteristic curve. The connectivity and the pore existence probability are the variables that influence the topological map of the network. These input variables are both related to the network pore fraction affected by the percolation phenomena. The average diameter of the pore size distribution has an influence on the mechanical or thermodynamical equilibrium

model, while the width of the pore size distribution changes the percolation map, thereby increasing the pore blocking phenomena.

A digital twin of an industrial alumina sample was created by generating a three-level hierarchical pore network model. During the parameter identification procedure, it was clearly shown that, in nitrogen porosimetry, the adsorption isotherm mainly provides information on the pore volume distribution of the structure, but it does not allow getting a statistically representative model that reproduces the effects of the topology of the solid. However, the desorption isotherm and the scanning curves are strongly influenced by the topology of the network. It is therefore computationally possible to have various representations with the same adsorption isotherm but with totally different desorption branches that represent different topologies. After the final parameter identification, a pore network model was obtained that provides a simulated nitrogen sorption isotherm that is in good agreement with the experimentally determined sorption isotherm. The same set of parameters also allows to correctly predict the nitrogen scanning curves, thereby validating the digital twin. The BJH pore size distribution obtained from the desorption branch of the simulated isotherm corresponds well to the experimental BJH pore size distribution for the pores above 10 nm.

It should be stressed that it is not yet possible to confirm that, from a given isotherm, the attributes of the pore network structure curve can be uniquely identified. Our results point in the direction that a family of topologies can generate the same isotherms. However, the use of the scanning curves in the objective function of the optimizer could help to reduce the number of structures that can generate the same characteristic curves as a given alumina sample, and therefore restricts the possible topologies of the solid.

Another way of validating the digital twin consists in predicting the tortuosity factor from the pore network model and comparing it to experimentally measured values. Using diffusion simulations on the pore network model fitted to the nitrogen sorption curves, a tortuosity factor was calculated that differs by less than 20% from the tortuosity factor measured by PFG-NMR. This illustrates how a digital twin allows to provide a reasonable estimate for the tortuosity factor of a catalyst sample from cheap, readily available, and commonly used nitrogen sorption characterization experiments.

As an alternative to the diffusion simulations, a fast PFG-NMR simulation method for the characterization of pore networks was developed. It is based on a Fickian diffusion simulation. The equation used for the interpretation of the results derives from the Stejskal and Tanner pulse sequence. A collection of different initial conditions is used to obtain a good representation of the diffusion into the pore network. Two simulation methods were implemented that correspond to two experimental practices: (i) variation of the diffusion

time  $\Delta$ , (ii) variation of the magnitude of the magnetic field gradient ( $g$ ). The size of the generated pore network is varied depending on the diffusion time  $\Delta$ . This is done to avoid mass loss and to save simulation time. The obtained tortuosity trends are reasonable, and the PFG-NMR simulation derived tortuosity values are of the same order of magnitude of the experimental values for gamma alumina support.

## 8.2. Perspectives

For the short-term perspectives, multiple questions remain open and there is room for numerous improvements in the developed numerical tools:

- The texture and roughness of the pore surface is not considered in the model presented here. The influence of this property therefore remains an open question.
- A broader topological study should be carried out to better understand the interaction between the multiple pore population in terms of the percolation and topological maps. The different pore populations organized as isolated pore domains can be interpreted as grains into the material matrix. The understanding of their impact on the results from different experimental characterization techniques and their digital equivalents is still to be studied. The scanning curves for nitrogen sorption are a valuable tool for this study.
- The number of sets of pore network generation parameters that can fit the same nitrogen sorption is also to be studied. The flexibility of the model in terms of the types of the nitrogen sorption hysteresis loops that can be represented still remains a question.
- A digital tool to simulate cryoporometry measurements has been developed, but the lack of available experimental data did not allow to validate the simulations.
- The PFG-NMR diffusion simulation needs to be further validated. This is a valuable tool that can be used for several applications. The question of the influence of the network's architecture on the diffusion propagator remains open. The influence of the architecture of the sample added to the effect of chemical kinetics on the diffusion coefficient could also be studied.
- Better characterization of industrial alumina samples will of course allow generating better digital twins. Hence, the simulation tool should be extended to perform the structural optimization with an objective function that not only uses nitrogen porosimetry data, but also scanning curve, mercury porosimetry and NMR-cryoporometry simulations.
- The pore network model has demonstrated to be efficient and provide reasonable representations of the topology of the material. As the model is proposed now, each pore population has its own pore existing probability and pore size distribution.

However, new key features could be added to allow (i) to set different maximum connectivities for each pore population in order to better study the influence of the interaction of different pore domains, (ii) to set a different length distribution for each population, and (iii) to set the average volume fraction of each pore population.

The next major step is to study the influence of the network architecture on chemical diffusion-reaction systems. The network's architecture plays an important role on kinetics that must be better understood. Detailed diffusion-reaction simulations will be used to investigate and clarify the link between the topology of these solids and their tortuosity. To validate such systems, the architecture of different gamma alumina catalyst can be fitted using the numerical tools developed in this thesis. Then, the diffusion-reaction simulation would be validated using data generated from chemical reaction experiments that use the structurally fitted gamma alumina catalyst. This study would allow to understand how to optimize structural parameters to reach a target selectivity in different reaction systems.

Once the optimal pore network structure has been defined from the previous step, we still need to devise a way to produce a gamma alumina with this target structure. Mimetic models remain a cutting-edge solution to link the synthesis conditions of gamma alumina to its pore structure. However, the complexity of the generated morphology makes this methodology less attractive for simulating transport phenomena and diffusion-reaction systems. IFPEN has developed several mimetic modeling tools during thesis work of Giulia Ferri (Ferri 2021). By solving the inverse problem for the target structure, these numerical approaches could allow to define the right combination of synthesis parameters for the preparation of the optimum catalyst.

## Publication bibliography

Adloo, Hadi; L'Heureux, Ivan; Kharaghani, Abdolreza (2019): Effects of correlated morphological and topological heterogeneity of pore network on effective transport and reaction parameters. In *Chemical Engineering Science* 207, pp. 280–304. DOI: 10.1016/j.ces.2019.05.029.

Akoka S. (2002): Une introduction a la resonance magnetique nucleaire. Chapitre 1: Principes de Base. Available online at <http://www.sciences.univ-nantes.fr/CEISAM/data/43/akoka/UneintroRMN-Chap1.pdf>.

Allen, Terence (1990): Particle Size Measurement. Fourth edition. Dordrecht: Springer Netherlands (Powder Technology).

Ammus, Jamal M.; Androustopoulos, George P.; Tsetsekou, Athena H. (1987): An investigation of the deactivation phenomena associated with the use of commercial HDS catalysts. In *Ind. Eng. Chem. Res.* 26 (7), pp. 1312–1323. DOI: 10.1021/ie00067a009.

Androustopoulos, G. P.; Salmas, C. E. (2000a): A New Model for Capillary Condensation–Evaporation Hysteresis Based on a Random Corrugated Pore Structure Concept. Prediction of Intrinsic Pore Size Distribution. 2. Model Application. In *Ind. Eng. Chem. Res.* 39 (10), pp. 3764–3777. DOI: 10.1021/ie000163w.

Androustopoulos, George P.; Salmas, Constantinos E. (2000b): A New Model for Capillary Condensation–Evaporation Hysteresis Based on a Random Corrugated Pore Structure Concept. Prediction of Intrinsic Pore Size Distributions. 1. Model Formulation. In *Ind. Eng. Chem. Res.* 39 (10), pp. 3747–3763. DOI: 10.1021/ie0001624.

Armatas, Gerasimos S. (2006): Determination of the effects of the pore size distribution and pore connectivity distribution on the pore tortuosity and diffusive transport in model porous networks. In *Chemical Engineering Science* 61 (14), pp. 4662–4675. DOI: 10.1016/j.ces.2006.02.036.

Armatas, Gerasimos S.; Pomonis, Philippos J. (2004): A Monte Carlo pore network for the simulation of porous characteristics of functionalized silica. Pore size distribution, connectivity distribution and mean tortuosities. In *Chemical Engineering Science* 59 (24), pp. 5735–5749. DOI: 10.1016/j.ces.2004.06.047.

Aste, T.; Saadatfar, M.; Sakellariou, A.; Senden, T. J. (2004): Investigating the geometrical structure of disordered sphere packings. In *Physica A: Statistical Mechanics and its Applications* 339 (1-2), pp. 16–23. DOI: 10.1016/j.physa.2004.03.034.

Attari Moghaddam, Alireza; Kharaghani, Abdolreza; Tsotsas, Evangelos; Prat, Marc (2018): A pore network study of evaporation from the surface of a drying non-hygroscopic porous medium. In *AIChE J* 64 (4), pp. 1435–1447. DOI: 10.1002/aic.16004.

Balinov, B.; Jonsson, B.; Linse, P.; Soderman, O. (1993): The NMR Self-Diffusion Method Applied to Restricted Diffusion. Simulation of Echo Attenuation from Molecules in Spheres and between Planes. In *Journal of Magnetic Resonance, Series A* 104 (1), pp. 17–25. DOI: 10.1006/jmra.1993.1184.

Barrett, Elliott P.; Joyner, Leslie G.; Halenda, Paul P. (1951): The Determination of Pore Volume and Area Distributions in Porous Substances. I. Computations from Nitrogen Isotherms. In *J. Am. Chem. Soc.* 73 (1), pp. 373–380. DOI: 10.1021/ja01145a126.

Baychev, Todor G.; Jivkov, Andrey P.; Rabbani, Arash; Raeini, Ali Q.; Xiong, Qingrong; Lowe, Tristan; Withers, Philip J. (2019): Reliability of Algorithms Interpreting Topological and Geometric Properties of Porous Media for Pore Network Modelling. In *Transp Porous Med* 128 (1), pp. 271–301. DOI: 10.1007/s11242-019-01244-8.

Beeckman, J. W. (1990): Mathematical description of heterogeneous materials. In *Chemical Engineering Science* 45 (8), pp. 2603–2610. DOI: 10.1016/0009-2509(90)80148-8.

Beeckman, J. W.; Froment, G. F. (1980): Catalyst deactivation by site coverage and pore blockage. In *Chemical Engineering Science* 35 (4), pp. 805–815. DOI: 10.1016/0009-2509(80)85064-0.

Beeckman, Jean W.; Froment, Gilbert F. (1979): Catalyst Deactivation by Active Site Coverage and Pore Blockage. In *Ind. Eng. Chem. Fund.* 18 (3), pp. 245–256. DOI: 10.1021/i160071a009.

Bloch, F. (1946): Nuclear Induction. In *Phys. Rev.* 70 (7-8), pp. 460–474. DOI: 10.1103/PhysRev.70.460.

Blümich, Bernhard (1993): J. W. Hennel and J. Klinowski. Fundamentals of nuclear resonance longman scientific & Technical, 1993 £22.50 paperback, 288 pages. In *Magn. Reson. Chem.* 31 (10), p. 966. DOI: 10.1002/mrc.1260311017.

Blunt; King; Scher (1992): Simulation and theory of two-phase flow in porous media. In *Physical review. A, Atomic, molecular, and optical physics* 46 (12), pp. 7680–7699. DOI: 10.1103/PhysRevA.46.7680.

Blunt, Martin J. (2001): Flow in porous media — pore-network models and multiphase flow. In *Current Opinion in Colloid & Interface Science* 6 (3), pp. 197–207. DOI: 10.1016/S1359-0294(01)00084-X.

Blunt, Martin J.; Bijeljic, Branko; Dong, Hu; Gharbi, Oussama; Iglauer, Stefan; Mostaghimi, Peyman et al. (2013): Pore-scale imaging and modelling. In *Advances in Water Resources* 51, pp. 197–216. DOI: 10.1016/j.advwatres.2012.03.003.

Broekhoff (1967): Studies on pore systems in catalysts IX. Calculation of pore distributions from the adsorption branch of nitrogen sorption isotherms in the case of open cylindrical pores A. Fundamental equations. In *Journal of Catalysis* 9 (1), pp. 8–14. DOI: 10.1016/0021-9517(67)90174-1.

Brownstein, K. R.; Tarr, C. E. (1979): Importance of classical diffusion in NMR studies of water in biological cells. In *Phys. Rev. A* 19 (6), pp. 2446–2453. DOI: 10.1103/PhysRevA.19.2446.

Brunauer, Stephen; Emmett, P. H.; Teller, Edward (1938): Adsorption of Gases in Multimolecular Layers. In *J. Am. Chem. Soc.* 60 (2), pp. 309–319. DOI: 10.1021/ja01269a023.

Bruschi, Lorenzo; Mistura, Giampaolo; Nguyen, Phuong T. M.; Do, Duong D.; Nicholson, David; Park, Sang-Joon; Lee, Woo (2015): Adsorption in alumina pores open at one and at both ends. In *Nanoscale* 7 (6), pp. 2587–2596. DOI: 10.1039/c4nr06469k.

Bultreys, Tom; van Stappen, Jeroen; Kock, Tim De; Boever, Wesley De; Boone, Marijn A.; van Hoorebeke, Luc; Cnudde, Veerle (2016): Investigating the relative permeability behavior of microporosity-rich carbonates and tight sandstones with multiscale pore network models. In *J. Geophys. Res. Solid Earth* 121 (11), pp. 7929–7945. DOI: 10.1002/2016JB013328.

Chiche, David; Digne, Mathieu; Revel, Renaud; Chanéac, Corinne; Jolivet, Jean-Pierre (2008): Accurate Determination of Oxide Nanoparticle Size and Shape Based on X-Ray Powder Pattern Simulation. Application to Boehmite AlOOH. In *J. Phys. Chem. C* 112 (23), pp. 8524–8533. DOI: 10.1021/jp710664h.

Cimino, Richard; Cychosz, Katie A.; Thommes, Matthias; Neimark, Alexander V. (2013): Experimental and theoretical studies of scanning adsorption–desorption isotherms. In *Colloids and Surfaces A: Physicochemical and Engineering Aspects* 437, pp. 76–89. DOI: 10.1016/j.colsurfa.2013.03.025.

Coasne, Benoit; Gubbins, Keith E.; Pellenq, Roland J.-M. (2004): A Grand Canonical Monte Carlo Study of Adsorption and Capillary Phenomena in Nanopores of Various Morphologies and Topologies. Testing the BET and BJH Characterization Methods. In *Part. Part. Syst. Charact.* 21 (2), pp. 149–160. DOI: 10.1002/ppsc.200400928.

Cohan, Leonard H. (1944): Hysteresis and the Capillary Theory of Adsorption of Vapors 1. In *J. Am. Chem. Soc.* 66 (1), pp. 98–105. DOI: 10.1021/ja01229a028.

- Coles, Mary E. (1999): 8. X-Ray Imaging. In : *Methods in the Physics of Porous Media*, vol. 35: Elsevier (Experimental Methods in the Physical Sciences), pp. 301–336.
- Coppens, M. O.; Bhatt, J. (2017): *Models Representing Porous Media* (Confidential Report). EUROKIN.
- Cormen, T.; Leiserson, C.; Rivest, R.; Stein, C.: *Introduction to Algorithms*, Third Edition.
- Cotts, R.M; Hoch, M.J.R; Sun, T.; Markert, J.T (1989): Pulsed field gradient stimulated echo methods for improved NMR diffusion measurements in heterogeneous systems. In *Journal of Magnetic Resonance (1969)* 83 (2), pp. 252–266. DOI: 10.1016/0022-2364(89)90189-3.
- Cruz, M.; Mayagoitia, V.; Rojas, F. (1989): Mechanistic studies of capillary processes in porous media. Part 2.—Construction of porous networks by Monte-Carlo methods. In *J. Chem. Soc., Faraday Trans. 1* 85 (8), p. 2079. DOI: 10.1039/F19898502079.
- Dadyburjor, Dady B. (1988): *Catalyst supports and supported catalysts. Theoretical and applied concepts.* By Alvin B. Stiles, Butterworth Publishers, Stoneham, MA, 1987, 270 pp. In *AIChE J* 34 (1), pp. 174–175. DOI: 10.1002/aic.690340129.
- Daigle, Hugh; Ezidiegwu, Sandra; Turner, Raymond (2015): Determining Relative Permeability In Shales By Including The Effects Of Pore Structure On Unsaturated Diffusion And Advection. In : *SPE Annual Technical Conference and Exhibition. SPE Annual Technical Conference and Exhibition.* Houston, Texas, USA, 2015-09-28: Society of Petroleum Engineers.
- Dash, J. G.; Rempel, A. W.; Wettlaufer, J. S. (2006): The physics of premelted ice and its geophysical consequences. In *Rev. Mod. Phys.* 78 (3), pp. 695–741. DOI: 10.1103/RevModPhys.78.695.
- Dean C. Douglass, David W. McCall (1958): Diffusion in Paraffin Hydrocarbons. In *J. Phys. Chem. B* 62, 1958, pp. 1102–1107.
- Demichelis; Yves; Ugliengo; Zicovich; Dovesi (2011): Physico-Chemical Features of Aluminum Hydroxides As Modeled with the Hybrid B3LYP Functional and Localized Basis Functions. In *J. Phys. Chem. C* 115 (27), pp. 13107–13134. DOI: 10.1021/jp200523x.
- Digne, Mathieu; Sautet, Philippe; Raybaud, Pascal; Toulhoat, Hervé; Artacho, Emilio (2002): Structure and Stability of Aluminum Hydroxides. A Theoretical Study. In *J. Phys. Chem. B* 106 (20), pp. 5155–5162. DOI: 10.1021/jp014182a.
- Do, D. D.; Herrera, L.; Fan, Chunyan; Wongkoblak, A.; Nicholson, D. (2010): The role of accessibility in the characterization of porous solids and their adsorption properties. In *Adsorption* 16 (1-2), pp. 3–15. DOI: 10.1007/s10450-009-9203-8.
- Dullien, F. (1979): *Porous Media Fluid Transport and Pore Structure*: Elsevier.

El Hannach, Mohamed; Soboleva, Tatyana; Malek, Kourosh; Franco, Alejandro A.; Prat, Marc; Pauchet, Joël; Holdcroft, Steven (2014): Characterization of pore network structure in catalyst layers of polymer electrolyte fuel cells. In *Journal of Power Sources* 247, pp. 322–326. DOI: 10.1016/j.jpowsour.2013.08.049.

Enniful, Henry R. N. B.; Schneider, Daniel; Hoppe, Antonia; König, Sandra; Fröba, Michael; Enke, Dirk; Valiullin, Rustem (2019): Comparative Gas Sorption and Cryoporometry Study of Mesoporous Glass Structure. Application of the Serially Connected Pore Model. In *Frontiers in chemistry* 7, p. 230. DOI: 10.3389/fchem.2019.00230.

Euzen P., Raybaud P. et al. (2002): Handbook of Porous Solids. Alumina (3).

Ezeuko, C. C.; Sen, A.; Grigoryan, A.; Gates, I. D. (2011): Pore-network modeling of biofilm evolution in porous media. In *Biotechnology and bioengineering* 108 (10), pp. 2413–2423. DOI: 10.1002/bit.23183.

Farrar, Thomas Clark; Becker, Edwin D. (1971): Pulse and Fourier transform NMR. Introduction to theory and methods. New York etc.: Academic Press.

Fatt (1956a): The Network Model of Porous Media. In *Society of Petroleum Engineers*, 1956.

Fatt, I. (1956b): The Network Model of Porous Media. In *Transactions of the AIME* 207 (01), pp. 144–181. DOI: 10.2118/574-G.

Feng, Chester; Stewart, Warren E. (1973): Practical Models for Isothermal Diffusion and Flow of Gases in Porous Solids. In *Ind. Eng. Chem. Fund.* 12 (2), pp. 143–147. DOI: 10.1021/i160046a001.

Ferreira (2018): Modélisation du transport intragranulaire dans un réacteur catalytique. Université Claude Bernard - Lyon 1, France.

Ferri, Giulia (2021): Identification et étude des descripteurs pertinents du solide lors de la synthèse de la boehmite, Paris. Université Paris-Saclay.

Fischer, Ulrich; Celia, Michael A. (1999): Prediction of relative and absolute permeabilities for gas and water from soil water retention curves using a pore-scale network model. In *Water Resour. Res.* 35 (4), pp. 1089–1100. DOI: 10.1029/1998WR900048.

Foster, Richard N.; Butt, John B. (1966): A computational model for the structure of porous materials employed in catalysis. In *AIChE J* 12 (1), pp. 180–185. DOI: 10.1002/aic.690120132.

G. Jerauld et al. (1984): Percolation and conduction on Voronoi and triangular networks: a case study in topological disorder. In *J. Phys. C: Solid State Phys.* 17, 1984, p. 1519.

- Gavalda, S.; Gubbins, K. E.; Hanzawa, Y.; Kaneko, K.; Thomson, K. T. (2002): Nitrogen Adsorption in Carbon Aerogels. A Molecular Simulation Study. In *Langmuir* 18 (6), pp. 2141–2151. DOI: 10.1021/la011132o.
- Gelb; Gubbins (1999): Correlation functions of adsorbed fluids in porous glass. A computer simulation study. In *Molecular Physics* 96 (12), pp. 1795–1804. DOI: 10.1080/00268979909483123.
- Gheorghiu, Stefan; Coppens, Marc-Olivier (2004): Optimal bimodal pore networks for heterogeneous catalysis. In *AIChE J.* 50 (4), pp. 812–820. DOI: 10.1002/aic.10076.
- Glowska, Aleksandra (2021): Multi-technique analysis of pore networks in gamma-alumina catalyst supports. University College London, Department of Chemical Engineering, London.
- Gommes, Cedric J. (2012): Adsorption, capillary bridge formation, and cavitation in SBA-15 corrugated mesopores: a Derjaguin-Broekhoff-de Boer analysis. In *Langmuir : the ACS journal of surfaces and colloids* 28 (11), pp. 5101–5115. DOI: 10.1021/la2051228.
- Grebenkov, Denis S. (2011): A fast random walk algorithm for computing the pulsed-gradient spin-echo signal in multiscale porous media. In *Journal of magnetic resonance (San Diego, Calif. : 1997)* 208 (2), pp. 243–255. DOI: 10.1016/j.jmr.2010.11.009.
- Grebenkov, Denis S.; Nguyen, Hang T.; Li, Jing-Rebecca (2013): A fast random walk algorithm for computing diffusion-weighted NMR signals in multi-scale porous media. A feasibility study for a Menger sponge. In *Microporous and Mesoporous Materials* 178, pp. 56–59. DOI: 10.1016/j.micromeso.2013.02.040.
- Hahn, E. L. (1950): Spin Echoes. In *Phys. Rev.* 80 (4), pp. 580–594. DOI: 10.1103/PhysRev.80.580.
- Hamamoto, Shoichiro; Moldrup, Per; Kawamoto, Ken; Sakaki, Toshihiro; Nishimura, Taku; Komatsu, Toshiko (2016): Pore network structure linked by X-ray CT to particle characteristics and transport parameters. In *Soils and Foundations* 56 (4), pp. 676–690. DOI: 10.1016/j.sandf.2016.07.008.
- Hannaoui, R.; Horgue, P.; Larachi, F.; Haroun, Y.; Augier, F.; Quintard, M.; Prat, M. (2015): Pore-network modeling of trickle bed reactors. Pressure drop analysis. In *Chemical Engineering Journal* 262, pp. 334–343. DOI: 10.1016/j.cej.2014.09.098.
- Helfferich, F. G. (1985): Principles of adsorption & adsorption processes, by D. M. Ruthven, John Wiley & Sons, 1984, xxiv + 433 pp. In *AIChE J* 31 (3), pp. 523–524. DOI: 10.1002/aic.690310335.

Hitchcock, Iain; Holt, Elizabeth M.; Lowe, John P.; Rigby, Sean P. (2011): Studies of freezing–melting hysteresis in cryoporometry scanning loop experiments using NMR diffusometry and relaxometry. In *Chemical Engineering Science* 66 (4), pp. 582–592. DOI: 10.1016/j.ces.2010.10.027.

Hitchcock, Iain; Lunel, Marie; Bakalis, Serafim; Fletcher, Robin S.; Holt, Elizabeth M.; Rigby, Sean P. (2014): Improving sensitivity and accuracy of pore structural characterisation using scanning curves in integrated gas sorption and mercury porosimetry experiments. In *Journal of colloid and interface science* 417, pp. 88–99. DOI: 10.1016/j.jcis.2013.11.025.

Hollewand, M. P.; Gladden, L. F. (1991): Modelling of diffusion and reaction in porous catalysts using a random three-dimensional network model. In *Chemical Engineering Science* 47 (7), pp. 1761–1770. DOI: 10.1016/0009-2509(92)85023-5.

Hollewand, M. P.; Gladden, L. F. (1992): Representation of porous catalysts using random pore networks. In *Chemical Engineering Science* 47 (9-11), pp. 2757–2762. DOI: 10.1016/0009-2509(92)87125-A.

Hollewand, Michael P.; Gladden, Lynn F. (1995): Transport heterogeneity in porous pellets—II. NMR imaging studies under transient and steady-state conditions. In *Chemical Engineering Science* 50 (2), pp. 327–344. DOI: 10.1016/0009-2509(94)00219-H.

Hoshen, J.; Kopelman, R. (1976): Percolation and cluster distribution. I. Cluster multiple labeling technique and critical concentration algorithm. In *Phys. Rev. B* 14 (8), pp. 3438–3445. DOI: 10.1103/PhysRevB.14.3438.

Huang, Xinwo; Bandilla, Karl W.; Celia, Michael A. (2016): Multi-Physics Pore-Network Modeling of Two-Phase Shale Matrix Flows. In *Transp Porous Med* 111 (1), pp. 123–141. DOI: 10.1007/s11242-015-0584-8.

Ingram; Slade; Southern; Sylvain (1996): Dehydroxylation sequences of gibbsite and boehmite. Study of differences between soak and flash calcination and of particle-size effects. In *J. Mater. Chem.* 6 (1), p. 73. DOI: 10.1039/JM9960600073.

Javed, Muhammad Asadullah; Komulainen, Sanna; Daigle, Hugh; Zhang, Boyang; Vaara, Juha; Zhou, Bing; Telkki, Ville-Veikko (2019): Determination of pore structures and dynamics of fluids in hydrated cements and natural shales by various <sup>1</sup>H and <sup>129</sup>Xe NMR methods. In *Microporous and Mesoporous Materials* 281, pp. 66–74. DOI: 10.1016/j.micromeso.2019.02.034.

Johannessen, Eivind; Wang, Gang; Coppens, Marc-Olivier (2007): Optimal Distributor Networks in Porous Catalyst Pellets. I. Molecular Diffusion. In *Ind. Eng. Chem. Res.* 46 (12), pp. 4245–4256. DOI: 10.1021/ie061444s.

Johnson; Stewart (1965): Pore structure and gaseous diffusion in solid catalysts. In *Journal of Catalysis* 4 (2), pp. 248–252. DOI: 10.1016/0021-9517(65)90015-1.

Jolivet (2016): De la solution à l'oxyde. EDP Sciences.

Joseph P. Hornak (1997): The basics of NMR. Rochester Institute of Technology. Available online at <http://www.cis.rit.edu/htbooks/nmr/inside.htm>, updated on 2019.

Kansal, Anuraag R.; Torquato, Salvatore; Stillinger, Frank H. (2002): Computer generation of dense polydisperse sphere packings. In *The Journal of Chemical Physics* 117 (18), pp. 8212–8218. DOI: 10.1063/1.1511510.

Kaseman, D.; Ozcan S.; Du S. (2020): NMR - Theory. University of California, Davis. Available online at [https://chem.libretexts.org/Bookshelves/Physical\\_and\\_Theoretical\\_Chemistry\\_Textbook\\_Maps/Supplemental\\_Modules\\_\(Physical\\_and\\_Theoretical\\_Chemistry\)/Spectroscopy/Magnetic\\_Resonance\\_Spectroscopies/Nuclear\\_Magnetic\\_Resonance/NMR\\_-\\_Theory](https://chem.libretexts.org/Bookshelves/Physical_and_Theoretical_Chemistry_Textbook_Maps/Supplemental_Modules_(Physical_and_Theoretical_Chemistry)/Spectroscopy/Magnetic_Resonance_Spectroscopies/Nuclear_Magnetic_Resonance/NMR_-_Theory).

Kaufmann, Josef (2010): Pore space analysis of cement-based materials by combined Nitrogen sorption – Wood's metal impregnation and multi-cycle mercury intrusion. In *Cement and Concrete Composites* 32 (7), pp. 514–522. DOI: 10.1016/j.cemconcomp.2010.04.003.

Kaufmann, Josef; Loser, Roman; Leemann, Andreas (2009): Analysis of cement-bonded materials by multi-cycle mercury intrusion and nitrogen sorption. In *Journal of colloid and interface science* 336 (2), pp. 730–737. DOI: 10.1016/j.jcis.2009.05.029.

Keil, F. (1999): Diffusion and reaction in porous networks. In *Catalysis Today* 53 (2), pp. 245–258. DOI: 10.1016/S0920-5861(99)00119-4.

Keller, Lukas M.; Schuetz, Philipp; Erni, Rolf; Rossell, Marta D.; Lucas, Falk; Gasser, Philippe; Holzer, Lorenz (2013): Characterization of multi-scale microstructural features in Opalinus Clay. In *Microporous and Mesoporous Materials* 170, pp. 83–94. DOI: 10.1016/j.micromeso.2012.11.029.

Ketcham, Richard A.; Carlson, William D. (2001): Acquisition, optimization and interpretation of X-ray computed tomographic imagery. Applications to the geosciences. In *Computers & Geosciences* 27 (4), pp. 381–400. DOI: 10.1016/S0098-3004(00)00116-3.

Kikkinides, E. S.; Monson, P. A.; Valiullin, R. (2020): Sorption Isotherm Reconstruction and Extraction of Pore Size Distributions for Serially Connected Pore Model (SCPM) Structures Employing Algorithmic and Statistical Models. In *J. Phys. Chem. C* 124 (39), pp. 21591–21607. DOI: 10.1021/acs.jpcc.0c06710.

- Knackstedt, Mark A.; Sheppard, Adrian P.; Pinczewski, W. V. (1998): Simulation of mercury porosimetry on correlated grids. Evidence for extended correlated heterogeneity at the pore scale in rocks. In *Phys. Rev. E* 58 (6), R6923-R6926. DOI: 10.1103/PhysRevE.58.R6923.
- Kolesnikov, A. L.; Budkov, Yu A.; Gor, G. Y. (2020): Adsorption-induced deformation of mesoporous materials with corrugated cylindrical pores. In *The Journal of Chemical Physics* 153 (19), p. 194703. DOI: 10.1063/5.0025473.
- Kolitcheff (2017): Approche multitechnique des phénomènes de diffusion en hydrotraitement de distillats. Université Claude Bernard - Lyon 1, France.
- Kondrashova, Daria; Valiullin, Rustem (2013): Improving structural analysis of disordered mesoporous materials using NMR cryoporometry. In *Microporous and Mesoporous Materials* 178, pp. 15–19. DOI: 10.1016/j.micromeso.2013.02.053.
- Kotanigawa; Yamamoto; Masahiro; Hattori; Tanabe (1981): The influence of preparation methods on the pore structure of alumina. In *Applied Catalysis* 1 (3-4), pp. 185–200. DOI: 10.1016/0166-9834(81)80006-1.
- Lapidus, G.; Lane, A.; NG, K.; Conner, W. (2007): INTERPRETATION OF MERCURY POROSIMETRY DATA USING A PORE-THROAT NETWORK MODEL. In *Chemical Engineering Communications* 38 (1-2), pp. 33–56. DOI: 10.1080/00986448508911294.
- Larson, R. G.; Scriven, L. E.; Davis, H. T. (1981): Percolation theory of two phase flow in porous media. In *Chemical Engineering Science* 36 (1), pp. 57–73. DOI: 10.1016/0009-2509(81)80048-6.
- Latour, L. L.; Mitra, P. P.; Kleinberg, R. L.; Sotak, C. H. (1993): Time-Dependent Diffusion Coefficient of Fluids in Porous Media as a Probe of Surface-to-Volume Ratio. In *Journal of Magnetic Resonance, Series A* 101 (3), pp. 342–346. DOI: 10.1006/jmra.1993.1056.
- Levitt, Malcolm H. (2008): Spin dynamics. Basics of nuclear magnetic resonance. 2nd edition. Chichester, Hoboken (NJ): J. Wiley & sons.
- Li; Peters; Celia (2006): Upscaling geochemical reaction rates using pore-scale network modeling. In *Advances in Water Resources* 29 (9), pp. 1351–1370. DOI: 10.1016/j.advwatres.2005.10.011.
- Li, Jing-Rebecca; Nguyen, Van-Dang; Tran, Try Nguyen; Valdman, Jan; Trang, Cong-Bang; van Nguyen, Khieu et al. (2019): SpinDoctor. A MATLAB toolbox for diffusion MRI simulation. In *NeuroImage* 202, p. 116120. DOI: 10.1016/j.neuroimage.2019.116120.
- Li, Yimin; Somorjai, Gabor A. (2007): Surface Premelting of Ice. In *J. Phys. Chem. C* 111 (27), pp. 9631–9637. DOI: 10.1021/jp071102f.

- Liljeblad, Jonathan F. D.; Furó, István; Tyrode, Eric C. (2016): The premolten layer of ice next to a hydrophilic solid surface. Correlating adhesion with molecular properties. In *Physical chemistry chemical physics : PCCP* 19 (1), pp. 305–317. DOI: 10.1039/c6cp05303c.
- Lin, C.; Cohen, M. H. (1982): Quantitative methods for microgeometric modeling. In *Journal of Applied Physics* 53 (6), pp. 4152–4165. DOI: 10.1063/1.331238.
- Lin, Guoxing (2018): General pulsed-field gradient signal attenuation expression based on a fractional integral modified-Bloch equation. In *Communications in Nonlinear Science and Numerical Simulation* 63, pp. 404–420. DOI: 10.1016/j.cnsns.2018.04.008.
- Lin, Guoxing; Zhang, Jinghui; Cao, Haihui; Jones, Alan A. (2003): A Lattice Model for the Simulation of Diffusion in Heterogeneous Polymer Systems. Simulation of Apparent Diffusion Constants as Determined by Pulse-Field-Gradient Nuclear Magnetic Resonance. In *J. Phys. Chem. B* 107 (25), pp. 6179–6186. DOI: 10.1021/jp022619o.
- Lippens (1961): Structure and Texture of Aluminas. Technische Hogeschool te Delft, Delft.
- Liu, Hailing; Zhang, Lin; Seaton, Nigel A. (1993): Analysis of Sorption Hysteresis in Mesoporous Solids Using a Pore Network Model. In *Journal of colloid and interface science* 156 (2), pp. 285–293. DOI: 10.1006/jcis.1993.1113.
- López-Ramón, M. V.; Jagiełło, J.; Bandosz, T. J.; Seaton, N. A. (1997): Determination of the Pore Size Distribution and Network Connectivity in Microporous Solids by Adsorption Measurements and Monte Carlo Simulation. In *Langmuir* 13 (16), pp. 4435–4445. DOI: 10.1021/la970197h.
- Lowell, S.; Shields, Joan E. (1991): Powder Surface Area and Porosity. Cham: Springer International Publishing. Available online at <http://dx.doi.org/10.1007/978-94-015-7955-1>.
- MacMullin R. B.; Muccini, G. A. (1956): Characteristics of porous beds and structures. In *AIChE J* 2 (3), pp. 393–403. DOI: 10.1002/aic.690020320.
- Mann; Androusoyopoulos; Golshan, H. (1981): Application of a stochastic network pore model to oil-bearing rock with observations relevant to oil recovery. In *Chemical Engineering Science* 36 (2), pp. 337–346. DOI: 10.1016/0009-2509(81)85013-0.
- Mann, R.; Golshan, H. (1981): Application of a stochastic network pore model to a catalyst pellet. In *Chemical Engineering Communications* 12 (4-6), pp. 377–391. DOI: 10.1080/00986448108910845.
- Mann, R.; Thomson, G. (1987): Deactivation of a supported zeolite catalyst. Simulation of diffusion, reaction and coke deposition in a parallel bundle. In *Chemical Engineering Science* 42 (3), pp. 555–563. DOI: 10.1016/0009-2509(87)80017-9.

- Mascotto, Simone; Janke, Wolfhard; Valiullin, Rustem (2017): Ice Nucleation in Periodic Arrays of Spherical Nanocages. In *J. Phys. Chem. C* 121 (42), pp. 23788–23792. DOI: 10.1021/acs.jpcc.7b08490.
- Masson, Yder; Pride, Steven R. (2014): A Fast Algorithm for Invasion Percolation. In *Transp Porous Med* 102 (2), pp. 301–312. DOI: 10.1007/s11242-014-0277-8.
- Mayagoitia, V.; Rojas, F.; Kornhauser, I.; Pérez-Aguilar, H. (1997): Modeling of Porous Media and Surface Structures. Their True Essence as Networks. In *Langmuir* 13 (5), pp. 1327–1331. DOI: 10.1021/la950812m.
- Mayagoitia, V.; Rojas, F.; Kornhauser, I.; Zgrablich, G.; Faccio, J.; Gilot, B.; Guiglian, C. (1996): Refinements of the Twofold Description of Porous Media. In *Langmuir* 12 (1), pp. 211–216. DOI: 10.1021/la940704k.
- Mehmani, Ayaz; Prodanović, Maša (2014): The application of sorption hysteresis in nanopetrophysics using multiscale multiphysics network models. In *International Journal of Coal Geology* 128-129, pp. 96–108. DOI: 10.1016/j.coal.2014.03.008.
- Meyers, J. J.; Liapis, A. I. (1999): Network modeling of the convective flow and diffusion of molecules adsorbing in monoliths and in porous particles packed in a chromatographic column. In *Journal of Chromatography A* 852 (1), pp. 3–23. DOI: 10.1016/S0021-9673(99)00443-4.
- Meyers, J.J; Nahar, S.; Ludlow, D.K; Liapis, A.I (2001): Determination of the pore connectivity and pore size distribution and pore spatial distribution of porous chromatographic particles from nitrogen sorption measurements and pore network modelling theory. In *Journal of Chromatography A* 907 (1-2), pp. 57–71. DOI: 10.1016/S0021-9673(00)01018-9.
- Mezedur, Minas M.; Kaviany, Massoud; Moore, Wayne (2002): Effect of pore structure, randomness and size on effective mass diffusivity. In *AIChE J* 48 (1), pp. 15–24. DOI: 10.1002/aic.690480104.
- Mitchell, J.; Webber, J.; Strange, J. (2008): Nuclear magnetic resonance cryoporometry. In *Physics Reports* 461 (1), pp. 1–36. DOI: 10.1016/j.physrep.2008.02.001.
- Mitra; Sen (1992a): Effects of microgeometry and surface relaxation on NMR pulsed-field-gradient experiments. Simple pore geometries. In *Physical review. B, Condensed matter* 45 (1), pp. 143–156. DOI: 10.1103/physrevb.45.143.
- Mitra, Partha P.; Sen, Pabitra N. (1992b): Effects of surface relaxation on NMR pulsed field gradient experiments in porous media. In *Physica A: Statistical Mechanics and its Applications* 186 (1-2), pp. 109–114. DOI: 10.1016/0378-4371(92)90369-2.

- Mohanty; Scriven (1987): Physics of Oil Entrapment in Water-Wet Rock.
- Mohanty, K. K.; Davis, H. T.; Scriven, L. E. (2013): Physics of Oil Entrapment in Water-Wet Rock. In *SPE Reservoir Engineering 2* (01), pp. 113–128. DOI: 10.2118/9406-PA.
- Mohanty, Kishore K. (1981): Fluids in porous media: Two-phase distribution and flow. University of Minnesota, United States.
- Mohnke, O. (2014): Jointly deriving NMR surface relaxivity and pore size distributions by NMR relaxation experiments on partially desaturated rocks. In *Water Resour. Res.* 50 (6), pp. 5309–5321. DOI: 10.1002/2014WR015282.
- Montiel, B.; Moreno, C.; Sánchez, J.; Romero, M. (2019): Simulation of Dual Site-Bond Network Modeling for Porous Media through the Graphics Class in Java. In *International Journal of Chemical Engineering and Applications* 10, 2019.
- Moore, T. F.; Slobod, R. L. (2013): Displacement of Oil by Water-Effect of Wettability, Rate, and Viscosity on Recovery. In : Fall Meeting of the Petroleum Branch of AIME. Fall Meeting of the Petroleum Branch of AIME. New Orleans, Louisiana, 1955-10-02: Society of Petroleum Engineers.
- Morin, C. (2014): Préparation d'alumine à porosité contrôlée : étude de l'interaction de la boehmite dans des solvants et des propriétés fonctionnelles des matériaux résultants. SORBONNE, France.
- Murray, K. L.; Seaton, N. A.; Day, M. A. (1998): Analysis of the Spatial Variation of the Pore Network Coordination Number of Porous Solids Using Nitrogen Sorption Measurements. In *Langmuir* 14 (17), pp. 4953–4954. DOI: 10.1021/la980113k.
- Murray, K. L.; Seaton, N. A.; Day, M. A. (1999a): Use of Mercury Intrusion Data, Combined with Nitrogen Adsorption Measurements, as a Probe of Pore Network Connectivity. In *Langmuir* 15 (23), pp. 8155–8160. DOI: 10.1021/la990250x.
- Murray, K. L.; Seaton, N. A.; Day, M. A. (1999b): Use of Mercury Intrusion Data, Combined with Nitrogen Adsorption Measurements, as a Probe of Pore Network Connectivity. In *Langmuir* 15 (23), pp. 8155–8160. DOI: 10.1021/la990250x.
- Neuman, C. H. (1974): Spin echo of spins diffusing in a bounded medium. In *The Journal of Chemical Physics* 60 (11), pp. 4508–4511. DOI: 10.1063/1.1680931.
- Newsome, David; Gunawan, Sofranita; Baron, Gino; Denayer, Joeri; Coppens, Marc-Olivier (2014): Adsorption of CO<sub>2</sub> and N<sub>2</sub> in Na-ZSM-5. Effects of Na<sup>+</sup> and Al content studied by Grand Canonical Monte Carlo simulations and experiments. In *Adsorption* 20 (1), pp. 157–171. DOI: 10.1007/s10450-013-9560-1.

- Nguyen, Phuong T. M.; Do, D. D.; Nicholson, D. (2011): On the Hysteresis Loop of Argon Adsorption in Cylindrical Pores. In *J. Phys. Chem. C* 115 (11), pp. 4706–4720. DOI: 10.1021/jp111254j.
- Nicholson, Charles (2001): Diffusion and related transport mechanisms in brain tissue. In *Rep. Prog. Phys.* 64 (7), pp. 815–884. DOI: 10.1088/0034-4885/64/7/202.
- Ning, Lipeng; Özarlan, Evren; Westin, Carl-Fredrik; Rathi, Yogesh (2017): Precise Inference and Characterization of Structural Organization (PICASO) of tissue from molecular diffusion. In *NeuroImage* 146, pp. 452–473. DOI: 10.1016/j.neuroimage.2016.09.057.
- Øren, P. (2002). In *Transp Porous Med* 46 (2/3), pp. 311–343. DOI: 10.1023/A:1015031122338.
- Palmer, J. C.; Brennan, J. K.; Hurley, M. M.; Balboa, A.; Gubbins, K. E. (2009): Detailed structural models for activated carbons from molecular simulation. In *Carbon* 47 (12), pp. 2904–2913. DOI: 10.1016/j.carbon.2009.06.037.
- Parlar, M.; Yortsos, Y.C (1988): Percolation theory of vapor adsorption—desorption processes in porous materials. In *Journal of colloid and interface science* 124 (1), pp. 162–176. DOI: 10.1016/0021-9797(88)90337-2.
- Parlar, M.; Yortsos, Y.C (1989): Nucleation and pore geometry effects in capillary desorption processes in porous media. In *Journal of colloid and interface science* 132 (2), pp. 425–443. DOI: 10.1016/0021-9797(89)90257-9.
- Perkins, Emily L.; Lowe, John P.; Edler, Karen J.; Tanko, Nuradeen; Rigby, Sean P. (2008): Determination of the percolation properties and pore connectivity for mesoporous solids using NMR cryodiffusometry. In *Chemical Engineering Science* 63 (7), pp. 1929–1940. DOI: 10.1016/j.ces.2007.12.022.
- Peter Matthews, G.; Ridgway, Cathy J.; Small, Joe S. (1996): Modelling of simulated clay precipitation within reservoir sandstones. In *Marine and Petroleum Geology* 13 (5), pp. 581–589. DOI: 10.1016/0264-8172(95)00099-2.
- Petrov, Oleg V.; Furó, István (2009): NMR cryoporometry. Principles, applications and potential. In *Progress in Nuclear Magnetic Resonance Spectroscopy* 54 (2), pp. 97–122. DOI: 10.1016/j.pnmrs.2008.06.001.
- Price, William S. (1997): Pulsed-field gradient nuclear magnetic resonance as a tool for studying translational diffusion. Part 1. Basic theory. In *Concepts Magn. Reson.* 9 (5), pp. 299–336. DOI: 10.1002/(SICI)1099-0534(1997)9:5<299::AID-CMR2>3.0.CO;2-U.

- Price, William S. (1998): Pulsed-field gradient nuclear magnetic resonance as a tool for studying translational diffusion. Part II. Experimental aspects. In *Concepts Magn. Reson.* 10 (4), pp. 197–237. DOI: 10.1002/(SICI)1099-0534(1998)10:4<197::AID-CMR1>3.0.CO;2-S.
- Price, William S.; Hwang, Lian-Pin (1992): Some Recent Developments in NMR Approaches for Studying Liquid Molecular Dynamics and Their Biological Applications. In *Jnl Chinese Chemical Soc* 39 (6), pp. 479–496. DOI: 10.1002/jccs.199200082.
- Raouf, Amir; Hassanizadeh, S. Majid (2010): A New Method for Generating Pore-Network Models of Porous Media. In *Transp Porous Med* 81 (3), pp. 391–407. DOI: 10.1007/s11242-009-9412-3.
- Riccardo, J. L.; Pereyra, V.; Zgrablich, G.; Rojas, F.; Mayagoitia, V.; Kornhauser, I. (1993): Characterization of energetic surface heterogeneity by a dual site-bond model. In *Langmuir* 9 (10), pp. 2730–2736. DOI: 10.1021/la00034a037.
- Rieckmann, Christina; Keil, Frerich J. (1997): Multicomponent Diffusion and Reaction in Three-Dimensional Networks. General Kinetics †. In *Ind. Eng. Chem. Res.* 36 (8), pp. 3275–3281. DOI: 10.1021/ie9605847.
- Rigby, Sean P.; Fletcher, Robin S.; Raistrick, James H.; Riley, Sandra N. (2002): Characterisation of porous solids using a synergistic combination of nitrogen sorption, mercury porosimetry, electron microscopy and micro-focus X-ray imaging techniques. In *Phys. Chem. Chem. Phys.* 4 (14), pp. 3467–3481. DOI: 10.1039/b110781j.
- Rigby, Sean P.; Hasan, Muayad; Stevens, Lee; Williams, Huw E. L.; Fletcher, Robin S. (2017): Determination of Pore Network Accessibility in Hierarchical Porous Solids. In *Ind. Eng. Chem. Res.* 56 (50), pp. 14822–14831. DOI: 10.1021/acs.iecr.7b04659.
- Rodrigues, Alírio E.; LeVan, M. Douglas; Tondeur, Daniel (1989): Adsorption. Science and Technology. Dordrecht: Springer Netherlands (NATO ASI Series, Series E: Applied Sciences, 158).
- Rojas, F.; Kornhauser, I.; Felipe, C.; Esparza, J. M.; Cordero, S.; Domínguez, A.; Riccardo, J. L. (2002): Capillary condensation in heterogeneous mesoporous networks consisting of variable connectivity and pore-size correlation. In *Phys. Chem. Chem. Phys.* 4 (11), pp. 2346–2355. DOI: 10.1039/b108785a.
- Rosen, Gerald (1976): The mathematical theory of diffusion and reaction in permeable catalysis. In *Bltm Mathcal Biology* 38 (1), pp. 95–96. DOI: 10.1007/BF02459545.
- Rouquerol, Françoise; Rouquerol, J.; Sing, K. S. W.; Llewellyn, P. L.; Maurin, G. (2014a): Adsorption by powders and porous solids. Principles, methodology and applications. Second edition. Amsterdam: Elsevier/AP.

Rouquerol, Françoise; Rouquerol, J.; Sing, K. S. W.; Llewellyn, P. L.; Maurin, G. (2014b): Adsorption by powders and porous solids. Principles, methodology and applications. Second edition. Amsterdam: Elsevier/AP.

Rouquerol, Jean; Baron, Gino; Denoyel, Renaud; Giesche, Herbert; Groen, Johan; Klobes, Peter et al. (2011): Liquid intrusion and alternative methods for the characterization of macroporous materials (IUPAC Technical Report). In *Pure and Applied Chemistry* 84 (1), pp. 107–136. DOI: 10.1351/PAC-REP-10-11-19.

Saalfeld, H.; Wedde, M. (1974): Refinement of the crystal structure of gibbsite, Al(OH) 3. In *Zeitschrift für Kristallographie* 139 (1-2), pp. 129–135. DOI: 10.1524/zkri.1974.139.1-2.129.

Sadeghi, Mohammad Amin; Aghighi, Mahmoudreza; Barralet, Jake; Gostick, Jeff T. (2017): Pore network modeling of reaction-diffusion in hierarchical porous particles. The effects of microstructure. In *Chemical Engineering Journal* 330, pp. 1002–1011. DOI: 10.1016/j.cej.2017.07.139.

Sahimi, Muhammad; Gavalas, George R.; Tsotsis, Theodore T. (1990): Statistical and continuum models of fluid-solid reactions in porous media. In *Chemical Engineering Science* 45 (6), pp. 1443–1502. DOI: 10.1016/0009-2509(90)80001-U.

Salmas, Constantin E.; Androutsopoulos, George P. (2001): A Novel Pore Structure Tortuosity Concept Based on Nitrogen Sorption Hysteresis Data. In *Ind. Eng. Chem. Res.* 40 (2), pp. 721–730. DOI: 10.1021/ie000626y.

Santos; Kiyohara; Souza (1996): Thermal transformation of synthetic euhedral and fibrillar crystals of boehmite into aluminas. In *Materials Research Bulletin* 31 (7), pp. 799–807. DOI: 10.1016/0025-5408(96)00068-2.

Sasloglou, S.A; Petrou, J.K; Kanellopoulos, N.K; Androutsopoulos, G.P (2000): Realistic random sphere pack model for the prediction of sorption isotherms. In *Microporous and Mesoporous Materials* 39 (3), pp. 477–483. DOI: 10.1016/S1387-1811(00)00159-1.

Satik. C., Yortsos. Y. (1995): A Pore Network Model For Adsorption In Porous Media. United States, 1995. Available online at <https://www.osti.gov/biblio/889373>.

Schlüter, Steffen; Sheppard, Adrian; Brown, Kendra; Wildenschild, Dorte (2014): Image processing of multiphase images obtained via X-ray microtomography. A review. In *Water Resour. Res.* 50 (4), pp. 3615–3639. DOI: 10.1002/2014WR015256.

Schoen, R.; Roberson (1970): Structures of aluminum hydroxide and geochemical implication. In *American Mineralogist* 55, 1970, pp. 43–77.

- Schreiber, Andreas; Ketelsen, Ingke; Findenegg, Gerhard H. (2001): Melting and freezing of water in ordered mesoporous silica materials. In *Phys. Chem. Chem. Phys.* 3 (7), pp. 1185–1195. DOI: 10.1039/b010086m.
- Schüth, Ferdi (Ed.) (2002a): Handbook of porous solids. Weinheim: Wiley-VCH. Available online at <https://onlinelibrary.wiley.com/doi/book/10.1002/9783527618286>.
- Schüth, Ferdi (Ed.) (2002b): Handbook of porous solids. Weinheim: Wiley-VCH. Available online at <https://onlinelibrary.wiley.com/doi/book/10.1002/9783527618286>.
- Seaton, N. A. (1991): Determination of the connectivity of porous solids from nitrogen sorption measurements. In *Chemical Engineering Science* 46 (8), pp. 1895–1909. DOI: 10.1016/0009-2509(91)80151-N.
- Sharratt, P. N.; Mann, R. (1987): Some observations on the variation of tortuosity with Thiele modulus and pore size distribution. In *Chemical Engineering Science* 42 (7), pp. 1565–1576. DOI: 10.1016/0009-2509(87)80161-6.
- Sheppard, Adrian P.; Knackstedt, Mark A.; Pinczewski, W. V.; Sahimi, Muhammad (1999): Invasion percolation. New algorithms and universality classes. In *J. Phys. A: Math. Gen.* 32 (49), L521-L529. DOI: 10.1088/0305-4470/32/49/101.
- Silbert, Leonardo E.; Ertas, Deniz; Grest, Gary S.; Halsey, Thomas C.; Levine, Dov (2002): Geometry of frictionless and frictional sphere packings. In *Physical review. E, Statistical, nonlinear, and soft matter physics* 65 (3 Pt 1), p. 31304. DOI: 10.1103/PhysRevE.65.031304.
- Sing, K. S. W. (1985): Reporting physisorption data for gas/solid systems with special reference to the determination of surface area and porosity (Recommendations 1984). In *Pure and Applied Chemistry* 57 (4), pp. 603–619. DOI: 10.1351/pac198557040603.
- Šolcová, O.; Matějová, L.; Schneider, P. (2006): Pore-size distributions from nitrogen adsorption revisited. Models comparison with controlled-pore glasses. In *Applied Catalysis A: General* 313 (2), pp. 167–176. DOI: 10.1016/j.apcata.2006.07.021.
- Song, Wenhui; Yao, Jun; Wang, Dongying; Li, Yang; Sun, Hai; Yang, Yongfei (2020): Dynamic pore network modelling of real gas transport in shale nanopore structure. In *Journal of Petroleum Science and Engineering* 184, p. 106506. DOI: 10.1016/j.petrol.2019.106506.
- Spearing, Michael; Matthews, G. Peter (1991): Modelling characteristic properties of sandstones. In *Transp Porous Med* 6 (1), pp. 71–90. DOI: 10.1007/BF00136822.

- Stejskal, E. O.; Tanner, J. E. (1965): Spin Diffusion Measurements. Spin Echoes in the Presence of a Time-Dependent Field Gradient. In *The Journal of Chemical Physics* 42 (1), pp. 288–292. DOI: 10.1063/1.1695690.
- Strange; Rahman; Smith (1993): Characterization of porous solids by NMR. In *Physical review letters* 71 (21), pp. 3589–3591. DOI: 10.1103/PhysRevLett.71.3589.
- Tian, Xiao; Daigle, Hugh (2018): Permeability prediction from a pore-scale network model constrained by low-pressure nitrogen sorption isotherms. In *Journal of Petroleum Science and Engineering* 162, pp. 554–566. DOI: 10.1016/j.petrol.2017.10.062.
- Torrey, H. C. (1956): Bloch Equations with Diffusion Terms. In *Phys. Rev.* 104 (3), pp. 563–565. DOI: 10.1103/PhysRev.104.563.
- Tranter, T. G.; Gostick, J. T.; Burns, A. D.; Gale, W. F. (2018): Capillary Hysteresis in Neutrally Wettable Fibrous Media. A Pore Network Study of a Fuel Cell Electrode. In *Transp Porous Med* 121 (3), pp. 597–620. DOI: 10.1007/s11242-017-0973-2.
- Tsakiroglou, Christos D.; Payatakes, Alkiviades C. (1991): Effects of pore-size correlations on mercury porosimetry curves. In *Journal of colloid and interface science* 146 (2), pp. 479–494. DOI: 10.1016/0021-9797(91)90212-Q.
- Tycko, Robert (Ed.) (1994): Nuclear magnetic resonance probes of molecular dynamics. Dordrecht, Boston: Kluwer Academic Publishers (Understanding chemical reactivity).
- Uchic, Michael D.; Holzer, Lorenz; Inkson, Beverley J.; Principe, Edward L.; Munroe, Paul (2007): Three-Dimensional Microstructural Characterization Using Focused Ion Beam Tomography. In *MRS Bull.* 32 (5), pp. 408–416. DOI: 10.1557/mrs2007.64.
- Valvatne, Per H.; Blunt, Martin J. (2004): Predictive pore-scale modeling of two-phase flow in mixed wet media. In *Water Resour. Res.* 40 (7), p. 537. DOI: 10.1029/2003WR002627.
- van Kampen, N. G. (2007): Stochastic processes in physics and chemistry. 3rd ed. Amsterdam, Boston (Mass.), Heidelberg etc.: Elsevier (North-Holland personal library).
- van Keken, P. E.; Yuen, D. A.; Petzold, L. R. (1995): DASPK: A new high order and adaptive time-integration technique with applications to mantle convection with strongly temperature-and pressure-dependent rheology. In *Geophysical & Astrophysical Fluid Dynamics* 80 (1-2), pp. 57–74. DOI: 10.1080/03091929508229763.
- Villadsen, J. V.; Stewart, W. E. (1967): Solution of boundary-value problems by orthogonal collocation. In *Chemical Engineering Science* 22 (11), pp. 1483–1501. DOI: 10.1016/0009-2509(67)80074-5.
- Voronoi, Georges (1908): Nouvelles applications des paramètres continus à la théorie des formes quadratiques. Premier mémoire. Sur quelques propriétés des formes quadratiques

positives parfaites. In *Journal für die reine und angewandte Mathematik (Crelles Journal)* 1908 (133), pp. 97–102. DOI: 10.1515/crll.1908.133.97.

Wakao, N.; Smith, J. M. (1962): Diffusion in catalyst pellets. In *Chemical Engineering Science* 17 (11), pp. 825–834. DOI: 10.1016/0009-2509(62)87015-8.

Wang, Haisheng (2017): Morphological Modelling and Transport Properties of Mesoporous Alumina. l'Université de recherche Paris Sciences et Lettres, France.

Wang, Haisheng; Jeulin, Dominique; Willot, François; Sorbier, Loïc; Moreaud, Maxime (2018): Modelling of the microstructure of mesoporous alumina constrained by morphological simulation of nitrogen porosimetry. In *Colloids and Surfaces A: Physicochemical and Engineering Aspects* 553, pp. 378–396. DOI: 10.1016/j.colsurfa.2018.05.043.

Waudby, Christopher A.; Christodoulou, John (2011): GPU accelerated Monte Carlo simulation of pulsed-field gradient NMR experiments. In *Journal of magnetic resonance (San Diego, Calif. : 1997)* 211 (1), pp. 67–73. DOI: 10.1016/j.jmr.2011.04.004.

Wefers; Misra (1987): Oxides And Hydroxides of Aluminium. In *Alcoa Laboratories*, 1987.

Wheeler, Ahlborn (1951): Reaction Rates and Selectivity in Catalyst Pores. In, vol. 3: Elsevier (Advances in Catalysis), pp. 249–327.

Wilkinson D., Willemsen J. (1983): Invasion percolation: a new form of percolation theory. In *J. Phys. A: Math* 16.

Wilson, Robert C.; Hürlimann, Martin D. (2006): Relationship between susceptibility induced field inhomogeneities, restricted diffusion, and relaxation in sedimentary rocks. In *Journal of magnetic resonance (San Diego, Calif. : 1997)* 183 (1), pp. 1–12. DOI: 10.1016/j.jmr.2006.07.006.

Wirth, Richard (2009): Focused Ion Beam (FIB) combined with SEM and TEM. Advanced analytical tools for studies of chemical composition, microstructure and crystal structure in geomaterials on a nanometre scale. In *Chemical Geology* 261 (3-4), pp. 217–229. DOI: 10.1016/j.chemgeo.2008.05.019.

Wongkoblapp, A.; Do, D. D.; Birkett, G.; Nicholson, D. (2011): A critical assessment of capillary condensation and evaporation equations. A computer simulation study. In *Journal of colloid and interface science* 356 (2), pp. 672–680. DOI: 10.1016/j.jcis.2011.01.074.

Wood, J.; Gladden, L. F. (2002): Modelling diffusion and reaction accompanied by capillary condensation using three-dimensional pore networks. Part 1. Fickian diffusion and

pseudo-first-order reaction kinetics. In *Chemical Engineering Science* 57 (15), pp. 3033–3045. DOI: 10.1016/S0009-2509(02)00183-5.

Wood, J.; Gladden, L. F.; Keil, F. J. (2002): Modelling diffusion and reaction accompanied by capillary condensation using three-dimensional pore networks. Part 2. Dusty gas model and general reaction kinetics. In *Chemical Engineering Science* 57 (15), pp. 3047–3059. DOI: 10.1016/S0009-2509(02)00184-7.

Xie, Chiyu; Raeini, Ali Q.; Wang, Yihang; Blunt, Martin J.; Wang, Moran (2017): An improved pore-network model including viscous coupling effects using direct simulation by the lattice Boltzmann method. In *Advances in Water Resources* 100, pp. 26–34. DOI: 10.1016/j.advwatres.2016.11.017.

Xiong, Qingrong; Baychev, Todor G.; Jivkov, Andrey P. (2016): Review of pore network modelling of porous media. Experimental characterisations, network constructions and applications to reactive transport. In *Journal of contaminant hydrology* 192, pp. 101–117. DOI: 10.1016/j.jconhyd.2016.07.002.

Ye, Guanghua; Duan, Xuezhi; Zhu, Kake; Zhou, Xinggu; Coppens, Marc-Olivier; Yuan, Weikang (2015): Optimizing spatial pore-size and porosity distributions of adsorbents for enhanced adsorption and desorption performance. In *Chemical Engineering Science* 132, pp. 108–117. DOI: 10.1016/j.ces.2015.04.024.

Ye, Guanghua; Sun, Yuanyuan; Zhou, Xinggu; Zhu, Kake; Zhou, Jinghong; Coppens, Marc-Olivier (2017): Method for generating pore networks in porous particles of arbitrary shape, and its application to catalytic hydrogenation of benzene. In *Chemical Engineering Journal* 329, pp. 56–65. DOI: 10.1016/j.cej.2017.02.036.

Ye, Guanghua; Wang, Haizhi; Duan, Xuezhi; Sui, Zhijun; Zhou, Xinggu; Coppens, M. O.; Yuan, Weikang (2019a): Pore network modeling of catalyst deactivation by coking, from single site to particle, during propane dehydrogenation. In *AIChE J* 65 (1), pp. 140–150. DOI: 10.1002/aic.16410.

Ye, Guanghua; Wang, Haizhi; Zhou, Xinggu; Keil, Frerich J.; Coppens, Marc-Olivier; Yuan, Weikang (2019b): Optimizing catalyst pore network structure in the presence of deactivation by coking. In *AIChE J*. 65 (10), p. 277. DOI: 10.1002/aic.16687.

Ye, Guanghua; Zhou, Xinggu; Yuan, Weikang; Coppens, Marc-Olivier (2016): Probing pore blocking effects on multiphase reactions within porous catalyst particles using a discrete model. In *AIChE J*. 62 (2), pp. 451–460. DOI: 10.1002/aic.15095.

Zeng, Yonghong; Prasetyo, Luisa; Tan, S. Johnathan; Fan, C.; Do, D. D.; Nicholson, D. (2017): On the hysteresis of adsorption and desorption of simple gases in open end and

closed end pores. In *Chemical Engineering Science* 158, pp. 462–479. DOI: 10.1016/j.ces.2016.10.048.

Zhang, Ying; Lam, Frank Leung-Yuk; Yan, Zi-Feng; Hu, Xijun (2006): Review of Kelvin's Equation and Its Modification in Characterization of Mesoporous Materials. In *Chinese Journal of Chemical Physics* 19 (2), pp. 102–108. DOI: 10.1360/cjcp2006.19(2).102.7.

## APPENDICES

### Appendix A Pore network generation input text file

```
1-> 0 1 ! Optimization flag, Visualisation flag
2-> 50 50 1 ! Size of the network along x, y, z
3-> 0 0 0 ! Periodicity in the x, y, z direction
4-> 21e-9 0 ! Spacing of the fixed grid (m), Grid distortion (m)
5-> 3.1d3 ! Skeletal density of the solid (kg/m3)
6-> 50 ! Maximum number of classes in the Pore Size Distribution
7-> 1 ! Number of porosity levels: = 1 means a random pore network, > 1 means a
hierachical pore network

8-> 0.75 ! Pore existence probability for porosity level 1
9-> 1 ! Grid spacing for this porosity level
10-> 20 ! Number of classes for the cumulative pore diameter distribution
11-> 1.00E-09 0
12-> 9.00E-09 0.308537539
13-> 1.00E-08 0.5
14-> 1.10E-08 0.691462461
15-> 1.20E-08 0.841344746
16-> 2.00E-08 1

17-> 2 ! Size of the stencil or pattern
18-> 1 0 ! delta X, delta Y and delta Z for each direction
19-> 0 1 0

20-> 1 ! 1 for cilynder/2 spheres+cylinders
21-> 1 ! 1 non_diagonal pores/ 2 diagonal pores
```

Fig. Ap. A 1 Pore network generation input text file (example)

Appendix B Average textural properties as a function of the number of generations for different set of parameters ( $Z_{\max}=4$ ).

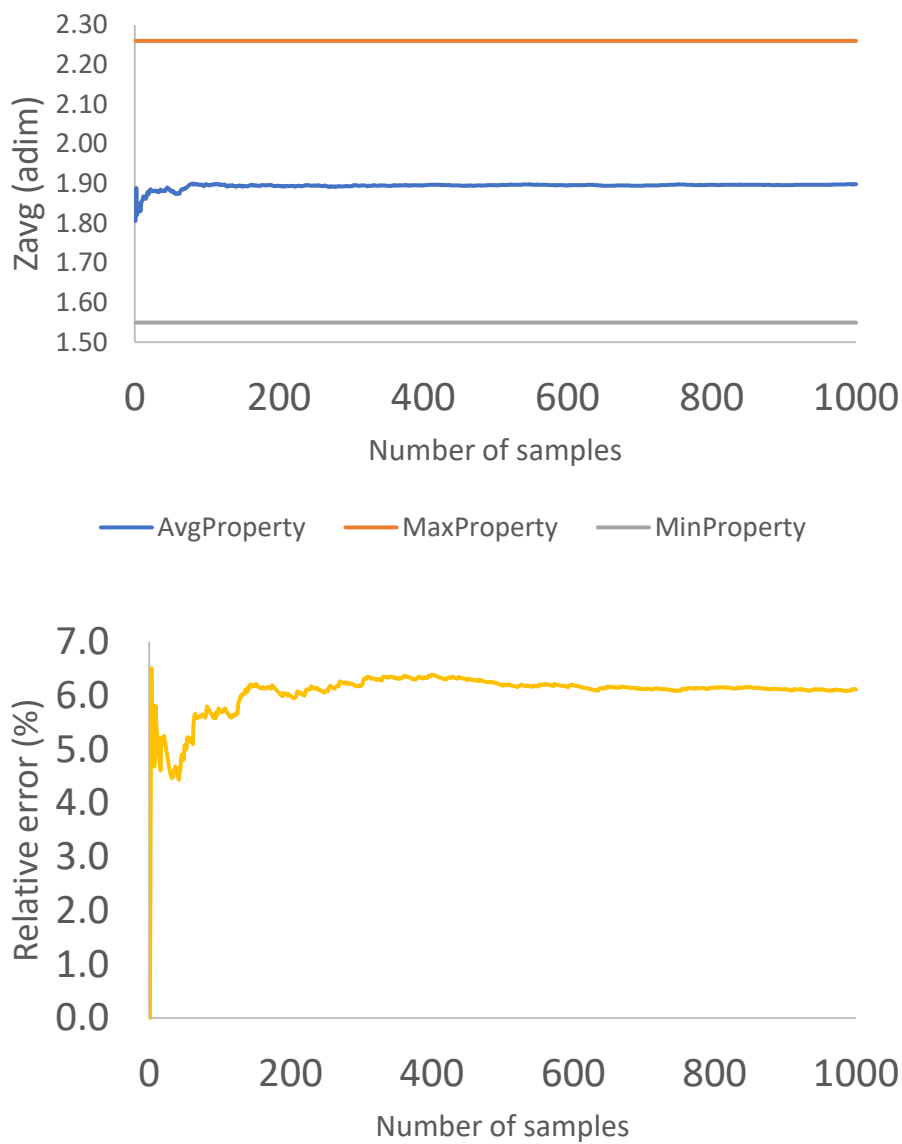


Fig. Ap. B 1. Evolution of the average connectivity and its relative error for a network of dimension 10x10. PSD=(10 ± 1.7) nm, PEP=0.5.

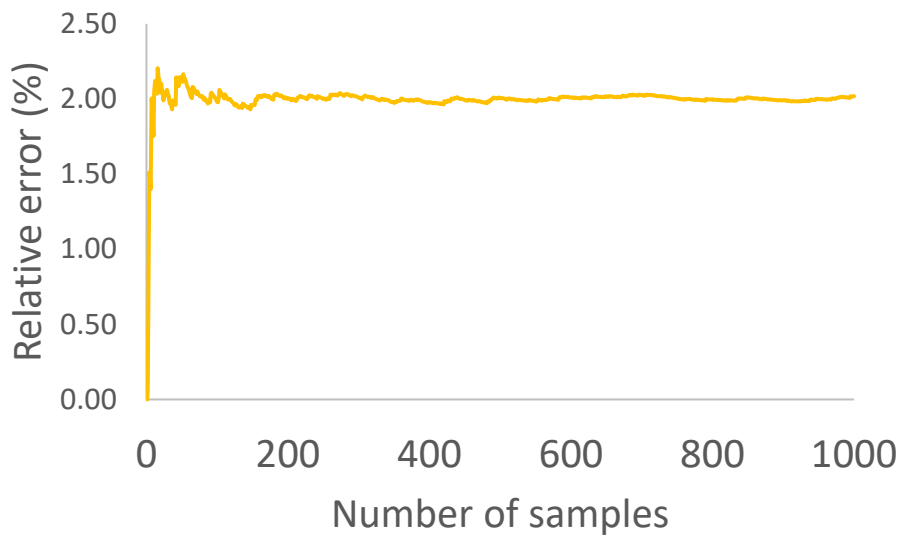
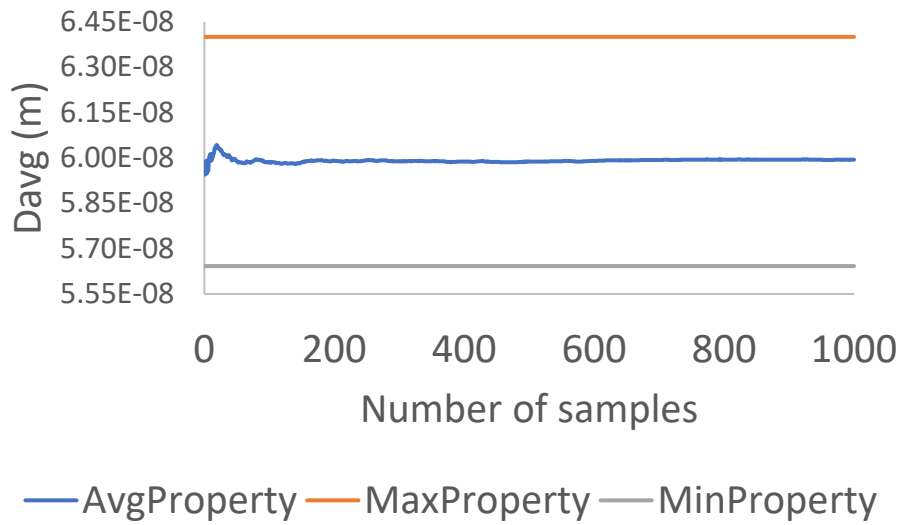
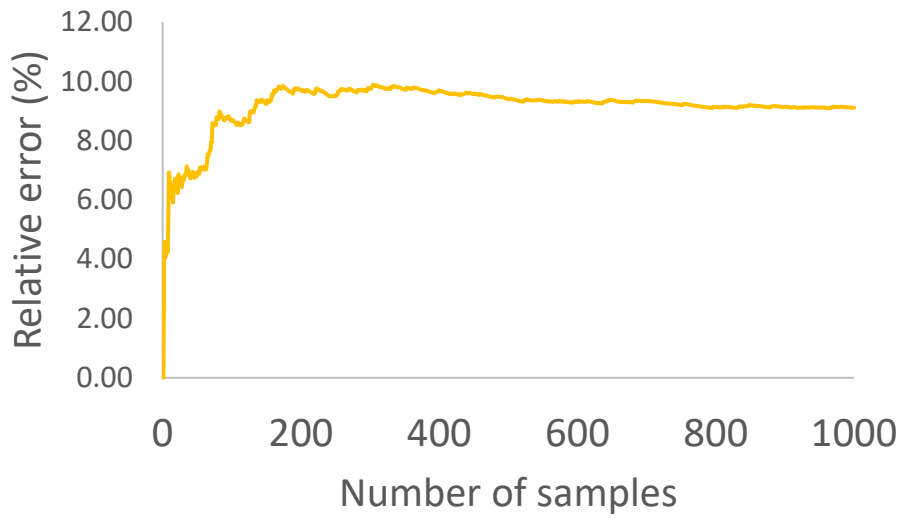
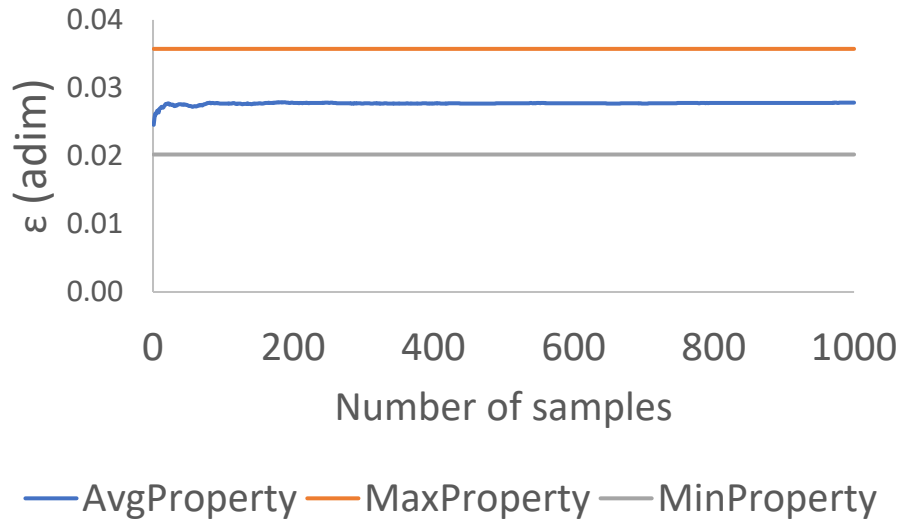
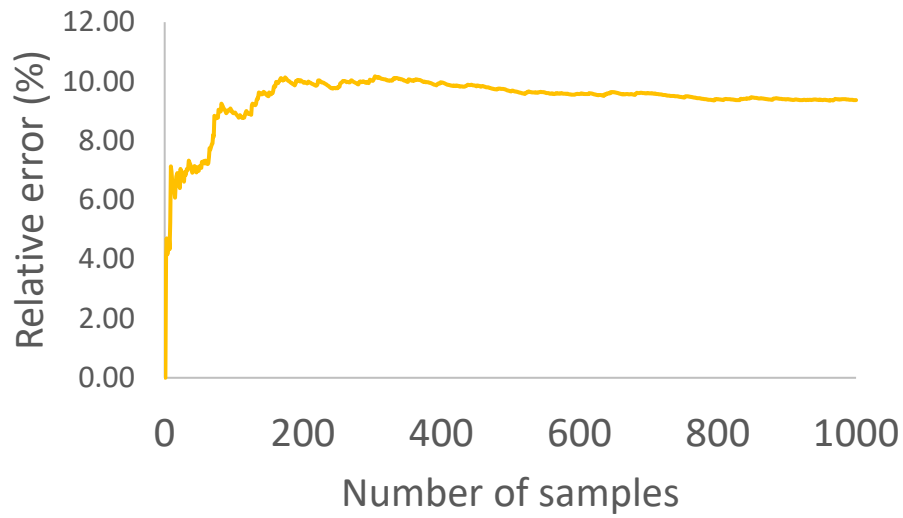
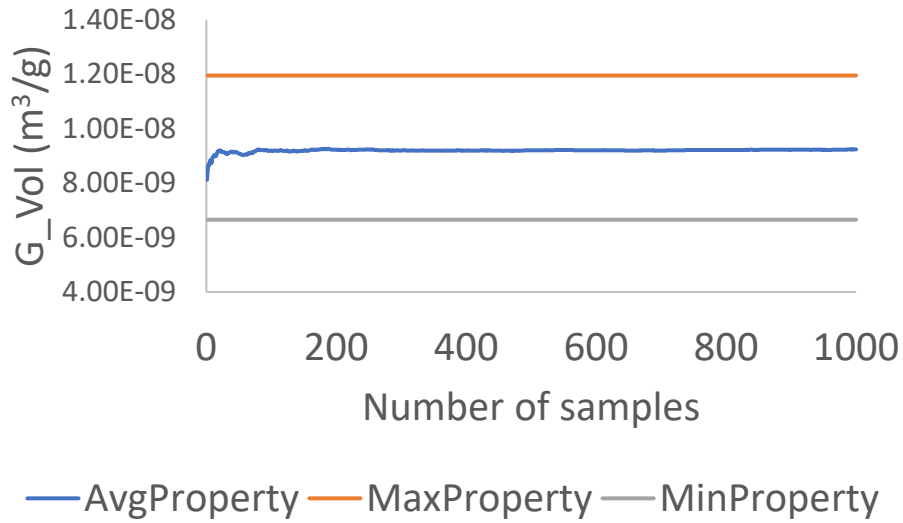


Fig. Ap. B 2. Evolution of the average diameter and its relative error for a network of dimension 10x10. PSD=(10 ± 1.7) nm, PEP=0.5.



**Fig. Ap. B 3. Evolution of the average porosity and its relative error for a network of dimension 10x10. PSD=(10 ± 1.7) nm, PEP=0.5.**



**Fig. Ap. B 4. Evolution of the average specific geometric volume and its relative error for a network of dimension 10x10. PSD=(10 ± 1.7) nm, PEP=0.5.**

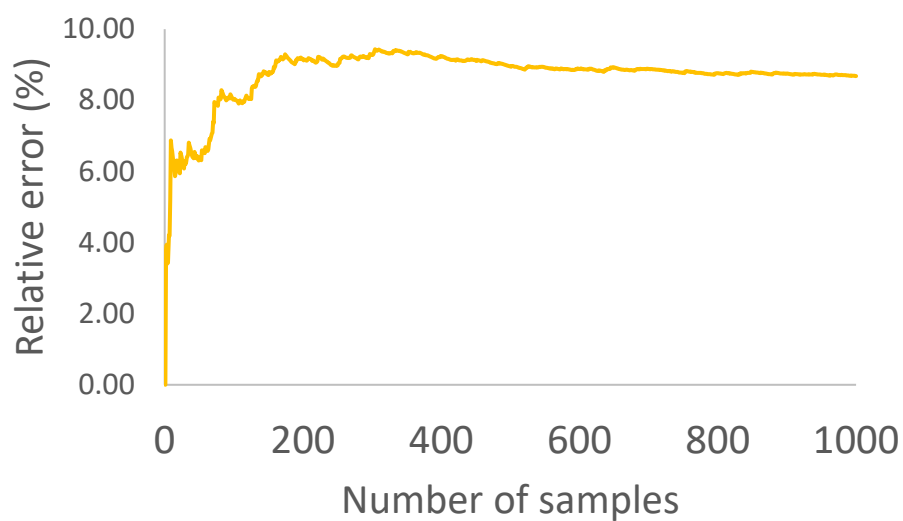
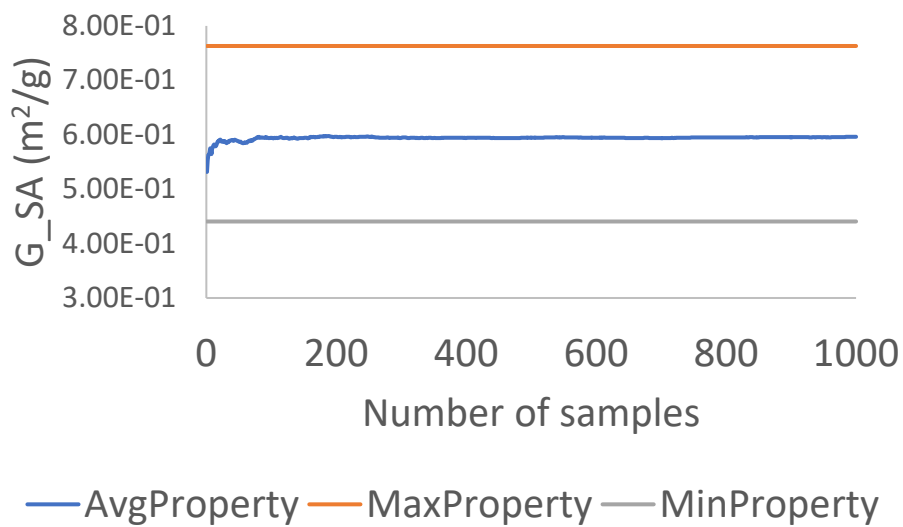


Fig. Ap. B 5. Evolution of the average specific geometric surface and its relative error for a network of dimension  $10 \times 10$ . PSD =  $(10 \pm 1.7)$  nm, PEP = 0.5.

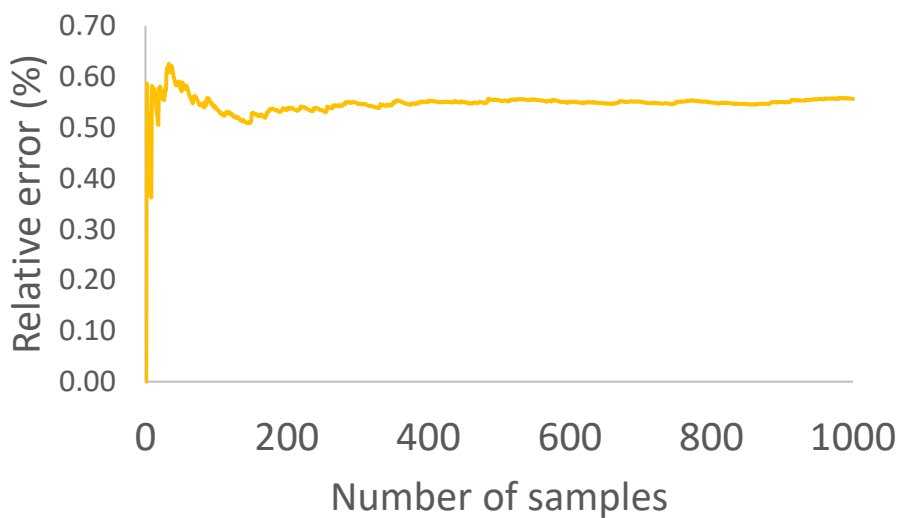
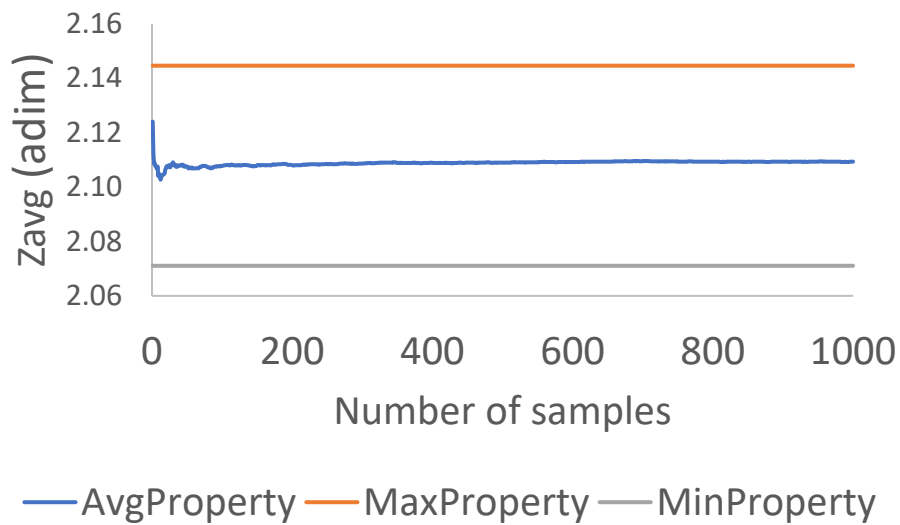


Fig. Ap. B 6. Evolution of the average connectivity and its relative error for a network of dimension 100x100. PSD=(10 ± 1.7) nm, PEP=0.5.

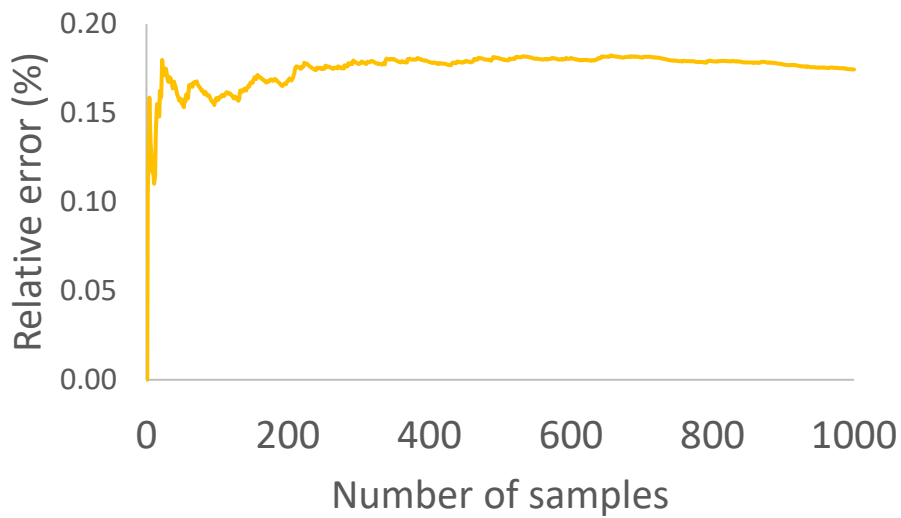
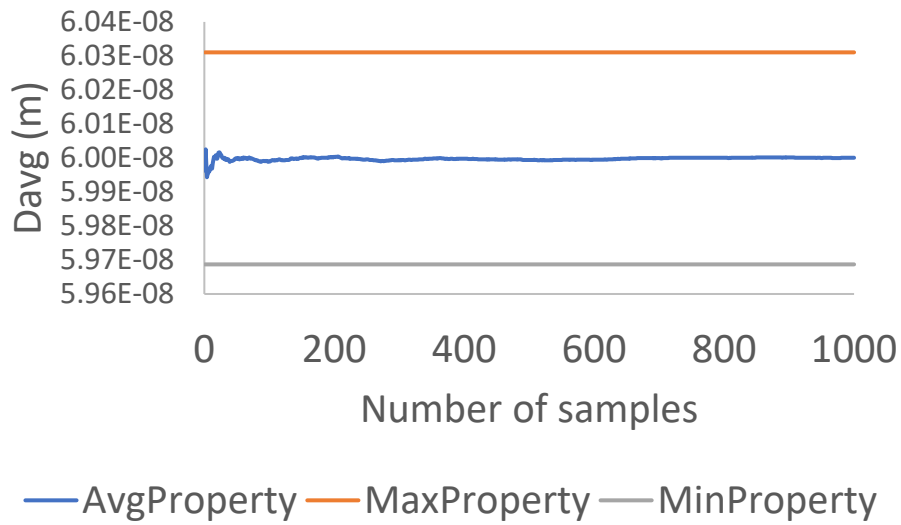
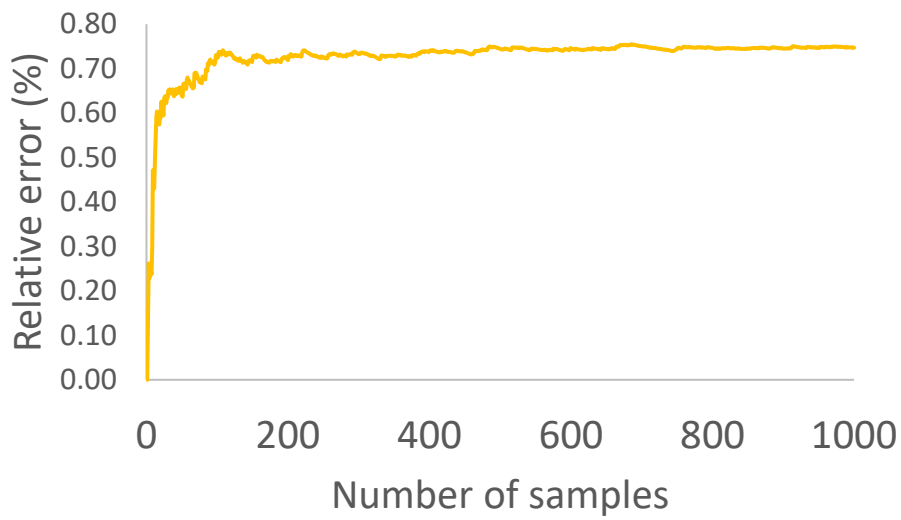
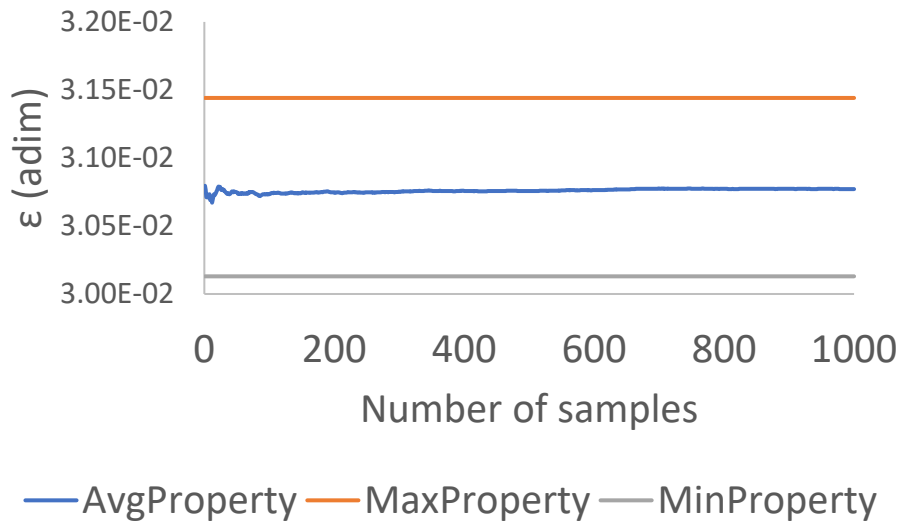
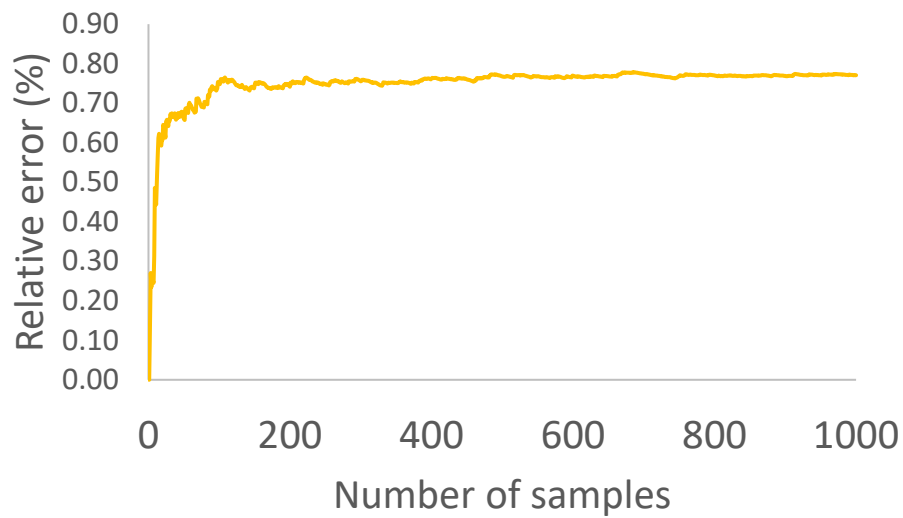
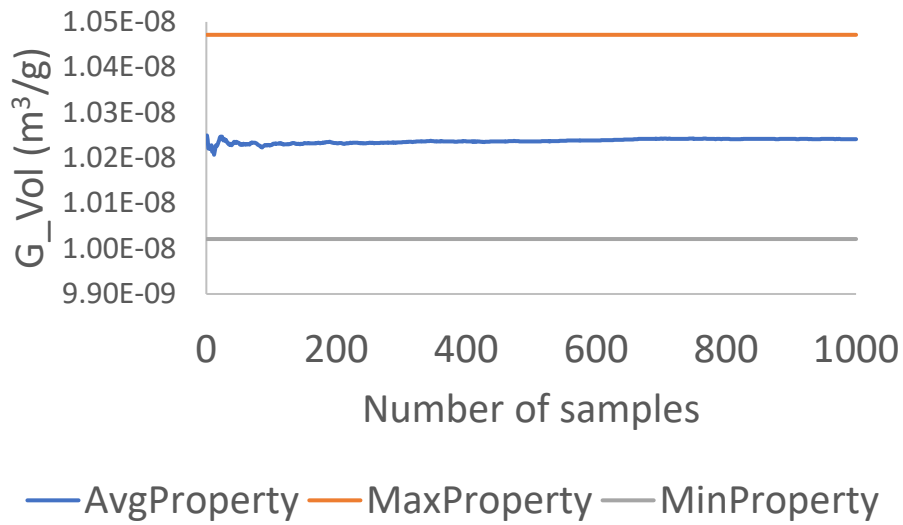


Fig. Ap. B 7. Evolution of the average diameter and its relative error for a network of dimension 100x100. PSD= $(10 \pm 1.7)$  nm, PEP=0.5.



**Fig. Ap. B 8. Evolution of the average porosity and its relative error for a network of dimension 100x100. PSD=(10 ± 1.7) nm, PEP=0.5.**



**Fig. Ap. B 9. Evolution of the average specific geometric volume and its relative error for a network of dimension 100x100. PSD=(10 ± 1.7) nm, PEP=0.5.**

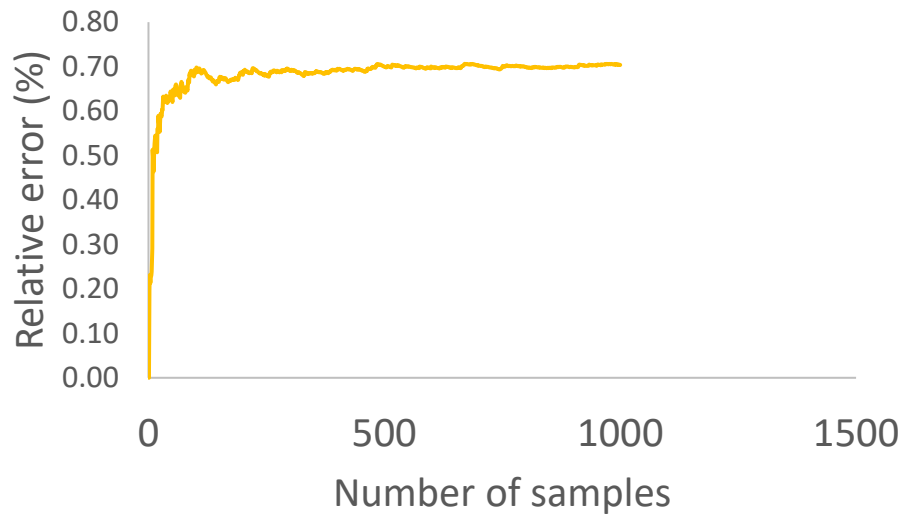
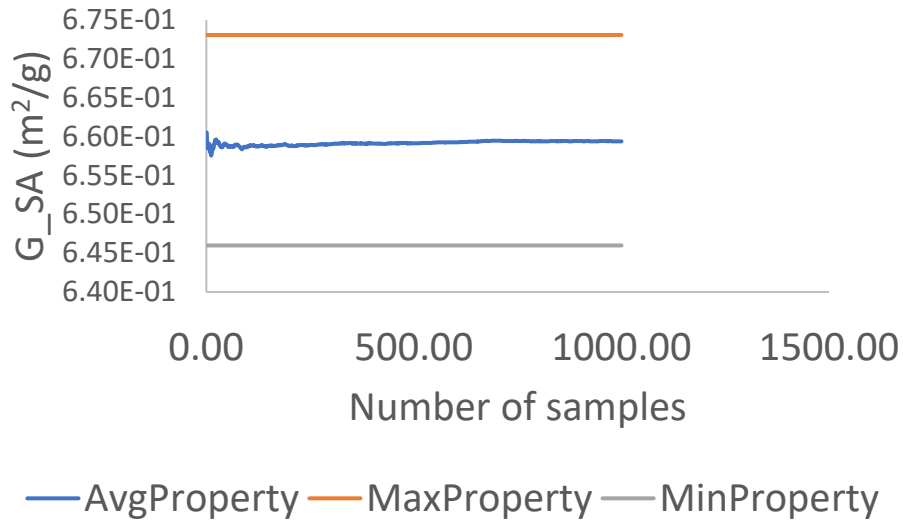


Fig. Ap. B 10. Evolution of the average specific geometric surface and its relative error for a network of dimension  $100 \times 100$ . PSD= $(10 \pm 1.7)$  nm, PEP=0.5.

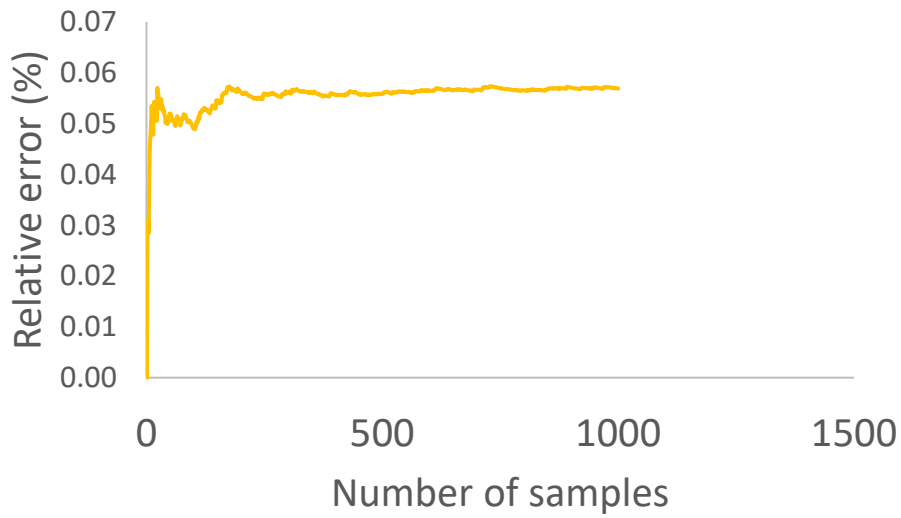
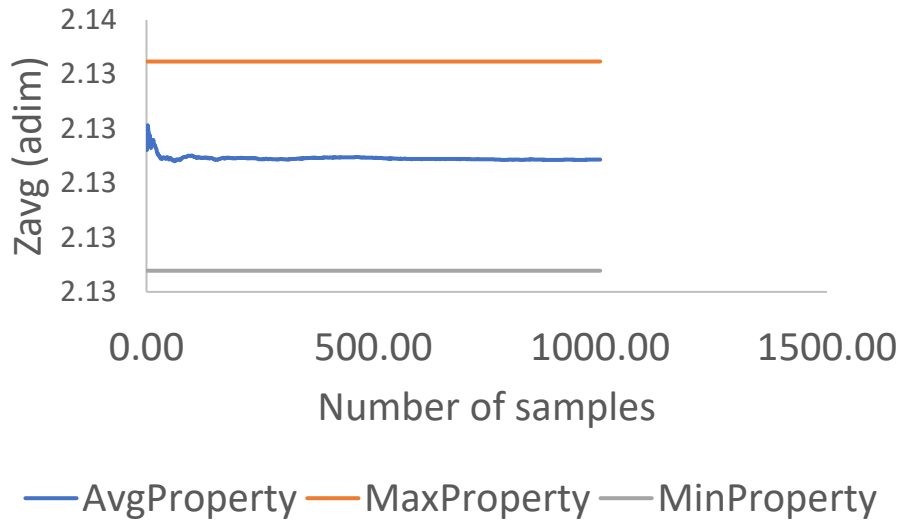


Fig. Ap. B 11. Evolution of the average connectivity and its relative error for a network of dimension 1000x1000. PSD=(10 ± 1.7) nm, PEP=0.5.

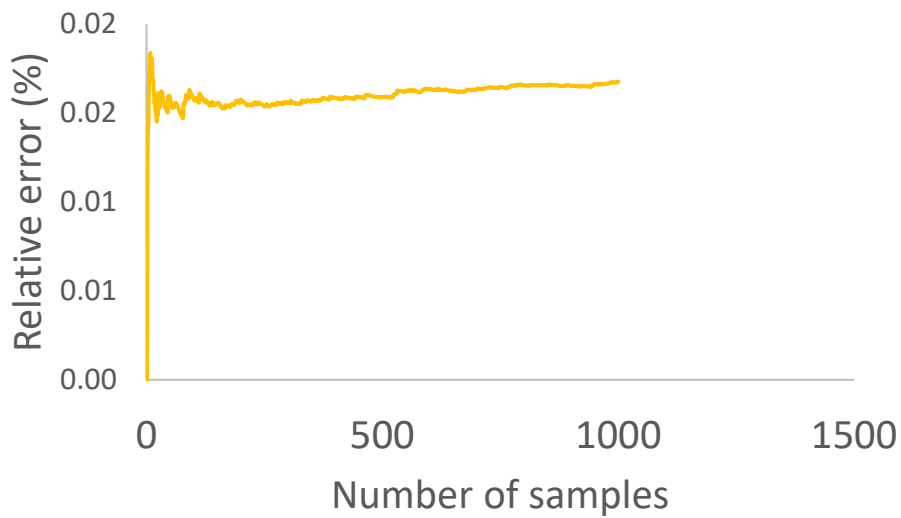
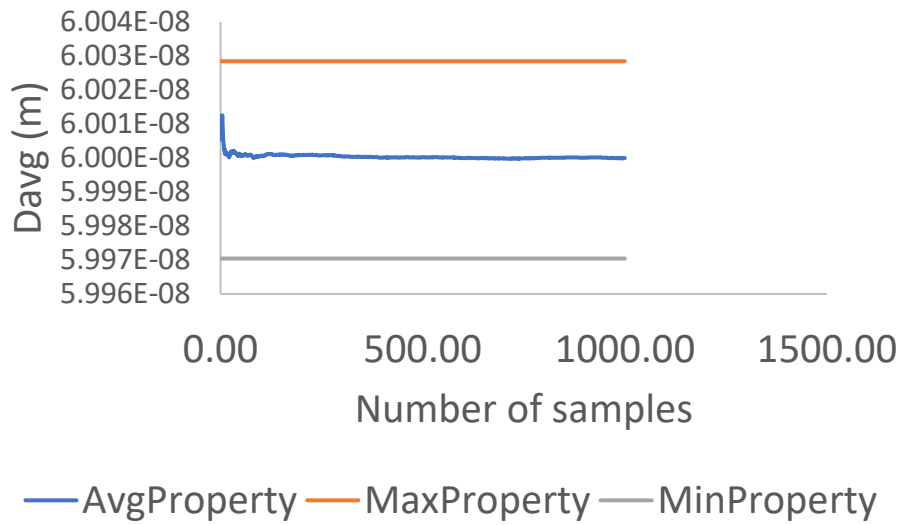


Fig. Ap. B 12. Evolution of the average diameter and its relative error for a network of dimension 1000x1000. PSD=(10 ± 1.7) nm, PEP=0.5.

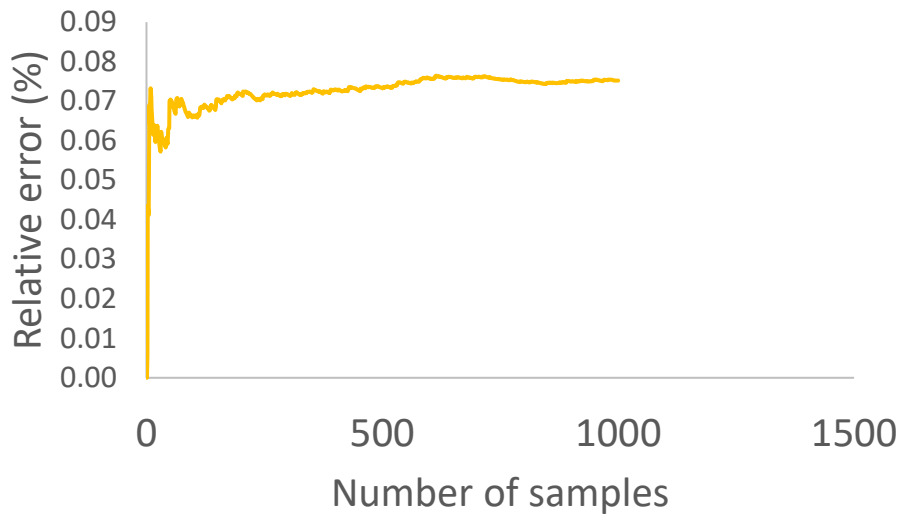
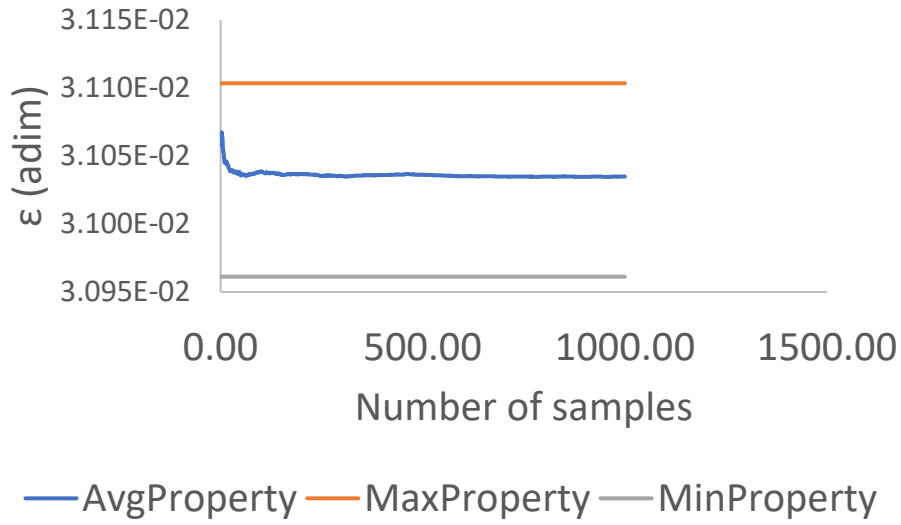


Fig. Ap. B 13. Evolution of the average porosity and its relative error for a network of dimension 1000x1000. PSD=(10 ± 1.7) nm, PEP=0.5.

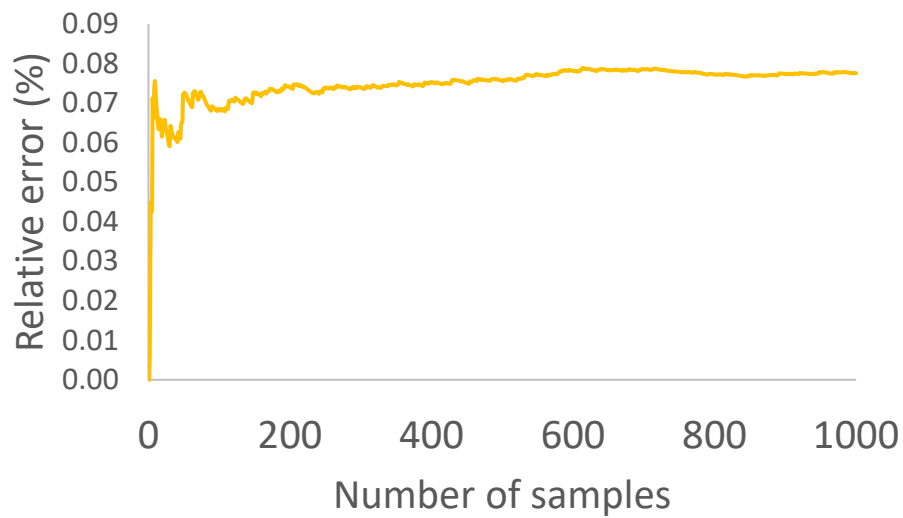
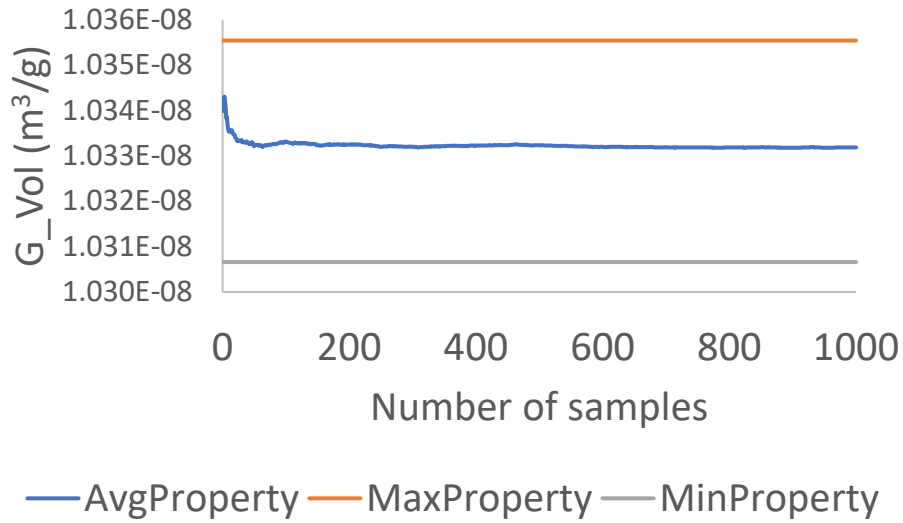


Fig. Ap. B 14. Evolution of the average specific geometric volume and its relative error for a network of dimension 1000x1000. PSD=(10 ± 1.7) nm, PEP=0.5.

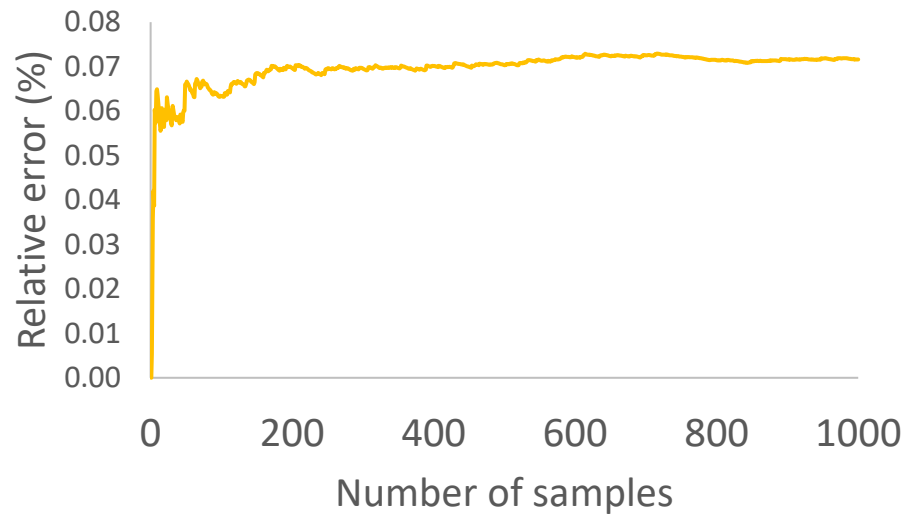
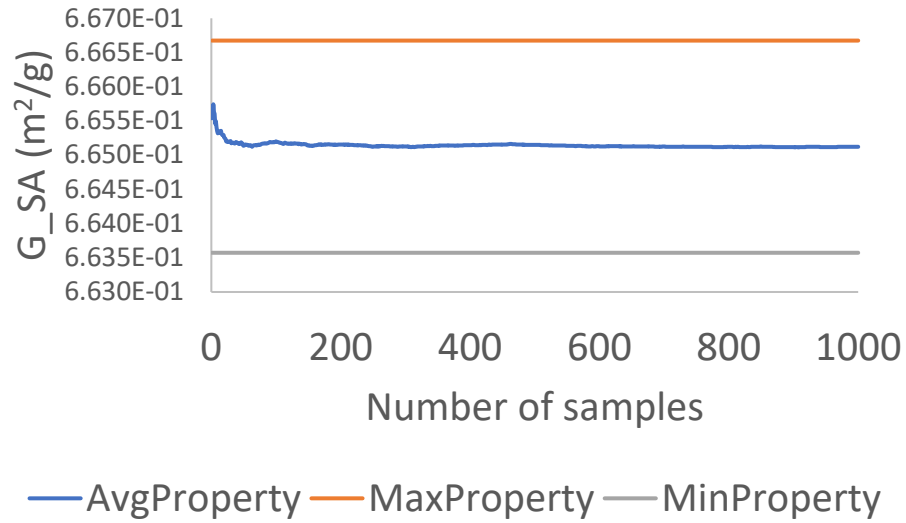
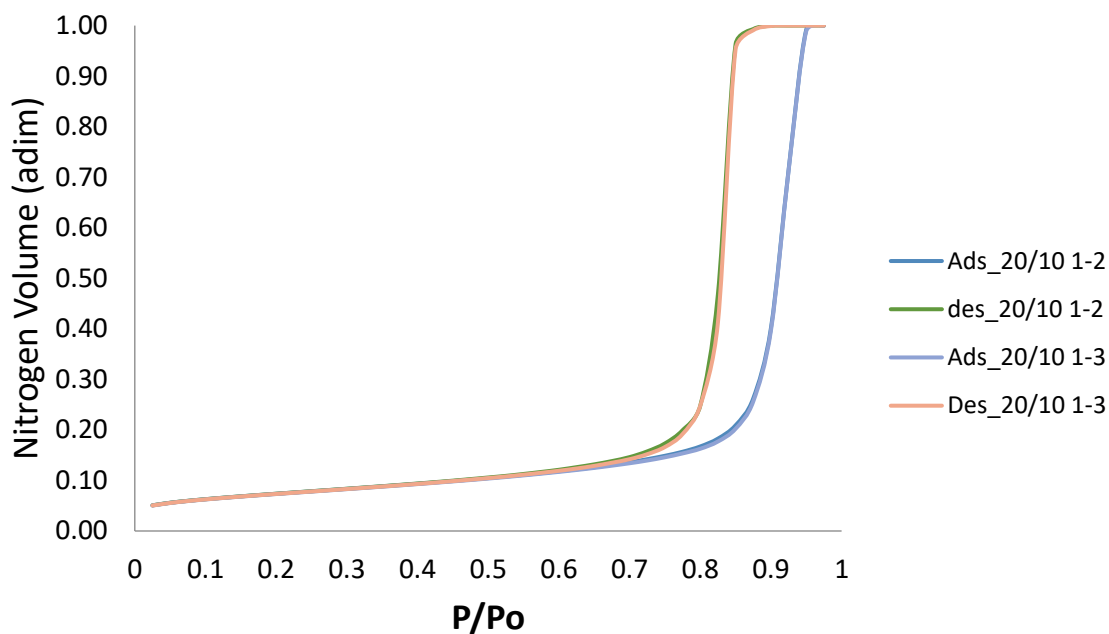


Fig. Ap. B 15. Evolution of the average specific geometric surface and its relative error for a network of dimension 1000x1000. PSD=(10 ± 1.7) nm, PEP=0.5.

## Appendix C Nitrogen isotherms for different hierarchical networks

a)



b)

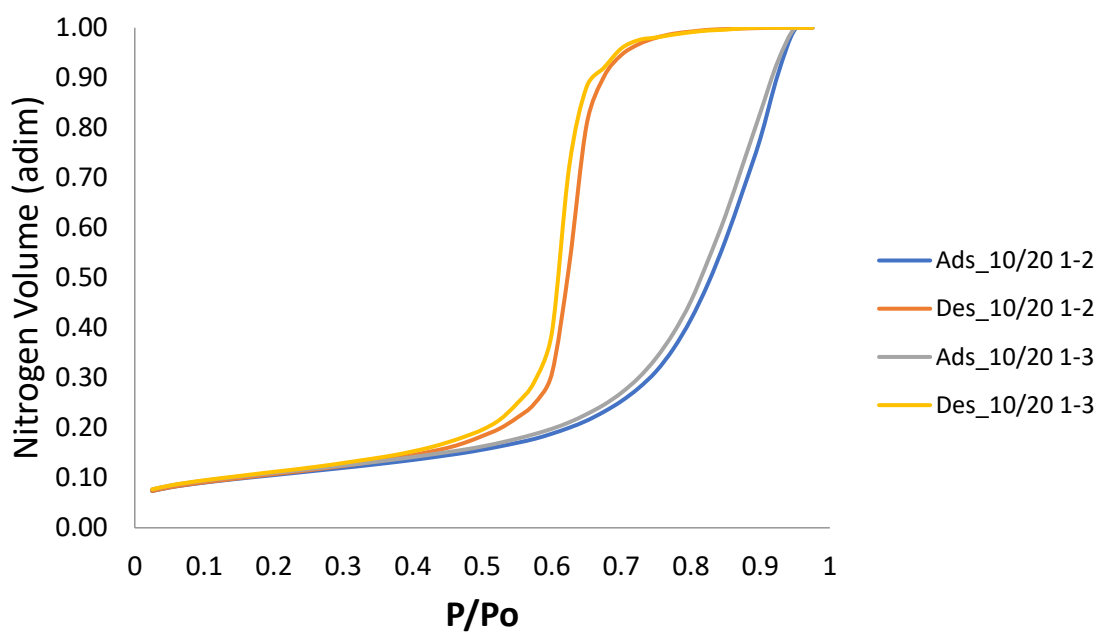
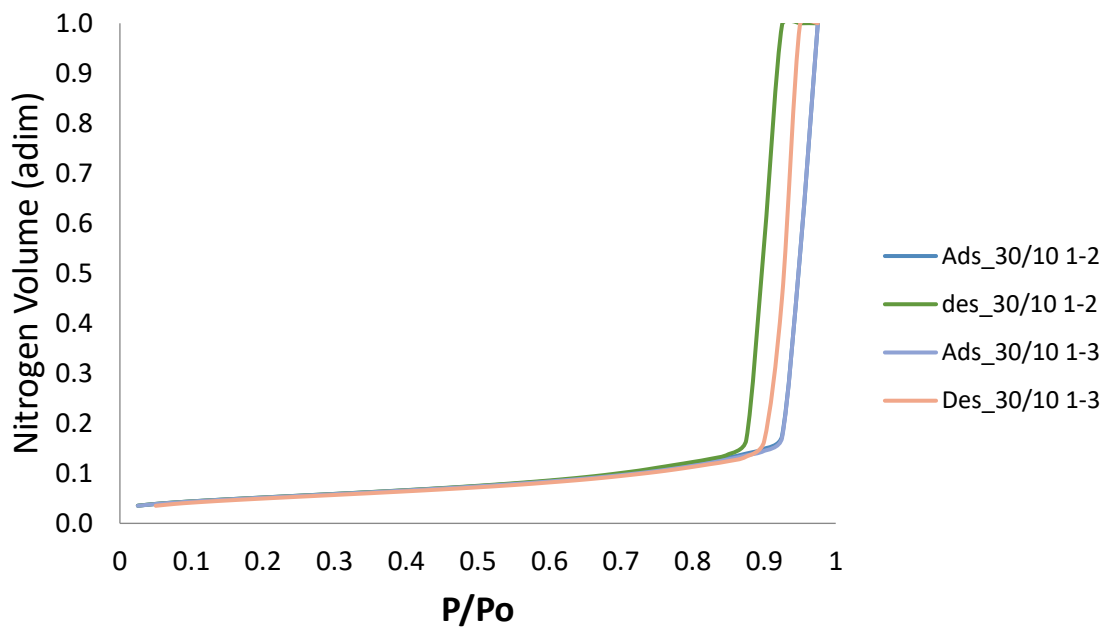


Fig. Ap. C 1. Nitrogen isotherm for two different populations created in different order and grid spacings.  $Z_{max}=4$ ,  $L=21$  nm a) Pop1: PSD= $(10 \pm 4)$  nm, grid spacing=2 or 3; Pop2: PSD= $(20 \pm 4)$  nm, grid spacing=1. b) Pop1: PSD= $(20 \pm 4)$  nm, grid spacing=2 or 3; Pop2: PSD= $(10 \pm 4)$  nm, grid spacing=1.

a)



b)

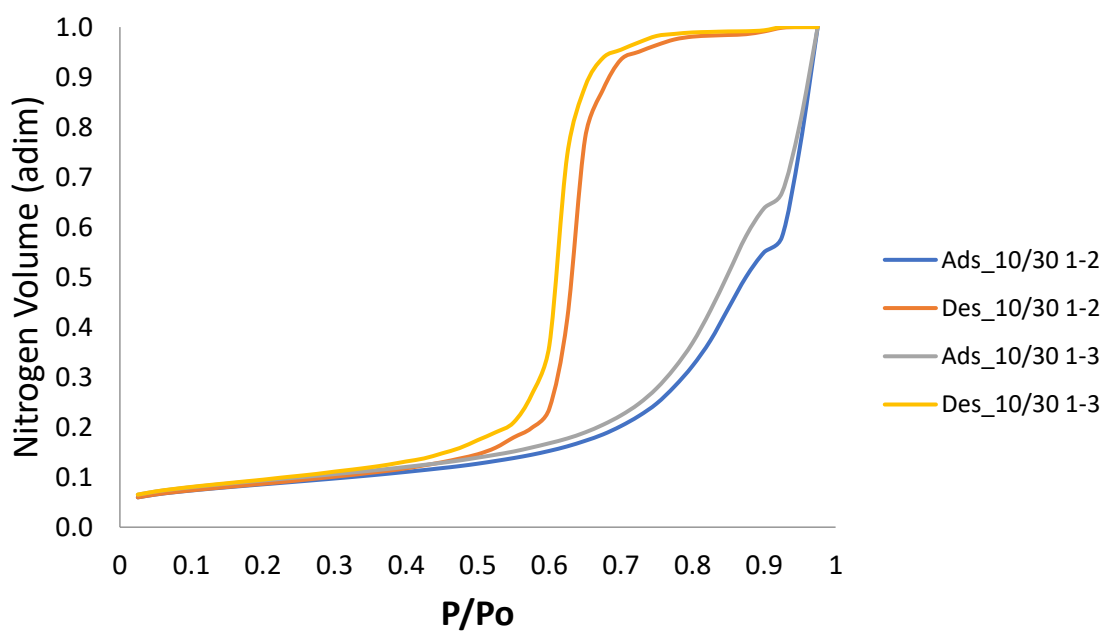
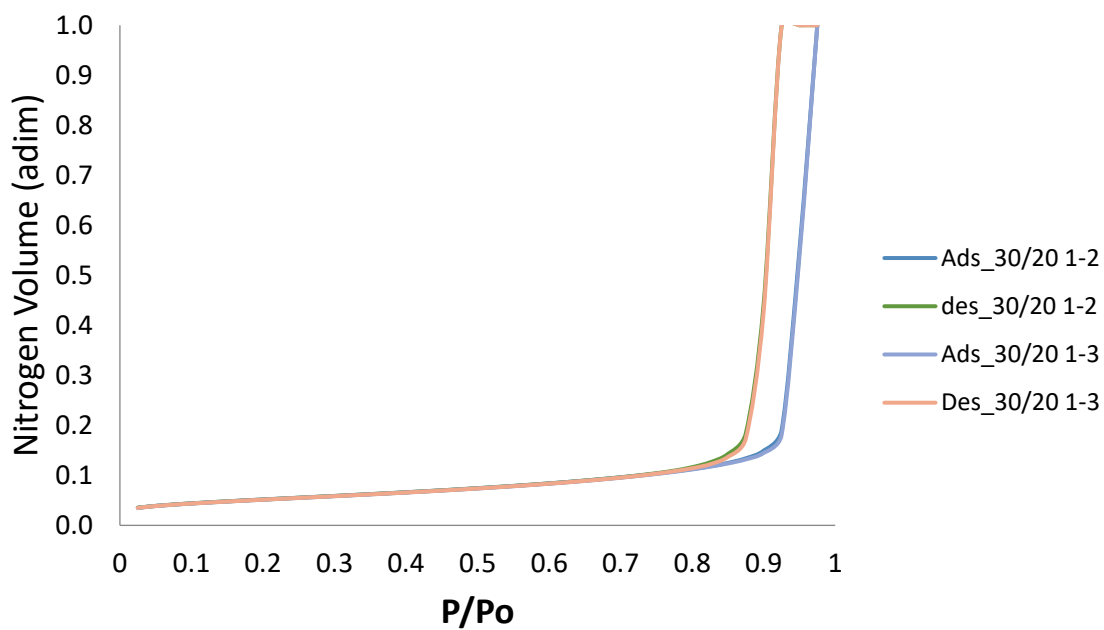


Fig. Ap. C 2. Nitrogen isotherm for two different populations created in different order and grid spacings.  $Z_{max}=4$ ,  $L=21$  nm a) Pop1: PSD= $(30 \pm 4)$  nm, grid spacing=2 or 3; Pop2: PSD= $(10 \pm 4)$  nm, grid spacing=1. b) Pop1: PSD= $(10 \pm 4)$  nm, grid spacing=2 or 3; Pop2: PSD= $(30 \pm 4)$  nm, grid spacing=1.

a)



b)

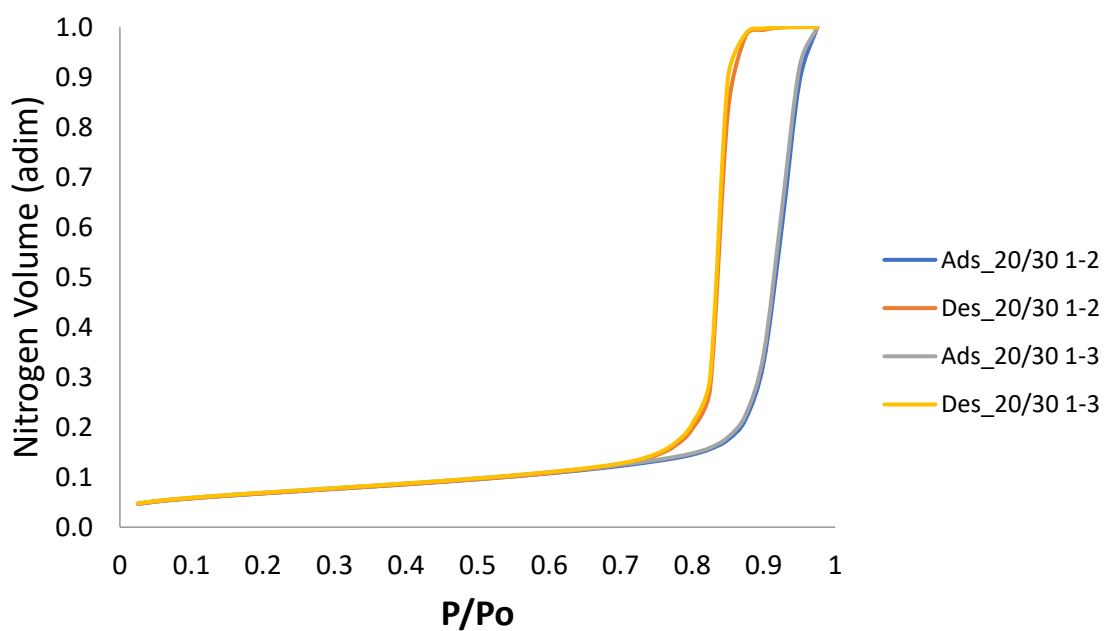
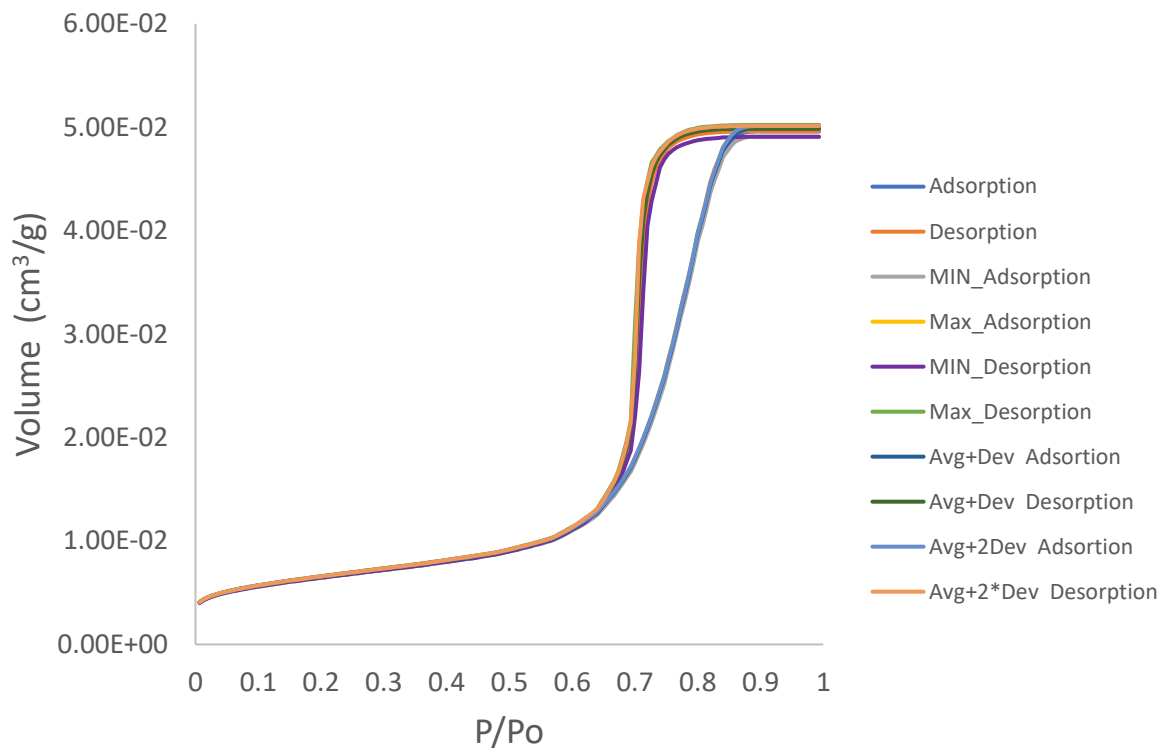
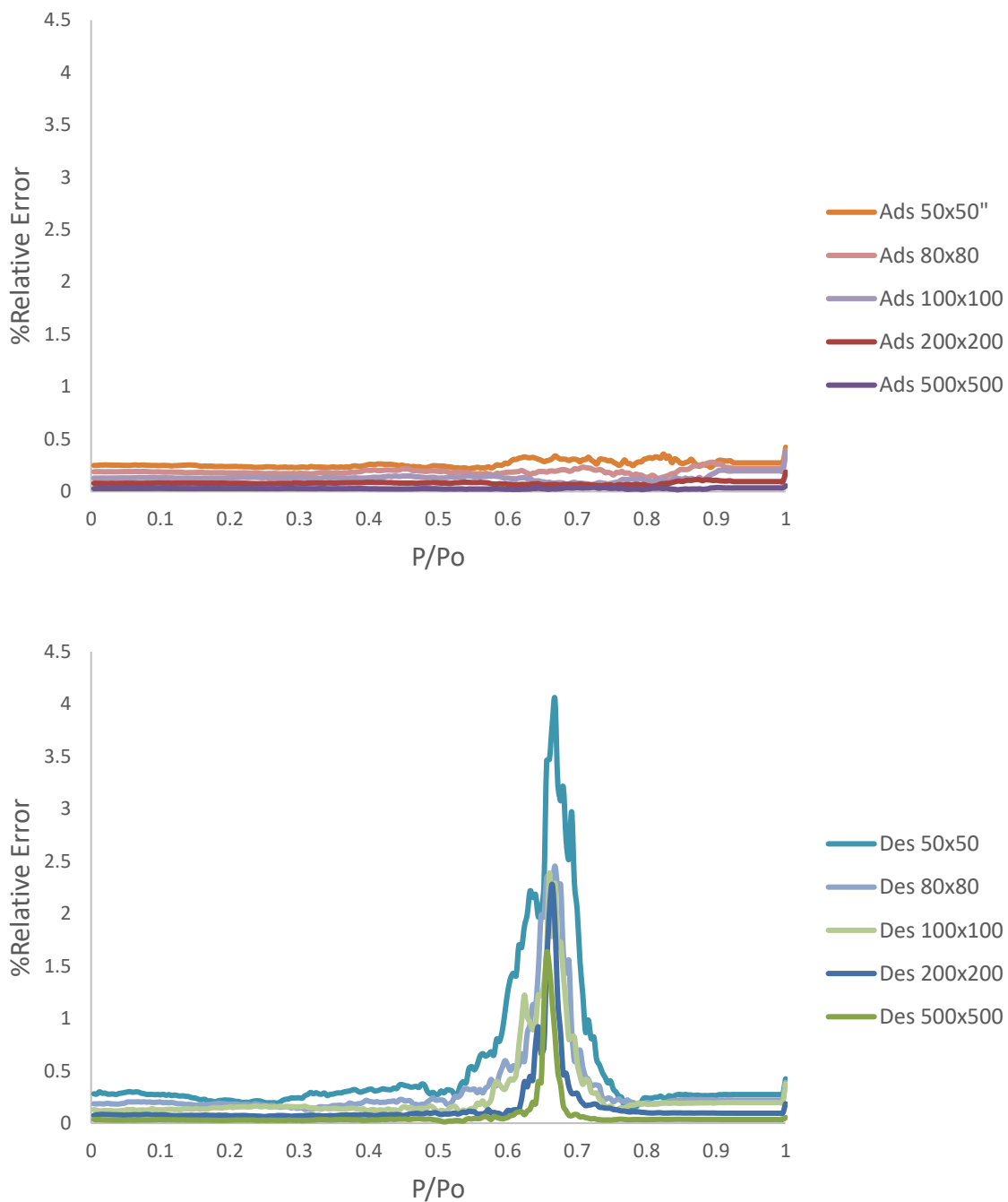


Fig. Ap. C 3. Nitrogen isotherm for two different populations created in different order and grid spacings.  $Z_{max}=4$ ,  $L=21$  nm a) Pop1: PSD= $(20 \pm 4)$  nm, grid spacing=2 or 3; Pop2: PSD= $(30 \pm 4)$  nm, grid spacing=1. b) Pop1: PSD= $(30 \pm 4)$  nm, grid spacing=2 or 3; Pop2: PSD= $(20 \pm 4)$  nm, grid spacing=1.

## Appendix D Repeatability of Nitrogen Sorption Simulations



**Fig. Ap. D 1. Sorption isotherm with minimum and maximum values for all the simulations. Network dimension=100x100 nodes,  $Z_{\max}=4$ , PEP=0.75, L=21 nm, PSD=(20  $\pm$  4) nm. Number of simulations=100.**



**Fig. Ap. D 2. Relative error (standard deviation divided by average value) for the adsorption (Ads) and desorption (Des) branches for different regular network sizes.  $Z_{max}=4$ ,  $PEP=0.75$ ,  $L=21$  nm,  $PSD=(20 \pm 4)$  nm. Number of simulations=100.**

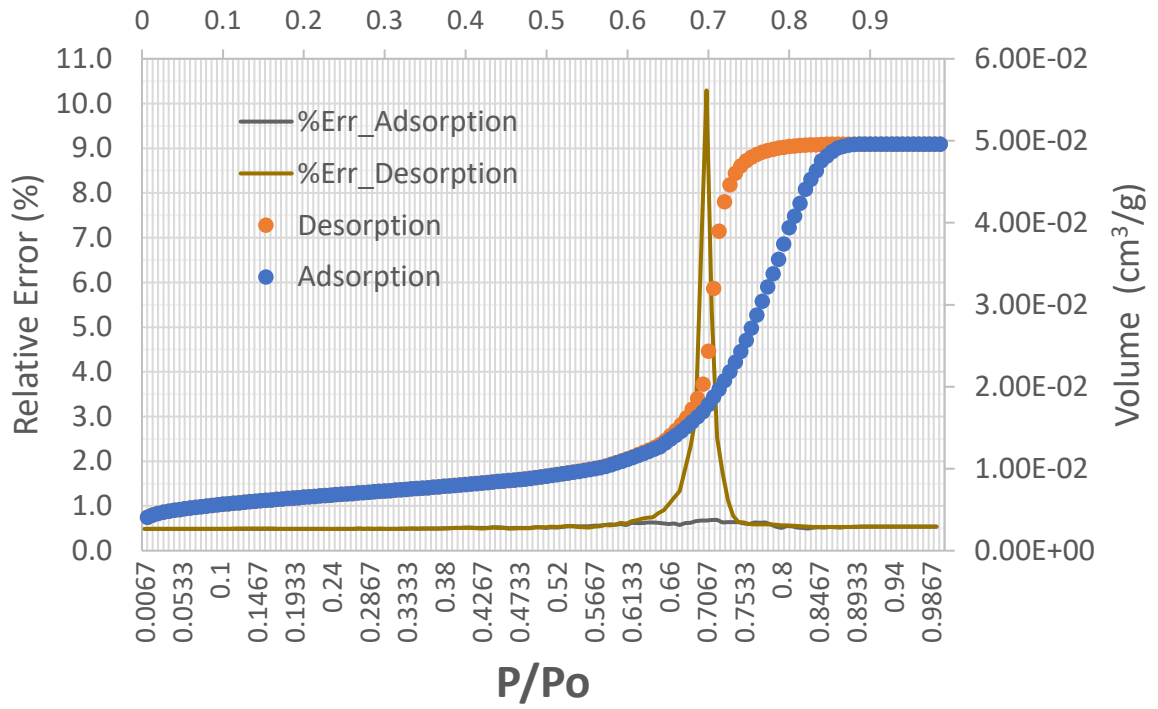


Fig. Ap. D 3. Relative error (standard deviation divided by average value) for the adsorption and desorption branches along the isotherm for a network of 100x100 nodes.  $Z_{\max}=4$ ,  $\text{PEP}=0.75$ ,  $L=21 \text{ nm}$ ,  $\text{PSD}=(20 \pm 4) \text{ nm}$ . Number of simulations=100.

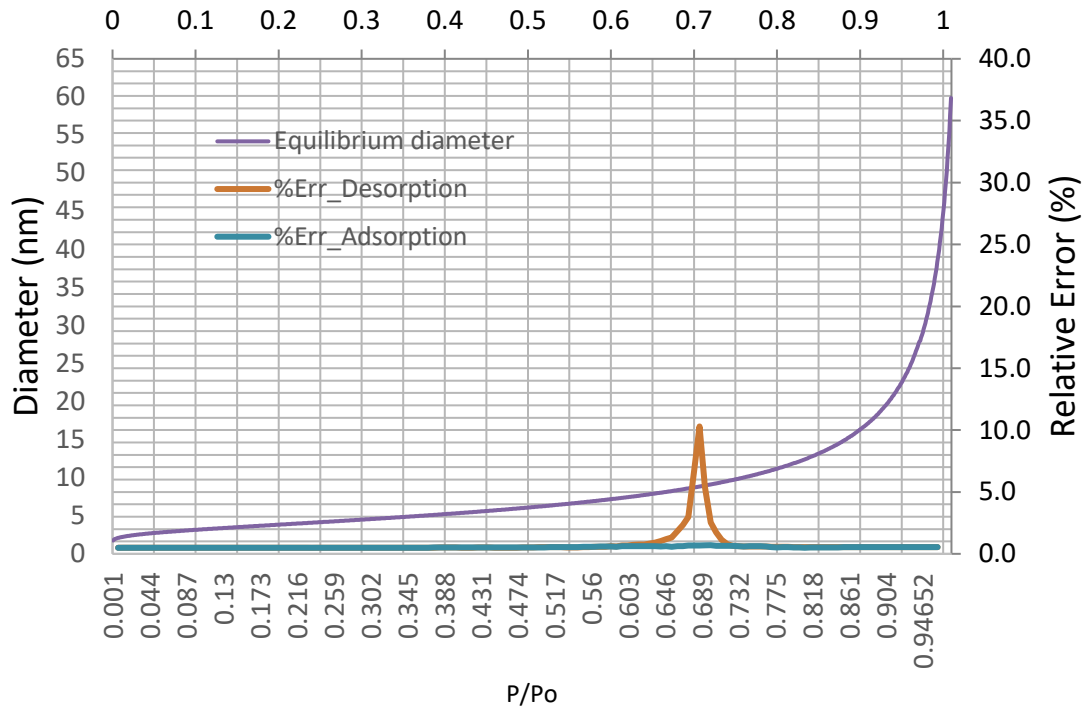


Fig. Ap. D 4. Relative error (standard deviation divided by average value) for the adsorption and desorption branches along the Kelvin-Cohan equation for a network of 100x100 nodes.  $Z_{max}=4$ , PEP=0.75,  $L=21$  nm, PSD=(20 ± 4) nm. Number of simulations=100.